

Journal of
**Electrical and Computer
Engineering Innovations
(JECEI)**

Vol. 9 No. 2 Summer-Fall 2021

| | |
|--|-----|
| Nonlinear Analysis of Colpitts Oscillator using Differential Transform Method <i>A. Ghomi Taheri, F. Setoudeh, M.B. Tavakoli</i> | 127 |
| Fault Diagnosis of a Permanent Magnet Synchronous Generator Wind Turbine <i>S. Khodakaramzadeh, M. Ayati, M.R. Ha'iri-Yazdi</i> | 143 |
| Design of a High-Speed and Low Power CMOS Comparator for A/D Converters <i>F. Shakibaei, A. Bijari, S.H. Zahiri</i> | 153 |
| An Approach for Solving Signal Cancellation Problem in Spherical Microphone Array <i>M. Kalantari</i> | 161 |
| Influence of Phase-Shifting Transformers (PSTs) on the Distance Protection of Transmission Lines and Improving the Performance of Distance Relay <i>H. Sahraei, M. Tolou Askari</i> | 173 |
| Realization of Ultra-Compact All-Optical Universal NOR Gate on Photonic Crystal Platform <i>F. Parandin</i> | 185 |
| Real-time Lane Detection Based on Image Edge Feature and Hough Transform <i>A.A. Fallah, A. Soleimani, H. Khosravi</i> | 193 |
| A Variational Level Set Approach to Multiphase Multi-Object Tracking in Camera Network Base on Deep Features <i>E. Pazouki, M. Rahmati</i> | 203 |
| State Space Modeling and Sliding Mode Current Control of the Grid Connected Multi-Level Flying Capacitor Inverters <i>N. Ghaffari, A. Zakipour, M. Salimi</i> | 215 |
| The Feasibility of Machine-Learning Methods to Extract the Surface Evaporation Quantity Using Satellite Imagery <i>E. Norouzi, S. Behzadi</i> | 229 |
| A High Voltage Isolated Pulse generator Using Magnetic Pulse Compression and Resonant Charging Techniques for Dielectric Barrier Discharge Applications <i>A.H. Nejadmalayeri, A. Bali Lashak, H. Bahrami, I. Soltani</i> | 239 |
| Hybrid Method of Recommender System to Decrement Cold Start and Sparse Data Issues <i>K. Vahidy Rodpysh, S.J. Mirabedini, T. Banirostan</i> | 249 |

JECEI

**Electrical and Computer
Engineering Innovations (JECEI)**

Electrical and Computer Engineering Innovations

Vol. 9, No. 2 Summer-Fall 2021

Semiannual Publication

Volume 9, Issue 2, Summer-Fall 2021



Editor-in-Chief:

Prof. Reza Ebrahimpour

Faculty of Computer Engineering, Shahid Rajaei University, Iran

Associate Editors:

Prof. Muhammad Taher Abuelma'atti

Faculty of Electrical Engineering, King Fahd University of Petroleum and Minerals, Saudi Arabia

Prof. Mojtaba Agha Mirsalim

Department of Electrical Engineering, Amirkabir University of Technology, Iran

Prof. Vahid Ahmadi

Faculty of Electrical and Computer Engineering, Tarbiat Modares University, Iran

Prof. Seyed Mohammad Taghi Bathaee

Faculty of Electrical Engineering, Power Department, K. N. Toosi University of Technology, Iran

Prof. Reza Ebrahimpour

Faculty of Computer Engineering, Shahid Rajaei University, Iran

Prof. Fary Ghassemloooy

Faculty of Engineering and Environment, Northumbria University, UK

Prof. Nosrat Granpayeh

Faculty of Electrical Engineering, K. N. Toosi University of Technology, Iran

Prof. Erich Leitgeb

Institute of Microwave and Photonic Engineering, Graz University of Technology, Austria

Prof. Juan C. Olivares-Galvan

Department of Energy, Universidad Autónoma Metropolitana, Mexico

Prof. Saeed Olyaei

Faculty of Electrical Engineering, Shahid Rajaei University, Iran

Prof. Masoud Rashidinejad

Department of Electrical Engineering, Shahid Bahonar University, Iran

Prof. Raj Senani

Division of Electronics and Communication Engineering, Netaji Subhas Institute of Technology, India

Prof. Vahid Tabataba Vakili

School of Electrical Engineering, Iran University of Science and Technology, Iran

Prof. Ahmed F. Zobaa

Department of Electronic and Computer Engineering, Brunel University, UK

Dr. Debasis Giri

Department of Computer Science and Engineering, Haldia Institute of Technology, India

Dr. Peyman Naderi

Faculty of Electrical Engineering, Shahid Rajaei University, Iran

Dr. Mahmood Seifouri

Faculty of Electrical Engineering, Shahid Rajaei University, Iran

Dr. Mohammad Shams Esfand Abadi

Faculty of Electrical Engineering, Shahid Rajaei University, Iran

Dr. Shahriar Shirvani Moghaddam

Faculty of Electrical Engineering, Shahid Rajaei University, Iran

Dr. Jian-Gang Wang

Department of Computer Vision and Image Understanding, Institute for Infocomm Research, Singapore

Executive Manager: Dr. Masoumeh Safkhani

Faculty of Computer Engineering, Shahid Rajaei University, Iran

Responsible Director: Prof. Saeed Olyaei

Faculty of Electrical Engineering, Shahid Rajaei University, Iran

Assisted by: Mrs. Fahimeh Hosseini

License Holder: Shahid Rajaei Teacher Training University (SRTTU)

Address: Lavizan, 16788-15811, Tehran, Iran.

Journal of Electrical and Computer Engineering Innovations

Vol. 9; Issue 2: 2021

Contents

| | |
|---|------------|
| Nonlinear Analysis of Colpitts Oscillator using Differential Transform Method <i>A. Ghomi Taheri, F. Setoudeh, M.B. Tavakoli</i> | 127 |
| Fault Diagnosis of a Permanent Magnet Synchronous Generator Wind Turbine <i>S. Khodakaramzadeh, M. Ayati, M.R. Ha'iri-Yazdi</i> | 143 |
| Design of a High-Speed and Low Power CMOS Comparator for A/D Converters <i>F. Shakibaei, A. Bijari, S.H. Zahiri</i> | 153 |
| An Approach for Solving Signal Cancellation Problem in Spherical Microphone Array <i>M. Kalantari</i> | 161 |
| Influence of Phase-Shifting Transformers (PSTs) on the Distance Protection of Transmission Lines and Improving the Performance of Distance Relay <i>H. Sahraei, M. Tolou Askari</i> | 173 |
| Realization of Ultra-Compact All-Optical Universal NOR Gate on Photonic Crystal Platform <i>F. Parandin</i> | 185 |
| Real-time Lane Detection Based on Image Edge Feature and Hough Transform <i>A.A. Fallah, A. Soleimani, H. Khosravi</i> | 193 |
| A Variational Level Set Approach to Multiphase Multi-Object Tracking in Camera Network Base on Deep Features <i>E. Pazouki, M. Rahmati</i> | 203 |
| State Space Modeling and Sliding Mode Current Control of the Grid Connected Multi-Level Flying Capacitor Inverters <i>N. Ghaffari, A. Zakipour, M. Salimi</i> | 215 |
| The Feasibility of Machine-Learning Methods to Extract the Surface Evaporation Quantity Using Satellite Imagery <i>E. Norouzi, S. Behzadi</i> | 229 |
| A High Voltage Isolated Pulse generator Using Magnetic Pulse Compression and Resonant Charging Techniques for Dielectric Barrier Discharge Applications <i>A.H. Nejadmalayeri, A. Bali Lashak, H. Bahrami, I. Soltani</i> | 239 |
| Hybrid Method of Recommender System to Decrement Cold Start and Sparse Data Issues <i>K. Vahidy Rodpysh, S.J. Mirabedini, T. Baniroostam</i> | 249 |



Research paper

Nonlinear Analysis of Colpitts Oscillator using Differential Transform Method

A. Ghomi Taheri¹, F. Setoudeh^{2,*}, M.B. Tavakoli¹

¹Department of Electrical Engineering, Arak Branch, Islamic Azad University, Arak, Iran.

²Department of Electrical Engineering, Arak University of Technology, Arak, Iran.

Article Info

Article History:

Received: 22 June 2020
Reviewed: 28 August 2020
Revised: 27 October 2020
Accepted: 26 December 2020

Keywords:

Differential transform method
Nonlinear analysis
Runge-Kutta
Lyapunov exponent
Analytically
Wolf method

*Corresponding author's Email
Address:

f.setoudeh@arakut.ac.ir

Abstract

Background and Objectives: The Differential transform method (DTM) is used in the analysis of ordinary, partial, and high-order differential equations. Recently, the DTM is used in the nonlinear analysis of physical nonlinear dynamic systems.

Methods: The DTM method is used to analyze and analytically solve the nonlinear mathematical model of bias current-controlled Colpitts oscillator with variable coefficients. Intervals of the validity of the proposed method are evaluated by using the fourth order Runge-Kutta method (RK4M). In this note, the Lyapunov exponent (LE) can be used to analyze the Colpitts oscillator. By using DTM, the LEs are calculated analytically with unknown parameters in a short interval of time $t \in [0, 3 \text{ Sec}]$.

Results: In this paper, intervals of the validity of the proposed method are evaluated using RK4M. In addition, LEs are calculated using analytical and numerical methods based on DTM technique and Wolf method, respectively. LEs of the proposed system are presented as a function of the control parameter to confirm the applied technique's usefulness.

Conclusion: By comparing these two methods, the proposed DTM analytical technique is relatively more precise. Simulation results confirmed the impact of different parameters on LEs with two different initial conditions. The results show good accuracy of the DTM in short time intervals $t \in [0, 3 \text{ Sec}]$.

©2021 JECEI. All rights reserved.

Introduction

Today, the study of nonlinear systems is an important topic for scientific research. Among the important topics discussed in nonlinear systems, we can mention behavioral analysis and control. Nonlinear systems show different behaviors such as stability, periodic, quasi-periodic, and chaotic [1], [2]. Among the differences between linear and nonlinear systems, we can mention their different behaviors. In linear systems, equilibrium point stability can be used to evaluate the stability of a dynamic system for all initial conditions.

In case of instability, the system response will be unstable for all initial conditions. However, in nonlinear systems, if the system equilibrium point is stable, for some initial conditions, the system response will be convergent (stable), and for others, the system response will be divergent (unstable), which is difficult to detect [3], [4]. Lyapunov exponent (LE) is one of the methods of behavioral analysis for nonlinear system [5]-[7]. Many methods are used to calculate the LE based on a mathematical model [8]-[11]. One of the important features of dynamic systems are their sensitivity to the initial conditions [12], [13]. Therefore, determining the

degree of this sensitivity is not an easy task. LE is one of the tools used for this purpose [14], [15]. There are various methods, such as Jacobian-based and direct methods for calculating LE [16], [17]. Several algorithms have been proposed to calculate LE using time series based on the direct method [17]-[20]. The Wolff algorithm searches for time series for close points in space. In this method, the proximity points in one direction is used to calculate LE [20], [21]. In [22] genetic algorithm is used to calculate the LE. In [23], a new method is applied for LE calculation based on QR decomposition [23]. Liao used a novel technique for sensitivity analysis of the derivatives of the Largest Lyapunov exponent (LLE) using least mean squares error based on known parameters [24].

Many engineering issues, including electrical engineering, are inherently nonlinear. All of these problems are described by ordinary and partial differential equations. Recently, different analytical methods are applied to solve nonlinear differential equations such as differential transform method (DTM), multi-stage differential transform method (MsDTM), Elzaki transform method (ETM), Adomian decomposition method (ADM) and other methods [25]-[32].

Various analytical methods have been proposed for solving nonlinear systems, but we are looking for simple, fast, and low-error methods. In [33], [34], the DTM is used to solve ordinary, partial and high-order differential equations. In this method, to solve linear and nonlinear differential equations, a time series based on the Taylor series is estimated [35]. The main advantages of this method are no linearization and discretization. This method, like other methods, has disadvantages, one of which is to obtain an incomplete series from the system. This system does not show the actual behavior of the system, but in most cases, offers a very good approximation of the correct solution in short time intervals. In fact, this method cannot provide a good answer in big times. Recently, the DTM has been used to solve physical nonlinear dynamic systems. In [36], the DTM is used to analytical solution of the cantilever beam system. In [37], to solve the Lane-Emden type equations analytically in different physical models, the improved DTM is used.

In [38], [39], the Duffing oscillator is solved using analytical and numerical methods based on DTM technique and Fourth order Runge-Kutta method (RK4M), respectively [38], [39]. In [40], the DTM is used to approximate an analytical solution for a dynamic model of the epidemiology of Corona-virus [40]. In this paper, the Colpitts oscillator is considered an example of a sine oscillator. To make a general conclusion about the design of this type of oscillators, there are many reasons to study and analyze this circuit, such as:

- 1- Colpitts oscillator is widely used in telecommunication systems.
- 2- The operating frequency of these oscillators, depending on the technology, which can vary from a few Hz to the microwave range (Gigahertz).
- 3- Since the transistor is a nonlinear device, therefore this oscillator has an intrinsic nonlinearity property.
- 4- Colpitts oscillator has nonsymmetrical and generic properties.
- 5- This oscillator have rich, dynamic behavior such as periodic and bursting oscillations [41].

In this paper, a new method for nonlinear analysis of colpitts oscillator is presented analytically using DTM technique. Another point that can be considered as an innovation of this research is the calculation of LE analytically using DTM.

Review of Differential Transform Method (DTM)

If $x(t)$ is an analytic continuous and derivative function, therefore, using the differential transform of $x(t)$ is shown as follow:

$$X(k) = \frac{1}{k!} \left[\frac{d^k x(t)}{dt^k} \right]_{t=t_0} \quad (1)$$

where $k = 0, 1, 2, \dots, n$, and $X(k)$ indicates the differential transform of $x(t)$ at $t = t_0$ in the k domain. So,

$$x(t) = \sum_{k=0}^{\infty} X(k)(t-t_0)^k \quad (2)$$

Using (1) and (2), some differential transform properties are shown in the table [36].

Table 1: Some of the essential mathematical properties

| Original function | Differential Transformed |
|-----------------------------------|---|
| $x(t) = Ax_1(t)$ | $X(k) = AX_1(k)$ |
| $\dot{x}(t) = \frac{dx}{dt}$ | $(k+1)X(k+1)$ |
| $f(x(t)) = x_1(t) \pm x_2(t)$ | $F(k) = X_1(k) \pm X_2(k)$ |
| $f(x(t)) = \frac{d^n x(t)}{dt^n}$ | $F(k) = \frac{(k+n)!}{k!} X(k+n)$ |
| $f(x(t)) = x_1(x(t)) x_2(x(t))$ | $F(k) = \sum_{k_1=0}^k X_1(k_1) X_2(k-k_1)$ |
| $x(t) = t^n$ | $X(k) = \delta(k-n)$ |
| $x(t) = e^{\lambda t}$ | $X(k) = \frac{\lambda^k}{k!}$ |
| $x(t) = \sin(\omega t + \alpha)$ | $X(k) = \frac{\omega^k}{k!} \sin\left(\frac{k\pi}{2} + \alpha\right)$ |
| $x(t) = \cos(\omega t + \alpha)$ | $X(k) = \frac{\omega^k}{k!} \cos\left(\frac{k\pi}{2} + \alpha\right)$ |

*where λ , ω , and α are constant values.

Using the DTM algorithm, the n th degree Taylor polynomial of $x(t)$ is:

$$x(t) = X(0) + X(1).t + X(2).t^2 + \dots + X(n).t^n \quad (3)$$

Bias Current Controlled Colpitts Oscillator

Figure 1(a) indicates a Bipolar Junction Transistor (BJT) based on the bias of current-controlled Colpitts oscillator [42]. Due to analyze the nonlinearities associated with a BJT based Colpitts oscillator the small-signal equivalent circuit model of a BJT is used. Figure 1(b) shows the small-signal equivalent circuit of the proposed Colpitts oscillator [42]. In Fig. 1 (a), Q_1 and Q_2 act as current mirror source that biases Q . The Colpitts oscillator consists of a gain device and the tank circuit including a combination of inductors and capacitors.

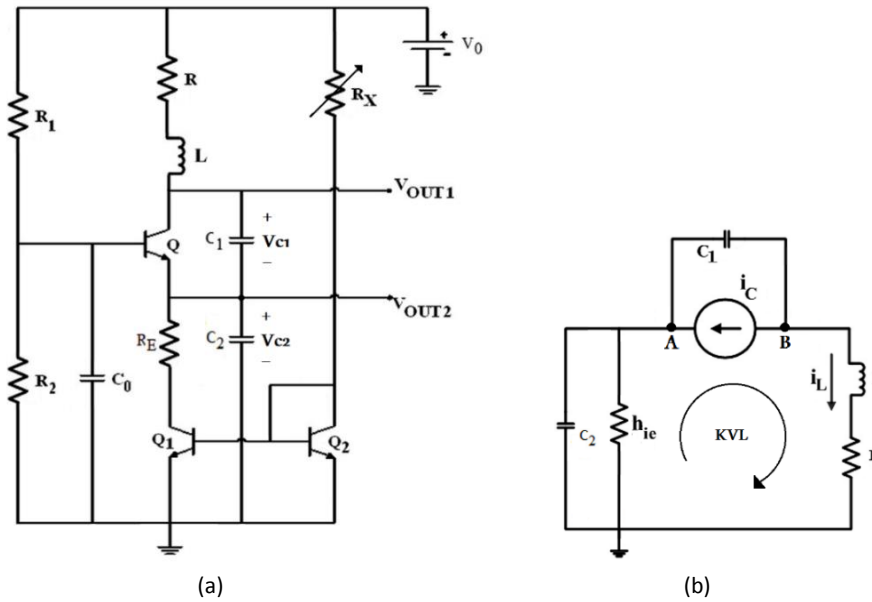


Fig. 1: (a) The schematic of Colpitts oscillator. (b) Small-signal equivalent circuit of the Colpitts oscillator.

The dynamic state equations are calculated as:

$$\begin{cases} KCL \ A \rightarrow C_1 \frac{dv_{c1}(t)}{dt} + i_L(t) + i_C(t) = 0 \\ KCL \ B \rightarrow C_2 \frac{dv_{c2}(t)}{dt} + \frac{v_{c2}(t)}{h_{ie}} + i_L(t) = 0 \\ KVL \rightarrow L \frac{di_L(t)}{dt} + R i_L(t) - v_{c1}(t) - v_{c2}(t) = 0 \end{cases} \quad (5)$$

where $v_{c1}(t)$ and $v_{c2}(t)$ are the voltages across C_1 and C_2 , respectively, and $i_L(t)$ is the current through inductor L .

Here,

$$i_C = f(v_{be}) \quad (6)$$

where [42],

$$f(v_{be}) = g_{m1} v_{be} - g_{m3} v_{be}^3 \quad (7)$$

The output of Colpitts oscillator is connected with an LC circuit feedback loop. A gain device is needed to compensate for the lost energy in the tank circuit and to maintain oscillation inside the tank circuit. One of the advantages of the Colpitts oscillator over other oscillators is that the Colpitts oscillator can be used to produce low-harmonic sine waveforms due to the low impedance paths of the capacitors at high frequencies. Also because of these capacitive reaction characteristics, the MOSFET-based Colpitts oscillator can operate at high frequencies (see Appendix).

The fundamental frequency of oscillation is given by:

$$f = \frac{1}{2\pi \sqrt{L \frac{C_1 C_2}{C_1 + C_2}}} \quad (4)$$

Such that,

$$f(-v_{c2}(t)) = -g_{m1} v_{c2}(t) + g_{m3} v_{c2}^3(t) \quad (8)$$

From (5) and (8), the following stands:

$$\begin{cases} \frac{dv_{c1}(t)}{dt} = -\frac{1}{C_1} \left(i_L(t) - g_{m1} v_{c2}(t) + g_{m3} v_{c2}^3(t) \right) \\ \frac{dv_{c2}(t)}{dt} = -\frac{1}{C_2} \left(i_L(t) + \frac{v_{c2}(t)}{h_{ie}} \right) \\ \frac{di_L(t)}{dt} = \frac{1}{L} \left((v_{c1}(t) + v_{c2}(t)) - R i_L(t) \right) \end{cases} \quad (9)$$

where g_{m1} and g_{m3} represent the linear and the nonlinear small signal transconductance of the proposed oscillator [42].

Let

$$x(t) = (v_{c1}(t) / v_T), y(t) = (v_{c2}(t) / v_T), z(t) = (i_L(t) / I_0),$$

$$\omega_0^{-1} = \sqrt{L C_1 C_2 / (C_1 + C_2)}, \quad h_r = L / (R (C_1 + C_2) h_{ie}),$$

$$\tau = \omega_0 t, \quad g = L I_0 / (R (C_1 + C_2) v_T), \quad k_c = (C_2 / (C_1 + C_2)),$$

$$Q = (\omega_0 L / R).$$

So, the normalized state dynamic equations are calculated as:

$$\begin{cases} \frac{dx(t)}{d\tau} = -\frac{g(z(t) - ay(t) + by(t)^3)}{Q(1-k_c)} \\ \frac{dy(t)}{d\tau} = -\frac{(gz(t) + h_r y(t))}{Qk_c} \\ \frac{dz(t)}{d\tau} = \frac{Qk_c(1-k_c)(x(t) + y(t))}{g} - \frac{z(t)}{Q} \end{cases} \quad (10)$$

where a and b indicate the normalized linear and nonlinear small signal transconductance. The parameters of the proposed oscillator can be found in Table 2 [42].

Table 2: Circuit parameters

| Parameter | Value |
|-----------|-------|
| g | 1.32 |
| Q | 4 |
| a | 2.36 |
| b | 0.2 |
| h_r | 0.04 |
| g_{m10} | 0.04 |
| I_0 | 1 mA |
| v_T | 25 mV |

In order to analyze the behavior of nonlinear systems, we can mention methods such as sensitivity to initial

conditions, stability analysis of equilibrium point, power spectrum, LE, Lyapunov dimension and dissipation. A sign of chaotic dynamics is its sensitive dependence on initial conditions, as indicated by the presence of positive LE.

LEs are used to describe the nonlinear behavior of the proposed oscillator [14], [15]. LE is a quantitative measure that indicates chaotic behavior. When at least one of LEs is zero, then the trajectory does not converge to a fixed point, in other words, the system oscillates. If LLE is zero, then the system oscillates around the equilibrium point. If LLE is positive, then the system is chaotic.

The LEs of the bias current-controlled Colpitts oscillator are shown in Fig. 2 for different initial conditions.

Since there is one positive LEs, then system (9) is a chaotic system [15], [43].

A. Fourth-Order Runge-Kutta Solution

The vector form of the proposed system (9) can be considered,

$$\frac{dW}{dt} = F(t, x(t), y(t), z(t)), \quad t \in [t_0, t_1] \quad (11)$$

with a given step length h through the interval $[t_0, t_1]$, successively producing approximations W_i to W_{i+1} .

Where,

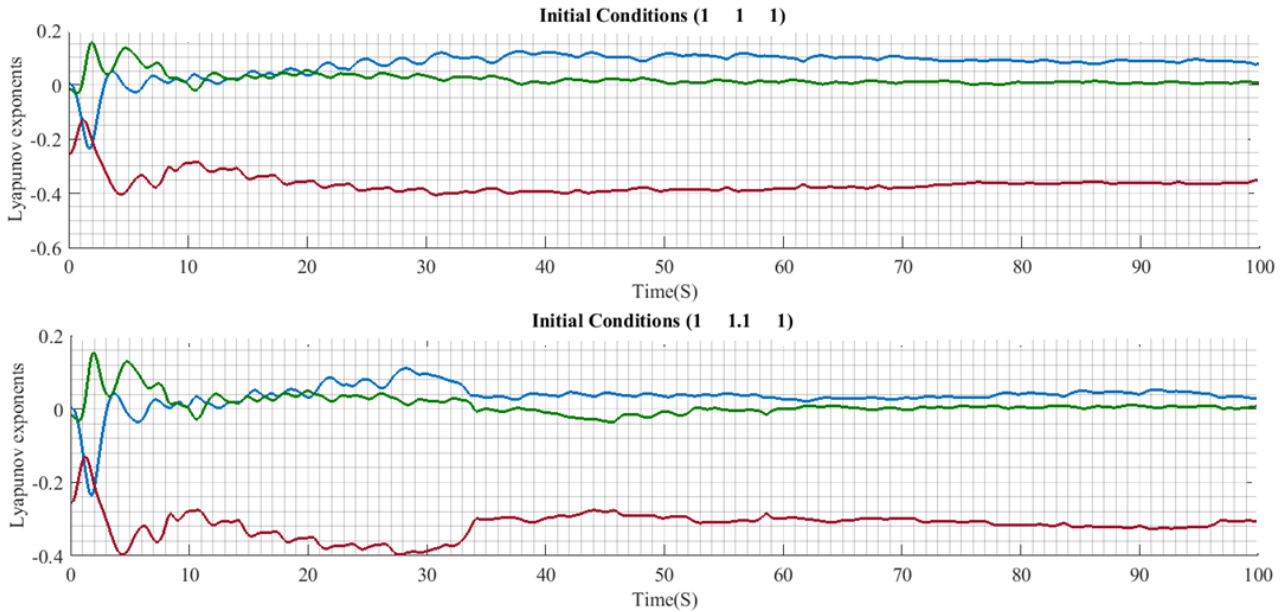


Fig. 2: LEs as a function of time for different initial conditions.

$$W = \begin{bmatrix} x(t) \\ y(t) \\ z(t) \end{bmatrix},$$

$$F(t, x(t), y(t), z(t)) = \begin{bmatrix} -\frac{g(z(t) - ay(t) + by(t)^3)}{Q(1-k_c)} \\ -\frac{(gz(t) + h_r y(t))}{Qk_c} \\ \frac{Qk_c(1-k_c)(x(t) + y(t))}{g} - \frac{z(t)}{Q} \end{bmatrix} \quad (12)$$

The RK4 method is the most popular method for solving state equations of nonlinear dynamic systems by using numerical approximations.

By applying the RK4 method for the proposed system (9), so,

$$W_{i+1} = W_i + \frac{h}{6}(K_1 + 2K_2 + 2K_3 + K_4), \quad (i=1, 2, \dots, n) \quad (13)$$

where $h = \frac{t_1 - t_0}{n}$ represents the step length through the

$$\text{interval } [t_0, t_1], \quad K_1 = \begin{bmatrix} k_{1x} \\ k_{1y} \\ k_{1z} \end{bmatrix}, \quad K_2 = \begin{bmatrix} k_{2x} \\ k_{2y} \\ k_{2z} \end{bmatrix}, \quad \text{and} \quad K_3 = \begin{bmatrix} k_{3x} \\ k_{3y} \\ k_{3z} \end{bmatrix}$$

represent slop at four places within each step.

The slop at four places within each step are calculated as follow:

$$K_1 = F(t_i, x_i(t), y_i(t), z_i(t))$$

$$K_2 = F\left(t_i + \frac{h}{2}, x_i(t) + \frac{h}{2}k_{1x}, y_i(t) + \frac{h}{2}k_{1y}, z_i(t) + \frac{h}{2}k_{1z}\right) \quad (14)$$

$$K_3 = F\left(t_i + \frac{h}{2}, x_i(t) + \frac{h}{2}k_{2x}, y_i(t) + \frac{h}{2}k_{2y}, z_i(t) + \frac{h}{2}k_{2z}\right)$$

$$K_4 = F\left(t_i + h, x_i(t) + hk_{3x}, y_i(t) + hk_{3y}, z_i(t) + hk_{3z}\right)$$

where $t_i = t_0 + ih$ and $i=1, 2, \dots, n$. By using numerical values for parameters of the proposed system (9), as shown in Table 2, the waveform time domain of state variables are calculated by applying the RK4 method with different initial conditions. Figure 3 illustrates the waveform time domain of the state variables with different initial conditions. As shown in Fig. 3, small alterations in initial conditions affect the response of the proposed system (Fig. 3). Therefore, system (9) is sensitive to initial conditions (Fig. 3). Figure 4 depicts typical stable periodic orbits with the different initial conditions.

Power spectrum can be applied to evaluate the behavioral analysis of proposed oscillator such as harmonic, bifurcation, chaos, etc. Harmonic distortion is evaluated by the power spectrum of the voltage or current signal. Existence of an exponential decay followed by a much slower decay (like an algebraic decay) in the power spectrum of time series can be a necessary condition for existence of chaotic signals [44]. The power spectrum of the state variables in the proposed Colpitts oscillator is shown in Fig. 5.

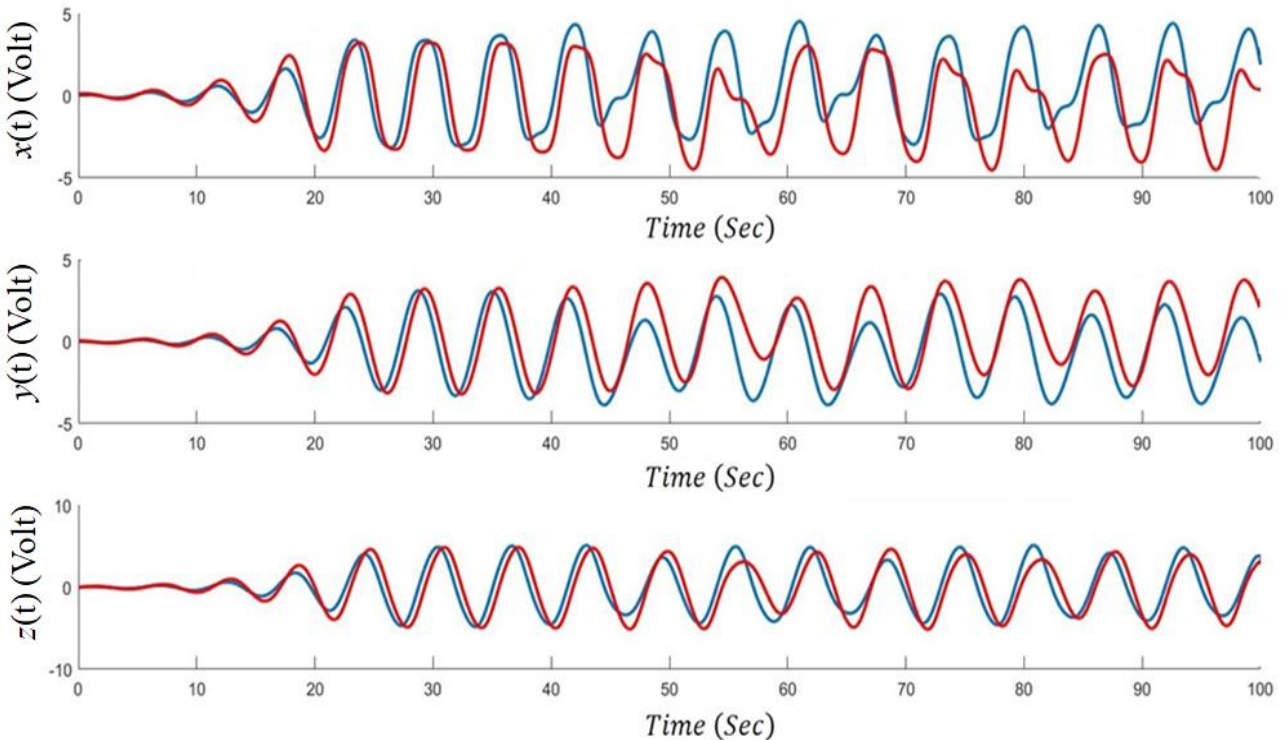


Fig. 3: Transient chaotic time-series with different initial conditions.

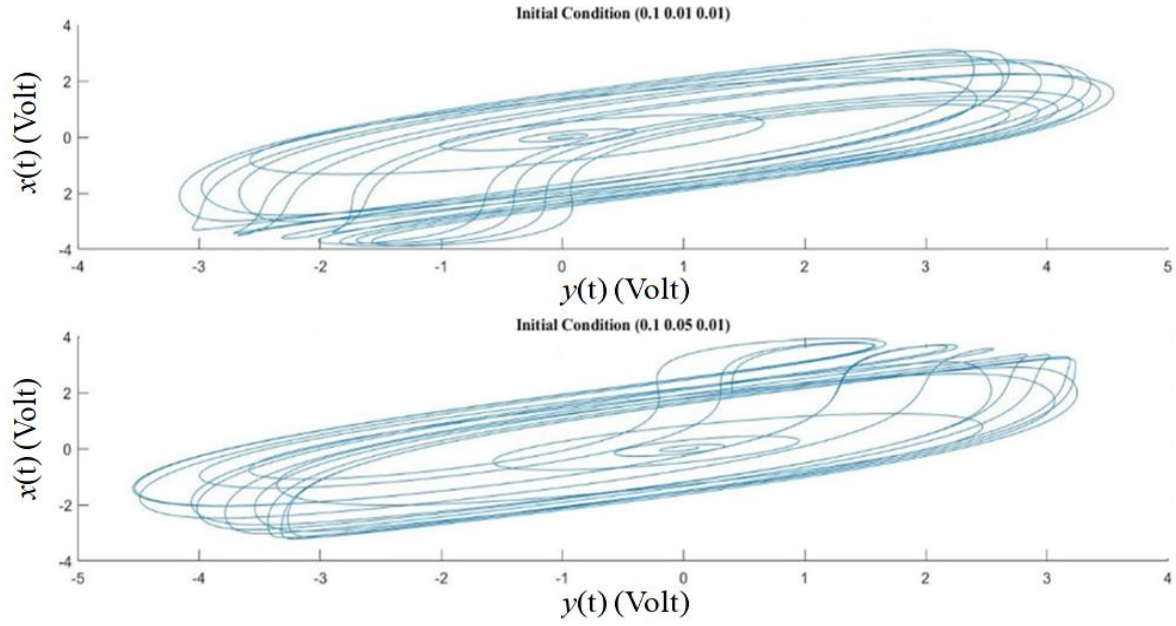


Fig. 4: Transient attractor with different initial conditions.

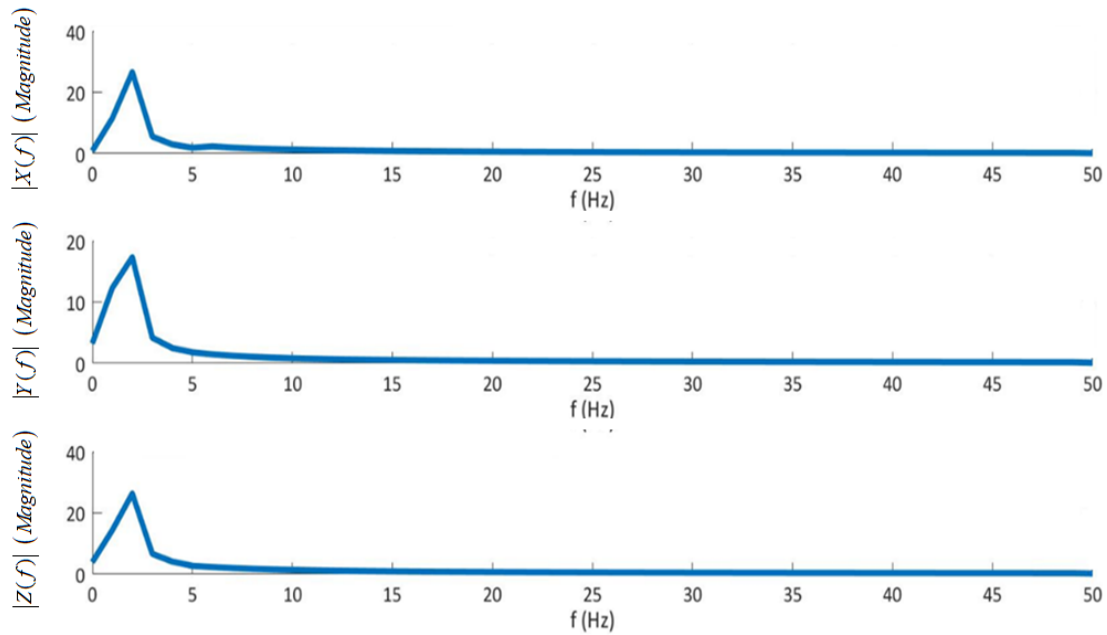


Fig. 5: Power spectrum of state variables in the proposed oscillator.

As shown in Fig. 5 existence of exponential decay demonstrate chaos in the proposed oscillator. Chaotic systems are a class of dynamic systems that have apparently random states of disorder and irregularities that have basic patterns and definite rules. These systems are very sensitive to the initial conditions that each point in a chaotic system is arbitrarily close to other points that have significantly different paths or paths in the future.

As it is expected from the definition of chaos and its variation in the different initial conditions, the spectrum of the chaos signal is broadband. It is also not worthwhile that the spectrum has strong frequency components at the period tripled frequency values. Figure 6 illustrates the bifurcation diagram based on a variation of $x(t)$ and $y(t)$ with respect to parameter $g \in [0.001 \ 1.6]$. Viewing the bifurcation diagram, chaotic areas can be detected.

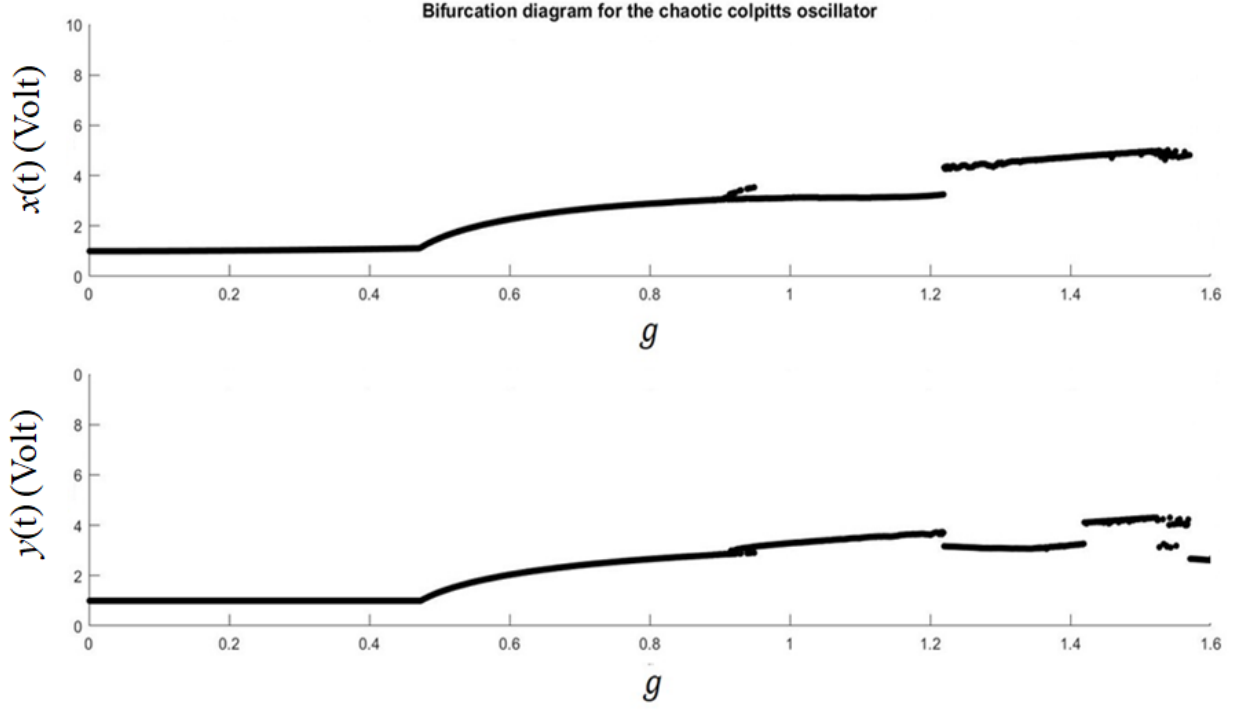


Fig. 6: The bifurcation diagram showing variation of $x(t)$ and $y(t)$ with respect to parameter g .

B. Analytical Analysis of Colpitts Oscillator Based on DTM Technique

The differential transform of $v_{c1}(t)$, $v_{c2}(t)$ and $i_L(t)$ is

considered as $V_{c1}(k)$, $V_{c2}(k)$ and $I_L(k)$. By using the DTM, system (9) is converted as follow:

$$\begin{cases} (k+1)V_{c1}(k+1) = -\frac{I_L(k)}{C_1} + \frac{\alpha V_{c2}(k)}{C_1} - \frac{\beta}{C_1} \sum_{k_2=0}^k \sum_{k_1=0}^{k_2} V_{c2}(k_1) V_{c2}(k_2 - k_1) V_{c2}(k - k_2) \\ (k+1)V_{c2}(k+1) = -\frac{I_L(k)}{C_2} - \frac{V_{c2}(k)}{h_{ie} C_2} \\ (k+1)I_L(k+1) = \frac{V_{c1}(k) + V_{c2}(k)}{L} - \frac{RI_L(k)}{L} \end{cases} \quad (15)$$

where $k=0,1,\dots,n$. The solution of the system (9) is calculated by:

$$\begin{cases} v_{c1}(t) = V_{c1}(0) + V_{c1}(1) \cdot t + V_{c1}(2) \cdot t^2 + \dots + V_{c1}(n) \cdot t^n \\ v_{c2}(t) = V_{c2}(0) + V_{c2}(1) \cdot t + V_{c2}(2) \cdot t^2 + \dots + V_{c2}(n) \cdot t^n \\ i_L(t) = I_L(0) + I_L(1) \cdot t + I_L(2) \cdot t^2 + \dots + I_L(n) \cdot t^n \end{cases} \quad (16)$$

where,

$$\begin{cases} V_{c1}(0) = 1 \\ V_{c1}(1) = -\frac{(1-\alpha+4\beta)}{C_1} \\ V_{c1}(2) = -\frac{1}{2C_1} \left(\left(\frac{2-R}{L} \right) + \left((\alpha-4\beta) \left(\frac{h_{ie}+1}{h_{ie}C_2} \right) \right) \right) \\ V_{c1}(3) = -\frac{1}{3C_1} \left(\left(\frac{(\alpha-1-4\beta)}{2LC_1} - \frac{h_{ie}+1}{2Lh_{ie}C_2} - \frac{2R-R^2}{2L^2} \right) + \left((4\beta-\alpha) \left(\frac{R-2}{2LC_2} + \frac{h_{ie}+1}{2h_{ie}^2C_2^2} \right) \right) \right) \end{cases} \quad (17)$$

and,

$$\begin{cases} V_{c2}(0) = 1 \\ V_{c2}(1) = -\frac{1}{C_2} \left(1 + \frac{1}{h_{ie}} \right) \\ V_{c2}(2) = \left(\frac{R-2}{2LC_2} + \frac{h_{ie}+1}{2h_{ie}^2C_2^2} \right) \\ V_{c2}(3) = -\frac{1}{3C_2} \left(\frac{(\alpha-1-4\beta)}{2LC_1} - \frac{h_{ie}+1}{2Lh_{ie}C_2} - \frac{2R-R^2}{2L^2} \right) - \frac{1}{3h_{ie}C_2} \left(\frac{R-2}{2LC_2} + \frac{h_{ie}+1}{2h_{ie}^2C_2^2} \right) \end{cases} \quad (18)$$

Now, by using DTM technique, (10) is converted as follow:

$$\begin{cases} (k+1)X(k+1) = -\frac{g \left(Z(k) - aY(k) + b \sum_{k_2=0}^k \sum_{k_1=0}^{k_2} Y(k_1)Y(k_2-k_1)Y(k-k_2) \right)}{Q(1-k_c)} \\ (k+1)Y(k+1) = -\frac{(gZ(k) + h_rY(k))}{Qk_c} \\ (k+1)Z(k+1) = \frac{Qk_c(1-k_c)(X(k) + Y(k))}{g} - \frac{Z(k)}{Q} \end{cases} \quad (19)$$

Calculating the DTM of $x(t)$, $y(t)$, and $z(t)$ with order k , denoted by $X(k)$, $Y(k)$, and $Z(k)$ yielded the following components for initial conditions $x_0, y_0, z_0 = 0.1, 0.01, 0.01$ as shown in Table 3:

Table 3: Numerical values for $X(k)$, $Y(k)$, and $Z(k)$

| k | $X(k)$ | $Y(k)$ | $Z(k)$ |
|-----|------------------------------------|------------------------------------|------------------------------------|
| 0 | 0.1 | 0.01 | 0.01 |
| 1 | 0.008975868 | -0.0068 | 0.0808333333333333 |
| 2 | -0.03197070536 | -0.026607 | -0.0092799742424242 |
| 3 | -0.0117724698910667 | 0.0022189743333333 | -0.0140190186515152 |
| 4 | 0.00317683685466210 | 0.00230204320583333 | -0.000933185492941919 |
| 5 | 0.000839855411252330 | 0.000113972312245 | 0.000876792617146404 |
| 6 | $-6.64511834461511 \times 10^{-5}$ | $-9.68270955935878 \times 10^{-5}$ | $8.38997676564415 \times 10^{-5}$ |
| 7 | $-2.90842752140743 \times 10^{-5}$ | $-7.63390067733995 \times 10^{-6}$ | $-2.06672296933295 \times 10^{-5}$ |
| 8 | $9.84609104495675 \times 10^{-6}$ | $1.72413120139303 \times 10^{-6}$ | $-2.83124906180071 \times 10^{-6}$ |
| 9 | $4.36636974794568 \times 10^{-7}$ | $2.03793528528957 \times 10^{-7}$ | $2.32062651703437 \times 10^{-7}$ |
| 10 | $2.66264015557214 \times 10^{-8}$ | $-1.57237220694848 \times 10^{-8}$ | $4.27158960804087 \times 10^{-8}$ |

Therefore, the exact solution of the proposed system by:
(10) by using the DTM approximated solution is applied

$$\begin{aligned} x(t) = & 0.1 + 0.008975868t - 0.03197070536t^2 - 0.0117724698910667t^3 + 0.0031768368546621t^4 \\ & + 0.000839855411252330t^5 - 6.64511834461511 \times 10^{-5}t^6 - 2.90842752140743 \times 10^{-5}t^7 + 9.84609104495675 \times 10^{-8}t^8 \\ & + 4.36636974794568 \times 10^{-7}t^9 + 2.66264015557214 \times 10^{-8}t^{10} + \dots \end{aligned} \quad (20)$$

$$\begin{aligned} y(t) = & 0.01 + -0.0068t - 0.026607t^2 + 0.0022189743333333t^3 + 0.0023020432058333t^4 + 0.000113972312245000t^5 \\ & - 9.68270955935878 \times 10^{-5}t^6 - 7.63390067733995 \times 10^{-6}t^7 + 1.72413120139303 \times 10^{-6}t^8 + 2.03793528528957 \times 10^{-7}t^9 \\ & - 1.57237220694848 \times 10^{-8}t^{10} + \dots \end{aligned} \quad (21)$$

$$\begin{aligned} z(t) = & 0.01 + 0.080833333333333t - 0.0092799742424242t^2 - 0.0140190186515152t^3 - 0.000933185492941919t^4 \\ & + 0.000876792617146404t^5 + 8.38997676564415 \times 10^{-5}t^6 - 2.06672296933295 \times 10^{-5}t^7 - 2.83124906180071 \times 10^{-6}t^8 \\ & + 2.32062651703437 \times 10^{-7}t^9 + 4.27158960804084 \times 10^{-8}t^{10} + \dots \end{aligned} \quad (22)$$

The solution points of the proposed system in (10) at different time steps by using the RK4M and DTM are calculated in Table 4.

Table 4: Numerical comparison for determination of $x(t)$, $y(t)$, and $z(t)$ for different values of t

| t | DTM | | | RK4M | | |
|-----|-----------------|---------------|-----------------|-----------------|------------------|-----------------|
| | $x(t)$ | $y(t)$ | $z(t)$ | $x(t)$ | $y(t)$ | $z(t)$ |
| 0 | 0.1 | 0.01 | 0.01 | 0.1 | 0.01 | 0.01 |
| 0.5 | 0.095247232451 | 0.00037149561 | 0.04631451035 | 0.095247232450 | 0.0003714956808 | 0.046314510352 |
| 1 | 0.069154411280 | -0.0188745589 | 0.06753862363 | 0.069154413293 | -0.0188745614562 | 0.067538623383 |
| 1.5 | 0.023025009693 | -0.0412393787 | 0.06553113684 | 0.023025102617 | -0.0412395952566 | 0.065531108763 |
| 2 | -0.034105715142 | -0.0584408546 | 0.03768295347 | -0.034105716380 | -0.058445932568 | 0.037681982560 |
| 2.5 | -0.087115020734 | -0.0626091225 | -0.01095040956 | -0.087141309621 | -0.0626673343872 | -0.010966716952 |
| 3 | -0.118494413767 | -0.0486773921 | -0.06758279642 | -0.118872016717 | -0.0491002086887 | -0.067749376285 |
| 3.5 | -0.112443409464 | -0.0158464329 | -0.11378076454 | -0.11535598343 | -0.018080895574 | -0.114961971915 |
| 4 | -0.05565022038 | 0.03338384908 | -0.12830578074 | -0.071274445331 | 0.024050338342 | -0.134651736944 |
| 4.5 | 0.07171947931 | 0.09840097092 | -0.087005638598 | 0.0082688441589 | 0.066622101201 | -0.113629326843 |

As shown in Table 4, the solutions of system (10) with DTM technique have a good accuracy. The solutions of the RK4M and DTM are shown in Fig. 7.

Lyapunov Exponent Calculation Based on Analytical DTM Technique

Let us define $x(1), x(2), \dots, x(N)$ as the elements of a time series. LE can be defined as [17], [19]:

$$\lambda = \frac{1}{T} \ln \frac{|x(i+T) - x(j+T)|}{|x(i) - x(j)|} \quad (23)$$

where T indicates the number of iterations or evolution times. $x(N)$ represents the time series value at the N th time.

From (2), so,

$$x(N) = \sum_{k=0}^n X(k) N^k \quad (24)$$

So, the LEs can be approximated analytically based on unknown parameters. In this case, according to the DTM technique and (24),

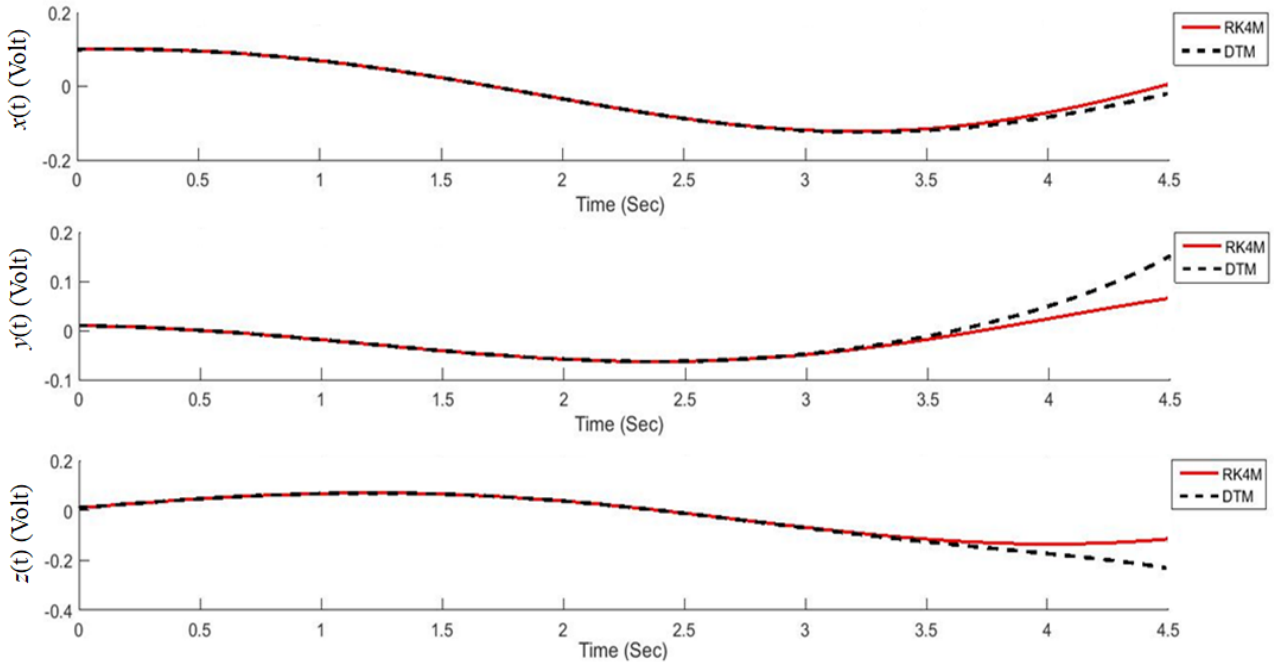


Fig. 7: Numerical comparison for time series of $x(t)$, $y(t)$ and $z(t)$ between RK4M and DTM.

$$\lambda = \frac{1}{T} \ln \frac{\left| \sum_{k=1}^n X(k)(i+T)^k - \sum_{k=1}^n X(k)(j+T)^k \right|}{\left| \sum_{k=1}^n X(k)i^k - \sum_{k=1}^n X(k)j^k \right|} \quad (25)$$

Note that,

$$\lambda = \frac{1}{T} \ln \frac{\left| X(1)(i-j) + \sum_{k=2}^n X(k) \left[(i+T)^k - (j+T)^k \right] \right|}{\left| X(1)(i-j) + \sum_{k=2}^n X(k) \left[i^k - j^k \right] \right|} \quad (26)$$

where λ is LE, $X(k)$ represents of the differential transform of $x(t)$, and n is decided by the convergence of natural frequency.

In the proposed current-controlled Colpitts oscillator described by (9), and according to (25), LEs of the proposed oscillator are calculated analytically in the following form:

$$\lambda_1 = \frac{1}{T} \ln \frac{\left| V_{c1}(1)(i-j) + \sum_{k=2}^n V_{c1}(k) \left[(i+T)^k - (j+T)^k \right] \right|}{\left| V_{c1}(1)(i-j) + \sum_{k=2}^n V_{c1}(k) \left[i^k - j^k \right] \right|} \quad (27)$$

$$\lambda_2 = \frac{1}{T} \ln \frac{\left| V_{c2}(1)(i-j) + \sum_{k=2}^n V_{c2}(k) \left[(i+T)^k - (j+T)^k \right] \right|}{\left| V_{c2}(1)(i-j) + \sum_{k=2}^n V_{c2}(k) \left[i^k - j^k \right] \right|} \quad (28)$$

$$\lambda_3 = \frac{1}{T} \ln \frac{\left| I_L(1)(i-j) + \sum_{k=2}^n I_L(k) \left[(i+T)^k - (j+T)^k \right] \right|}{\left| I_L(1)(i-j) + \sum_{k=2}^n I_L(k) \left[i^k - j^k \right] \right|} \quad (29)$$

where $V_{c1}(k)$, $V_{c2}(k)$, and $I_L(k)$ are the k th coefficient in Taylor series $v_{c1}(t)$, $v_{c2}(t)$, and $i_L(t)$, respectively.

Results and Discussion

With the help of MATLAB software, we have considered the current controlled Colpitts oscillator described by (9) and the LE based on the Wolf method [1] with respect to the variation of C_1 and L in a short interval time $t \in [0, 3\text{Sec}]$ are numerically calculated and presented in Tables 5 and 6. Besides, according to the DTM technique, the LE based on DTM with respect to the variation of C_1 and L in a short interval time $t \in [0, 3\text{Sec}]$ are calculated analytically in Tables 7 and 8.

Table 5: Results of the numerical method for LEs calculations with respect to parameter C_1

| Parameters Values | | λ_1 | λ_2 | λ_3 |
|---|-------------------------|-------------|-------------|-------------|
| Constant | Variable | | | |
| $R = 35 \Omega$, $L = 0.055 \text{ mH}$, $h_{ie} = 688$, $C_2 = 0.1 \text{ nF}$, $\alpha = 0.088$, $\beta = 0.008$ | $C_1 = 0.1 \text{ nF}$ | 0.061432 | 0.000465 | -0.033188 |
| $R = 35 \Omega$, $L = 0.055 \text{ mH}$, $h_{ie} = 688$, $C_2 = 0.1 \text{ nF}$, $\alpha = 0.088$, $\beta = 0.008$ | $C_1 = 0.2 \text{ nF}$ | 0.283190 | 0.100539 | 0.025467 |
| $R = 35 \Omega$, $L = 0.055 \text{ mH}$, $h_{ie} = 688$, $C_2 = 0.1 \text{ nF}$, $\alpha = 0.088$, $\beta = 0.008$ | $C_1 = 0.01 \text{ nF}$ | -0.151487 | -0.151991 | -2.207523 |

Table 6: Results of the numerical method for LEs calculations with respect to parameter L

| Parameters Values | | λ_1 | λ_2 | λ_3 |
|---|------------------------|-------------|-------------|-------------|
| Constant | Variable | | | |
| $R = 35 \Omega$, $C_1 = 0.1 \text{ nF}$, $h_{ie} = 688$, $C_2 = 0.1 \text{ nF}$, $\alpha = 0.088$, $\beta = 0.008$ | $L = 0.025 \text{ mH}$ | 0.001242 | -0.2211698 | -0.0656512 |
| $R = 35 \Omega$, $C_1 = 0.1 \text{ nF}$, $h_{ie} = 688$, $C_2 = 0.1 \text{ nF}$, $\alpha = 0.088$, $\beta = 0.008$ | $L = 0.1 \text{ mH}$ | 0.485387 | -0.1248960 | -0.515123 |
| $R = 35 \Omega$, $C_1 = 0.1 \text{ nF}$, $h_{ie} = 688$, $C_2 = 0.1 \text{ nF}$, $\alpha = 0.088$, $\beta = 0.008$ | $L = 0.092 \text{ mH}$ | 0.275904 | 0.106224 | 0.035907 |
| $R = 35 \Omega$, $C_1 = 0.1 \text{ nF}$, $h_{ie} = 688$, $C_2 = 0.1 \text{ nF}$, $\alpha = 0.088$, $\beta = 0.008$ | $L = 0.055 \text{ mH}$ | 0.061432 | 0.000465 | -0.331888 |

Table 7: Results of the analytical method for LEs based on DTM calculations with respect to parameter C_1 for $t \in [0, 3\text{Sec}]$

| Parameters Values | | λ_1 | λ_2 | λ_3 |
|---|-------------------------|-------------|-------------|-------------|
| Constant | Variable | | | |
| $R = 35 \Omega$, $L = 0.055 \text{ mH}$, $h_{ie} = 688$, $C_2 = 0.1 \text{ nF}$, $\alpha = 0.088$, $\beta = 0.008$ | $C_1 = 0.1 \text{ nF}$ | 0.08235 | 0.0000123 | -0.451888 |
| $R = 35 \Omega$, $L = 0.055 \text{ mH}$, $h_{ie} = 688$, $C_2 = 0.1 \text{ nF}$, $\alpha = 0.088$, $\beta = 0.008$ | $C_1 = 0.2 \text{ nF}$ | 0.384491 | 0.21546 | 0.036465 |
| $R = 35 \Omega$, $L = 0.055 \text{ mH}$, $h_{ie} = 688$, $C_2 = 0.1 \text{ nF}$, $\alpha = 0.088$, $\beta = 0.008$ | $C_1 = 0.01 \text{ nF}$ | -0.251567 | -0.231411 | -3.152214 |

Table 8: Results of the analytical method for LEs based on DTM calculations with respect to parameter L for $t \in [0, 3\text{Sec}]$

| Parameters Values | | λ_1 | λ_2 | λ_3 |
|---|------------------------|-------------|-------------|-------------|
| Constant | Variable | | | |
| $R = 35 \Omega$, $C_1 = 0.1 \text{ nF}$, $h_{ie} = 688$, $C_2 = 0.1 \text{ nF}$, $\alpha = 0.088$, $\beta = 0.008$ | $L = 0.025 \text{ mH}$ | 0.0001323 | -0.2212745 | -0.0725411 |
| $R = 35 \Omega$, $C_1 = 0.1 \text{ nF}$, $h_{ie} = 688$, $C_2 = 0.1 \text{ nF}$, $\alpha = 0.088$, $\beta = 0.008$ | $L = 0.1 \text{ mH}$ | 0.573286 | -0.2136854 | -0.485534 |
| $R = 35 \Omega$, $C_1 = 0.1 \text{ nF}$, $h_{ie} = 688$, $C_2 = 0.1 \text{ nF}$, $\alpha = 0.088$, $\beta = 0.008$ | $L = 0.092 \text{ mH}$ | 0.375401 | 0.125321 | 0.032832 |
| $R = 35 \Omega$, $C_1 = 0.1 \text{ nF}$, $h_{ie} = 688$, $C_2 = 0.1 \text{ nF}$, $\alpha = 0.088$, $\beta = 0.008$ | $L = 0.055 \text{ mH}$ | 0.08235 | 0.0000123 | -0.451888 |

As shown in Tables 5 and 7, by considering $R = 35 \Omega$, $L = 0.055 \text{ mH}$, $h_{ie} = 688$, $C_2 = 0.1 \text{ nF}$, $\alpha = 0.088$, $\beta = 0.008$, and $C_1 = 0.01 \text{ nF}$, the proposed Colpitts oscillator described in (9) doesn't oscillate, and for the other parameters listed in Tables 5-8, the equilibrium point of the system is unstable and the system never converges to a fixed point.

In other words, the system can have strong attractor for these parameters. The accuracy of the numerical method based on the Wolf method in comparison with the analytical method based on DTM for the LEs calculation, with respect to the variation of different parameters, such as C_1 and L , are calculated in Tables 9 and 10.

Table 9: Differences between Numerical methods based on Wolf method and DTM for LEs calculations with respect to a variation of parameter C_1

| Parameters Values | | $\Delta_{\lambda} = \lambda_{Numerical} - \lambda_{DTM} $ | | |
|---|-------------------------|--|----------------------|----------------------|
| Constant | Variable | Δ_{λ_1} | Δ_{λ_2} | Δ_{λ_3} |
| $R = 35 \Omega$, $L = 0.055 \text{ mH}$, $h_{ie} = 688$, $C_2 = 0.1 \text{ nF}$, $\alpha = 0.088$, $\beta = 0.008$ | $C_1 = 0.1 \text{ nF}$ | 0.020918 | 0.0004527 | 0.120000 |
| $R = 35 \Omega$, $L = 0.055 \text{ mH}$, $h_{ie} = 688$, $C_2 = 0.1 \text{ nF}$, $\alpha = 0.088$, $\beta = 0.008$ | $C_1 = 0.2 \text{ nF}$ | -0.101301 | 0.114921 | 0.010998 |
| $R = 35 \Omega$, $L = 0.055 \text{ mH}$, $h_{ie} = 688$, $C_2 = 0.1 \text{ nF}$, $\alpha = 0.088$, $\beta = 0.008$ | $C_1 = 0.01 \text{ nF}$ | 0.100080 | 0.079420 | 0.9446910 |

Table 10: Differences between Numerical methods based on Wolf method and DTM for LEs calculations with respect to a variation of parameter L

| Parameters Values | | $\Delta_{\lambda} = \lambda_{Numerical} - \lambda_{DTM} $ | | |
|---|------------------------|--|----------------------|----------------------|
| Constant | Variable | Δ_{λ_1} | Δ_{λ_2} | Δ_{λ_3} |
| $R = 35 \Omega$, $C_1 = 0.1 \text{ nF}$, $h_{ie} = 688$, $C_2 = 0.1 \text{ nF}$, $\alpha = 0.088$, $\beta = 0.008$ | $L = 0.025 \text{ mH}$ | 0.0011097 | 0.0001047 | 0.0068899 |
| $R = 35 \Omega$, $C_1 = 0.1 \text{ nF}$, $h_{ie} = 688$, $C_2 = 0.1 \text{ nF}$, $\alpha = 0.088$, $\beta = 0.008$ | $L = 0.1 \text{ mH}$ | 0.0908990 | 0.0887894 | 0.0295890 |
| $R = 35 \Omega$, $C_1 = 0.1 \text{ nF}$, $h_{ie} = 688$, $C_2 = 0.1 \text{ nF}$, $\alpha = 0.088$, $\beta = 0.008$ | $L = 0.092 \text{ mH}$ | 0.0994970 | 0.0190970 | 0.0030750 |
| $R = 35 \Omega$, $C_1 = 0.1 \text{ nF}$, $h_{ie} = 688$, $C_2 = 0.1 \text{ nF}$, $\alpha = 0.088$, $\beta = 0.008$ | $L = 0.055 \text{ mH}$ | 0.0209180 | 0.0004527 | 0.1200010 |

As shown in Tables 9 and 10, Δ_{λ} indicates the differences between Numerical methods based on Wolf method and DTM for each of LEs in the proposed oscillator. In addition, the numbers mentioned in Tables 9 and 10 show the accuracy of the DTM analytical method in calculating LEs relative to the numerical method. In the other words, these tables are presented to show the accuracy of the analytical methods in comparison with the numerical analysis results for LEs calculations. By comparing the numerical simulations and the analytic results for LEs calculations, we have excellent agreement between the LEs variations for the Colpitts oscillator in a short interval time studied here.

Conclusion

This paper applied a novel analytical method for nonlinear analysis of the mathematical model of bias current-controlled Colpitts oscillator using its parameters, then proposed an analytical estimate of the LE based on the DTM technique. Simulation results have been provided to verify the effectiveness of unknown parameters on LEs with different initial conditions. To validate the applied method in the analytical solution of the Colpitts oscillator dynamic model, the RK4 method is used. The results show good accuracy of DTM in short time intervals $t \in [0, 3 \text{ Sec}]$. In this paper, comparing an analytical method and a numerical method for calculating LEs in the Colpitts oscillator with respect to various parameters is presented.

Finally, according to the numerical and analytical results, different parameters on LEs values are investigated.

Appendix

The Colpitts oscillator consists of a gain device and the tank circuit including a combination of inductors and capacitors. The output of Colpitts oscillator is connected with an LC circuit feedback loop. A gain device is needed to compensate for the lost energy in the tank circuit and to maintain oscillation inside the tank circuit. One of the advantages of the Colpitts oscillator over other oscillators is that the Colpitts oscillator can be used to produce low-harmonic sine waveforms due to the low impedance paths of the capacitors at high frequencies. Also because of these capacitive reaction characteristics, the MOSFET-based Colpitts oscillator can operate at very high frequencies. Of course, any MOSFET used as an amplifier must be able to operate at the required high frequencies. Due to analyze the nonlinearities associated with a MOSFET based circuit. Figure 8 (a) illustrates the Colpitts oscillator based on MOSFET. The control parameter of this oscillator is the current source connected to the circuit between the source (S) of the MOSFET and the ground. Due to analyze the nonlinearities associated with a MOSFET based circuit; the small-signal equivalent circuit model of a MOSFET is used. In order for the diode at the gate-drain junction with its anode at the gate to be in reverse bias, the drain voltage must be higher than that of the gate voltage. The

nonlinearity in the model of this transistor is due to the effect of the diodes in the p-n gate-source junction,

which is determined by the current from the drain to the source i_d . This current can be calculated as:

$$i_d = \begin{cases} 0 & v_{gs} \leq V_{th} \text{ (Cutoff region)} \\ g_{m0} (v_{gs} - V_{th}) & v_{gs} \leq V_{th} \text{ (Saturation region)} \\ g_{m0} (v_{gs} - V_{th}) (v_{gs} + v_{gd} - 2V_{th}) & v_{gs} \leq V_{th} \text{ (Triode region)} \end{cases} \quad (30)$$

where $V_{th} < 0$ the cutoff is value of the voltage between the gate and the source; g_{m0} is the current gain of the MOSFET.

The equivalent circuit is illustrated in Fig. 8 (b).

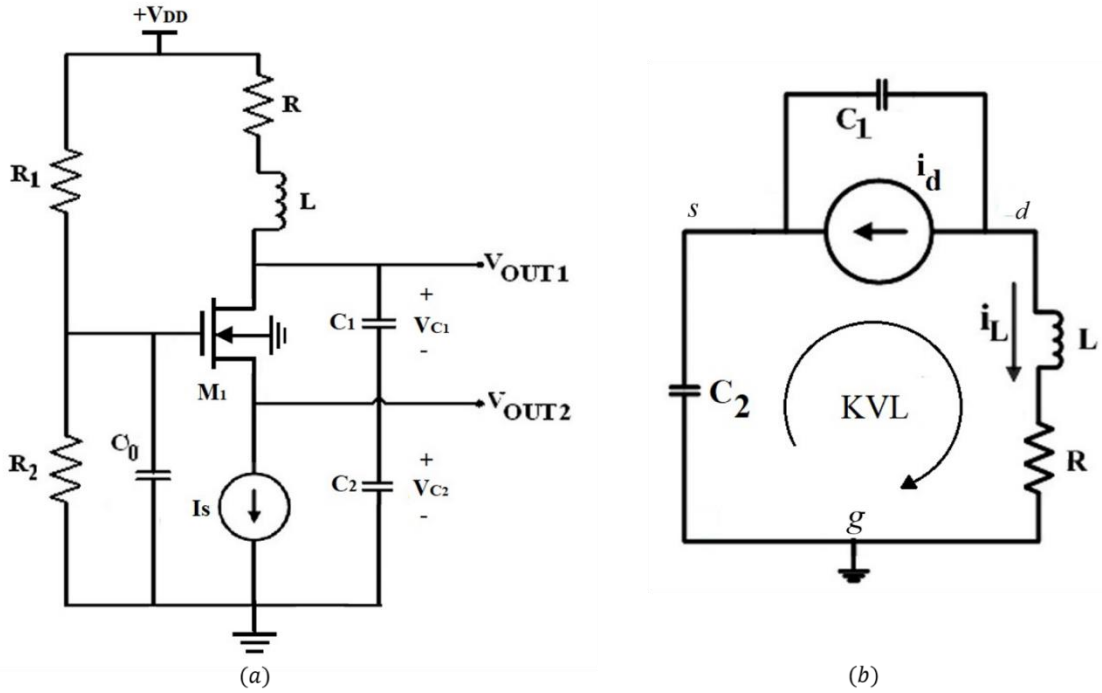


Fig. 8: (a) The schematic of MOSFET based Colpitts oscillator. (b) Small-signal equivalent circuit of the Colpitts oscillator.

The dynamic state equations are calculated as:

$$\begin{cases} KCL \ d \rightarrow C_1 \frac{dv_{c1}(t)}{dt} + i_L(t) + i_d(t) = 0 \\ KCL \ s \rightarrow C_2 \frac{dv_{c2}(t)}{dt} + i_L(t) = 0 \\ KVL \rightarrow L \frac{di_L(t)}{dt} + R i_L(t) - v_{c1}(t) - v_{c2}(t) = 0 \end{cases} \quad (31)$$

where $v_{c1}(t)$ and $v_{c2}(t)$ are the voltages across C_1 and C_2 , respectively, and $i_L(t)$ is the current through inductor L . Here, $i_d(t)$ is calculated from (30).

So,

In order to nonlinear analysis of (32) differential transform method can be used. The high frequency operation of the Colpitts oscillators is a challenging issue due to the parasitic capacitance of the junctions of a MOSFET. Due to nonlinear analysis of high frequency chaotic oscillator, high-frequency small-signal equivalent circuit model of MOSFET can be used.

In order to nonlinear analysis of the MOSFET-based Colpitts oscillator similar to BJT, based Colpitts oscillator the DTM technique can be used.

Author Contributions

F. Setoudeh and A. Ghomi Taheri designed the experiments. A. Ghomi Taheri and F. Setoudeh collected the data. A. Ghomi Taheri, F. Setoudeh, M.B. Tavakoli interpreted the results and wrote the manuscript.

Acknowledgment

This work is completely self-supporting, thereby no any financial agency's role is available.

Conflict of Interest

The authors declare no potential conflict of interest regarding the publication of this work. In addition, the ethical issues including plagiarism, informed consent, misconduct, data fabrication and, or falsification, double publication and, or submission, and redundancy have been completely witnessed by the authors.

Abbreviations

| | |
|--------------------|---|
| <i>DTM</i> | Differential transform method |
| <i>RK4M</i> | Fourth order Runge-Kutta method |
| <i>LE</i> | Lyapunov exponent |
| <i>LLE</i> | Largest Lyapunov exponent |
| <i>MsDTM</i> | Multi-stage differential transform method |
| <i>ADM</i> | Adomian decomposition method |
| <i>ETM</i> | Elzaki transform method |
| <i>BJT</i> | Bipolar Junction Transistor |
| <i>MOSFET</i> | Metal oxide semiconductor field effect transistor |
| $x(t), y(t), z(t)$ | State variable |
| $X(k), Y(k), Z(k)$ | Differential transform of State variable |
| k | Order DTM |
| h_{ie}, g_m | Small-signal parameter BJT transistor |
| V_{C1} | Voltages across C_1 |
| V_{C2} | Voltages across C_2 |
| i_L | Current through inductor L |
| g_{m1}, g_{m3} | Small-signal transconductance |
| α, β | Constant parameter |

| | |
|------------------|--|
| k_1, k_2, k_3 | Four places within each step |
| T | Number of iterations or evolution times |
| $x(N)$ | Time series value |
| λ | Symbol of Lyapunov exponent |
| Δ_λ | Differences between Numerical methods based on Wolf method and DTM |

References

- [1] M.J. Feigenbaum, "Universal behavior in nonlinear systems," *Physica D*, 7(1-3): 16-39, 1983.
- [2] H. Lin, S. Yim, "Analysis of a nonlinear system exhibiting chaotic, noisy chaotic, and random behaviors," *J. Appl. Mech.* Jun, 63(2): 509-516, 1996.
- [3] M.S. Soliman, "Global stability properties of equilibria, periodic, and chaotic solutions," *Appl. Math. Modell.*, 20(7): 488-500, 1996.
- [4] B. Radziszewski, A. Sławiński, "Estimation of stability in non-linear systems," *Mach. Dyn. Probl.*, 24(3): 113-125, 2000.
- [5] E.A. Best, "Stability assessment of nonlinear systems using the lyapunov exponent," Ohio University, 2003.
- [6] M. Balcerzak, D. Pikunov, A. Dabrowski, "The fastest, simplified method of Lyapunov exponents spectrum estimation for continuous-time dynamical systems," *Nonlinear Dyn.*, 94(4): 3053-3065, 2018.
- [7] T. Zeren, M. ÖZBEK, N. Kutlu, M. Akilli, "Significance of using a nonlinear analysis technique, the Lyapunov exponent, on the understanding of the dynamics of the cardiorespiratory system in rats," *Turk. J. Med. Sci.*, 46(1): 159-165, 2016.
- [8] H. Kantz, T. Schreiber, *Nonlinear Time Series Analysis*, Cambridge university press, 2004.
- [9] J.B. Dingwell, L.C. Marin, "Kinematic variability and local dynamic stability of upper body motions when walking at different speeds," *J. Biomech.*, 39(3): 444-452, 2006.
- [10] J.B. Dingwell, *Lyapunov Exponents*, Wiley encyclopedia of biomedical engineering, 2006.
- [11] C. Yang, Q. Wu, "On stability analysis via Lyapunov exponents calculated from a time series using nonlinear mapping—a case study," *Nonlinear Dyn.*, 59(1-2): 239, 2010.
- [12] M.A. Fuentes, Y. Sato, C. Tsallis, "Sensitivity to initial conditions, entropy production, and escape rate at the onset of chaos," *Phys. Lett. A*, 375(33): 2988-2991, 2011.
- [13] E. Glasner, B. Weiss, "Sensitive dependence on initial conditions," *Nonlinearity*, 6(6): 1067-1075, 1993.
- [14] I. Khovanov, N. Khovanova, V. Anishchenko, P. McClintock, "Sensitivity to initial conditions and lyapunov exponent of a quasiperiodic system," *Tech. Phys.*, 45(5): 633-635, 2000.
- [15] C. Abraham, G. Biau, B. Cadre, "On Lyapunov exponent and sensitivity," *J. Math. Anal. Appl.*, 290(2): 395-404, 2004.
- [16] G.-C. Wu, D. Baleanu, "Jacobian matrix algorithm for Lyapunov exponents of the discrete fractional maps," *Commun. Nonlinear Sci. Numer. Simul.*, 22(1-3): 95-100, 2015.

- [17] A. Wolf, J.B. Swift, H.L. Swinney, J.A. Vastano, "Determining Lyapunov exponents from a time series," *Physica D*, 16(3): 285-317, 1985.
- [18] H.D. Abarbanel, R. Brown, M.B. Kennel, "Local Lyapunov exponents computed from observed data," *J. Nonlinear Sci.*, 2(3): 343-365, 1992.
- [19] R. Gencay, W.D. Dechert, "An algorithm for the N-Lyapunov exponents of an N-dimensional unknown dynamical system," *Physica D*, 59(1-3): 142-157, 1992.
- [20] X. Zeng, R. Eykholt, R. Pielke, "Estimating the Lyapunov-exponent spectrum from short time series of low precision," *Phys. Rev. Lett.*, 66(25): 3229, 1991.
- [21] M.B. Tayel, E.I. AlSaba, "Robust and sensitive method of lyapunov exponent for heart rate variability," *arXiv preprint arXiv:1508.00996*, 2015.
- [22] L. G. de la Fraga, E. Tlelo-Cuautle, "Optimizing the maximum Lyapunov exponent and phase space portraits in multi-scroll chaotic oscillators," *Nonlinear Dyn.* 76(2): 1503-1515, 2014.
- [23] Y. Liu, X.C. Zhang, "A new method based on Lyapunov exponent to determine the threshold of chaotic systems," *Appl. Mech. Mater.*, 511-512, 2014.
- [24] H. Liao, "Novel gradient calculation method for the largest Lyapunov exponent of chaotic systems," *Nonlinear Dyn.* 85(3): 1377-1392, 2016.
- [25] F. Ayaz, "Solutions of the system of differential equations by differential transform method," *Appl. Math. Comput.*, 147(2): 547-567, 2004.
- [26] K. Al Ahmad, Z. Zainuddin, F.A. Abdullah, "Solving non-autonomous nonlinear systems of ordinary differential equations using multi-stage differential transform method," *Aust. J. Math. Anal. Appl.*, 17(2): 1-18, 2020.
- [27] Y. Do, B. Jang, "Enhanced multistage differential transform method: application to the population models," *Abstr. Appl. Anal.*, 2012: 1-14, 2012.
- [28] E.A. Az-Zo'bi, K. Al-Khaled, A. Darweesh, "Numeric-Analytic solutions for nonlinear oscillators via the modified multi-stage decomposition method," *Mathematics*, 7(6): 550, 2019.
- [29] T.M. Elzaki, "Solution of nonlinear differential equations using mixture of Elzaki transform and differential transform method," in *International Mathematical Forum*, 7(13): 631-638, 2012.
- [30] T.M. Elzaki, E.M. Hilal, J.-S. Arabia, J.-S. Arabia, "Homotopy perturbation and Elzaki transform for solving nonlinear partial differential equations," *Math. Theor. Model.*, 2(3): 33-42, 2012.
- [31] A.-M. Wazwaz, "A reliable modification of Adomian decomposition method," *Appl. Math. Comput.*, 102(1): 77-86, 1999.
- [32] S. Abbasbandy, "Improving Newton-Raphson method for nonlinear equations by modified Adomian decomposition method," *Appl. Math. Comput.*, 145(2-3): 887-893, 2003.
- [33] A. Arikoglu, I. Ozkol, "Solution of boundary value problems for integro-differential equations by using differential transform method," *Appl. Math. Comput.*, 168(2): 1145-1158, 2005.
- [34] C. Huang, J. Li, F. Lin, "A new algorithm based on differential transform method for solving partial differential equation system with initial and boundary conditions," *Adv. Pure. Math.*, 10(5): 337, 2020.
- [35] S. Al-Ahmad, I. M. Sulaiman, M. Mamat, K. Kamfa, "Solutions of classes of differential equations using modified differential transform method," *J. Math. Comput. Sci.*, 10(6): 2360-2382, 2020.
- [36] H. Abbasi, A. Javed, "Implementation of Differential Transform Method (DTM) for large deformation analysis of cantilever beam," in *Proc. IOP Conference Series: Materials Science and Engineering*, 899(1): 012003, 2020.
- [37] L.-j. Xie, C.-l. Zhou, S. Xu, "Solving the systems of equations of Lane-Emden type by differential transform method coupled with adomian polynomials," *Mathematics*, 7(4): 377, 2019.
- [38] S. Mukherjee, B. Roy, S. Dutta, "Solution of the Duffing-van der Pol oscillator equation by a differential transform method," *Phys. Scripta*, 83(1): 015006, 2010.
- [39] I. Khatami, E. Zahedi, M. Zahedi, "Efficient solution of nonlinear Duffing oscillator," *J. Comput. Appl. Mech.*, 6(2): 219-234, 2020.
- [40] A.J. Christopher, N. Magesh, G.T. Preethi, "Dynamical Analysis of Corona-virus (COVID- 19) Epidemic Model by Differential Transform Method, 2020.
- [41] R.M. Kouayep, A.F. Talla, J.H. T. Mbé, P. Wofo, "Bursting oscillations in Colpitts oscillator and application in optoelectronics for the generation of complex optical signals," *Opt. Quantum Electron*, 2(291), 2020.
- [42] S. Sarkar, S. Sarkar, B.C. Sarkar, "On the dynamics of a periodic Colpitts oscillator forced by periodic and chaotic signals," *Commun. Nonlinear Sci. Numer. Simul.*, 19(8): 2883-2896, 2014.
- [43] Z. Wei, W. Zhang, "Hidden hyperchaotic attractors in a modified Lorenz-Stenflo system with only one stable equilibrium," *Int. J. Bifurcation Chaos*, 24(10): 1450127, 2014.
- [44] M. Valsakumar, S. Satyanarayana, V. Sridhar, "Signature of chaos in power spectrum," *Pramana*, 48(1): 69-85, 1997.

Biographies



Alireza Ghomi Taheri is currently PhD student in electrical engineering at the Islamic Azad University, branch of Arak. His research interest includes signal processing and nonlinear system.



Farbod Setoudeh received his PhD degree in electrical engineering from Science and research branch of Islamic Azad University and is currently an assistant professor at electrical engineering department of Arak University of Technology. His research interests include intelligent system, signal processing, and nonlinear system.



Mohammad Bagher Tavakoli received his PhD degree in electrical engineering from Science and Research branch of Azad University in 2012 and is currently an assistant professor at electrical engineering department of Azad University. His research interests include linear integrated circuits.

Copyrights

©2021 The author(s). This is an open access article distributed under the terms of the Creative Commons Attribution (CC BY 4.0), which permits unrestricted use, distribution, and reproduction in any medium, as long as the original authors and source are cited. No permission is required from the authors or the publishers.



How to cite this paper:

A. Ghomi Taheri F. Setoudeh, M.B. Tavakoli, "Nonlinear analysis of colpitts oscillator using differential transform method," J. Electr. Comput. Eng. Innovations, 9(2): 127-142, 2021.

DOI: [10.22061/JECEI.2020.7543.402](https://doi.org/10.22061/JECEI.2020.7543.402)

URL: http://jecei.sru.ac.ir/article_1496.html





Research paper

Fault Diagnosis of a Permanent Magnet Synchronous Generator Wind Turbine

S. Khodakaramzadeh, M. Ayati*, M.R. Ha'iri-Yazdi

Department of Mechanical Engineering, University of Tehran, Tehran, Iran.

Article Info

Article History:

Received 09 June 2020

Reviewed 23 August 2020

Revised 08 October 2020

Accepted 15 December 2020

Keywords:

Wind energy conversion system (WECS)

Fault diagnosis of wind turbine

Permanent magnet synchronous generator (PMSG) wind turbine

Blade imbalance fault (BIF)

Terminal sliding mode observer (TSMO)

*Corresponding Author's Email Address:

m.ayati@ut.ac.ir

Abstract

Background and Objectives: Designing a terminal sliding mode observer (TSMO) in order to estimate the potential faults in a wind turbine with a doubly fed induction generator (DFIG) has been studied in previous research works. In this paper, a method for fault detection of a permanent magnet synchronous generator (PMSG) wind turbine using a TSMO is developed.

Methods: The wind turbine (WT) dynamic model including, blades, drive train, 3kw PMSG, maximum power capture controller, and pitch controller is linearized around its equilibrium point and is simulated in MATLAB Simulink. A PID controller is designed for capturing the maximum power from wind. Also, a PI controller is designed in order to control the pitch angle. In this research, the blade imbalance fault (BIF), which is due to the difference between turbine blades' mass distribution, is investigated. This fault may happen over time and causes rotor mass imbalance that leads to vibrations in the generator's shaft rotating speed. A fault detection system (FDS) is proposed using a terminal sliding mode observer in order to diagnose the BIF.

Results: Using the designed TSMO, the estimation errors of not only measured states but also unmeasured states converge to zero in finite time. This leads to the fast action of the FDS before a failure happens. Using the proposed FDS, the states and fault are estimated such that the estimation errors of states and the fault converge to zero in 0.033 seconds.

Conclusion: The convergence of state estimation errors to zero in finite time, which is verified by simulation results, satisfies the authors' expectation that using TSMO, the estimation errors of both output and non-output states converge to zero in finite time.

©2021 JECEI. All rights reserved.

Introduction

Wind turbine, which is a type of renewable energy systems, is excited by a random wind profile. Among characteristics of this system are nonlinear dynamics, operation in an uncertain environment, and the dependence of the wind turbine power on geographical and weather conditions [1], [2]. Installation errors, manufacturing deficiencies or aging effects, and challenging environmental conditions are common reasons for the shut-down condition [3].

Overall, a wind turbine is in shut-down condition for 0.595% to 2.705% of a year. Wind turbines are mostly located in remote areas. In addition, performing inspection and maintenance work on WTs is problematic due to the height of the turbine. Therefore, WTs requiring less maintenance are desirable. Moreover, because of complications of a WT system and also due to variations of wind speed, the fault occurrence probability of this system is high. Hence, minimization of the adverse economic effects of the faults is a

challenging problem [4], [5]. Concerning the probability of failure occurrence in a wind energy conversion system (WECS) such as the fraction of gear, drive train, and bearing, condition monitoring and fault detection have an essential role in reducing maintenance costs [6]. For a turbine with more than 20 years of operation, the operation and maintenance (OM) and components costs are estimated to be around 10-15% of the total wind farm income. Although larger turbines have fewer OM costs per unit of power, failure costs are higher for these turbines. Therefore, condition monitoring and fault diagnosis are profitable [7]. Furthermore, fault detection in primitive levels and repairing faulty parts in a timely manner is essential for maintenance costs, component costs, downtime reduction, and preventing catastrophic damages [8]. Fault detection in fault-tolerant systems is vital because it provides the required information for fault isolation and system reconfiguration [9]. Modern wind turbines that take advantage of fault diagnosis and fault-tolerant schemes are highly reliable. They operate efficiently and produce economic electrical energy [10]. Due to simple mechanical structures, light weight, high power density, high efficiency, and high reliability of PMSGs, these types of generators are often installed on wind turbines [11], [12]. Moreover, other desired features of PMSGs are their fast dynamical response and low noise [13]. Using an observer for state estimation and fault detection is one of the most useful approaches in wind turbine FDS.

Blades are of weakest parts of a wind turbine. Some faults may occur directly on blades such as hub or blade corrosion/crack and rotor imbalance [6]. Blade bending moment sensor fault, blade root bending sensor fault, and pitch actuator fault are examples of faults that occur in blade sensors and actuators [14]. Pitch dynamic that has hydraulic nature may change because of pressure drop, which occurs in the hydraulic supply system or additional air in the oil [15].

The imbalance fault of the generator shaft causes an additional force in the shaft. The blade imbalance fault in which the mass distribution of one blade is different from other blades causes rotor mass imbalance, which leads to vibrations in the generator's shaft rotating speed [16]. Blade imbalance mainly occurs due to the construction or manufacturing errors, icing condition, and degradation as a result of aging [17]. A fault detection method based on adaptive fuzzy Q-learning (FQL) for PMSG WT blade imbalance fault detection, which is proposed in [18], has 99.9% classification accuracy and uses 3999 samples of generator's current signals. The advantage of this method is that it needs no prior knowledge of the system for fault detection however, it is limited to the working condition of the sampled signals. Blade imbalance fault detection using

gene expression programming (GEP) based classifier and empirical mode decomposition (EMD) has been studied in [19].

In this study, blade imbalance fault detection within a PMSG wind turbine is studied. For this purpose, a terminal sliding mode observer (TSMO) is designed for the wind turbine system including blades, drive train, and PMSG with nonlinear dynamics, which estimates both output and non-output states in a finite time. Therefore, TSMO estimates all states and BIF in a finite time.

In the next section, the complete dynamic model of the WECS is explained. In third section, the TSMO's equations, the linearized state-space equations of WECS, and the fault estimation method are described. The complete WECS model including wind turbine, PMSG, controller, and fault models is simulated in MATLAB Simulink and the simulation results are represented in the next section. Finally, last section concludes the research.

Wind Turbine Dynamic Model

The WECS includes a wind turbine, a PMSG, and two controllers. In order to detect the WT's faults, it is necessary to obtain the dynamic equations of the entire system including the WT, the PMSG, the controllers, and the fault. In the following subsection, the dynamic model of the entire WECS is explained.

A. System's Dynamic Model

In this section, the WECS dynamic model including dynamic equations of the wind turbine, the PMSG, the controllers, and BIF is explained. The WECS has four states, two inputs, and one output. The state variables vector is $x = [x_1 \ x_2 \ x_3 \ x_4]^T = [i_d \ i_q \ \beta \ \omega_g]^T$. The dynamical equations of i_d , i_q , ω_g , and β are presented based on Boulouma et al. [20] and Tong and Zhao studies [21]. The input control signals vector is: $u = [R_L \ \beta_{ref}]^T$ and output is $y = \omega_g$.

The state-space equations are given in (1). In this equation, i_d and i_q are the stator current's d/q components. L_d and L_q are inductances of the stator. R_s is the stator resistance. Φ_m is the linkage flux. P is the number of pole pairs. ω_g is the generator speed. The power electronics and load with highly fast dynamic in comparison to other parts are represented by an equivalent load with constant inductance L_L and the adjustable resistance R_L . τ_β is the pitch actuator's time constant. β is the pitch angle. β_{ref} is the pitch reference angle which is also the pitch controller's output and also the second control input of the wind turbine system. η is the gearbox efficiency. ρ is the air

density. The radius of the rotor swept area is represented by R . v is the wind speed. $C_T(\lambda, \beta)$ is the torque coefficient. N_g is the gear ratio. The equivalent inertia transformed into the generator side is represented by J_h . λ is the tip speed ratio (TSR).

$$\begin{aligned} \begin{bmatrix} \dot{x}_1 \\ \dot{x}_2 \\ \dot{x}_3 \\ \dot{x}_4 \end{bmatrix} &= \begin{bmatrix} -\frac{R_s}{L_d + L_L}x_1 + \frac{P(L_q - L_L)}{L_d + L_L}x_2x_4 \\ -\frac{R_s}{L_q + L_L}x_2 - \frac{P(L_d + L_L)}{L_q + L_L}x_1x_4 + \frac{P\Phi_m}{L_q + L_L}x_4 \\ -\frac{1}{\tau_\beta}x_3 \\ \frac{\eta\pi\rho R^3 v^2}{2N_g J_h}C_T(x_3, x_4) - \frac{P\Phi_m}{J_h}x_2 \end{bmatrix} \\ &+ \begin{bmatrix} -\frac{1}{L_d + L_L}x_1 & 0 \\ -\frac{1}{L_q + L_L}x_2 & 0 \\ 0 & \frac{1}{\tau_\beta} \\ 0 & 0 \end{bmatrix} \begin{bmatrix} R_L \\ \beta_{ref} \end{bmatrix} \\ y &= \begin{bmatrix} 0 & 0 & 0 & 1 \end{bmatrix} \begin{bmatrix} x_1 \\ x_2 \\ x_3 \\ x_4 \end{bmatrix} \\ \tau_\beta &= \frac{\beta_{ref} - \beta}{\frac{d\beta}{dt}} \end{aligned} \quad (1)$$

B. WT Closed-loop System

In this system, two controllers including a maximum power capture controller and a pitch controller are designed separately, as shown in Fig. 1. In the maximum power capture controller design, the first, second, and fourth states have participated. The third state is considered in the pitch controller design.

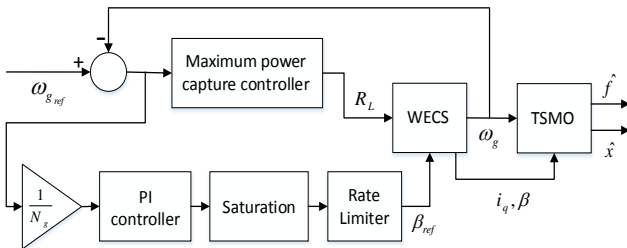


Fig. 1: Block diagram of WECS with maximum power capture controller, pitch controller, and TSMO.

$\omega_{g,ref}$ is calculated in order that TSR is maintained close or equal to its optimal value to capture maximum

power. β_{ref} and R_L are the control inputs.

B.1: Maximum Power Capture Controller

A PID controller is considered for maximum power capturing as follows:

$$G_{CMP}(s) = P + I \frac{1}{s} + D \frac{N}{1 + N \frac{1}{s}} \quad (2)$$

In the above equation, P is the proportional term, I is considered as the integral coefficient, the derivative coefficient is represented by D , and N is the filter coefficient.

B.2: Pitch Controller

The pitch controller is implemented in the third state equation of (1). The difference between actual power and maximum allowable power is being used to calculate the required pitch angle [22]. In order to control the pitch angle, a PI controller, a rate limiter, and a saturation function are used. The equation of the controller is as follows:

$$G_{CP}(s) = \frac{\beta_{ref}}{\omega_{ref} - \omega_r} = k_p + \frac{k_i}{s} \quad (3)$$

β_{ref} is the pitch reference angle, ω_r is the rotor speed, ω_{ref} is the reference rotor speed, k_p and k_i are the PI controller proportional and integral coefficients, respectively.

C. Model Linearization

For the sake of simplicity, the state-space equation's coefficients are defined as:

$$\begin{aligned} a_s &= -\frac{R_s}{L_d + L_L}, & b_s &= \frac{P(L_q - L_L)}{L_d + L_L}, & c_s &= -\frac{1}{L_d + L_L} \\ d_s &= -\frac{R_s}{L_q + L_L}, & f_s &= -\frac{P(L_d + L_L)}{L_q + L_L}, & g_s &= \frac{P\Phi_m}{L_q + L_L} \\ h_s &= -\frac{1}{L_q + L_L}, & p_s &= -\frac{1}{\tau_\beta}, & m_s C_T &= \frac{\eta\pi\rho R^3 v^2}{2N_g J_h} C_T(\lambda, \beta), \\ n_s &= -\frac{P\Phi_m}{J_h} \end{aligned}$$

Computing Jacobian matrix, the linearized state-space is:

$$\begin{aligned} \begin{bmatrix} \dot{x}_1 \\ \dot{x}_2 \\ \dot{x}_3 \\ \dot{x}_4 \end{bmatrix} &= \begin{bmatrix} a_s & b_s x_{40} & 0 & b_s x_{20} \\ f_s x_{40} & d_s & 0 & f_s x_{10} + g_s \\ 0 & 0 & p_s & 0 \\ 0 & n_s & m_s \frac{\partial C_T}{\partial x_3} \Big|_{\substack{x=x_0 \\ u=u_0}} & m_s \frac{\partial C_T}{\partial x_4} \Big|_{\substack{x=x_0 \\ u=u_0}} \end{bmatrix} \begin{bmatrix} x_1 \\ x_2 \\ x_3 \\ x_4 \end{bmatrix} \\ &+ \begin{bmatrix} c_s x_{10} & 0 \\ h_s x_{20} & 0 \\ 0 & -p_s \\ 0 & 0 \end{bmatrix} \begin{bmatrix} u_1 \\ u_2 \end{bmatrix} \end{aligned} \quad (4)$$

where $x_0 = [x_{10} \ x_{20} \ x_{30} \ x_{40}]^T$ is the equilibrium point, which is determined by solving the following set of equations:

$$\begin{cases} a_s x_{10} + b_s x_{20} x_{40} = 0 \\ d_s x_{20} + f_s x_{10} x_{40} + g_s x_{40} = 0 \\ p_s x_{30} = 0 \\ m_s C_T(x_{30}, x_{40}) + n_s x_{20} = 0 \end{cases} \quad (5)$$

D. Blade Imbalance Fault Dynamic Model

When blade imbalance fault occurs, the frequency f_r (1P frequency) of the turbine shaft torque variates. Therefore, the turbine shaft torque in the existence of blade imbalance fault equals to:

$$T(t) = T_0 + T_v \cos(2\pi f_r t) \quad (6)$$

T is the turbine shaft torque, T_0 is the torque due to the wind power, and T_v is the amplitude of the shaft torque variations as a consequence of blade imbalance fault [23]. Hence, when blade imbalance fault exists, the state-space equations of (4) are changed as follows:

$$\begin{bmatrix} \dot{x}_1 \\ \dot{x}_2 \\ \dot{x}_3 \\ \dot{x}_4 \end{bmatrix} = \begin{bmatrix} a_s & b_s x_{40} & 0 & b_s x_{20} \\ f_s x_{40} & d_s & 0 & f_s x_{10} + g_s \\ 0 & 0 & p_s & 0 \\ 0 & n_s & m_s \frac{\partial C_T}{\partial x_3} \Big|_{\substack{x=x_0 \\ u=u_0}} & m_s \frac{\partial C_T}{\partial x_4} \Big|_{\substack{x=x_0 \\ u=u_0}} \end{bmatrix} \begin{bmatrix} x_1 \\ x_2 \\ x_3 \\ x_4 \end{bmatrix} \quad (7)$$

$$+ \begin{bmatrix} c_s x_{10} & 0 \\ h_s x_{20} & 0 \\ 0 & -p_s \\ 0 & 0 \end{bmatrix} \begin{bmatrix} u_1 \\ u_2 \end{bmatrix} + \begin{bmatrix} 0 \\ 0 \\ 0 \\ 1 \end{bmatrix} f_{BIF}$$

Substituting (6) into state-space equations of (1) and (4), f_{BIF} is obtained as follows:

$$f_{BIF} = \frac{\eta}{N_g J_h} T_v \cos(2\pi f_r t) \quad (8)$$

Terminal Sliding Mode Observer (TSMO) Design

Classical sliding mode observers are widely used for output and state estimations of linear/nonlinear systems in practical researches because of their intrinsic robustness to the uncertainties. The output estimation errors' convergences in a finite time are guaranteed by classical sliding mode observers, while non-output errors converge to zero asymptotically. This means states not directly affected by the output converge to the actual values in infinite time. Hence, terminal sliding mode observers are developed, which guarantee convergence of both output (measured) and non-output (unmeasured) state estimation errors in a finite time [24].

A. TSMO Implementation on WECS

In this section, TSMO is implemented on the linearized system [24], [25]. Primarily, the linearized system model is considered and conditions for state and fault estimation are mentioned. Then, the coordinate is transformed and system and observer equations in the new coordinate system are obtained and design parameters are introduced. Finally, the observer equation is obtained in the original coordinate and fault is estimated.

A.1: Linearized State Model

Consider the time-invariant linear system as follows:

$$\begin{cases} \dot{x}(t) = \bar{A}_L x(t) + \bar{B}u(t) + \bar{F}_a f_a(x, t) \\ y(t) = \bar{C}x(t) \end{cases} \quad (9)$$

In this system n is the number of states, m is the number of control inputs, p is the number of outputs, and q is the number of faults. f_a is the fault vector and \bar{F}_a is the fault intensity matrix. It is supposed that $\|f_a\| \leq \gamma$ and the system is observable. The Matrices \bar{C} and \bar{F}_a must be full-rank. Also, the following assumptions must be held.

$$A_1 : \text{rank}(\bar{C}\bar{F}_a) = \text{rank}(\bar{F}_a) = q \quad (10)$$

$$A_2 : 2p \geq n + q$$

The transformation matrix T_L has the structure:

$$T_L = \begin{bmatrix} T_1 & T_2 & 0 & 0 \\ 0 & 1 & 0 & 0 \\ 0 & 0 & 1 & 0 \\ 0 & 0 & 0 & 1 \end{bmatrix} \quad (11)$$

T_1 and T_2 must be chosen such that the following inequality holds:

$$\bar{a}_{11} + \bar{a}_{21} \frac{T_2}{T_1} < 0 \quad (12)$$

In the above equation, \bar{a}_{11} and \bar{a}_{21} are the first and second elements of the first column of the matrix \bar{A}_L . Using the transformation matrix T_L , changing of coordinate is done and the new state matrices are obtained as follows:

$$\begin{aligned} A_L &= \begin{bmatrix} A_1 & A_2 \\ A_3 & A_4 \end{bmatrix}, A_3 = \begin{bmatrix} A_{31} \\ A_{32} \end{bmatrix}, B = \begin{bmatrix} B_1 \\ B_2 \end{bmatrix}, \\ F_a &= \bar{F}_a = \begin{bmatrix} F_1 \\ F_2 \end{bmatrix}, C = \bar{C} = [0 \ C_2] \end{aligned} \quad (13)$$

where:

$$A_1 \in R^{(n-p) \times (n-p)}, A_3 \in R^{p \times (n-p)}, A_{31} \in R^{(n-p) \times (n-p)},$$

$$F_1 \in R^{(n-p) \times q}, F_2 \in R^{p \times q}, C_2 \in R^{p \times p}$$

$$F_1 = 0_{(n-p) \times q}, F_2 = \begin{bmatrix} 0_{(p-1) \times q} \\ 1_{1 \times q} \end{bmatrix}.$$

C_2 is a full-rank matrix. A_{31} is full-rank because the system is observable. Hence, the system state equations are transformed as follows:

$$\begin{cases} \dot{z}_1(t) = A_1 z_1(t) + A_2 z_2(t) + B_1 u(t) \\ \dot{z}_2(t) = A_3 z_1(t) + A_4 z_2(t) + B_2 u(t) + F_2 f_a(z, t) \\ y(t) = C z(t) \end{cases} \quad (14)$$

where, z_1 and z_2 are non-output and output states vectors in the new coordinate system respectively.
 $z_1 \in R^{(n-p) \times 1}$, $z_2 \in R^{p \times 1}$.

A.2: Observer Design

In this section, a TSMO is designed for the linearized system using [24]. The observer state equations are defined as follows:

$$\begin{cases} \dot{\hat{z}}_1(t) = A_1 \hat{z}_1(t) + A_2 \hat{z}_2(t) + B_1 u(t) + l_1 e_y(t) + l_2 v^{\frac{\alpha}{\beta}} \\ \dot{\hat{z}}_2(t) = A_3 \hat{z}_1(t) + A_4 \hat{z}_2(t) + B_2 u(t) + l_3 e_y(t) + l_4 v \\ \hat{y}(t) = C \hat{z}(t) \end{cases} \quad (15)$$

α and β are odd integers ($\alpha < \beta$). The observer's coefficients are obtained as follows:

$$l_1 = -A_2, l_2 = [l_{21} \quad 0_{1 \times 2}], l_3 = -A_4 + A_{4s}, l_4 = -\phi \quad (16)$$

where $A_{4s} \in R^{3 \times 3}$ is a desired stable matrix and $\phi = \text{diag}(\rho_1, \rho_2, \rho_3)$. ρ_1 , ρ_2 and ρ_3 are positive scalars and

$$l_{21} = -\frac{p_1^{\frac{\alpha-\beta}{2\beta}}}{A_{31}} \quad (17)$$

Since A_1 is stable, two positive scalars p_1 and q_1 exist that satisfy the following condition:

$$p_1 A_1 + A_1^T p_1 = 2A_1 p_1 \leq -q_1 \quad (18)$$

$A_{4s} \in R^{3 \times 3}$ is a desired stable matrix. Moreover, A_3 is partitioned as $A_3 = [A_{31} \quad A_{32}]^T$. The error vectors are defined as:

$$\begin{cases} e_1 = \hat{z}_1 - z_1 \\ e_2 = e_y = \hat{z}_2 - z_2 \end{cases} \quad (19)$$

e_1 and e_2 are non-output and output variables estimation errors. The convergence of e_1 and e_2 to zero in a finite time is proved using the Lyapunov functions

$$\bar{V}_1 = p_1 \bar{e}_1^2 \quad \text{and} \quad V_2 = \frac{1}{2} e_2^T e_2 \quad [24]. \quad \bar{e}_1 \text{ is defined as}$$

$$\bar{e}_1 = A_{31} e_1.$$

Using an inverse coordinate transformation, the observer's equations in the original coordinate system are as follows:

$$\begin{cases} \dot{\hat{x}}(t) = \bar{A}_L \hat{x}(t) + \bar{B} u(t) + R_1 e_y(t) + R_2 v(t) + R_3 v^{\frac{\alpha}{\beta}}(t) \\ y(t) = \bar{C} \hat{x}(t) \end{cases} \quad (20)$$

where:

$$v = \begin{bmatrix} \text{sign}(e_{21}) \\ \text{sign}(e_{22}) \\ \text{sign}(e_{23}) \end{bmatrix}, \text{sign}(e_i) = \frac{e_i}{|e_i| + \delta_i} \quad (21)$$

δ_i is a small positive constant, which is considered in order to prevent zero denominators. The observer's coefficients are:

$$R_1 = T_L^{-1} \begin{bmatrix} l_1 \\ l_3 \end{bmatrix}, R_2 = T_L^{-1} \begin{bmatrix} 0 \\ l_4 \end{bmatrix}, R_3 = T_L^{-1} \begin{bmatrix} l_2 \\ 0 \end{bmatrix} \quad (22)$$

Considering the Lyapunov function V_2 , the following inequality holds [24]:

$$\dot{V}_2 < -\sigma_1 \|e_2\| \quad (23)$$

σ_1 is a positive design scalar. V_2 can be written as $V_2 = \frac{1}{2} \|e_2\|^2$. Therefore, using (23):

$$\frac{dV_2}{2\sqrt{V_2}} < -\frac{\sigma_1}{\sqrt{2}} dt \quad (24)$$

Defining t_2 as the e_2 convergence time to zero and integrating (24), the convergence time of output states estimation errors to zero is calculated as the below equation:

$$t_2 < \frac{\sqrt{2V_2(0)}}{\sigma_1} \quad (25)$$

In time duration of t_2 seconds, V_2 will become zero and sliding motion will occur on $e_2 = 0$.

Using \bar{V}_1 , the following equation is obtained [24]:

$$\dot{\bar{V}}_1 < -2\rho_1^{-\frac{\alpha}{\beta}} (p_1 \bar{e}_1^2)^{\frac{\alpha+\beta}{2\beta}} \quad (26)$$

Integrating (26), the convergence time of non-output states estimation errors to zero is calculated as the below equation:

$$t_1 < \frac{\beta}{\beta-\alpha} \rho_1^{-\frac{\alpha}{\beta}} \bar{V}_1^{\frac{\beta-\alpha}{2\beta}}(0) \quad (27)$$

After convergence of e_2 to zero, in time duration of

t_1 , $V_1(t_1)$ will become zero and sliding motion will occur on $e_1 = e_2 = 0$. Therefore, $V_1(0)$ is the initial value of V_1 , after convergence of e_2 to zero.

A.3: Fault Estimation

The fault is estimated as follows:

$$\hat{f}_a = -F_2^+ \phi v_{eq} \quad (28)$$

v_{eq} is equivalent injection switching term to establish sliding motion on $e = 0$, which is calculated using (21) and $F_2^+ = (F_2^T F_2)^{-1} F_2^T$.

Results and Discussion

In this section, wind turbine controllers and TSMO are implemented in order that the control objectives are achieved and also output estimation errors converge to zero in finite time.

A. Wind Turbine, Controllers, and TSMO Simulation

The 3kW PMSG wind turbine, which is introduced in section 2, the controllers, and the observer are simulated. The system's state-space equations, maximum power capture controller (2), pitch controller (3), and TSMO are simulated in Simulink. Then, the states, outputs, and fault are estimated. The optimum value of the power coefficient of the WT proportional to the optimum TSR $\lambda^* = 7.14$ is $C_{p_{max}} = 0.439$ [26]. Karman spectrum model with a mean wind speed of 8 meters per second is considered as the wind model. Wind rated speed equals to 10.5 m/s and simulation is implemented in the low-speed region for 10 seconds. The parameters of the wind turbine are given in Table 1.

Table 1: 3kW PMSG wind turbine parameters [27]

| PMSG | Drive train and rotor |
|--|-----------------------------------|
| $p = 3$, $R_s = 3.3 \Omega$ | |
| $\Phi_m = 0.4382 \text{ Wb}$ | Gear ratio: $N_g = 7$ |
| $L_d = 41.56 \text{ mH}$ | Moment of inertia: |
| $L_q = 41.56 \text{ mH}$ | $J_h = 0.5042 \text{ kg.m}^2$ |
| | Efficiency: $\eta = 1$ |
| $R_{in} = 80 \Omega$, $V_s = 380 \text{ V}$ | Blade length: $R = 2.5 \text{ m}$ |
| $\rho = 1.25 \text{ kg/m}^3$ | |

The inductance of the equivalent load equals to $L_L = 0.08 \text{ H}$ [28]. The control accuracy of pitch angle equals to 0.3 degrees [29]. Pitch rate is between ± 2 and ± 18 degrees per second practically [30]. In this research, the maximum value of the pitch rate is considered as ± 15 degrees per second. Using (1), the

pitch actuator's time constant equals to $\tau_\beta = 0.3/15 = 0.02$.

B. Linearized Systems, Controllers, and Observer Simulation

Using the system of equations of (5) the equilibrium point is:

$$x_0 = [-1.38 \quad 4.66 \quad 0 \quad 8.46]^T \quad (29)$$

The stability of this equilibrium point is investigated using the matrix \bar{A}_L . Since all eigenvalues of the matrix \bar{A}_L lie in the left half plane, this equilibrium point is stable. According to the condition A_2 in (10), it is necessary to increase the number of sensors in order that the observer can estimate the states and the fault. Hence, the number of measurable outputs are increased to three. Therefore, two sensors must be added to the wind turbine system in order to measure the first and second outputs. It is not required to add an additional sensor to measure the generator speed, which is the third output, because it is already measured in the wind turbine systems.

$$A_2 : 2p \geq n + q \rightarrow A_2 : 2 \times 3 \geq 4 + 1$$

Hence, \bar{C} matrix changes as below:

$$\bar{C} = \begin{bmatrix} 0 & 1 & 0 & 0 \\ 0 & 0 & 1 & 0 \\ 0 & 0 & 0 & 1 \end{bmatrix} \quad (30)$$

The following maximum power controller is used in the simulations:

$$G_{CMP}(s) = 2.542 + 2.319 \frac{1}{s} + 0.178 \frac{130.843}{1 + 130.843 \frac{1}{s}} \quad (31)$$

The pitch angle controller (3) is designed as follows:

$$G_{CP}(s) = 2 + \frac{0.05}{s} \quad (32)$$

According to (11) the coordinate transformation matrix T_L is:

$$T_L = \begin{bmatrix} -10 & 1 & 0 & 0 \\ 0 & 1 & 0 & 0 \\ 0 & 0 & 1 & 0 \\ 0 & 0 & 0 & 1 \end{bmatrix} \quad (33)$$

The value of other parameters of the observer are chosen as below:

$$\begin{aligned} \rho_1 &= \rho_2 = \rho_3 = 1000 \\ \alpha &= 3, \beta = 5 \\ p_1 &= 1, q_1 = 1 \\ A_{4s} &= \text{diag} \{-1, -2, -3\} \\ \delta_i &= 0.01 \end{aligned} \quad (34)$$

The convergence time of output and non-output

states equals to:

$$t_2 < \frac{\sqrt{0.076}}{50} = 5.51 \times 10^{-3} \text{ s} \quad (35)$$

$$t_1 < \frac{5}{2} 1000^{-\frac{3}{5}} (2.538 \times 0.15)^{\frac{4}{10}} = 0.027 \text{ s} \quad (36)$$

The simulation results are presented in Figs. 2 to 8:

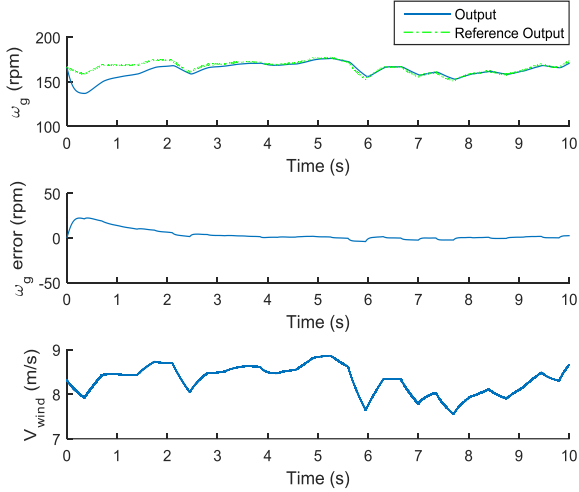


Fig. 2: Generator's reference speed, generator's speed, generator's speed tracking error, and wind speed.

According to Fig. 2, the generator speed converges to the desired output after 3 seconds using a PID controller.

Using TSMO, state estimation errors converge to zero in finite time as represented in Figs 3 and 4.

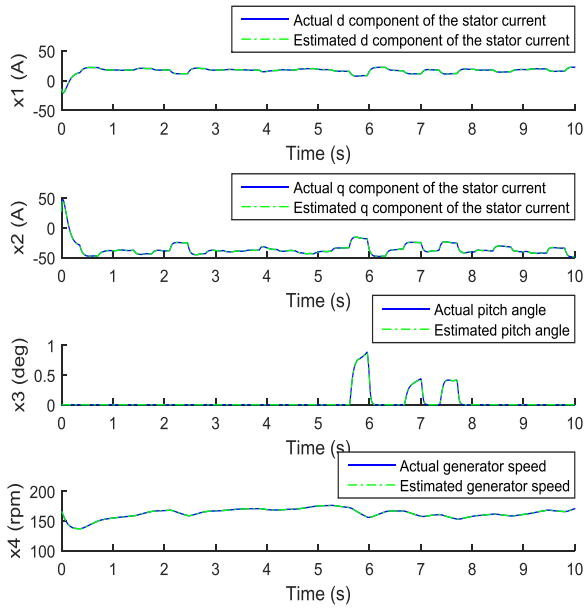


Fig. 3: Actual and estimated states.

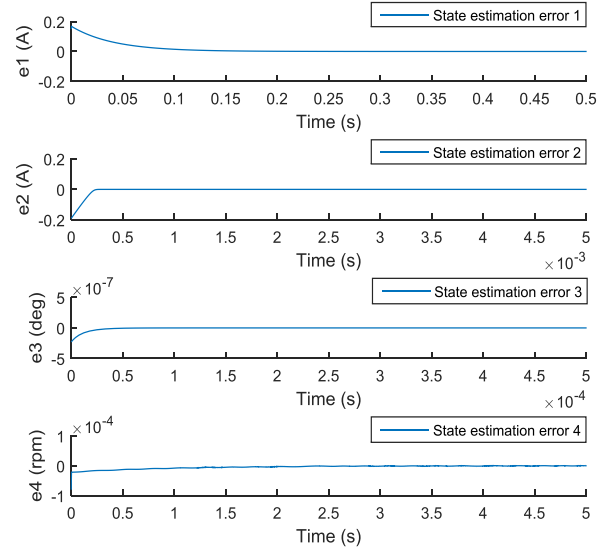


Fig. 4: State estimation errors (zoomed).

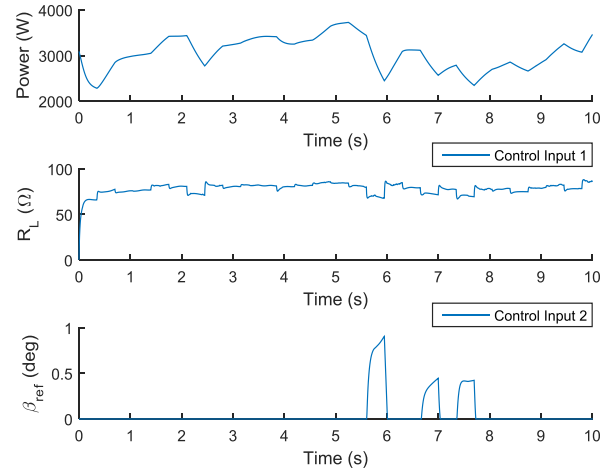


Fig. 5: Power and control inputs.

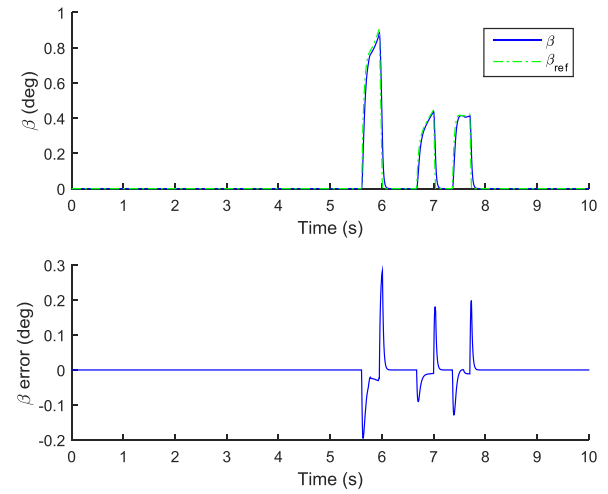


Fig. 6: Pitch angle, reference pitch angle, and pitch angle error with respect to reference pitch angle.

According to Figs. 5 and 6, the wind turbine's power is variable between 2 and 4 kW. In addition, in order for the desired control objective, which is maximum power capturing, to be achieved, R_L should vary between $65\ \Omega$ and $90\ \Omega$ and β_{ref} should be between 0 and 1 deg.

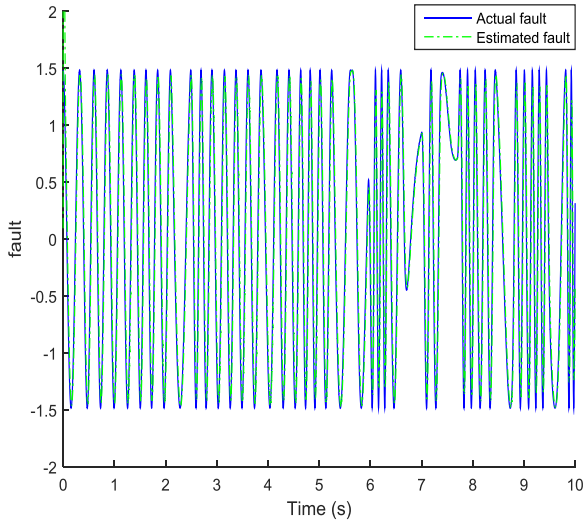


Fig. 7: Actual and estimated fault.

As it is presented in Fig. 7, the WT fault is detected and the actual fault and estimated fault diagrams approximately coincide.

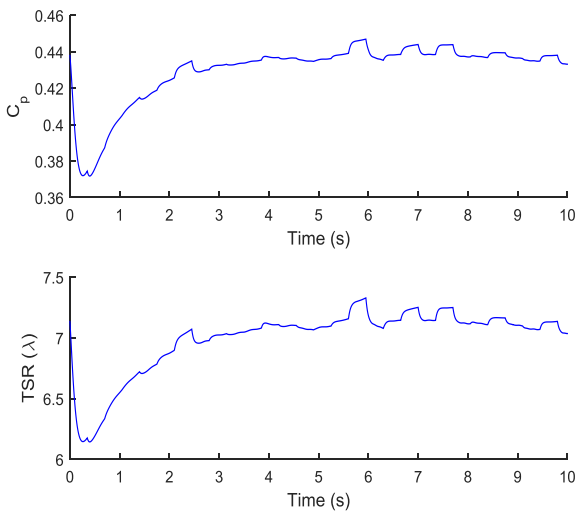


Fig. 8: Power coefficient and TSR.

According to Fig. 8, after a time duration of 3 seconds, in which the system's output traces the desired output, the power coefficient and TSR have variations in the ranges close to their optimum values, which are 0.439 and 7.14, respectively. Therefore, the maximum power is captured.

Furthermore, both measured and unmeasured states

and BIF are estimated in a finite time.

Conclusion

According to simulation results, which are presented in the previous section, using TSMO, BIF is detected and the states are estimated. BIF is modeled as a sinusoidal function with a frequency equal to the rotating frequency of the wind turbine shaft. The frequency of BIF is time-varying because of the time-varying nature of wind speed.

Using the designed observer, the sinusoidal function of BIF with variable frequency is estimated as well. TSMO's advantage in comparison to sliding mode observer (SMO) is that using TSMO not only output estimation errors, but also non-output estimation errors converge to zero in finite time.

In future research works, a TSMO could be designed in order to estimate the states and detect the fault considering nonlinear state-space equations of the PMSG wind turbine.

Author Contributions

S. Khodakaramzadeh, worked on conceptualization, developed the methodology and simulations, and edited/reviewed the paper. M. Ayati is the supervisor, worked on conceptualization, developed the methodology and he edited/reviewed the paper. M. R. Ha'iri-Yazdi is the supervisor and he edited the paper.

Acknowledgment

The author gratefully acknowledges the (American Control Conference, P. F. Odgaard and K. E. Johnson, for their work on WT modeling), (Automatica, C.P. Tan, X. Yu, Z. Man, for their work on terminal sliding mode observers), and (Renewable Energy, M. Rahnavard, M. Ayati, M. R. Hair-Yazdi, and M. Mousavi, for their work on the finite-time fault estimation of WT).

Conflict of Interest

The authors declare no potential conflict of interest regarding the publication of this work. In addition, the ethical issues including plagiarism, informed consent, misconduct, data fabrication and, or falsification, double publication and, or submission, and redundancy have been completely witnessed by the authors.

Abbreviations

| | |
|-------------|--------------------------------|
| <i>BIF</i> | Blade Imbalance Fault |
| <i>DFIG</i> | Doubly Fed Induction Generator |
| <i>EMD</i> | Empirical Mode Decomposition |
| <i>FDS</i> | Fault Detection System |
| <i>FQL</i> | Fuzzy Q-Learning |
| <i>GEP</i> | Gene Expression Programming |
| <i>OM</i> | Operation and Maintenance |

| | |
|-------------|--|
| PMSG | Permanent Magnet Synchronous Generator |
| SMO | Sliding Mode Observer |
| TSMO | Terminal Sliding Mode Observer |
| TSR | Tip Speed Ratio |
| WECS | Wind Energy Conversion System |
| WT | Wind Turbine |

References

- [1] M. Rahnavard, M. Ayati, M.R. Hairi Yazdi, "Robust actuator and sensor fault reconstruction of wind turbine using modified sliding mode observer," *Trans. Inst. Meas. Control*, 41(6): 1504–1518, 2018.
- [2] M. HojatyDana, M. AlizadehPahlavani, "Control strategies for performance assessment of an autonomous wind energy conversion system," *J. Electr. Comput. Eng. Innov.*, 2(1): 15–20, 2014.
- [3] H. Malik, S. Mishra, "Application of LVQ network in fault diagnosis of wind turbine using turbsim , FAST and simulink," in *Proc. Michael Faraday IET Int. Summit*: 474–480, 2015.
- [4] M.L. Corradini, A. Cristofaro, S. Pettinari, "Diagnosis and accommodation of faults affecting the PMSG in variable-speed sensorless wind turbines - A deterministic approach," *2014 Eur. Control Conf. (ECC)*: 1957–1962, 2014.
- [5] C.C. Cang, J. Lee, H. Bang, "Structural health monitoring for a wind turbine system : a review of damage detection methods," *Meas. Sci. Technol.*, 19(12), 2008.
- [6] S.M. Miryousefi Aval, A. Ahadi, "Wind turbine fault diagnosis techniques and related algorithms," *Int. J. Renew. Energy Res.*, 6(1): 80–89, 2016.
- [7] B. Lu, Y. Li, X. Wu, Z. Yang, "A review of recent advances in wind turbine condition monitoring and fault diagnosis," presented at the 2009 IEEE Power Electron. Mach. Wind Appl., Lincoln, NE, USA, 2009.
- [8] D. Lu, W. Qiao, "Frequency Demodulation-Aided Condition Monitoring for Drivetrain Gearboxes," presented at the 2013 IEEE Transp. Electrification Conf. Expo, Detroit, MI, USA, 2013.
- [9] N.M. A. Freire, J.O. Estima, A.J. M. Cardoso, "A new approach for current sensor fault diagnosis in pmsg drives for wind energy conversion systems," in *Proc. 2012 IEEE Energy Convers. Congr. Expo.*:2083–2090, 2012.
- [10] M. Rahnavard, M.R. Hairi Yazdi, M. Ayati, "On the development of a sliding mode observer- based fault diagnosis scheme for a wind turbine benchmark model," *J. Energy Equipments Syst.*, 5(1): 13–26, 2017.
- [11] J. Guo, S. Lu, C. Zhai, Q. He, "Automatic bearing fault diagnosis of permanent magnet synchronous generator in wind turbine subjected to noise interference," *Meas. Sci. Technol.*, 29(2), 2017.
- [12] R.K. Ibrahim, S. Watson, "Condition Monitoring of Permanent Magnet Synchronous Generator for wind turbine applications," in *Proc. 2016 3rd Conf. Control Fault-Tolerant Syst.*: 648–653, 2016.
- [13] M.L. Corradini, G. Ippoliti, G. Orlando, "Sensorless fault-tolerant control of VS Wind Turbines maximizing efficiency in the presence of electrical faults," in *Proc. 2015 IEEE 54th Annu. Conf. Decis. Control*: 682–687, 2015.
- [14] P.F. Odgaard, K.E. Johnson, "Wind turbine fault detection and fault tolerant control - an enhanced benchmark challenge," *2013 Am. Control Conf.*: 4447–4452, 2013.
- [15] E. Sales-Setien, I. Penarrocha, D. Dolz, R. Sanchis, "Fault detection in the blade and pitch system of a wind turbine with H2 PI observers," *J. Phys. Conf. Ser.*, 659: 1-10, 2015.
- [16] X. Gong, W. Qiao, "Imbalance fault detection of direct-drive wind turbines using generator current signals," *IEEE Trans. Energy Convers.*, 27(2): 468–476, 2012.
- [17] H. Malik, S. Mishra, "Proximal support vector machine (PSVM) based imbalance fault diagnosis of wind turbine using generator current signals," *J. Energy Procedia*, 90: 593–603, 2016.
- [18] H. Malik, S. Mishra, "Application of Fuzzy Q Learning (FQL) technique to wind turbine imbalance fault identification using generator current signals," presented at the 2016 IEEE 7th Power India Int. Conf., Bikaner, India, 2016.
- [19] H. Malik, S. Mishra, "Application of Gene Expression Programming (GEP) to investigate the health condition of direct-drive wind turbine," presented at the 2016 7th India Int. Conf. Power Electron., Patiala, India, 2016.
- [20] S. Boulouma, H. Belmili, S. Labiod, "Robust adaptive maximum power capture control scheme for a PMSG based WECS," presented at the 2015 4th Int. Conf. Electr. Eng. ICEE 2015, Bumerdes, Algeria, 2015.
- [21] X. Tong, X. Zhao, "Power generation control of a monopile hydrostatic wind turbine using an H ∞ loop-shaping torque controller and an LPV pitch controller," *IEEE Trans. Control Syst. Technol.*, 26(6): 2165–2172, 2017.
- [22] N.A. Orlando, M. Liserre, R.A. Mastromauro, A.D. Aquila, "A survey of control issues in PMSG-based small wind-turbine systems," *IEEE Trans. Ind. informatics*, 9(3): 1211–1221, 2013.
- [23] J. Hang, J. Zhang, M. Cheng, "Fault diagnosis of wind turbine using control loop current signals," in *Proc. 2014 IEEE Energy Convers. Congr. Expo.*: 3119–3124, 2014.
- [24] M. Rahnavard, M. Ayati, M.R. Hairi Yazdi, M. Mousavi, "Finite time estimation of actuator faults, states, and aerodynamic load of a realistic wind turbine," *Renew. Energy*, 130: 256–267, 2019.
- [25] M. Mousavi, M. Rahnavard, S. Haddad, "Observer based fault reconstruction schemes using terminal sliding modes," *Int. J. Control*, 93(4): 881–888, 2018.
- [26] S. M. Mueen, J. Tamura, T. Murata, *Stability Augmentation of a Grid-connected Wind Farm*. Springer, 2009.
- [27] I. Munteanu, A. Bratcu, N. Cutululis, E. Ceanga, *Optimal Control of Wind Energy Systems: Toward a Global Approach*. Springer, 2008.
- [28] H.M. Nguyen and D. S. Naidu, "Direct fuzzy adaptive control for standalone wind energy conversion systems," presented at the World Congr. Eng. Comput. Sci., San Francisco, USA, 2012.
- [29] S. Baburajan, "Improving the efficiency of a wind turbine system using a fuzzy-pid controller," presented at the 2018 Adv. Sci. Eng. Technol. Int. Conf., Dubai, United Arab Emirates, 2018.
- [30] M.A. Mosa, A.A. Elsyed, A.M.A. Amin, A.M.A. Ghany, "Variable speed wind turbine pitch angle controller with rate limiter anti-windup," presented at the 2016 Eighteenth Int. Middle East Power Syst. Conf., Cairo, Egypt, 2016.

Biographies



Shabnam Khodakaramzadeh was born in Tehran, Iran, in 1993. She received her B.Sc. from Sharif University of Technology in 2016 and M.Sc. from University of Tehran in 2018, both in mechanical engineering. Her research interests include control, automation, and fault diagnosis.



Moosa Ayati received his B.Sc. degree from Isfahan University of Technology, Isfahan, Iran, in 2004, and his M.Sc. and Ph.D. degrees in 2006 and 2011 from K. N. Toosi University of Technology, Tehran, Iran, all in Electrical Engineering with the first rank honors. He spent two years as a Post-Doctoral Fellow at the University of Tehran School of Electrical Engineering, College of Engineering, Tehran, Iran, working on fault detection systems. He is currently head of the Advanced Instrumentation Laboratory (AIL) and an Associate Professor with the control division, School of Mechanical Engineering, College of Engineering, at University of Tehran, Tehran, Iran. His area of interest includes adaptive control and system identification, fault detection systems, instrumentation and industrial automation, Mechatronics,

and hybrid systems. Professor Ayati is a member of Iranian Society of Instrumentation and Control, Iranian Society of Mechanical Engineers, and National Society of Mechatronics.



Mohammad Reza Hairi Yazdi received his B.Sc. and M.Sc. degrees in Mechanical Engineering from Amir Kabir University of Technology, Tehran, Iran in 1985 and 1987 respectively. He received his Ph.D. degree from Imperial College London in 1992 and since then he has been at the University of Tehran, Tehran, Iran where he is now a Professor at the School of Mechanical Engineering. His main research interests include design, simulation, manufacturing and control of dynamic systems.

Copyrights

©2021 The author(s). This is an open access article distributed under the terms of the Creative Commons Attribution (CC BY 4.0), which permits unrestricted use, distribution, and reproduction in any medium, as long as the original authors and source are cited. No permission is required from the authors or the publishers.



How to cite this paper:

S. Khodakaramzadeh, M. Ayati, M.R. Ha'iri-Yazdi, "Fault diagnosis of a permanent magnet synchronous generator wind turbine," *J. Electr. Comput. Eng. Innovations*, 9(2): 143-152, 2021.

DOI: [10.22061/JECEI.2020.7424.408](https://doi.org/10.22061/JECEI.2020.7424.408)

URL: http://jecei.sru.ac.ir/article_1512.html





Research paper

Design of a High-Speed and Low Power CMOS Comparator for A/D Converters

F. Shakibaei, A. Bijari*, S.H. Zahiri

Department of Electrical Engineering, Faculty of Electrical and Computer Engineering, University of Birjand, Birjand, Iran.

Article Info

Article History:

Received 14 June 2020
Reviewed 15 August 2020
Revised 25 October 2020
Accepted 27 December 2020

Keywords:

Dynamic comparator
High-speed
Low-power
Bulk driven

*Corresponding Author's Email
Address:

a.bijari@birjand.ac.ir

Abstract

Background and Objectives: Comparators play a critical role in the analog to digital converters (ADCs) and digital to analog converters (DACs). Therefore, different structures have been proposed to improve their performance. Power, delay, offset, and noise are the important factors that have significantly affect the comparator's performance. In low power applications, power consumption and delay are the critical concerns that should be minimized to obtain better performance. In this work, a low-power and high-speed comparator has been proposed, which is suitable for applications operating at a low power supply.

Methods: Based on the conventional structure of the comparator, some modifications are implemented to achieve better performance in terms of power consumption and delay. Additionally, the proposed structure gives great performance when the difference of inputs is very small. To verify the proposed structure, it is designed and simulated in a 0.18 μm CMOS technology with a power supply of 1 V and sampling frequency of 2 MHz.

Results: To draw a fair comparison, the conventional and proposed structure is simulated in equal circumstance. The size of transistors is designed with appropriate W/L ratios to achieve appropriate performance. The proposed structure not only reduces the power consumption by 44%, but also it decreases the delay by 9.1%. The power consumption of the proposed structure is around 0.12 μW . The total occupied area by the proposed structure is approximately 127.44 μm^2 .

Conclusion: In this paper, we presented a delay analysis for the proposed dynamic comparator. In addition, based on theoretical analyses, a new dynamic comparator consumes less power and operates faster compared with the conventional structure. The simulation results verify the theoretical analysis.

©2021 JECEI. All rights reserved.

Introduction

The comparator [1], [2], [3], [4], [5], [6] is one of the most important blocks in the integrated circuits, which compares two analog inputs and produces digital outputs. Open-loop comparators, regenerative latch comparators, and preamplifier latch comparators are three important architectures of voltage comparators.

Each of them is superior to others from the point of view of power consumption, delay, offset, input referred noise [7], and so on. In other words, the high-resolution and high-speed comparator can be achieved by implementing open-loop architectures. Furthermore, the latch comparator is the most useful structure due to its high-speed and low-power consumption.

So, the prominent aspect of the latch-type comparators by comparison with others is its power, particularly at the applications with low power supply. The comparator is a building block in data conversion circuits, including successive approximate register (SAR) [8], [9], [10], [11], Pipeline [12], [13], [14], and Flash [15], [16], [17]. Therefore, the optimal design of the comparator is very important, particularly in terms of power consumption, speed, offset and occupied space on the chip [18], [19], [20], [21].

It should be noted the comparators have a critical influence on the overall performance in analog-to-digital converters. To obtain a high effective number of bits (ENOB), an appropriate comparator is required. As a result, the designers are always looking to achieve the best features of the comparator for special purposes.

In recent years, according to shrinking the feature size of CMOS devices and reduction of the supply voltage (V_{DD}), the power consumption of circuits is diminished, and thereby, the requirement goes toward comparators, which can follow these.

Different structures have been proposed, such as dynamic comparators [22]. However, there is a trade-off between power consumption and speed in low supply voltage of these comparators. In the low supply voltage, they can operate fast.

However, during the two phases, latch and reset phases, the comparator consumes the static current. Therefore, they have a crucial restriction in low-power applications.

To address the problem of dynamic power consumption, a self-reset method is implemented [23]. Moreover, bulk-driven [24], [25], [26] is another technique to improve the speed and power consumption.

However, the technique suffers from lower transconductance (backgate transconductance (g_{mb})) in comparison with its gate-driven counterpart. Furthermore, the popularity of the technique is reduced due to the unique fabrication process.

The comparator with double-tail dynamic structure is presented in [27]. The comparator is designed based on separating the input stage and cross-coupled part. This separation forces comparator to operate fast over a wide input common-mode range and power supply voltage.

In this paper, a new comparator with no additional circuits has been introduced. The proposed comparator is simulated in 180 nm CMOS technology, and exhibits high speed and low-power consumption. Additionally, the delay analysis has been carried out for the proposed structure.

The rest of the paper is organized as follows: the next

section is named the proposed comparator, which explains the conventional and proposed structures and analyses the delay. Next, the simulation results are presented and compared with other structures, and finally the last section contains the conclusion of the proposed study.

Proposed structure

Figure 1 shows conventional comparator's schematic with a current source, which input signals are applied to the gate terminal of transistors [28]. The operation of the conventional comparator can be described as follows.

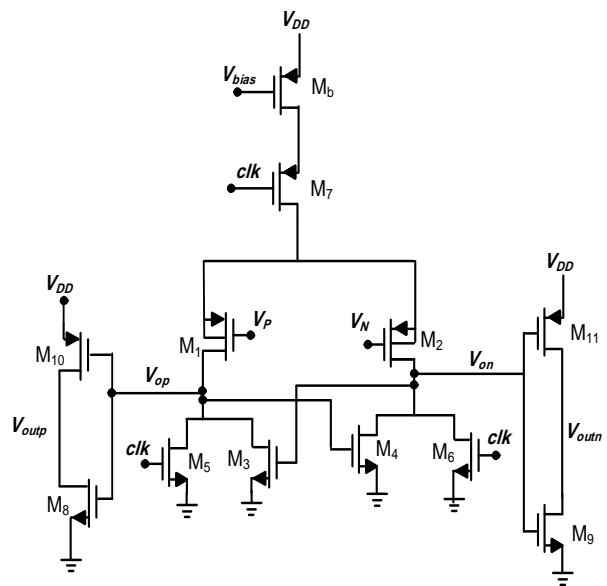


Fig. 1: Schematic circuit of the conventional dynamic comparator.

During the reset phase, when the $clk=1$, transistor M_7 is cut-off, and both points of V_{op} and V_{on} are reset to ground by transistors of M_5 and M_6 to determine an initial condition for the output of the comparator.

Also, the output inverters pull both outputs of the comparator (V_{outp} and V_{outn}) to V_{DD} .

In the comparison phase, when the $clk=0$, the transistors M_5 and M_6 are off, and M_7 turns on. Assuming that $V_p > V_{N_r}$, both output point values of V_{op} and V_{on} change according to the differential input voltage. First, the both output points start to decrease until M_4 of cross-coupled nMOS load transistors achieves the turn-on voltage.

In other words, the different voltage between gate and source is higher than the threshold voltage. Then, the output point of V_{on} will continue to discharge to the ground, and at the same moment, the output point of V_{op} will be changed its way and charged to the high level as shown in Fig. 2.

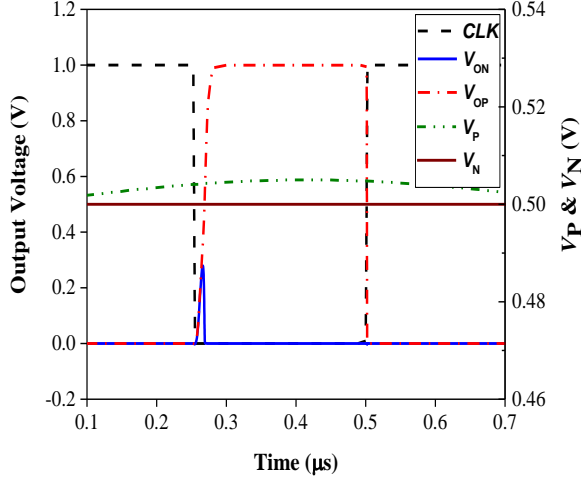


Fig. 2: Transient simulation of the conventional comparator.

The comparator will operate vice versa if V_N is greater than V_P . The total delay of the conventional comparator can be expressed as follows [29]:

$$t_{\text{delay}} = t_0 + t_{\text{latch}} \quad (1)$$

where t_0 represents the time for discharging C_L capacitor until the nMOS transistors of M_4 or M_3 turn on.

$$t_0 = \frac{V_{th} \times C_L}{I_{B1}} = \frac{2V_{th} \times C_L}{I_{tail}} \quad (2)$$

where I_{B1} is the drain current of the input transistor. C_L represents the total load capacitance of the comparator, and V_{th} is the threshold voltage of transistor. t_{latch} denotes the latching delay time of the two cross-coupled transistors of inverter and is given by:

$$t_{\text{latch}} = \frac{C_L}{g_{m,\text{Total}}} \ln\left(\frac{\Delta V_{\text{out}}}{\Delta V_0}\right) = \frac{C_L}{g_{m,\text{Total}}} \ln\left(\frac{V_{DD}}{2\Delta V_0}\right) \quad (3)$$

where $g_{m,\text{Total}}$ is the sum of the transconductance of the differential pair transistors (g_{m1} and g_{m2}) and the transconductance of the cross-coupled nMOS loads. It is assumed that $\Delta V_{\text{out}} = V_{DD}/2$, and the ΔV_0 can be obtained as follows:

$$\begin{aligned} \Delta V_0 &= |V_{op}(t=t_0) - V_{on}(t=t_0)| \\ &= V_{th} - \frac{I_{B2} \times t_0}{C_L} = V_{th} \left(1 - \frac{I_{B2}}{I_{B1}}\right) \end{aligned} \quad (4)$$

By assuming ΔI_{latch} as (5), the (4) can be rewritten as below:

$$\Delta I_{\text{latch}} = |I_{B1} - I_{B2}| = g_{m1,2} \Delta V_{in} \quad (5)$$

$$\Delta V_0 = V_{thp} \frac{\Delta I_{\text{latch}}}{I_{B2}} \approx 2V_{thn} \frac{g_{m1,2} \Delta V_{in}}{I_{tail}} \quad (6)$$

where ΔV_{in} is the small differential input voltage. Substituting (6) in (3), the total delay of the conventional comparator is obtained as follows:

$$\begin{aligned} t_{\text{delay}} &= \frac{2V_{th}C_L}{I_{tail}} + \frac{C_L}{g_{m,\text{Total}}} \ln\left(\frac{V_{DD}}{2\Delta V_0}\right) \\ &= \frac{2V_{th}C_L}{I_{tail}} + \frac{C_L}{g_{m,\text{Total}}} \ln\left(\frac{V_{DD}I_{tail}}{4\Delta V_{in}V_{th}g_{m1,2}}\right) \end{aligned} \quad (7)$$

Therefore, there are several parameters that have a significant effect on the delay of the comparator, such as the differential input voltage, transconductance of the input transistors, latch tail current, the capacitance ratio of the output nodes, and transconductance of the intermediate stage transistors.

To address the issues of the delay and power consumption in the conventional comparator, a new structure has been proposed. Figure 3 demonstrates the schematic circuit of the proposed comparator, which consists of two inverters, a current source, and a cross-coupled inverter.

The input signal is applied to gate and body terminals, additionally, a cross-coupled inverter is implemented. These modifications will have a positive effect on the speed and power consumption of the comparator. Moreover, for a given power supply, the speed of the comparator is increased because both g_m and g_{mb} have a significant effect on it.

The operation of the proposed comparator at the reset phase is similar to the conventional comparator. When $clk=1$, M_7 is cut off, and both transistors of M_5 and M_6 are turned on, and the nodes of V_{op} and V_{on} are connected to the ground.

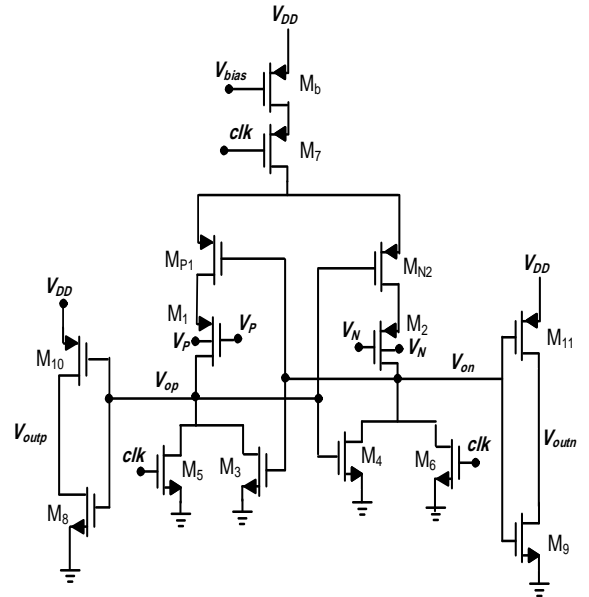


Fig. 3: Proposed dynamic comparator.

Also, at the aforementioned phase, the output nodes of V_{outp} and V_{outn} are charged to the power supply.

As shown in Fig. 3 when clk goes low ($clk=0$), the transistor M_7 turns on, and the transistors M_5 and M_6 are cut-off. Therefore, the comparator goes to the comparison phase.

Assume the case that V_p is greater than V_n , both output V_{op} and V_{on} nodes can be started to charge to V_{DD} with different rates according to the differential input voltage. This increment continues until the transistors of cross-coupled achieve the turn-on voltage ($V_{gs} > V_{th}$). Then, the values of output nodes are determined. The output node of V_{on} will have the same trend and continues to discharge to the ground.

At the same time, the output node of V_{op} will be charged to the power supply.

The final output of the comparator can be obtained by the two inverters. The cross-coupled transistors and the transconductance (g_{mb} and g_m) of the input transistors have a constructive effect on the speed and then the delay of the comparator.

Theoretically, the following equation demonstrates how this structure improves the speed of the comparator.

$$\begin{aligned}
 t_{delay} &= \frac{2V_{th}C_L}{I_{tail}} + \frac{C_L}{(g_{mb1.2} + g_{m.Total})} \ln\left(\frac{V_{DD}}{2\Delta V_0}\right) \\
 &= \frac{2V_{th}C_L}{I_{tail}} + \frac{C_L}{(g_{mb1.2} + g_{m.Total})} \\
 &\quad \times \ln\left(\frac{V_{DD} I_{tail}}{4\Delta V_{in} V_{thn} (g_{m1.2} + g_{mb1.2})}\right) \quad (8)
 \end{aligned}$$

According to (8), the proposed structure increases the total effective transconductance of the input transistors. As a result, the time constant is reduced, thereby improving the speed of the proposed comparator.

Simulation Results and Discussion

To verify the proposed structure, the simulation results are presented. The proposed comparator is designed and simulated in 180 nm CMOS technology. The simulation results are obtained at $V_{DD}=1$ V, frequency of 2 MHz, and $C_L=10$ fF.

The transistors' size is the same in both structures (conventional and proposed structures) to provide a fair comparison.

Moreover, the minimum channel length of all transistors is considered 0.18 μm .

In Table 1, the values of the device parameters are presented. As shown, the size of the input transistors is designed large enough in comparison to other transistors to satisfy a specified offset.

Table 1: Transistor sizing of the proposed comparator

| Transistor | $W (\mu m)/L (\mu m)$ |
|-------------------------------|-----------------------|
| M_1, M_2 | 3/0.18 |
| M_3, M_4 | 0.22/0.18 |
| M_5, M_6 | 0.22/0.18 |
| M_7 | 1/0.18 |
| M_b | 1/0.18 |
| M_{p1}, M_{n2} | 0.22/0.18 |
| $M_9, M_{10}, M_{11}, M_{12}$ | 0.22/0.18 |

Figure 4 shows the results of power consumption for the different common-voltage.

The proposed structure's power consumption is decreased remarkably when the common voltage sweeps from 0.4 V to 0.7 V.

However, the conventional comparator exhibits the proper operation at $V_{cm} > 0.65$ V. Additionally, the delay is decreased in comparison with the conventional structure.

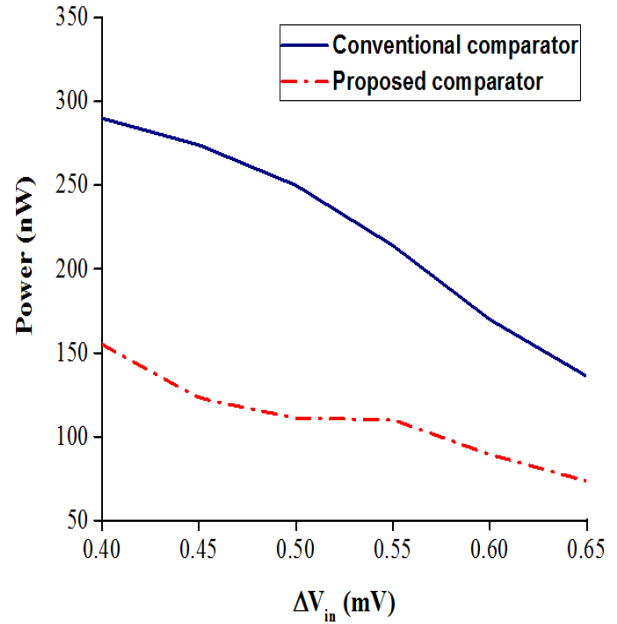


Fig. 4: Power with a different common-mode variation.

As shown in Fig. 5, by increasing the common-voltage, the difference of delays in the conventional and proposed structures becomes more significant. Therefore, the proposed structure presents better performance.

The proposed and conventional comparators are simulated for different input amplitudes to evaluate comparators' operation under this condition.

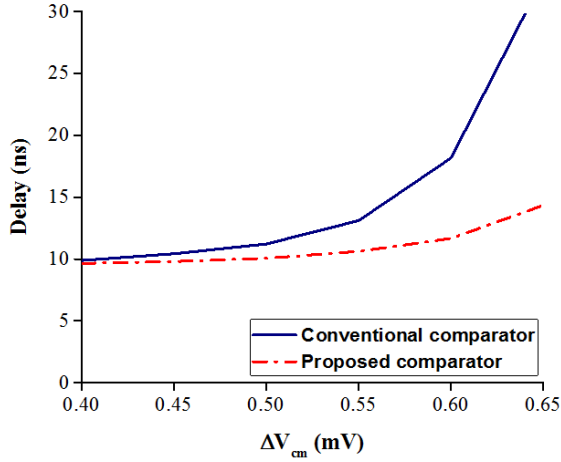


Fig. 5: Delay versus different common-mode variation at $\Delta V_{in}=0.1$ mV.

As shown in Fig. 6, for $\Delta V_{in}=0.1$ mV, proposed comparator's delay is 9.968 ns at $V_{DD}=1$ V, while the conventional one exhibits the delay of 11.12 ns.

According to the performance of the proposed structure, it is suitable for the applications that have low input amplitude, such as bioelectronics.

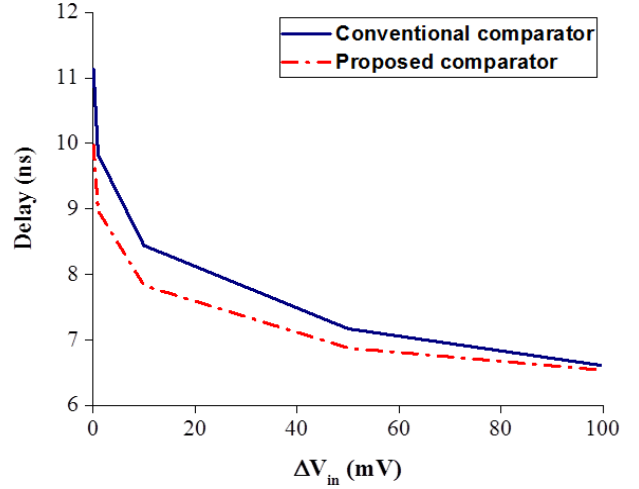


Fig. 6: Delay versus different input amplitude.

Table 2: Performance summary of the proposed mixer and comparison with previous studies

| | [21] | [22] | [25] | [28] | [29] | [30] | Conventional Structure | Proposed Structure |
|--------------------------------------|--------|--------|-------|-------|-------|-------|------------------------|--------------------|
| CMOS Technology | 180 nm | 130 nm | 65 nm | 180nm | 180nm | 180nm | 180nm | 180nm |
| Power Supply (V) | 1.2 | 1.2 | 1.2 | 1.2 | 1.2 | 1.8 | 1 | 1 |
| Sample frequency (MHz) | 62.5 | 1250 | - | 50 | 500 | 1 | 2 | 2 |
| Delay ($\Delta V_{in}=0.1$ mV) (ns) | 1.837 | 0.1 | 0.120 | 3.169 | 0.55 | - | 12 | 9.968 |
| Power (μ W) | 18.6 | 600 | 0.75 | 23.46 | 329 | 130 | 0.25 | 0.12 |
| Meas./Sim. | Sim. | Sim. | Sim. | Meas. | Sim. | Sim. | Sim. | Sim. |

* Meas.=Measurement

* Sim.=Simulation

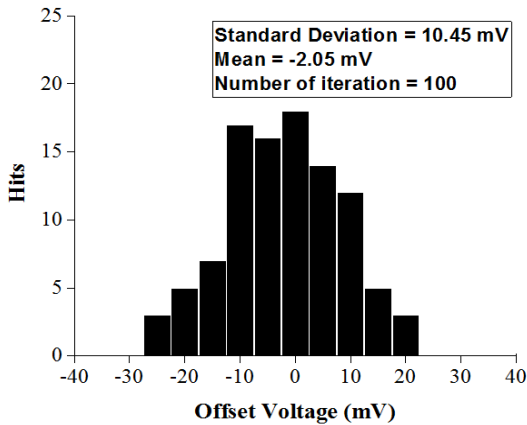


Fig. 7: Monte Carlo simulation of the offset in the proposed dynamic comparator.

Figure 7 illustrates the results of Monte Carlo simulations for a run of 100 samples. The standard deviation of the offset of the proposed comparator is achieved $\sigma=10.45$ mV. The value of the offset increases in comparison to the conventional structure by approximately 1 mV. This value is proportional to the backgate transconductance of g_{mb} . Kick back noise of the comparator is another factor should be considered and simulated [18]. At the regeneration phase, the high voltage variations of nodes have a significant effect on the input of the comparator due to parasitic capacitors. The input voltage is disturbed because of the lack of zero output impedance of the preceding stage. To evaluate the kick back noise of the comparator, the circuit as shown in Fig. 8 is implemented.

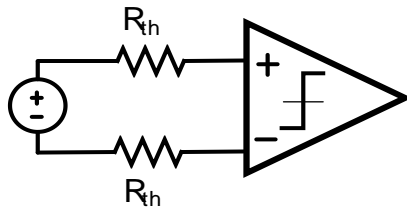


Fig 8: Kick back noise circuit.

The maximum kick back noise which is coupled to the input voltage signal, is 0.28 mV without any compensation.

Moreover, proposed comparator's layout is shown in Fig. 9 that the total active silicon area is $10.8 \mu\text{m} \times 11.8 \mu\text{m}$.

The performance of the proposed dynamic comparator is summarized in Table 2, and made a comparison with the similar reported works.

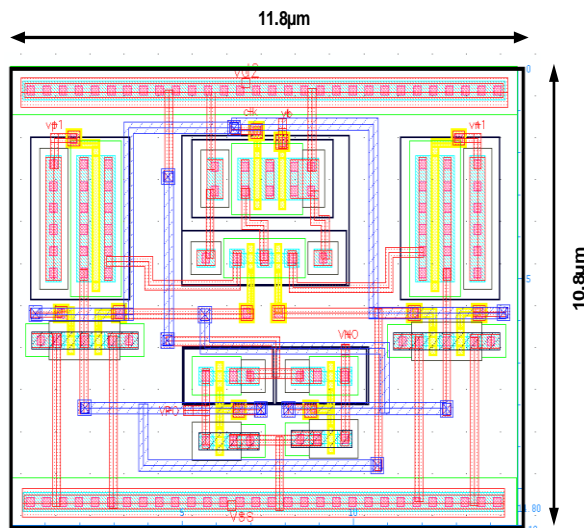


Fig. 9: Layout of the proposed structure.

Conclusion

In this paper, a new structure is proposed for low power and low voltage dynamic comparator. The input signal is applied to bulk and gate terminals.

As a result, both transconductance (g_m) and backgate transconductance (g_{mb}) contribute to the reduction of delay.

With a power voltage of 1 V and frequency of 2 MHz, simulation results in 180 nm CMOS technology show that the proposed structure is achieved 0.12 μW and 9.968 ns power consumption and delay, respectively.

The proposed comparator not only reduces the power consumption by 44%, but also it has decreased the delay by 9.1%.

Author Contributions

F. Shakibaei and A. Bijari developed the theoretical idea and performed the analytic calculations. F. Shakibaei carried out the simulations. All authors discussed the results and contributed to the final manuscript. A. Bijari and S. H. Zahiri supervised the project.

Acknowledgment

We thank our colleagues from the university of Mashhad (FUM) who provided insight and expertise that greatly assisted the research. We thank R. Lotfi assistance for comments that greatly improved the manuscript.

Conflict of Interest

The authors declare no potential conflict of interest regarding the publication of this work. In addition, the ethical issues including plagiarism, informed consent, misconduct, data fabrication and, or falsification, double publication and, or submission, and redundancy have been completely witnessed by the authors.

Abbreviations

| | |
|------|---|
| ADC | Analog to Digital converter |
| CMOS | Complementary Metal Oxide Semiconductor |
| DAC | Digital to Analog converter |
| ENOB | Effective Number of Bits |
| SAR | Successive Approximate Register |

References

- [1] F. Rabbi, S. Das, Q.D. Hossain, N.S. Pathan, "Design of a low-power ultra-high-speed dynamic latched comparator in 90-nm CMOS technology," in Proc. International IEEE Conference on Computer, Communication, Chemical, Material and Electronic Engineering (IC4ME2): 1-4, 2018.
- [2] M. Gangwar, A. Nishad, "Design and simulation of modified ultra-low power CMOS comparator for sigma delta modulator," in Proc. The Second International Conference on Intelligent Computing and Control Systems: 1425-1427, 2018.
- [3] A. Khorami, M. Baraani Dastjerdi, A. Fotowat Ahmadi, "A low-power high-speed comparator for analog to digital converters," in Proc. IEEE International Symposium on Circuits and Systems (ISCAS): 2011-2013, 2016.
- [4] J. Lu, J. Holleman, "A low-power high-precision comparator with time-domain bulk-tuned offset cancellation," IEEE Trans. Circuits Syst. I Regul. Pap., 60(5): 1158-1167, 2013.
- [5] M. Nasrollahpour, C. Yen, S. Hamed-hagh, "A high-speed, low-offset and low-power differential comparator for analog to digital converters," in Proc. International SoC Design Conference (ISOC): 220-221, 2017.

- [6] M. Vaijayanthi, K. Vivek, "Analysis of dynamic comparators in ultra-low supply voltages for high speed ADCs," presented at the 2nd International Conference on Innovations in Information, Embedded and Communication systems (ICIIECS), Tehran, Iran, 2015.
- [7] Y. Ishijima, S. Nakagawa, H. Ishikuro, "Measurement time reduction technique for input referred noise of dynamic comparator," presented at the 2018 IEEE International Conference on Microelectronic Test Structures (ICMTS), Austin, TX, 2018.
- [8] M.D. Scott, B.E. Boser, K.S.J. Pister, "An ultralow-energy ADC for smart dust," *IEEE J. Solid-State Circuits*, 38(7): 1123-1129, 2003.
- [9] F. Shakibae, F. Sajedi, M. Saberi, "Low-power successive approximation ADC using split-monotonic," *IET Circuits Devices Syst.*, 12: 203-208, 2017.
- [10] K. Inoue, T. Matsuura, A. Hyogo, H. San, "Non-binary cyclic and binary SAR hybrid ADC," presented at the MIXDES - 24th International Conference "Mixed Design of Integrated Circuits and Systems, 2017.
- [11] M. Saberi, R. Lotfi, "Segmented architecture for successive approximation analog-to-digital converters," *IEEE Trans. Very Large Scale Integr. VLSI Syst.*, 22: 593-606, 2014.
- [12] M. Taherzadeh-Sani, A. Hamoui, "A reconfiguration 10-12b 0.4-44MS/s pipelined ADC in 1.2V 90nm digital CMOS," in *Proc. ESSCIRC*: 382-385, 2010.
- [13] C. Srikar Datta, G. Prasad, V.S. Prasad Nayak, G. Bhargav, "Design and analysis of a 16-bit 10MHz pipeline ADC in 0.25 μ CMOS," presented at the IEEE International Conference on Computational Intelligence and Computing Research (ICCIC), Madurai, India, 2015.
- [14] S. Bakhtar, S. Dalu, "Design and implementation of low power pipeline ADC," presented at the International Conference on Research in Intelligent and Computing in Engineering (RICE), San Salvador, 2018.
- [15] P. Arunkumar, G. Rekha, P. Narashimaraja, "An efficient design of 3bit and 4bit flash ADC," *Int. J. Comput. Appl.*, 61(11): 32-37, 2013.
- [16] A. Inamdar, A. Sahu, J. Ren, S. Setoodeh, R. Mansour, D. Gupta, "Design and evaluation of flash ADC," *IEEE Trans. Appl. Supercond.*, 25(3): 1-5, 2015.
- [17] P. Rahul, A. Kulkarni, S. Sankanur, M. Raghavendra, "Reduced comparators for low power flash ADC using TSMC018," presented at the International conference on Microelectronic Devices, Circuits and Systems (ICMDCS), Vellore, 2017.
- [18] P.M. Figueiredo, J.C. Vital, "Kickback noise reduction techniques for CMOS latched comparators," *IEEE Trans. Circuits Syst.*, 53(7): 541 – 545, 2006.
- [19] M. Aldacher, M. Nasrollahpour, S. Hamed-hagh, "A low-power, high-resolution, 1 GHz differential comparator with low-offset and low-kickback," presented at the 2017 24th IEEE International Conference on Electronics, Circuits and Systems (ICECS), Batumi, 2017.
- [20] H. Yousefi, S.M. Mirsanei, "Design of a novel high speed and low kick back noise dynamic latch comparator," presented at the 28th Iranian Conference on Electrical Engineering (ICEE), Iran, 2020.
- [21] X. Xin, J. Cai, R. Xie, P. Wang, "Ultra-low power comparator with dynamic offset cancellation for SAR ADC," *Electron. Lett.*, 53(24): 1572–1574, 2017.
- [22] J. F. Gao, G. J. Li, Q. Li, "High-speed low-power common-mode insensitive dynamic comparator," *Electron. Lett.*, 51(2): 134–136, 2015.
- [23] D.G. Xu, S.L. Xu, G.B. Chen, "High-speed low-power and low power supply voltage dynamic comparator," *Electron. Lett.*, 51(23): 1914–1916, 2015.
- [24] B.J. Blalock, "Body-driving as a low-voltage analog design technique for CMOS technology," in *Proc. IEEE Southwest Symp. Mixed-Signal Design*: 113–118, 2000.
- [25] Z. Huang, H. Zhang, "Low-voltage bulk-drive high-speed comparator for ADCs," *Electron. Lett.*, 55(13): 735–737, 2019.
- [26] M. Maymandi-Nejad, M. Sachdev, "1-bit quantiser with rail to rail input range for sub-1V modulators," *IEEE Electron. Lett.*, 39: 894–895, 2003.
- [27] D. Shinkel, E. Mensink, E. Klumperink, E. van Tuijl, B. Nauta, "A double-tail latch-type voltage sense amplifier with 18ps setup hold time," in *Proc. IEEE Int. Solid-State Circuits Conf., Dig. Tech. Papers*: 314–315, 2007.
- [28] C.C. Liu, S.J. Chang, G.Y. Huang, "A 10-bit 50-MS/s SAR ADC with a monotonic capacitor switching procedure," *IEEE J. Solid State Circuits*, 45(4): 731–740, 2010.
- [29] S. Babayan-Mashhadi, R. Lotfi, "Analysis and design of a low voltage low-power double-tail comparator," *IEEE Trans. Very Large Scale Integr. (VLSI) Syst.*, 22: 343–352, 2014.
- [30] H. Aghabeigi, M. Jafaripana, "High speed low power voltage comparator in 0.18 μ m CMOS process for flash ADC," in *Proc. International Conference on Knowledge-Based Engineering and Innovation*: 418-421, 2017.

Biographies



Fatemeh Shakibae received the B.S. and M.Sc. degrees in Electronics Engineering, respectively from Ferdowsi University of Mashhad, Iran, 2012 and 2015 respectively, where she is currently pursuing the Ph.D. degree in the Department of Electronics Engineering, University of Birjand, Iran. Her current research interests include low-power, low-voltage analog and mixed-signal integrated circuits.



Abolfazl Bijari was born in Birjand, Iran in 1982. He received B.S. degree in Telecommunication Engineering and M.S. and Ph.D. in Electronics Engineering from Ferdowsi University of Mashhad (FUM), Iran in 2005, 2007, and 2013, respectively. He is currently an assistant professor in department of Electronics Engineering, University of Birjand, Iran. His research interests include RFIC design, microwave filters and MEMS-based devices.



Seyed Hamid Zahiri received the B.Sc., M.Sc. and Ph.D. degrees in Electronics Engineering from the Sharif University of Technology, Tehran, Iran, Tarbiat Modares University, Tehran, and Ferdowsi University of Mashhad, Mashhad, Iran, in 1993, 1995, and 2005, respectively. He is a Professor in the Department of Electronics Engineering, University of Birjand, Iran. His research interests include pattern recognition, evolutionary algorithms, swarm intelligence algorithms, and soft computing.

Copyrights

©2021 The author(s). This is an open access article distributed under the terms of the Creative Commons Attribution (CC BY 4.0), which permits unrestricted use, distribution, and reproduction in any medium, as long as the original authors and source are cited. No permission is required from the authors or the publishers.

**How to cite this paper:**

F. Shakibaei, A. Bijari, S.H. Zahiri, "Design of a high-speed and low power CMOS comparator for A/D converters," J. Electr. Comput. Eng. Innovations, 9(2): 153-160, 2021.

DOI: [10.22061/JECEI.2021.7602.409](https://doi.org/10.22061/JECEI.2021.7602.409)

URL: http://jecei.sru.ac.ir/article_1517.html





Research paper

An Approach for Solving Signal Cancellation Problem in Spherical Microphone Array

M. Kalantari

Artificial Intelligence Department, Faculty of Computer Engineering, Shahid Rajaei Teacher Training University, Tehran, Iran.

Article Info

Article History:

Received 27 June 2020
Reviewed 12 August 2020
Revised 28 October 2020
Accepted 30 December 2020

Keywords:

Spherical microphone array
Beamforming
Signal cancellation problem
Cross-spectrum matrix of noise

Corresponding Author's Email
Address:

mkalantari@sru.ac.ir

Abstract

Background and Objectives: One major problem in the minimum power distortionless response (MPDR) beamformer is the signal cancellation problem, i.e., the desired signal is canceled by the reflected signal, even though the distortionless response constraint is satisfied. Solving this problem is the objective of this paper.

Methods: It is well known that the signal cancellation problem can be avoided by minimizing the cross-spectrum matrix of noise, i.e., using the minimum variance distortionless response (MVDR) beamformer. But, in the case of disturbance signals which have correlation with the desired signal, estimation of this matrix is a challenging problem. In this paper we propose an approach for estimating the cross-spectrum matrix of noise signal from which we can solve the signal cancellation problem.

Results: Simulation examples show that using the proposed method we can bypass the signal cancellation problem completely.

Conclusion: A common belief is that in the case of a disturbance that is a reflected version of the desired signal, due to cohesive appearance and disappearance of both the disturbance and the desired signal, the estimation of cross-spectrum matrix of noise signal is typically not possible in practice. So, based on this common belief, we can't use the MVDR beamformer in this case. In this paper we show that this common belief is a fault. We propose a general approach for estimating the cross-spectrum matrix of noise signal that is applicable even in the case of correlated disturbances.

©2021 JECEI. All rights reserved.

Introduction

Spherical microphone array is a type of microphone arrays that has a spherical structure in which microphones are placed on a sphere surface. This kind of microphone arrays has been an interesting field of study for the past decade [1], [2], [3], [4], [5], [6]. The microphone array produces an output signal with some desired properties from the microphones input signals. One such desired property is to enhance signal coming from a particular direction and to weaken signals coming from other directions, therefore forming a directional, or

spatial filter. This filter forms the beam that looks at a desired direction, so it is called beamformer [1], [2], [3], [7]. Noise minimization beamformer is one important type of beamformer in which the beam pattern is adapted to the actual sound field.

This beamformer discerns the desired signal from the noise and, therefore achieves better performance in real, and noisy sound fields. When the noise field is not perfectly diffuse, the optimality of the beamformers which are optimal in decreasing noise due to diffuse sound field, such as maximum directivity beamformer, is

not maintained any more [1]. In this case an optimum beam pattern, adapted to the true measured noise, should be constructed. The minimum power distortionless response (MPDR) is one such a construction in which the beam pattern is restricted to be unity in the look direction, meanwhile the power of the array output is minimized [1], [2]. The MPDR beamformer is beneficial especially when the desired signal propagates with a plane wave coming from the look direction, and all other signals considered as noise that to be minimized.

One of the main problems in the MPDR beamformer is signal cancellation [1], [8], [9], [10], [11], [12], [13]. This problem occurs when the disturbance signals contain some signals that have correlation with the desired signal. For example, whenever the desired signal being reflected from neighboring surfaces such as walls in a room, signal cancellation may happen. So, these disturbance signals are the weakened and phase shifted versions of the desired signal. The signal cancellation means that, in place of retaining the desired signal unchanged and weakening the disturbances, the distortionless response constraint in the look direction is satisfied by the beamformer, but then it uses the correlated disturbances to remove the desired signal via minimizing the cross-spectrum matrix of the overall signal that involves contributions from both [1].

One approach to overcome the signal cancellation problem is by introducing nulls at the directions of the disturbances through additional constraints. The linearly constrained minimum variance (LCMV) beamformer employs this approach [14], [15], [16]. Although the null is obtained irrespective of the characteristic of disturbance signals, we need to determine the arriving direction of the disturbances in the LCMV beamformer. On the other hand, in the MPDR beamformer the nulls in the direction of disturbances are achieved via minimizing the cross-spectrum matrix of the overall signal, and as we have mentioned above, if the disturbance has correlation with the desired signal, MPDR design is remarkably degraded, due to signal cancellation [1].

Another approach to avoid the signal cancellation problem is by minimizing the cross-spectrum matrix of the noise. This approach is called minimum variance distortionless response (MVDR) beamforming [1], [17], [18]. Estimation of this matrix in presence of correlated disturbance is a challenging problem. For example, a common belief is that in a situation where a disturbance is a reflected form of the desired signal, due to cohesive appearance and disappearance of both the disturbance and the desired signal, estimation of cross-spectrum matrix of the noise signal is typically not possible in practice. So, based on this common belief, we cannot

use the MVDR beamformer in this case for the purpose of solving the signal cancellation problem.

In this paper we show that this common belief is a fault. We propose a general approach for estimating the cross-spectrum matrix of noise signal that is applicable even on situation of correlated disturbance. For that, at first we determine the amplitude densities and arrival directions of the disturbance signals from which we can estimate the cross-spectrum matrix of overall noise. Then, using this matrix we are able to bypass the signal cancellation problem effectively using MVDR beamformer equipped with this matrix. Note that, it is in contrast to the classical MVDR beamformer in which we don't need to specify the arriving direction of disturbance signals.

This paper is organized as follows. The second section reviews the spherical array processing fundamentals. The third section presents the proposed method for solving the signal cancellation problem. Simulation examples are presented in the fourth section, and the end section concludes the paper.

Spherical Array Processing

This section shortly explains the theory of spherical microphone array processing [1], [4], [19], [20]. The formulation provided in this section will be utilized in the following sections to develop the proposed method.

A. Array processing in Spherical Harmonic Domain

Consider a sound field composed of multiple "single frequency plane wave" each with amplitude density denoted by $a(k, \theta_k, \phi_k)$ arriving from direction (θ_k, ϕ_k) with a wave vector $\tilde{\mathbf{k}} = -\mathbf{k} = (k, \theta_k, \phi_k)$ and wave number k . The sound pressure at $\mathbf{r} = (r, \theta, \phi)$ due to this sound field can be written as follows [1]

$$p(k, r, \theta, \phi) = \sum_{n=0}^{\infty} \sum_{m=-n}^n p_{nm}(k, r) Y_n^m(\theta, \phi), \quad (1)$$

where $p_{nm}(k, r)$ are the spherical harmonic coefficients of the sound pressure, and $Y_n^m(\theta, \phi)$ are the spherical harmonics.

The relation between the amplitude of the plane waves producing the sound field and the pressure on the sphere in the spherical harmonic domain is

$$p_{nm}(k, r) = b_n(kr) a_{nm}(k), \quad (2)$$

where $a_{nm}(k)$ is the spherical Fourier transform of $a(k, \theta_k, \phi_k)$, i.e.,

$$a_{nm}(k) = \int_0^{2\pi} \int_0^\pi a(k, \theta_k, \phi_k) [Y_n^m(\theta_k, \phi_k)]^* \sin \theta_k d\theta_k d\phi_k, \quad (3)$$

and $b_n(kr)$ defines the projection of the sound field

onto the surface of sphere. The expression for $b_n(kr)$ depends on the array configuration. For example, in the case of a single open sphere, we have

$$b_n(kr) = 4\pi i^n j_n(kr), \quad (4)$$

where $j_n(x)$ is the spherical Bessel function of the first kind [1].

In the case of order-limited pressure function, we have $p_{nm}(k, r) = 0 \ \forall n > N$, so we can represent the function by a limited number of spherical harmonics and we have

$$p(k, r, \theta, \phi) = \sum_{n=0}^N \sum_{m=-n}^n p_{nm}(k, r) Y_n^m(\theta, \phi). \quad (5)$$

Equation (1) is, in fact, the inverse spherical Fourier transform of the pressure function [5]. So, we have

$$p_{nm} = \int_0^{2\pi} \int_0^\pi p(\theta, \phi) [Y_n^m(\theta, \phi)]^* \sin \theta d\theta d\phi, \quad (6)$$

which is the spherical Fourier transform of $p(\theta, \phi)$. For simplicity, we omitted the parameters k, r .

According to the Cubature method, it can be possible to compute the multiple integrations of a specified function using a summation over samples of that function [1]. So,

$$p_{nm} \approx \sum_{q=1}^Q \alpha_q p(\theta_q, \phi_q) [Y_n^m(\theta_q, \phi_q)]^* = \hat{p}_{nm}, \quad (7)$$

where Q is the total number of samples and α_q is the sampling weight whose value depends on the sampling method. The approximation becomes equality for order-limited function provided a sufficiently large Q . In this case, using the inverse spherical Fourier transform, $p(\theta, \phi)$ can be reconstructed perfectly on the sphere. But, in the case of p_{nm} of infinite order, due to aliasing, perfect reconstruction is not possible [4], [21], [22], [23], [24].

Several sampling methods, such as Gaussian, equal-angle, and uniform sampling, have been previously presented [4], [25], for which the sampling points (θ_q, ϕ_q) and sampling weight α_q have been derived such that for order-limited functions (7) is maintained with equality. Due to some constraints, we may want to use any arbitrary given sampling set. So, Assume that the samples of the function, $p(\theta_q, \phi_q)$, are given, together with the positions of the samples, (θ_q, ϕ_q) , for $q = 1, \dots, Q$. Using (5) we have

$$p(\theta_q, \phi_q) = \sum_{n=0}^N \sum_{m=-n}^n p_{nm} Y_n^m(\theta_q, \phi_q), \quad 1 \leq q \leq Q \quad (8)$$

Equation (8) may be written in matrix form as

$$\mathbf{p} = \mathbf{Y} \mathbf{p}_{nm}, \quad (9)$$

where vectors \mathbf{p} of length Q and \mathbf{p}_{nm} of length $(N + 1)^2$ are defined as

$$\mathbf{p} = [p(\theta_1, \phi_1), p(\theta_2, \phi_2), \dots, p(\theta_Q, \phi_Q)]^T \quad (10)$$

and

$$\mathbf{p}_{nm} = [p_{00}, p_{1(-1)}, p_{10}, p_{11}, \dots, p_{NN}]^T, \quad (11)$$

and the matrix \mathbf{Y} of dimensions $Q \times (N + 1)^2$ is given by

$$\mathbf{Y} = \begin{bmatrix} Y_0^0(\theta_1, \phi_1) & Y_1^{-1}(\theta_1, \phi_1) & Y_1^0(\theta_1, \phi_1) & Y_1^1(\theta_1, \phi_1) & \dots & Y_N^N(\theta_1, \phi_1) \\ Y_0^0(\theta_2, \phi_2) & Y_1^{-1}(\theta_2, \phi_2) & Y_1^0(\theta_2, \phi_2) & Y_1^1(\theta_2, \phi_2) & \dots & Y_N^N(\theta_2, \phi_2) \\ \vdots & \vdots & \vdots & \vdots & \ddots & \vdots \\ Y_0^0(\theta_Q, \phi_Q) & Y_1^{-1}(\theta_Q, \phi_Q) & Y_1^0(\theta_Q, \phi_Q) & Y_1^1(\theta_Q, \phi_Q) & \dots & Y_N^N(\theta_Q, \phi_Q) \end{bmatrix} \quad (12)$$

Equation (9) is called inverse discrete spherical Fourier transform [26]. Also,

$$\mathbf{p}_{nm} = \mathbf{Y}^\dagger \mathbf{p}, \quad (13)$$

is called discrete spherical Fourier transform, where $\mathbf{Y}^\dagger = (\mathbf{Y}^H \mathbf{Y})^{-1} \mathbf{Y}^H$ is the pseudo-inverse of \mathbf{Y} . Generally, the discrete spherical Fourier transform may be written as

$$\mathbf{p}_{nm} = \mathbf{S} \mathbf{p} \quad (14)$$

In the situation of a general sampling, matrix \mathbf{S} is given by $\mathbf{S} = \mathbf{Y}^\dagger$, in the situation of Gaussian and equal-angle sampling methods is given by $\mathbf{S} = \mathbf{Y}^H \text{diag}(\boldsymbol{\alpha})$, where $\boldsymbol{\alpha} = [\alpha_0, \alpha_1, \dots, \alpha_Q]^T$ holds the sampling weights, and for nearly uniform and uniform sampling methods is given by $\mathbf{S} = \frac{4\pi}{Q} \mathbf{Y}^H$.

B. Spherical Array Beamforming

Array equations or beamforming equations is as follows [1], [4], [25], [27], [28], [29],

$$y = \int_0^{2\pi} \int_0^\pi w^*(k, \theta, \phi) p(k, r, \theta, \phi) \sin \theta d\theta d\phi \\ = \sum_{n=0}^{\infty} \sum_{m=-n}^n w_{nm}^*(k) p_{nm}(k, r). \quad (15)$$

where $w^*(k, \theta, \phi)$ are the beamforming coefficient. The standard discrete form of beamforming in the space domain is

$$y = \mathbf{w}^H \mathbf{p}, \quad (16)$$

where \mathbf{p} is as (10) with a little modification in notation

$$\mathbf{p} = [p_1(k), p_2(k), \dots, p_Q(k)]^T \quad (17)$$

with $p_q(k) = p(k, r, \theta_q, \phi_q)$, $q = 1, \dots, Q$, and \mathbf{w} is the $Q \times 1$ weight vector as follows

$$\mathbf{w} = [w_1(k), w_2(k), \dots, w_Q(k)]^T \quad (18)$$

Assuming $w_{nm} = 0 \forall n > N$, the discrete form of beamforming in spherical harmonic domain is as

$$\mathbf{y} = \mathbf{w}_{nm}^H \mathbf{p}_{nm}, \quad (19)$$

where the $(N+1)^2 \times 1$ vector \mathbf{w}_{nm} is given by

$$\begin{aligned} \mathbf{w}_{nm} \\ = [w_{00}(k), w_{1(-1)}(k), w_{10}(k), w_{11}(k) \dots, w_{NN}(k)]^T \end{aligned} \quad (20)$$

and the $(N+1)^2 \times 1$ vector \mathbf{p}_{nm} is given by

$$\begin{aligned} \mathbf{p}_{nm} \\ = [p_{00}(k, r), p_{1(-1)}(k, r), p_{10}(k, r), \dots, p_{NN}(k, r)]^T \end{aligned} \quad (21)$$

In these equations $p_{nm}(k)$ and $w_{nm}(k)$ are the spherical Fourier transform of $p(k, r, \theta, \phi)$ and $w(k, \theta, \phi)$ respectively and N is called the effective order of the array.

The output of the array due to a unit-amplitude plane-wave, i.e, array beam pattern, is defined as

$$y = \mathbf{w}_{nm}^H \mathbf{v}_{nm}, \quad (22)$$

where \mathbf{v}_{nm} is a $(N+1)^2 \times 1$ column vector as

$$\begin{aligned} \mathbf{v}_{nm} \\ = [v_{00}(k, r), v_{1(-1)}(k, r), v_{10}(k, r), \dots, v_{NN}(k, r)]^T \end{aligned} \quad (23)$$

with v_{nm} represents the array input owing to the sound field created by plane wave. Since for unit amplitude plane wave we have [1],

$$a_{nm}(k) = [Y_n^m(\theta_k, \phi_k)]^*, \quad (24)$$

According to (2) we have

$$v_{nm}(k, r) = b_n(kr) [Y_n^m(\theta_k, \phi_k)]^* \quad (25)$$

where (θ_k, ϕ_k) is the plane wave arrival direction.

Using a different set of beamforming coefficients, different beam patterns can be designed. For instance, axis-symmetric beamformers with $w_{nm}(k) = \frac{d_n(k)}{b_n(kr)} Y_n^m(\theta_l, \phi_l)$ of which two famous beamformers are

the maximum directivity (MD) beamformer and the maximum white noise gain (WNG) beamformer [20]. Note that the beamformer coefficients are function of look direction which denoted by (θ_l, ϕ_l) in the above relation.

C. The MPDR and MVDR Beamformers

Consider a desired signal $s(k)$, arriving from direction (θ_k, ϕ_k) . The corresponding distant source creates a plane wave at the location of array. Array input may be written as follows

$$\mathbf{x} = \mathbf{p} + \mathbf{n} = \mathbf{v}s + \mathbf{n} \quad (26)$$

where \mathbf{v} is the transfer function from the source to the microphone array input, also called the steering vector,

$$\mathbf{p} = [p_1(k), p_2(k), \dots, p_Q(k)]^T \quad (27)$$

is the sound pressure at the Q microphones due to the desired source and,

$$\mathbf{n} = [n_1(k), n_2(k), \dots, n_Q(k)]^T \quad (28)$$

is the noise at the microphones [1], [14]. The array output is as follows

$$y = \mathbf{w}^H \mathbf{x} \quad (29)$$

The array output variance is

$$E[|y|^2] = E[\mathbf{w}^H \mathbf{x} \mathbf{x}^H \mathbf{w}] = \mathbf{w}^H \mathbf{S}_{xx} \mathbf{w} \quad (30)$$

where

$$\mathbf{S}_{xx} = E[\mathbf{x} \mathbf{x}^H] \quad (31)$$

is the spatial spectral matrix of the array input. Each element in this matrix represents the cross-spectral density between the signals at two microphones at wave number k . From (26) and (31) the spatial cross-spectral density matrix of the array input may be written as

$$\mathbf{S}_{xx} = \mathbf{S}_{pp} + \mathbf{S}_{nn} + \mathbf{S}_{pn} + \mathbf{S}_{np} \quad (32)$$

with

$$\mathbf{S}_{pp} = E[\mathbf{p} \mathbf{p}^H] \quad (33)$$

and

$$\mathbf{S}_{nn} = E[\mathbf{n} \mathbf{n}^H] \quad (34)$$

With the assumption of independent pressure signal and the noise signal, (32) is rewritten as

$$\mathbf{S}_{xx} = \mathbf{S}_{pp} + \mathbf{S}_{nn} \quad (35)$$

So, we can rewrite (30) as follows

$$\begin{aligned} E[|y|^2] &= \mathbf{w}^H \mathbf{S}_{xx} \mathbf{w} = \mathbf{w}^H \mathbf{S}_{pp} \mathbf{w} + \mathbf{w}^H \mathbf{S}_{nn} \mathbf{w} \\ &= |\mathbf{w}^H \mathbf{v}|^2 E[|s|^2] + \mathbf{w}^H \mathbf{S}_{nn} \mathbf{w} \end{aligned} \quad (36)$$

We have the following design objective

$$\begin{aligned} &\underset{\mathbf{w}}{\text{minimize}} \quad \mathbf{w}^H \mathbf{S}_{xx} \mathbf{w} \\ &\text{subject to} \quad \mathbf{w}^H \mathbf{v} = 1 \end{aligned} \quad (37)$$

Owing to the distortionless response restriction, $\mathbf{w}^H \mathbf{v} = 1$, in the above optimization problem, $|\mathbf{w}^H \mathbf{v}|^2 E[|s|^2]$ can not be modified, so, the minimization of $\mathbf{w}^H \mathbf{S}_{xx} \mathbf{w}$ leads to minimization of $\mathbf{w}^H \mathbf{S}_{nn} \mathbf{w}$, i.e., the noise variance at the array output. The optimal value of \mathbf{w} is

$$\mathbf{w}^H = \frac{\mathbf{v}^H \mathbf{S}_{xx}^{-1}}{\mathbf{v}^H \mathbf{S}_{xx}^{-1} \mathbf{v}} \quad (38)$$

It is the minimum power distortionless response (MPDR) beamformer [1], [2], [3]. The MVDR beamformer is the same as in (38) with \mathbf{S}_{xx}^{-1} is replaced by \mathbf{S}_{nn}^{-1} ,

$$\begin{aligned} &\underset{\mathbf{w}}{\text{minimize}} \quad \mathbf{w}^H \mathbf{S}_{nn} \mathbf{w} \\ &\text{subject to} \quad \mathbf{w}^H \mathbf{v} = 1 \end{aligned} \quad (39)$$

with a solution

$$\mathbf{w}^H = \frac{\mathbf{v}^H \mathbf{S}_{nn}^{-1}}{\mathbf{v}^H \mathbf{S}_{nn}^{-1} \mathbf{v}} \quad (40)$$

The spherical harmonic domain formulation of MPDR is as follows. In the spherical harmonic domain, (26) may be written as

$$\mathbf{x}_{nm} = \mathbf{p}_{nm} + \mathbf{n}_{nm} = \mathbf{v}_{nm} s + \mathbf{n}_{nm} \quad (41)$$

The MPDR optimization problem can be written as

$$\begin{aligned} &\underset{\mathbf{w}}{\text{minimize}} \quad \mathbf{w}_{nm}^H \mathbf{S}_{x_{nm}x_{nm}} \mathbf{w}_{nm} \\ &\text{subject to} \quad \mathbf{w}_{nm}^H \mathbf{v}_{nm} = 1 \end{aligned} \quad (42)$$

Similar to (38), a solution may be written for beamforming coefficients in the spherical harmonic domain as

$$\mathbf{w}_{nm}^H = \frac{\mathbf{v}_{nm}^H \mathbf{S}_{x_{nm}x_{nm}}^{-1}}{\mathbf{v}_{nm}^H \mathbf{S}_{x_{nm}x_{nm}}^{-1} \mathbf{v}_{nm}} \quad (43)$$

For the MVDR beamformer we have

$$\mathbf{w}_{nm}^H = \frac{\mathbf{v}_{nm}^H \mathbf{S}_{n_{nm}n_{nm}}^{-1}}{\mathbf{v}_{nm}^H \mathbf{S}_{n_{nm}n_{nm}}^{-1} \mathbf{v}_{nm}} \quad (44)$$

The Proposed Method

In this section we propose a general approach for estimating the cross-spectrum matrix of noise signal. We assume that the amplitude of the desired signal is s_0 , and the disturbance signals satisfy $s_i = A_i s_0$, $i = 1, 2, \dots, k$, where A_i is a complex constant. We also assume that the desired signal propagates via a plane wave arriving from direction (θ_0, ϕ_0) , with variance of $\sigma_0^2 = E[|s_0|^2]$, and the disturbances are other plane waves with arrival direction (θ_i, ϕ_i) with $\sigma_i^2 = |A_i|^2 \sigma_0^2$. Specially uncorrelated sensor noise with variance σ_n^2 is also assumed.

Suppose that the noise at the array input is owing to the sensor noise. Using the discrete spherical Fourier transform, as in (14) the sensor noise in the spherical harmonic domain can be written as

$$\mathbf{n}_{nm} = \mathbf{S} \mathbf{n} \quad (45)$$

where matrix \mathbf{S} depends on the sampling method as mentioned in the second section of the paper. This leads to

$$\begin{aligned} \mathbf{S}_{n_{nm}n_{nm}} &= E[\mathbf{n}_{nm} \mathbf{n}_{nm}^H] = E[\mathbf{S} \mathbf{n} \mathbf{n}^H \mathbf{S}^H] \\ &= \mathbf{S} E[\mathbf{n} \mathbf{n}^H] \mathbf{S}^H = \sigma_n^2 \mathbf{S} \mathbf{S}^H \end{aligned} \quad (46)$$

where we have assumed the IID noise. i.e, independent and identically distributed noise. As seen in (46), the spatial cross-spectrum of the noise depends on the sampling method.

The spatial spectrum matrix of the overall noise can be computed using the following theorem.

Theorem 1: The spatial spectrum matrix of the noise, including the contributions from the disturbances, is as

$$\begin{aligned} \mathbf{S}_{n_{nm}n_{nm}}^{Overall} &= \sigma_n^2 \mathbf{S} \mathbf{S}^H + \sum_{i=1}^k \sigma_i^2 \mathbf{v}_{nmi} \mathbf{v}_{nmi}^H \\ &\quad + \sum_{i \neq j} (A_i A_j^* \sigma_0^2 \mathbf{v}_{nmi} \mathbf{v}_{nmj}^H \\ &\quad + A_i^* A_j \sigma_0^2 \mathbf{v}_{nmj} \mathbf{v}_{nmi}^H) \end{aligned} \quad (47)$$

where

$$\begin{aligned} \mathbf{v}_{nmi} &= [v_{00}(k, r), v_{1(-1)}(k, r), v_{10}(k, r), \dots, v_{NN}(k, r)]^T, \\ v_{nm}(k, r) &= b_n(kr) [Y_n^m(\theta_i, \phi_i)]^* \text{ and } (\theta_i, \phi_i) \text{ is the arrival direction of } i\text{th disturbance.} \end{aligned}$$

Proof: The array input in the spherical harmonic domain is as

$$\begin{aligned} \mathbf{x}_{nm} &= \mathbf{p}_{nm0} + \mathbf{n}_{nm} + \sum_{i=1}^k \mathbf{p}_{nmi} \\ &= \mathbf{v}_{nm0} s_0 + \mathbf{n}_{nm} + \sum_{i=1}^k \mathbf{v}_{nmi} s_i \end{aligned} \quad (48)$$

where \mathbf{p}_{nmi} , $i = 1, 2, \dots, k$ is the spherical Fourier transform of pressure due to the i th disturbance, and \mathbf{p}_{nm0} is the spherical Fourier transform of pressure due to the desired signal.

Now, the overall noise is $\mathbf{n}_{nm} + \sum_{i=1}^k \mathbf{v}_{nmi} S_i$, so the spatial spectrum matrix of the noise is

$$\begin{aligned} \mathbf{S}_{\mathbf{n}_{nm}\mathbf{n}_{nm}}^{Overall} &= E \left[\left(\mathbf{n}_{nm} + \sum_{i=1}^k \mathbf{v}_{nmi} S_i \right) \left(\mathbf{n}_{nm} + \sum_{i=1}^k \mathbf{v}_{nmi} S_i \right)^H \right] \\ &= E[\mathbf{n}_{nm}\mathbf{n}_{nm}^H] \\ &\quad + E \left[\left(\sum_{i=1}^k \mathbf{v}_{nmi} S_i \right) \left(\sum_{j=1}^k \mathbf{v}_{nmj}^H S_j^* \right) \right] \quad (49) \\ &= \sigma_n^2 \mathbf{S}\mathbf{S}^H + \sum_{i=1}^k \sigma_i^2 \mathbf{v}_{nmi} \mathbf{v}_{nmi}^H \\ &\quad + \sum_{i \neq j} (A_i A_j^* \sigma_0^2 \mathbf{v}_{nmi} \mathbf{v}_{nmj}^H \\ &\quad + A_i^* A_j \sigma_0^2 \mathbf{v}_{nmj} \mathbf{v}_{nmi}^H) \end{aligned}$$

For computing $\mathbf{S}_{\mathbf{n}_{nm}\mathbf{n}_{nm}}^{Overall}$, in the situation of uncorrelated disturbance, it is adequate to record the input signal during the time intervals when the disturbance is active but the desired signal is not active. However, in the case of correlated disturbance, both the disturbance and the desired signal appear and disappear cohesively. So, we need to have a mechanism to extract information for computing $\mathbf{S}_{\mathbf{n}_{nm}\mathbf{n}_{nm}}^{Overall}$ from the array input, i.e., \mathbf{x} . This information includes A_i , $i = 1, 2, \dots, k$ and s_0 . The following theorem can be used for this purpose.

Theorem 2. The amplitude of the disturbance plane waves can be computed using an axis-symmetric beamformer with $d_n(k) = 1$.

Proof: We consider the axis-symmetric beamformers. As mentioned in the second section, axis-symmetric beamformers are beamformers with the following weights [30]

$$w_{nm}^*(k) = \frac{d_n(k)}{b_n(kr)} Y_n^m(\theta_l, \phi_l) \quad (50)$$

If we set $d_n(k)$ to unity, we have

$$w_{nm}^*(k) = \frac{1}{b_n(kr)} Y_n^m(\theta_l, \phi_l) \quad (51)$$

So, (15) can be rewritten for this case as

$$\begin{aligned} y &= \sum_{n=0}^{\infty} \sum_{m=-n}^n w_{nm}^*(k) p_{nm}(k, r) \\ &= Y_n^m(\theta_l, \phi_l) \frac{p_{nm}(k, r)}{b_n(kr)} \end{aligned} \quad (52)$$

From (2) we have

$$\frac{p_{nm}(k, r)}{b_n(kr)} = a_{nm}(k) \quad (53)$$

So, we have

$$\begin{aligned} y &= \sum_{n=0}^{\infty} \sum_{m=-n}^n a_{nm}(k) Y_n^m(\theta_l, \phi_l) \\ &= a(k, \theta_l, \phi_l) = A_l \end{aligned} \quad (54)$$

Equation (54) shows that y , as a function of look direction, gives A_l . Using these values we can compute $\mathbf{S}_{\mathbf{n}_{nm}\mathbf{n}_{nm}}^{Overall}$, and finally the beamforming weight can be computed as

$$\mathbf{w}_{nm}^H = \frac{\mathbf{v}_{nm}^H \mathbf{S}_{\mathbf{n}_{nm}\mathbf{n}_{nm}}^{Overall^{-1}}}{\mathbf{v}_{nm}^H \mathbf{S}_{\mathbf{n}_{nm}\mathbf{n}_{nm}}^{Overall^{-1}} \mathbf{v}_{nm}} \quad (55)$$

Finally, the beam pattern is computed using \mathbf{w}_{nm} and (22) as

$$\begin{aligned} y(\theta, \phi) &= \mathbf{w}_{nm}^H \mathbf{v}_{nm}(\theta, \phi) \\ &= \sum_{n=0}^N \sum_{m=-n}^n w_{nm}^*(k) b_n(kr) [Y_n^m(\theta, \phi)]^* \end{aligned} \quad (56)$$

Simulation Examples

Examples of beam patterns designed using the proposed method are presented in this section. A spherical microphone array around a rigid sphere, operating at $kr = N$, with $N = 4$ is assumed. We also consider $Q = 36$ nearly-uniformly arranged microphones, with spatially uncorrelated sensor noise and with variance $\sigma_n^2 = 0.1$. So, $\mathbf{S}_{\mathbf{n}_{nm}\mathbf{n}_{nm}}$ due to sensor noise can be written as

$$\mathbf{S}_{\mathbf{n}_{nm}\mathbf{n}_{nm}} = \sigma_n^2 \mathbf{S}\mathbf{S}^H = \sigma_n^2 \frac{4\pi}{Q} \mathbf{I} \quad (57)$$

A. The First Example

In the first example we assume that the desired signal propagates with a plane wave coming from direction $(\theta_0, \phi_0) = (30, 45)$, with variance of $\sigma_0^2 = 1$. A disturbance signal is included that has correlation with the desired signal and propagates with another plane wave coming from direction $(\theta_1, \phi_1) = (30, 270)$, with $\sigma_1^2 = |A_1|^2 \sigma_0^2$ and $A_1 = 0.7e^{-i\pi/3}$.

In the first step we must approximate s_0 and A_1 . For that we compute $y(\theta_l, \phi_l)$ using (54). An equal angle of 60×60 points was utilized to create (θ_l, ϕ_l) . Figure 1 shows the normalized magnitude of $y(\theta_l, \phi_l)$.

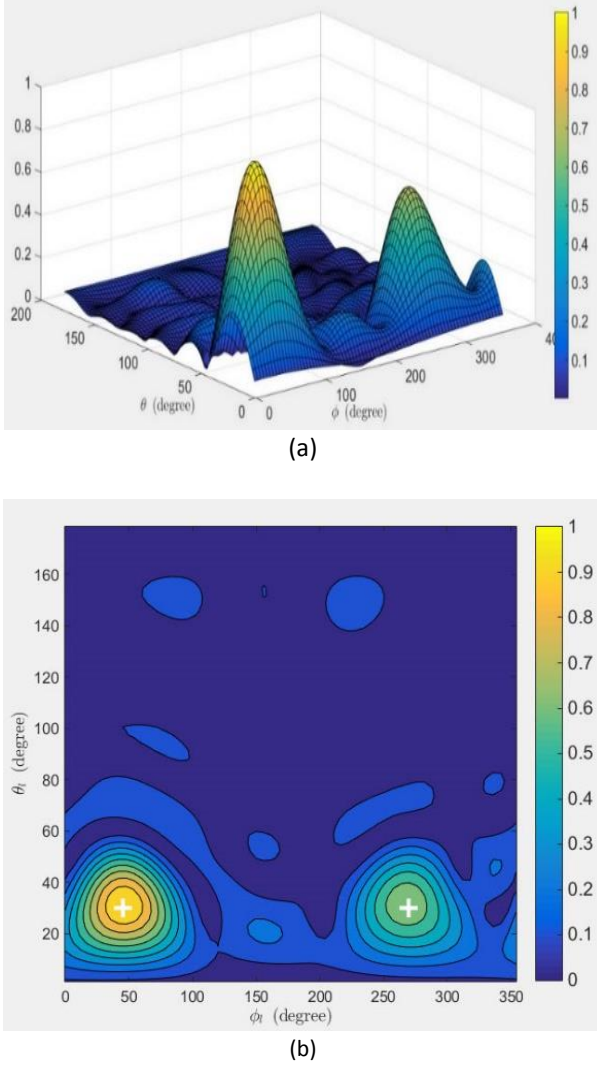


Fig. 1: Normalized magnitude of $y(\theta_l, \phi_l)$. (a) surface plot. (b) contour plot. The arrival directions of the two plane waves are indicated with white "+".

The peaks in these plots indicates $a(k, \theta_l, \phi_l)$, i.e., the plane wave amplitude density that is identical to $|A_l|$. In this example we obtain amplitude density of $1e^{-i0.025}$ and $0.682e^{-i1.029}$, and also arrival directions of $(30.375, 45)$ and $(32.625, 270)$ for the desired signal and disturbance signal respectively. Using these values as s_0 , A_1 , (θ_0, ϕ_0) and (θ_1, ϕ_1) , we can compute $\sigma_0^2 = E[|s_0|^2]$ and $\sigma_1^2 = |A_1|^2 \sigma_0^2$. Finally, according to (49) we compute $\mathbf{S}_{\mathbf{n}_{nm}\mathbf{n}_{nm}}^{Overall}$, and then the spherical harmonic domain beamforming weights may be computed from (55). The resulting beam pattern is then computed using (56). The magnitude of the beam

pattern has been shown in Fig. 2. As we can see in this figure, the first side lobe has a null in the disturbance signal arrival direction. So, the proposed method has the ability to shape the beam pattern to consider the correlated disturbances in the sound field.

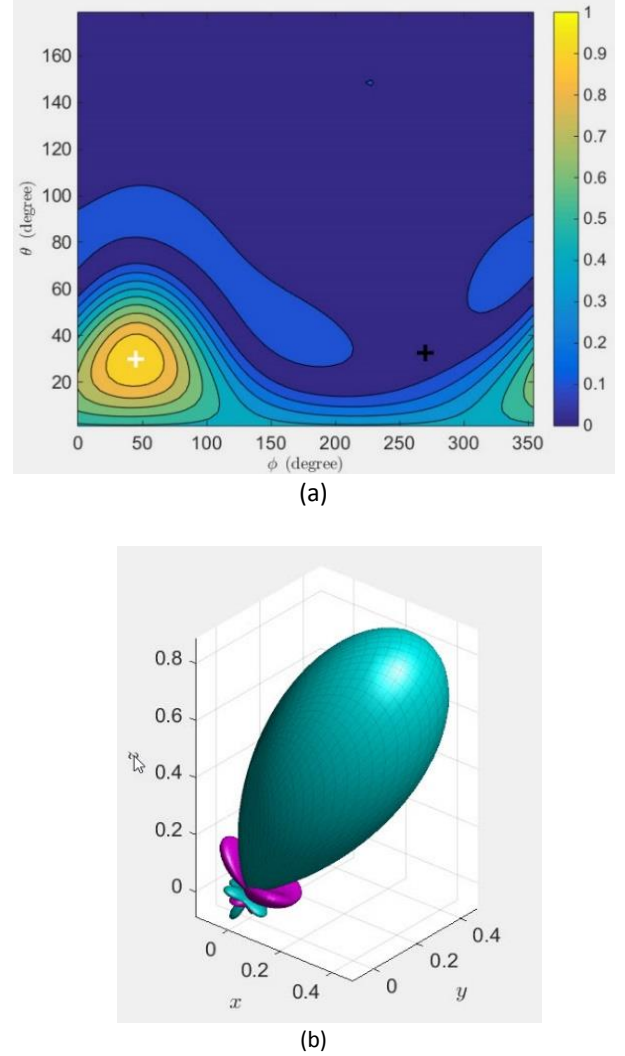


Fig. 2: $|y(\theta, \phi)|$ for MVDR beamformer with the cross-spectrum matrix of noise obtained by the proposed method. (a) contour plot, arrival direction of the desired plane wave is indicated by the white "+", and the arrival direction of the disturbance plane wave is indicated by the black "+". (b) balloon plot. In this plot cyan color represents positive values of $\text{Re}\{y(\theta, \phi)\}$, and magenta color represents negative values of $\text{Re}\{y(\theta, \phi)\}$.

Without the proposed method, s_0 and A_1 are not available. So, we have to use MPDR beamformer as expressed in (38). For this, we calculate the spatial spectrum matrix of the overall input signal, i.e., \mathbf{x} , using (35) and then using (38) and (22) we can calculate the corresponding beam pattern. This beam pattern has been shown in Fig. 3 in which we can see the signal cancellation phenomenon clearly.

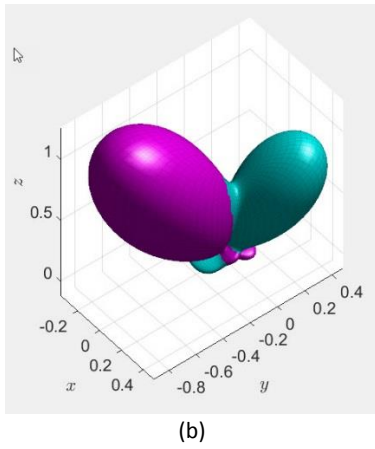
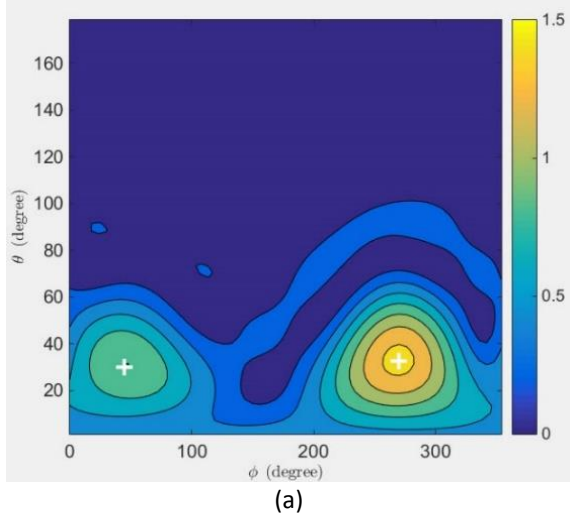


Fig. 3: $|y(\theta, \phi)|$ for MPDR beamformer. (a) contour plot, arrival direction of the disturbance plane wave and desired plane wave are indicated by the white "+". (b) balloon plot.

B. The Second Example

In the second example, the first example is further extended to include another disturbance propagates with a plane wave with arrival direction $(\theta_2, \phi_2) = (80, 100)$, with $\sigma_2^2 = |A_2|^2 \sigma_0^2$ and $A_2 = 0.8e^{-i\pi/2}$. Fig. 4, Fig. 5, and Fig. 6 show the simulation results. We can see again the ability of the proposed method in solving the signal cancellation problem.

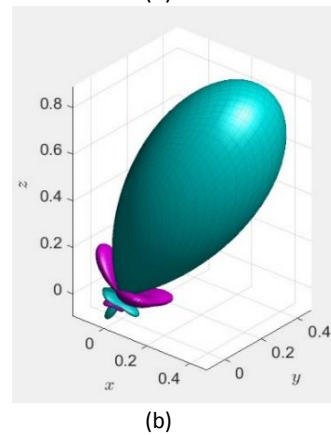
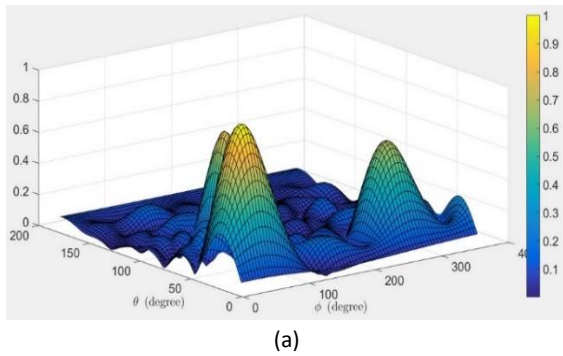
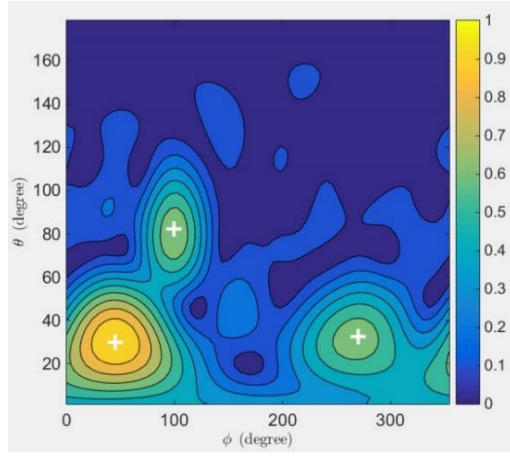
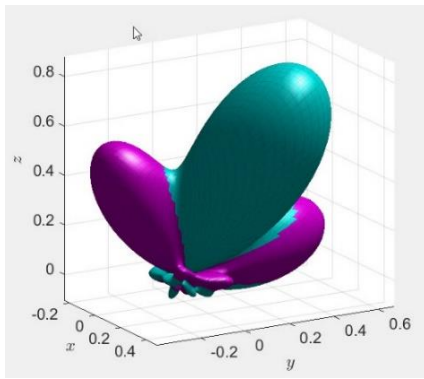


Fig. 5: $|y(\theta, \phi)|$ for MVDR beamformer which use the cross-spectrum matrix of noise obtained by the proposed method. (a) contour plot, arrival direction of the disturbance plane wave is indicated by the black "+", and the arrival direction of the desired plane wave is indicated by the white "+". (b) balloon plot.



(a)



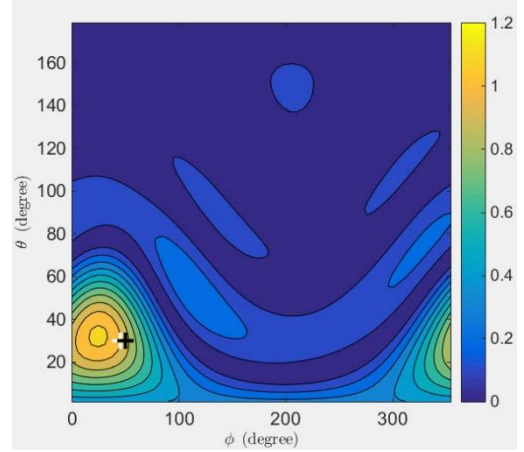
(b)

Fig. 6: $|y(\theta, \phi)|$ for MPDR beamformer. (a) contour plot, arrival direction of the disturbance plane wave and desired plane wave are indicated by the white "+". (b) balloon plot.

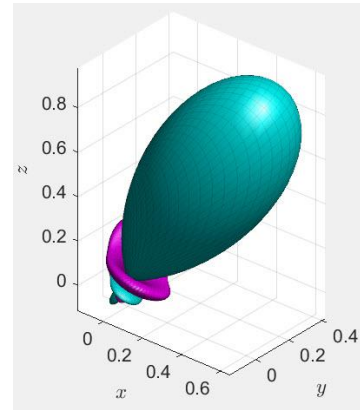
C. Comparison with BF-LCMV method

In this section we compare the proposed method with the rival method presented in [16] in which the signal cancellation problem has been solved using direction of arrival (DOA) estimation and the LCMV beamformer. For this purpose two performance measures have been considered: directivity factor (DF) which is the ratio between the array response in the look direction and the average response over all directions, and white noise gain (WNG) which is a general measure for array robustness and is defined as the improvement in signal-to-noise ratio (SNR) at the array output relative to the array input. Experimental results show that two methods have similar performance in term of these two performance measures in almost all cases. For example with simulation setup as in the first example, the two methods gain DF of 23.97 and WNG of 39.91 dB. But, in the case of disturbance arriving from direction that is near the look direction and with amplitude that is a small fraction of the desired signal, the proposed method is superior as shown in Fig. 7. The parameters in this simulation is as in the first example except the

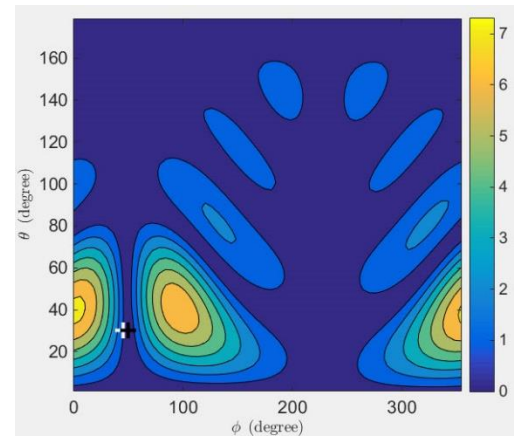
disturbance signal parameters which are $(\theta_1, \phi_1) = (30, 50)$ and $A_1 = 0.2e^{-i\pi/3}$. In this case, the DF and WNG for the proposed method are 19.19 and 37.5 dB respectively, and for the BF-LCMV method, these objective measures are 0.275 and 5.23 dB. This phenomenon is probably due to the role that the amplitude density characteristic of the disturbance signal plays in this specific case. The proposed method considers this characteristic but the BF-LCMV method only takes into account the arriving direction of the disturbance.



(a)



(b)



(c)

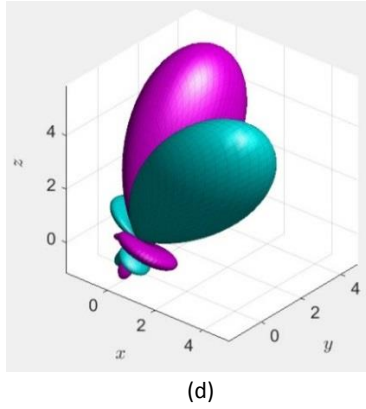


Fig. 7: (a) and (b), $|y(\theta, \phi)|$ for MVDR beamformer which use the cross-spectrum matrix of noise obtained by the proposed method. (c) and (d), $|y(\theta, \phi)|$ for RF-LCMV method.

Results and Discussion

The simulation results show that the proposed method has the ability to shape the beam pattern to consider the correlated disturbances in the sound field and consequently to solve the signal cancellation problem. The comparisons with the rival method show that both methods have the same performance in almost all cases except in the case of disturbance arriving from direction that is near the look direction and with amplitude that is a small fraction of the desired signal, in which the proposed method is superior.

Conclusion

The signal cancellation problem is a major problem in the MPDR beamformer. It occurs whenever the disturbance signals include at least one signal that is correlated with the desired signal. Using the MVDR beamformer, we can avoid this problem, but this approach requires that the cross-spectrum matrix of the noise signal is available. A common belief is that in the case of correlated disturbance, the estimation of this matrix is not possible. In this paper we showed that this common belief is a fault. We proposed a general approach for estimating the cross-spectrum matrix of noise signal that is applicable even in the case of correlated disturbance. Simulation examples show that using the proposed method along with the MVDR beamformer, we can bypass the signal cancellation problem completely.

Author Contributions

M. Kalantari has written the whole paper without participation of anybody. All parts of this work have been accomplished by the author as the single author and the corresponding author of the paper.

Acknowledgment

This work was supported by Shahid Rajaee Teacher Training University under contract number 25874.

Conflict of Interest

The author declare no potential conflict of interest regarding the publication of this work. In addition, the ethical issues including plagiarism, informed consent, misconduct, data fabrication and, or falsification, double publication and, or submission, and redundancy have been completely witnessed by the authors.

Abbreviations

| | |
|-----------------------------|--|
| LCMV | Linearly constrained minimum variance |
| MPDR | Minimum power distortionless response |
| MVDR | Minimum variance distortionless response |
| SNR | Signal-to-noise ratio |
| WNG | White noise gain |
| α_q | Sampling weights |
| α | Vector of sampling weights |
| θ | Elevation angle |
| ϕ | Azimuth angle |
| $a(\cdot)$ | Plane-wave decomposition in the space domain |
| a_{nm} | Plane-wave decomposition in the spherical-harmonics domain |
| $b_n(\cdot)$ | Function relating pressure to plane-wave decomposition |
| DF | Directivity factor |
| d_n | Axis-symmetric beamforming weighting function |
| $j_n(\cdot)$ | Spherical Bessel function of the first kind |
| k | Wave number |
| \mathbf{k} | Wave vector denoting propagation direction |
| $\tilde{\mathbf{k}}$ | Wave vector denoting arrival direction |
| N | Order of spherical harmonics |
| \mathbf{n} | Noise vector in the space domain |
| \mathbf{n}_{nm} | Noise vector in the spherical harmonics domain |
| p | Sound pressure in the space domain |
| p_{nm} | Sound pressure in the spherical harmonics domain |
| \mathbf{p} | Sound pressure vector in the space domain |
| \mathbf{p}_{nm} | Sound pressure vector in the spherical harmonics domain |
| Q | Number of samples or microphones |
| \mathbf{r} | Vector of spherical coordinates |
| \mathbf{S} | Spherical Fourier transform matrix |
| \mathbf{S}_{xx} | Cross-spectrum matrix in the space domain |
| $\mathbf{S}_{x_{nm}x_{nm}}$ | Cross-spectrum matrix in the spherical harmonics domain |
| \mathbf{S}_{nn} | Noise cross-spectrum matrix in the space domain |

| | |
|--------------------|--|
| $S_{n_{nm}n_{nm}}$ | Noise cross-spectrum matrix in the spherical harmonics domain |
| \mathbf{v} | Steering vector in the space domain |
| \mathbf{v}_{nm} | Steering vector in the spherical harmonics domain |
| $w(\cdot)$ | Beamforming weighting function in the space domain |
| w_{nm} | Beamforming weighting function in the spherical harmonics domain |
| \mathbf{w} | Beamforming weighting vector in the space domain |
| \mathbf{w}_{nm} | Beamforming weighting vector in the spherical harmonics domain |
| $Y_n^m(\cdot)$ | Spherical harmonics |
| \mathbf{Y} | Matrix of Spherical harmonics |

References

- [1] B. Rafaely, *Fundamentals of Spherical Arrays Processing*, 2 edn. Springer, 2018.
- [2] D. P. Jarret, E.A.P. Habets, P.A. Naylor, *Theory and Applications of Spherical Microphone Array Processing*, Springer, 2017.
- [3] S. Yan, *Broadband Array Processing*, Springer, 2019.
- [4] B. Rafaely, "Analysis and design of spherical microphone arrays," *IEEE Trans. Speech and Audio Processing*, 13(1): 135–143, 2005.
- [5] M.R.P. Thomas, "Practical concentric open sphere cardioid microphone array design for higher order sound field capture", in *Proc. ICASSP - IEEE Acoustics, Speech and Signal Processing (ICASSP) Confrance*: 666-670, 2019.
- [6] H. Beit-On, B. Rafaely, "Focusing and frequency smoothing for arbitrary arrays with application to speaker localization," *IEEE/ACM Trans. Audio Speech Lang. Process.*, 28: 2184-2193, 2020.
- [7] N. Solgi, "TDL-based wideband beamforming for radio sources close to the array endfire," *J. Electr. Comput. Eng. Innovations*, 3(1): 47-53, 2015.
- [8] A.H. Moore, P.A. Naylor, "Linear prediction based dereverberation for spherical microphone arrays," *IEEE Workshop on Acoustic Signal Enhancement (IWAENC)*: 1-5, 2016.
- [9] J. Li, J. Ding, C. Zheng, X. Li, "An efficient and robust speech dereverberation method using spherical microphone array," in *Proc. IEEE Digital Signal Processing (DSP)*: 1-5, 2018.
- [10] Y. Yamamoto, Y. Haneda, "Spherical microphone array post-filtering for reverberation suppression using isotropic beamformings," *IEEE International Workshop on Acoustic Signal Enhancement (IWAENC)*: 1-5, 2016.
- [11] Y. Peled, B. Rafaely, "Method for dereverberation and noise reduction using spherical microphone arrays," in *Proc. IEEE Acoustics, Speech and Signal Processing (ICASSP)*: 113-116, 2010.
- [12] P.K.T. Wu, N. Epain, C. Jin, "A dereverberation algorithm for spherical microphone arrays using compressed sensing techniques," in *Proc. IEEE Acoustics, Speech and Signal Processing (ICASSP)*: 4053-4056, 2012.
- [13] D.P. Jarrett, E.A. P. Habets, M.R.P. Thomas, N.D. Gaubitch, P.A. Naylor, "Dereverberation performance of rigid and open spherical microphone arrays: Theory & simulation," *IEEE Workshop on Hands-free Speech Communication and Microphone Arrays*: 145-150, 2011.
- [14] H.L. Van Trees, *Optimum Array Processing (Detection, Estimation, and Modulation Theory, Part IV)*, 1 edn. Wiley, 2002.
- [15] Y. Peled, B. Rafaely, "Linearly constrained minimum variance method for spherical microphone arrays in a coherent environment," *Joint Workshop on Hands-free Speech Communication and Microphone Array*: 86-91, 2011.
- [16] Y. Peled, B. Rafaely, "Linearly-constrained minimum-variance method for spherical microphone arrays based on plane-wave decomposition of the sound field," *IEEE Trans. Audio Speech Lang. Process.*, 21(12): 2532-2540, 2013.
- [17] D.P. Jarret, E.A.P. Habets, P.A. Naylor, "Spherical harmonic domain noise reduction using an MVDR beamformer and DOA-based second-order statistics estimation", in *Proc. IEEE Acoustics, Speech and Signal Processing*: 654-658, 2013.
- [18] D.P. Jarret, E.A.P. Habets, P.A. Naylor, "On the noise reduction performance of a spherical harmonic domain tradeoff beamformer," *IEEE Signal Process Lett.*, 19(11): 773-776, 2012.
- [19] R.A. Kennedy, P. Sadeghi, *Hilbert Space Methods in Signal Processing*, Cambridge University Press, 2013.
- [20] T.D. Abhayapala, "Generalized framework for spherical microphone arrays: Spatial and frequency decomposition," in *Proc. IEEE Acoustics, Speech and Signal Processing (ICASSP)*: 5268-5271, 2008.
- [21] J. Meyer, G.W. Elko, "Handling spatial aliasing in spherical array applications," in *Proc. IEEE Hands-Free Speech Communication and Microphone Arrays*: 1-4, 2008.
- [22] D.L. Alon, B. Rafaely, "Beamforming with optimal aliasing cancellation in spherical microphone arrays," *IEEE/ACM Trans. Audio Speech Lang. Process.*, 24(1): 196-210, 2016.
- [23] B. Rafaely, B. Weiss, E. Bachmat, "Spatial aliasing in spherical microphone arrays," *IEEE Trans. Signal Process.*, 55(3): 1003-1010, 2007.
- [24] D.L. Alon, B. Rafaely, "Spherical microphone array with optimal aliasing cancellation," in *Proc. IEEE Electrical and Electronics Engineers*: 1-5, 2012.
- [25] B. Rafaely, "Spatial sampling and beamforming for spherical microphone arrays," in *Proc. IEEE Hands-Free Speech Communication and Microphone Arrays*: 5-8, 2008.
- [26] J.R. Driscoll, D.M. Healy, "Computing Fourier transforms and convolutions on the 2-sphere", *Adv. Appl. Math.*, 15 (2): 202–250, 1994.
- [27] J. Atkins, "Robust beamforming and steering of arbitrary beam patterns using spherical arrays," in *Proc. IEEE Workshop on Applications of Signal Processing to Audio and Acoustics (WASPAA)*: 237-240, 2011.
- [28] T. Taguchi et al., "Investigation on optimal microphone arrangement of spherical microphone array to achieve shape beamforming," in *Proc. IEEE Intelligent Systems, Modelling and Simulation*: 330-333, 2014.
- [29] G.W. Elko, J. Meyer, "Adaptive beamformer for spherical eigenbeamforming microphone arrays," in *Proc. IEEE Workshop on Hands-free Speech Communication and Microphone Arrays (HSCMA)*: 52-56, 2014.
- [30] J. Meyer, G. Elko, "A highly scalable spherical microphone array based on an orthonormal decomposition of the sound field," in *Proc. IEEE Acoustics, Speech, and Signal Processing (ICASSP)*: II–1781–II–1784, 2002.

Biography



Mohammad Kalantari received B.Sc. degree in Computer Engineering from Iran University of Science and Technology (IUST), Tehran, Iran and M.Sc. and Ph.D. in Computer Engineering from Amirkabir University of Technology (AUT), Tehran, Iran in 2001 and 2009 respectively. He is currently working as Assistant Professor at Signal Processing Laboratory in Computer Engineering Department at Shahid Rajaee Teacher Training University (SRTTU), Tehran, Iran. His area of interest includes, Statistical signal processing, Spherical array processing, Sampling theory, and Compressed sensing.

Copyrights

©2021 The author(s). This is an open access article distributed under the terms of the Creative Commons Attribution (CC BY 4.0), which permits unrestricted use, distribution, and reproduction in any medium, as long as the original authors and source are cited. No permission is required from the authors or the publishers.

**How to cite this paper:**

M. Kalantari, "An approach for solving signal cancellation problem in spherical microphone array," J. Electr. Comput. Eng. Innovations, 9(2): 161-172, 2021.

DOI: [10.22061/JECEI.2021.7640.415](https://doi.org/10.22061/JECEI.2021.7640.415)

URL: https://jecei.sru.ac.ir/article_1516.html





Research paper

Influence of Phase-Shifting Transformers (PSTs) on the Distance Protection of Transmission Lines and Improving the Performance of Distance Relay

H. Sahraei, M. Tolou Askari*

Department of Electrical Engineering, Semnan Branch, Islamic Azad University, Semnan, Iran.

Article Info

Article History:

Received 23 July 2020

Reviewed 13 September 2020

Revised 01 December 2020

Accepted 02 January 2021

Keywords:

Phase Shifting Transformer

Flexible AC Transmission
Systems (FACTS)

Distance Relay

Transmission Line

Corresponding Author's Email
Address:

m.askari@semnaniau.ac.ir

Abstract

Background and Objectives: With the ever-increasing growth of electric loads, the need for generating electric power grows correspondingly. By considering the limitations of power generation, utilizing novel technologies has gained persistent momentum, one of which is deploying Phase-Shifting Transformers (PSTs). Among the more important available relays for the transmission lines are Distance Relays. To this end, Distance Relays measure the voltage and current of the transmission line in its final installation location. On the other hand, the existence of Phase-Shifting Transformers on transmission lines alters the voltage and current signals at the relay location. This issue causes the impedance calculated by the relay to differ from its actual value at the fault location. As a result, the relay detects the fault location falsely, or in some cases does not recognize it at all.

Methods: The effect of phase shifting transformer on the relay performance of the distances has been investigated in this study. Furthermore, the digital distance relays are modeled in a software environment and its validity is investigated through analytical relationships. Next, the efficacy of the transformer on distance protection is analytically studied. Finally, a new method has been proposed to improve distance relay performance.

Results: Results from analysis and modelling shows that the effect of phase shifting transformers in relay-computed impedance has two faces, the first of which is related to the internal impedance of the transformer, while the other regards the serial voltage of the transformer. The latter face is much more influential than the former one.

Conclusion: This fact renders the mere inner Impedance of phase-shifting transformer insufficient for using it to eliminate its effect. To this end, a method has been developed in which the voltages of both ends of the phase shifting transformer are measured by the PMUs and then sent to the facility for protecting power system after synchronization. There, this voltage is reduced from the voltage calculated by the relay, which renders the effect of the phase shifting transformer in the impedance calculated by the relay completely eliminated.

©2021 JECEI. All rights reserved.

Introduction

Given the recent surge of power consumption in power

systems, various methods have been devised and implemented to increase transmission power, among

which are capacitive compensation or the use of Flexible AC Transmission System (FACTS) devices such as phase-shifting transformers. On one hand, reviewing systems consisted of compensators and FACTS devices reveals new dynamics in power systems, necessitating the analysis, by protection engineers, of rapid changes in system parameters including line impedance, power angle, line currents and transient conductivity generated by control functions as well as harmonics injected into the AC power system [5].

Meanwhile, Distance Relays are widely used as a means to protect transmission lines, whose function is based on calculation of the line impedance from the location of the relay to the fault location [6]. To this end, and to calculate the amount of impedance, the relay continuously monitors the voltage and current of its installation location. With the emergence of fault on transmission lines, the existence of FACTS devices leads to alterations of voltage and current signals, thus altering the performance of the relay, which is dependent on such signals. Moreover, FACTS devices have variable impedance, and since they behave randomly for different errors, they would also affect computed impedance by the relay due to their existence in error loop [1], [2]. Therefore, it is necessary to consider this issue in full, and the functionality of the relay should be checked, as its faulty operation may cause serious damage to the power system [7]. In this project, one of the most widely employed FACTS devices, i.e. Phase-Shifting Transformers, is considered. Its performance, and its effect on the transmission power of the power system is analyzed. Next, the performance of distance relays is studied in the presence of such transformers. Moreover, it is necessary to review the issue considering various performance cases of Phase-Shifting Transformers and different kinds of errors. As a pioneering contribution in this literature, the effect of Phase-Shifting Transformers on Mho distance relays is studied. Also for the first time, various kinds of faults, and particularly, high-resistant faults are considered in the analyses. Distance relays of this research are all digital [8].

Various technologies have been previously used regarding the implementation of protection functions to accurately discover disruption in power grids and to activate the relevant operations for isolating erroneous components. It seemed in the late 1960s that electric relays have consolidated their status as the alternative technology for electromechanical relays [9], [10]. This shift pertained to an era where researchers were inclined to use computers as to protect power grids. Such endeavors, accompanied by the advances in the fields of compact circuit technology and software methods in the 70s, led to introduction of

microprocessor-based relays as commercial devices in 1979 [11], [12]. Microprocessor-based relays have various deficiencies, among which are short life cycle, proneness to transient waves and the need for multiple configurations [4]. Parallel transmission lines are widely used in advanced power systems to increase their security margin. In order to investigate distance relay algorithm, the system considered in this study functions as a parallel transmission line [3], [5]. This algorithm is not as effective as the full-wave method in eliminating harmonics, and as previously stated, this drawback pertains to even-numbered harmonics and if harmonics are omitted from inputs with actuated harmonics, this method would become effective in removing harmonics and yield rapid response time [13], [14]. As it is evident from the algorithm, utilization of anti-parallel analog filters leads to group delay. The group delay is the time it takes for a signal to pass through the filter [15], [16]. The effects of PST on distance relay was investigated in [17]. All studies were investigated in EMTWorks for two different types of faults, Phase to ground and phase to phase. The effects of location of faults as well as the two phase to ground fault was neglected in [17]. Also the alteration of transformer tap was not investigated in [17]. The active power based method for estimating the fault resistance is presented in [16], [17], which it is suitable for transmission lines with negligible line resistance. In [7] an independent fault resistance and communication-aided method was proposed to develop the fault detection in the presence of TCSC. In [29] an adaptive algorithm was proposed to investigate the operation of distance protection of transmission line by considering the shunt FACT device.

A simultaneous method was given in [18] to eliminate the STATCOM and fault resistance based on active power calculation of buses. Furthermore, the fault resistance in addition the PST impedance causes a mistake in operation of distance relay which was neglected in [7], [17], [19], [20].

In this study, the effects of PST as well as the resistance for three types of faults, phase to ground, phase to phase and two phase to ground faults, are investigated. Furthermore, to obtain the protection boundaries of distance relay the location of fault as well as the resistance of fault are considered. Also, The Effect of number of winding Turns of the PST that can be altered the power transmitted through the transmission line is studied. Then, a single-line circuit along with a phase shifting transformer and positive sequence networks, phase shifting transformer is modeled as a controlled voltage source, which has a momentary response to change the system conditions. Finally, a method has been developed in which the voltages of both ends of the phase shifting transformer are

measured by the PMUs and then sent to the facility for protecting power system after synchronization. There, this voltage is reduced from the voltage calculated by the relay, which renders the effect of the phase shifting transformer in the impedance calculated by the relay completely eliminated. The proposed method are simulated in MATLAB software.

Investigating the Effect of Phase Shifting Transformer on Distance Protection

Analytical Investigation

The single-line circuit of the studied system, along with the phase shifting transformer and the positive, negative and zero sequence networks are shown in Fig. 1, which shows the effect of the phase shifting transformer in the middle of the transmission line 1. Two distance relays are implemented to support and protect transmission lines at bus P [21].

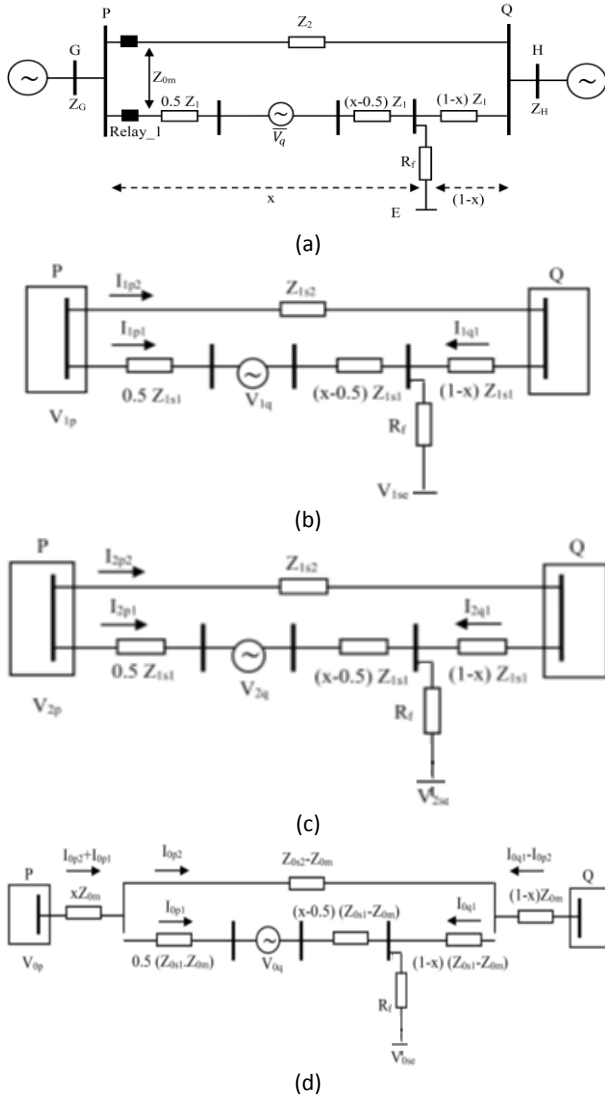


Fig. 1: (a) the single-line circuit of the studied system including (b) the positive sequence network, (c) the negative sequence network, and (d) the zero sequence network.

According to [22] the positive sequence circuit which is shown in Fig. 1 (b) for the error line and the error-free line in the P bus is given as follows:

$$V_{1p} = xZ_{1s1}I_{1p1} + V_{1q} + V_{1se} + \frac{R_f}{(1-x)}(I_{1p1} - k_1I_{1p2} + \frac{V_{1q}}{Z_{1s1}}) \quad (1)$$

Also, the negative sequence network are explain as follows [7]:

$$V_{2p} = xZ_{1s1}I_{2p1} + V_{2q} + V_{2se} + \frac{R_f}{(1-x)}(I_{2p1} - k_1I_{2p2} + \frac{V_{2q}}{Z_{1s1}}) \quad (2)$$

Given the zero sequence network shown in Fig. 1 (d), we arrive at the following equations [10]:

$$V_{0p} = x(Z_{0m}I_{0p2} + Z_{0s1}I_{0p1}) + R_f(I_{0p1} + I_{0q1}) + V_{0q} + V_{0se} \quad (3)$$

$$V_{0p} = xZ_{0m}(I_{0p2} + I_{0p1}) + (Z_{0s2} - Z_{0m})I_{0p2} + (Z_{0s1} - Z_{0m})(1-x)I_{0q1} + R_f(I_{0p1} + I_{0q1}) + V_{0se} \quad (4)$$

Similar to previous methods, the value of V_{0p} equals to:

$$V_{0p} = x(Z_{0m}I_{0p2} + Z_{0s1}I_{0p1}) + V_{0q} + V_{0se} + \frac{R_f}{(1-x)}(I_{0p1} - k_0I_{0p2} + \frac{V_{0q}}{(1-x)(Z_{0s1} - Z_{0m})}) \quad (5)$$

where k_0 is equal to:

$$k_0 = (Z_{0s2} - Z_{0m}) / (Z_{0s1} - Z_{0m}) \quad (6)$$

For transmission lines with similar parameters, k_0 is equal to k_1 . In the following section, the value of the impedance calculated by the relay is obtained for different types of errors:

A. Single-phase-to-ground fault

For a Single-phase ground fault, we have:

$$V_p = xZ_{1s1}I_{p1} + x(Z_{0s1} - Z_{1s1})I_{0p1} + xZ_{0m}I_{0p2} + \boxed{V_q} + \frac{R_f}{(1-x)}(I_{p1} - k_1I_{p2} + (k_1 - k_0)I_{0p2} + \frac{V_q}{Z_{1s1}} + V_{0q}(\frac{1}{(Z_{0s1} - Z_{0m})} - \frac{1}{Z_{1s1}})) \quad (7)$$

For the provided system, and without the presence of Phase-Shifting Transformers, Impedance calculated by the distance relay can be obtained by the following equation [23], [24]:

$$Z = \frac{V_p}{I_{p1} + (\frac{Z_{0s1} - Z_{1s1}}{Z_{1s1}})I_{0p1}} = \frac{V_p}{I_{Relay}} \quad (8)$$

Now, in case the phase-shifting transformer is placed in the middle of transmission line 1, V_p in (8) takes the form (7), and thus the Impedance calculated by the distance relay in the presence of the PST takes the following form:

$$Z = xZ_{1s1} + xZ_{0m} \frac{I_{0p2}}{I_{Relay}} + \frac{\frac{V_q}{I_{Relay}}}{(1-x)I_{Relay}} \left(I_{p1} - k_1 I_{p2} + (k_1 - k_0) I_{0p2} + \frac{V_q}{Z_{1s1}} + V_{0q} \left(\frac{1}{(Z_{0s1} - Z_{0m})} - \frac{1}{Z_{1s1}} \right) \right) \quad (9)$$

By considering (9), and by the virtue of the highlighted part, it is evident that the existence of phase-shifting transformer in the fault loop causes the impedance calculated by the relay to increase, an issue which is discussed with more details in Simulation Results.

B. Two-phase fault

Under a two-phase fault (a-b), with resistance R_f , we arrive to the following relation [25]:

$$V_{1p} - aV_{2p} = xZ_{1s1} (I_{1p1} - aI_{2p1}) + (V_{1q} - aV_{2q}) + \frac{R_f}{(1-x)} \left((I_{1p1} - aI_{2p1}) + k_1 (aI_{2p2} - I_{1p2}) + \frac{(V_{1q} - aV_{2q})}{Z_{1s1}} \right) \quad (10)$$

In the absence of PST for two-phased fault, impedance may be calculated using the following relation [20]:

$$Z = \frac{V_{1p} - aV_{2p}}{I_{1p1} - aI_{2p1}} = \frac{V_{1p} - aV_{2p}}{I_{Relay}} \quad (11)$$

As a result, with the presence of the phase shifting transformer in the fault loop, impedance can be obtained through the following formula [26]:

$$Z = xZ_{1s1} + \frac{\frac{(V_{1q} - aV_{2q})}{I_{Relay}}}{(1-x)I_{Relay}} \left((I_{1p1} - aI_{2p1}) + k_1 (aI_{2p2} - I_{1p2}) + \frac{(V_{1q} - aV_{2q})}{Z_{1s1}} \right) \quad (12)$$

Given the aforementioned relation, it is evident that the effect of phase shifting transformer on the relay impedance is originated from the difference in vectors of the voltage between positive and negative sequences, which is described in the simulation results section [27].

C. Two-phase-to-ground fault

Under a Two-phase-to-ground fault (a-b-g), impedance calculated by agents A-B, B-G, and A-G in the relay are subject to change. Using the impedance relation for the B-G agent, the following relation is obtained:

$$a^2 V_{1p} + aV_{2p} + V_{0p} = xZ_{1s1} (a^2 I_{1p1} + aI_{2p1} + \frac{Z_{0s1}}{Z_{1s1}} I_{0p1}) + (a^2 V_{1q} + aV_{2q} + V_{0q}) + xZ_{0m} I_{0p2} + \frac{R_f}{(1-x)} \left((a^2 I_{1p1} + aI_{2p1} + I_{0p1}) - k_1 (a^2 I_{1p2} + aI_{2p1} + \frac{k_0}{k_1} I_{0p1}) + \frac{(a^2 V_{1q} + aV_{2q})}{Z_{1s1}} + \frac{V_{0q}}{(Z_{0s1} - Z_{0m})} \right) \quad (13)$$

In the absence of the PST, impedance calculated by B-G agent is calculated from the following equation:

$$Z = \frac{a^2 V_{1p} + aV_{2p} + V_{0p}}{a^2 I_{1p1} + aI_{2p1} + \frac{Z_{0s1}}{Z_{1s1}} I_{0p1}} = \frac{a^2 V_{1p} + aV_{2p} + V_{0p}}{I_{Relay}} \quad (14)$$

Thus, (14) takes the following form when the phase-shifting transformer is introduced in the fault loop:

$$Z = xZ_{1s1} + \frac{\frac{(a^2 V_{1q} + aV_{2q} + V_{0q})}{I_{Relay}}}{(1-x)I_{Relay}} \left((a^2 I_{1p1} + aI_{2p1} + I_{0p1}) - k_1 \left(a^2 I_{1p2} + aI_{2p1} + \frac{k_0}{k_1} I_{0p1} \right) + \frac{(a^2 V_{1q} + aV_{2q})}{Z_{1s1}} + \frac{V_{0q}}{(Z_{0s1} - Z_{0m})} \right) + \frac{I_{0p2}}{I_{Relay}} \quad (15)$$

where,

$I_{ap2}, I_{bp2}, I_{cp2}$ are phase currents through transmission line 2 at relay location of bus P without fault.

V_{0p}, V_{1p}, V_{2p} are sequence phase voltages (Zero, positive and negative) at relay location

$I_{0p1}, I_{1p1}, I_{2p1}$ are sequence current phase at relay location through transmission line 1

$I_{0p2}, I_{1p2}, I_{2p2}$ are sequence current phase at relay location through transmission line 2 under fault

$I_{0q1}, I_{1q1}, I_{2q1}$ are sequence current phase at relay location through transmission line 1 under fault

$V_{0se}, V_{1se}, V_{2se}$ are sequence phase voltages (Zero, positive and negative) at fault location E

R_f is Fault resistance

V_{0q}, V_{1q}, V_{2q} are sequence phase voltages injected by PST

$Z_{0s1}, Z_{1s1}, Z_{2s1}$ are sequence impedance through transmission line 1 with fault

$Z_{0s2}, Z_{1s2}, Z_{2s2}$ are sequence impedance through transmission line 2 without fault

Z_{0m} is coupling zero sequence between transmission line 1 and 2

$Z_{0G}, Z_{1G}, Z_{2G}, Z_{0H}, Z_{1H}, Z_{2H}$ are sequence impedances of generators G and H

Simulation of Problem statement

A. The Effects of PST on the location of phase to ground fault

The studied power system is depicted in Fig. 2. Here, three transmission lines are situated in series [28]. At the beginning of every transmission line, a distance relay is considered.

This power system is strictly selected as to show the effect phase-shifting transformers on the supportive protection of relays. For this purpose, 3 protection areas are considered for every distance relay.

In Fig. 2, these three areas are shown for transmission line 1. Area 1 contains 80% of transmission line 1, while Area 2 covers the entire transmission line 1 and half of the transmission line 2.

Finally, Area 3 covers the entire transmission lines 1 and 2, and 20% of the transmission line 3. Function delays are used to configure this area, so that Area 1 has

no delay, Area 2 presents 0.5 seconds of delay, and Area 3 introduces 1 second of function delay. In this power system, the PST is placed in the middle of transmission line 2. The transmission lines are equal in distance, each being 200 kilometers. The impedance calculated by the relay of transmission line 1 (RA) for a fault occurring 100 kilometers of RA relay is shown in Fig. 3. It can be seen from the figure that, in the absence of a phase shifting transformer, the relay detects the fault correctly at 100 km of the RA and in Area 1. It is also seen that the phase shifting transformer has no effect on the relay function, which is normal, as for

the fault occurred on the transmission line 1, the phase shifting transformer is not situated in the fault loop of RA relay, and thus bears no effect on its performance.

The impedance calculated by the RA relay for fault occurring 350 kilometers away is shown in Fig. 4. According to the results shown in Fig. 4, it is evident that in the absence of a phase shifting transformer, the RA relay can correctly detect the faults in its area 3. The impedance calculated by the RB relay is also shown in Fig. 5. As can be seen, this relay also correctly detects faults at a distance of 150 kilometers in Area 1 in the absence of a transformer.

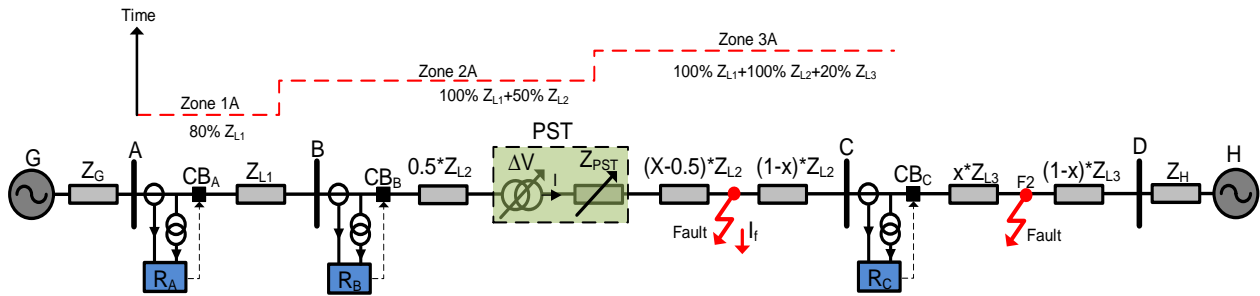


Fig. 2: Modeled power system with phase shifting transformer at middle of transmission line 2 and distance relays.

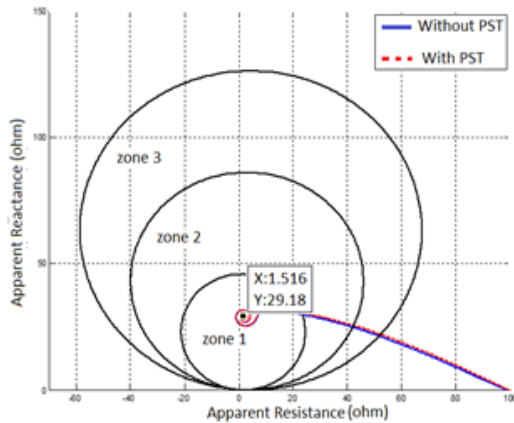


Fig. 3: Impedance calculated by RA relay for A-G fault in 100 km of RA.

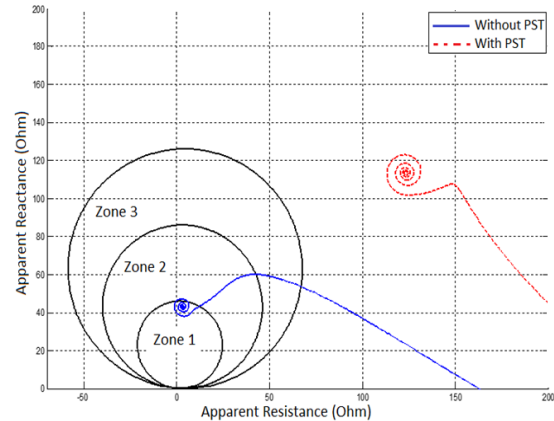


Fig. 5: Impedance calculated by RB relay for A-G fault in 150 km of RB.

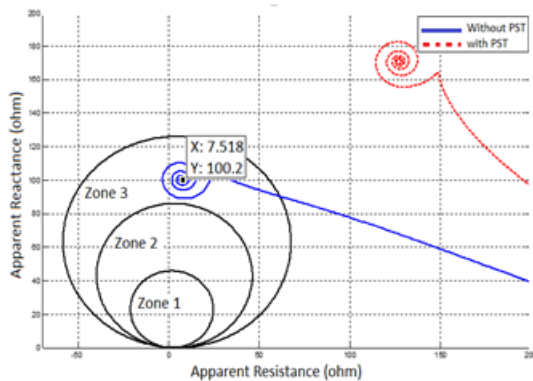


Fig. 4: Impedance calculated by RA relay for A-G fault in 350 km of RA.

It can be seen from the results that existence of PST renders the relays unable to detect faults, a deficiency which may incur severe damages to the power system. The impedances of Relays RA, RB and RC for fault A-G in transmission line 3 are respectively depicted in Fig. 6, Fig. 7 and Fig. 8. The location of this fault in Fig. 8 is marked with F2. This fault occurs at 10 Kilometers of RC Relay, i.e. in its Area 1, Area 2 of RB Relay, and in Area 3 of Relay RC. As can be seen for cases where phase-shifting transformers are missing, all three relays detect the fault accurately. Yet in the presence of a PST, Relays RA and RB are subject to severe range loss, to the extent

that they are now unable to detect any fault whatsoever. Relay RC, however, is still able to detect the fault correctly, as the PST is situated outside its fault loop. This causes the RC relay to lack supporting protection, and thus in case of failure, Relays RA and RB are also ineffective in detecting the faults.

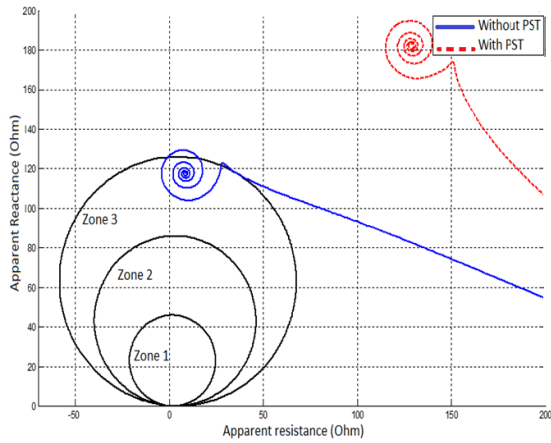


Fig. 6: Impedance calculated by RA relay for A-G fault at 410 km of RA.

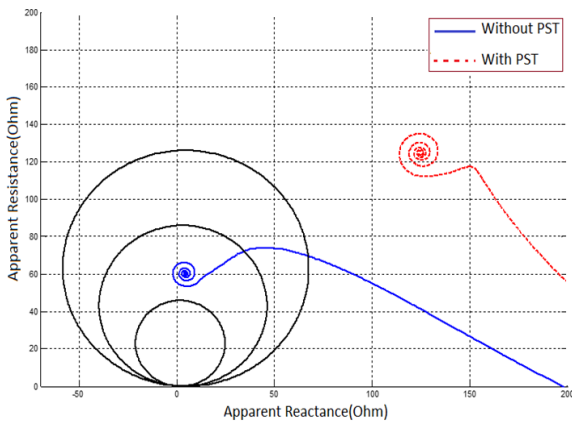


Fig. 7: Impedance calculated by RB relay for A-G fault at 210 km of RB.

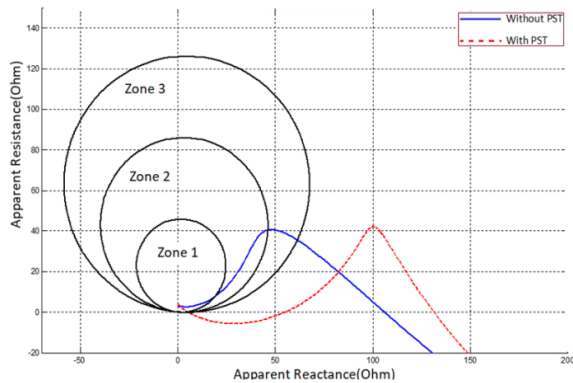


Fig. 8: Impedance calculated by RC relay for A-G fault at 10 km of RC.

B. The Effect of number of winding Turns of the Transformer

The power transmitted through the transmission line can be altered by varying the Tap of the PST [30].

There have been various cases where the extent phase-shifting depended on the alterations of the Tap. Prior modellings have considered the transformer tap to be 1 in the direction of increasing transmission power, i.e. Tap=-1.

Results from modelling an A-G fault at 350 kilometers of RA Relay for various Taps are depicted in Fig. 9 and Fig. 10.

Figure 9 illustrates results for negative tap, in which it is evident that for cases involving negative taps, the range of relay is greatly reduced.

Results for positive taps are shown in Fig. 10, according to which, it is evident that for higher Taps, the presence of PST has caused negative resistance as per the calculations of the relay. In positive taps, the phase-shifting transformer causes the transmission to drop, to the extent that after certain taps, the transformer negates the transmitted power and hence the direction of the power is reserved.

Here, the direction of power transmission is reversed for Tap=5, 10, and thus the impedance calculated by the relay has a negative resistance.

It can be concluded from the comparison of the results that the effect of the transformer in positive taps is greater than that of negative taps.

Figure 11 demonstrates a case where Tap is altered at 0.05 s, with a fault occurring at $t=0.2$ s. in case of Tap=1, the transmission power remains positive after the fault, while for the other values, power remains negative after the fault, and hence the impedance calculated by the relay retains a positive resistance for Tap=1, yet in Tap=5, 10, the corresponding value is negative.

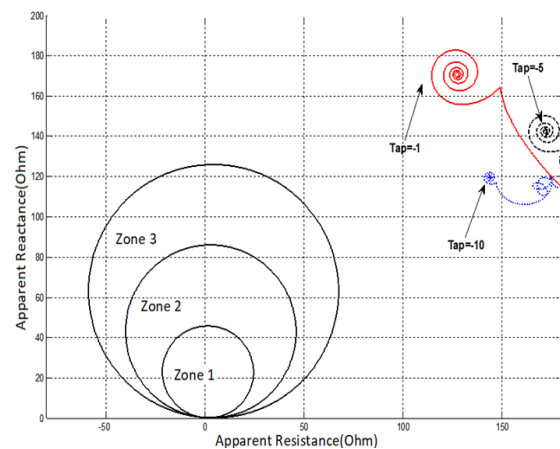


Fig. 9: impedance calculated by RA relay for A-G at 350 kilometers of RA for negative Taps of the PST.

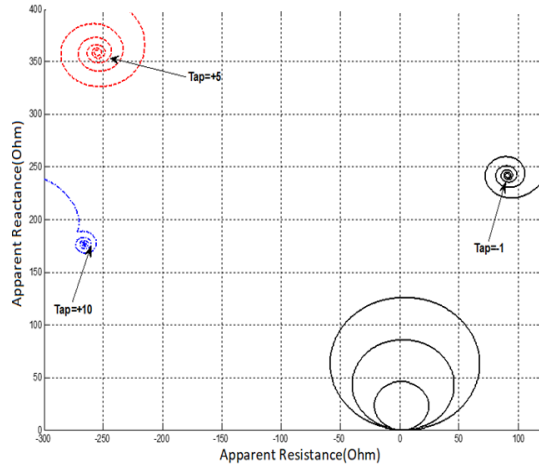


Fig. 10: impedance calculated by RA relay for A-G at 350 kilometers of RA for positive Taps of the PST.

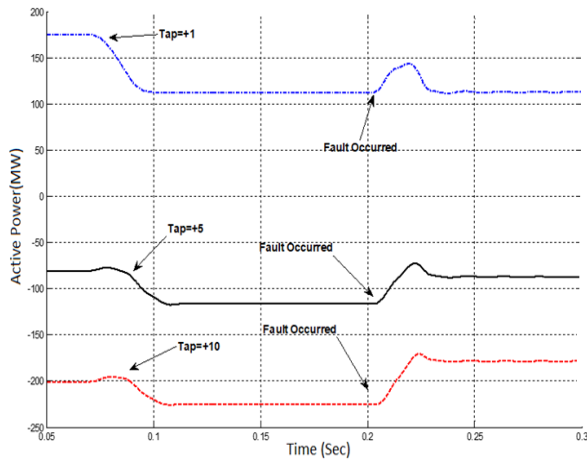


Fig. 11: transmitted active power in transmission line 1 with the presence of PST, for various Tap values and A-G fault occurred at $t=0.2$ s.

C. The Effect of Internal Impedance of Phase-Shifting Transformer

Impedances calculated by RA and RB relays for an A-G fault at 410 kilometers of RA for various values of positive and negative sequence impedance of the PST are shown in Fig. 12 and Fig. 13, respectively, from which it is evident that the Internal Impedance of Phase-Shifting Transformer influences the impedance variations of the relay.

Moreover, one can observe that the effect of zero sequence impedance of the phase-shifting transformer is greater than that of the positive sequence impedance. From Fig. 13, it can be concluded that with the increased zero sequence impedance of the PST, the impedance calculated by the relay is also greater, hence revealing a direct relation.

The comparison of results from this section to those

of the previous section arrives us to the fact that the effect of Tap numbers in the PST, i.e. injected voltage of the transformer, on the performance of the relay is greater than the internal impedance, as it was observed in the previous section the variation of Tap even led to a negative resistance for the impedance.

One of the rather traditional ways of neutralizing the effect PST on the relay-calculated impedance was to add the internal Impedance of the transformer to line impedance and to introduce the results in the calculations made by relay.

Nonetheless, this procedure was only able to eliminate the effect of the internal impedance of the PST on the performance of the relay, while as observed, the greatest effect pertained to the main transformer voltage, and hence this method proved ineffective.

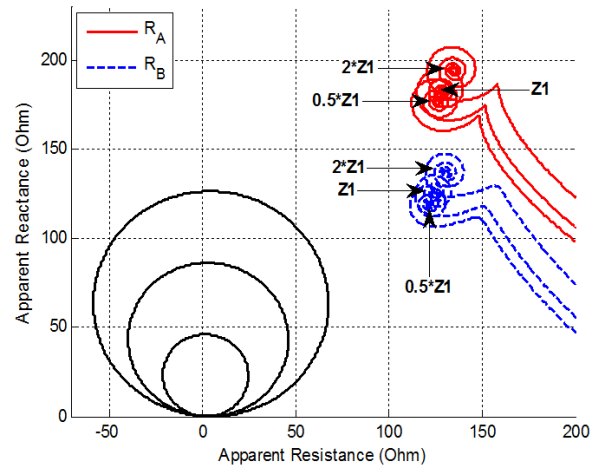


Fig. 12: impedance calculated by RA and RB relays for an A-G fault at 410 kilometers of RA for various values of positive sequence impedance of the PST.

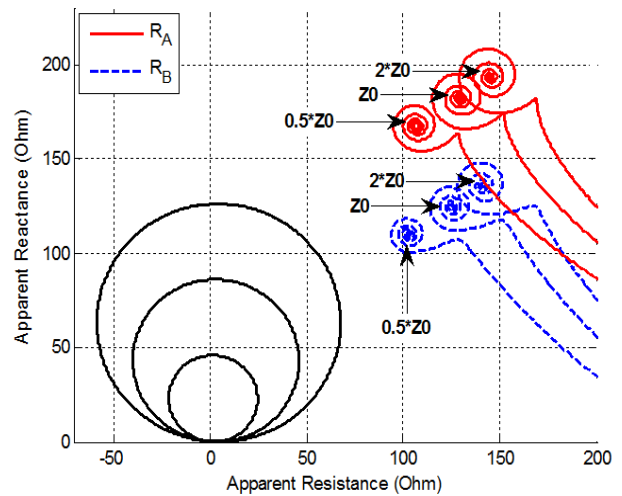


Fig. 13: impedance calculated by RA and RB relays for an A-G fault at 410 kilometers of RA for various values of negative sequence impedance of the PST.

D. Studying the Effect of Phase-Shifting Transformers at Protection Boundaries

To acquire the protection boundaries, two parameters of location of the fault and resistance of the fault are considered. First, the value of the fault resistance is set zero and the location is varied along the path. In this study, this process was performed with 20 kilometer steps. This process resulted in the formation of the AB section in Fig. 14.

In the next step, the location of the fault is considered constant, and the resistance is varied from 0 to 300 ohms, a process which is done with 30-hms steps, yielding the BC section. In the third step, the resistance is preserved at 300 ohms while the location is decreased from the end of the line to its beginning, the result of which is CD. In the fourth and final step, the location of the fault is kept at the beginning of the line, while the resistance of the fault is decreased from 300 ohms to zero.

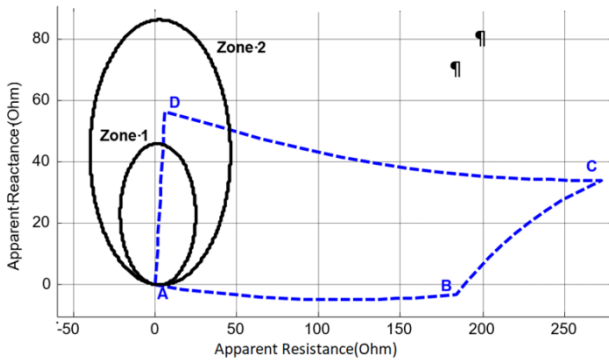


Fig. 14: protection boundaries of distance relay for A-G fault.

This issue causes the formation of DA section. Thus, every fault occurring anywhere along the transmission line with a resistance range of 0-300 ohm situated well within ABCDA protection boundary, and hence the effect of fault resistance is nullified. The protection boundary for A-G fault is depicted in Fig. 14.

As the transmission lines are similar, such protection area are similar for all relays as well. The effect of phase shifting transformers on these boundaries are investigated in the following section. Results from Fig. 15 pertain to condition where Tap=-5 and the operation mode is to increase the transmission power, while Fig. 16 demonstrates the results for Tap=+5 and power reduction mode. Considering the results from both cases, the presence of phase-shifting transformers has divided the protection boundaries in two sections. The section where the effect is more pronounced (C1D1E1F1) pertains to the right-hand side faults of the PST, in which the transformer is situated in the fault loop. For faults occurred at the left-hand side of phase-

shifting transformer, the presence of transformer on protection boundaries is only effective when the resistance is non-zero. It is also evident from the results that A1F1 has remained unchanged, as the resistance is zero along this path. It can also be seen from the results that for Tap=+5, the effect of transformer is greater on protection boundaries, and this effect is pronounced on both the resistance and the reactance of the Impedance, to such extent that the value of resistance has increased to 500 Ohms at E1, while for Tap=-5, the corresponding value is 360 ohms. Reactance varies similar to resistance.

Parameters of case study are described in Table 1 [7], [23], [31]:

Table 1: Case study and distance relay parameters

| Parameters | Value |
|--|--|
| Positive sequence impedance of transmission line | $0.0201+j0.2868 \Omega / km$ |
| Negative sequence of transmission line | $0.1064+j0.8670 \Omega / km$ |
| Zero sequence impedance of transmission line | $0.1718+j0.6930 \Omega / km$ |
| Positive sequence impedance of source P | $1.7431+j19.424 \Omega$ |
| Zero sequence impedance of source P | $2.6147+j4.886 \Omega$ |
| Positive sequence impedance of source Q | $0.8716+j9.7120 \Omega$ |
| Zero sequence impedance of source Q | $1.3074+j2.4430 \Omega$ |
| Voltages of P&Q | $V_p=V_q=500kv$ |
| Load angle between 2 sources | 30 |
| Anti-aliasing filter parameters | Cut-off frequency=250Hz Damping factor Zeta $Q=1/(2*Zeta)=0.707$ |

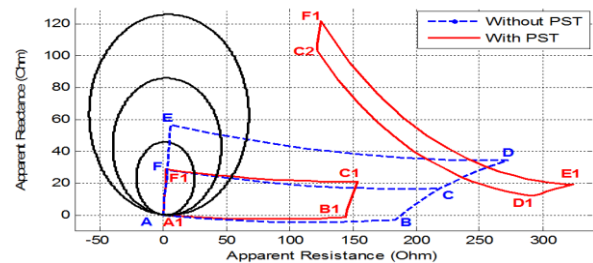


Fig. 15: protection boundaries for distance relay for A-G fault with presence of Phase Shifting Transformer in increased transmission power mode.

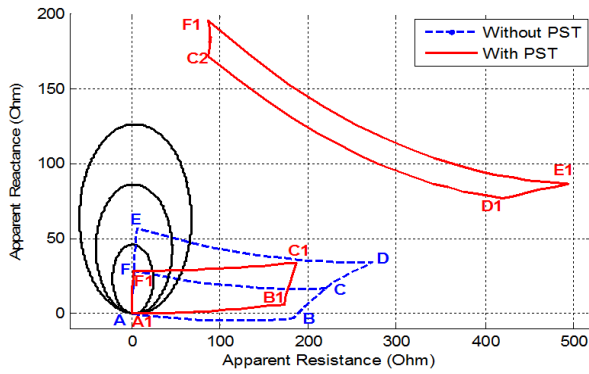


Fig. 16: protection boundaries for distance relay for A-G fault with presence of Phase Shifting Transformer in reduced transmission power mode.

Proposed Method to Improve Distance Relay Performance

It may be observed from the results that the voltage difference across the phase-shifting transformer causes the relays to operate faulty. So if the voltage can be involved in the calculations, the effect of the phase shifting transformer can be eliminated with ease.

For this purpose, the voltage across the phase shifting transformer can be measured by the phasor measurement units (PMU) in the smart grid and have sent to the Protection Center. There, reducing the acquired voltage from the relay's local voltage is sufficient to eliminate its effect in the relay computation. The corresponding power system in this situation is shown in Fig. 17. In this figure, the transformer and bus data are sent to the System Protection Center (SPC) by the virtue communication channels. Further details on PMUs are provided in Fig. 18.

In this figure, similar to what happens in the digital distances relay, the voltage and current signals in the bus are measured by VT and CT, and then passed through the corresponding filters to remove the harmonics, and next they are sampled. From the samples obtained by the full wave Fourier method, the phasor of the signals is obtained. In this way, because the signals received in the SPC are obtained from different locations in the power system, different delays are yielded. As a result, they must be first synchronized before use, for which GPS is used, and the signals are next time-stamped to be used in calculations.

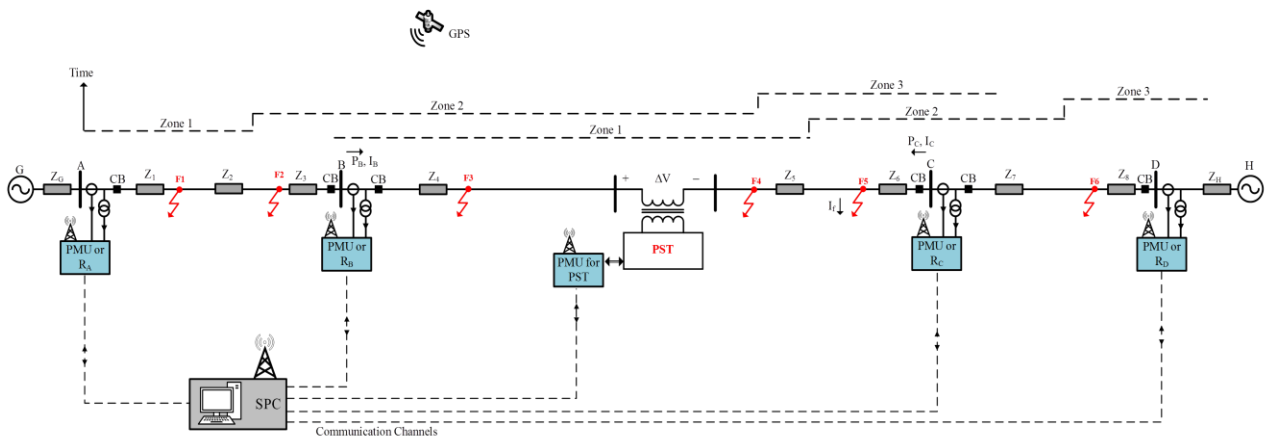


Fig. 17: Smart grid in the presence of phase shifting transformers.

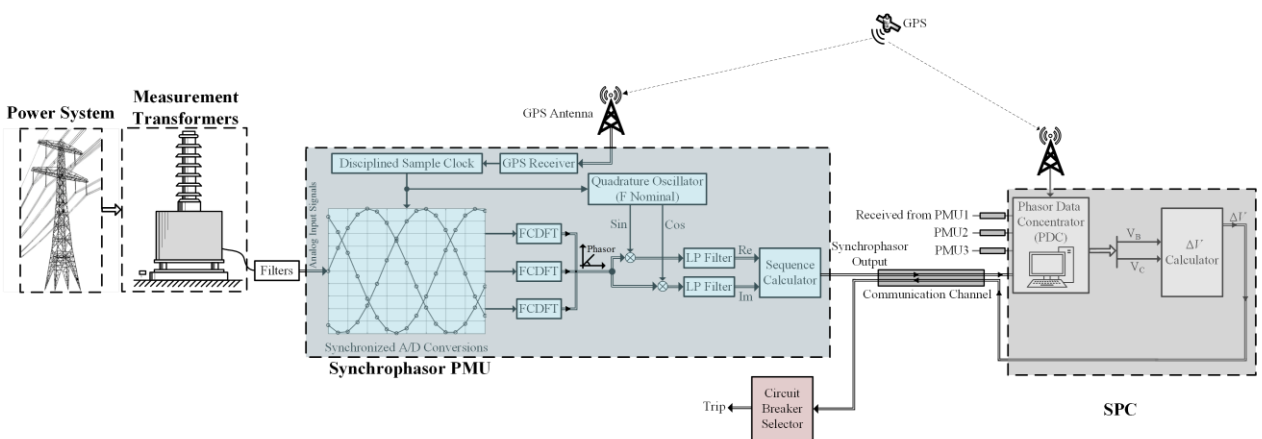


Fig. 18: Details of the PMUs.

Results and Discussion

The results from modelling based on the proposed model are presented in the following. The result for the single-phase-to-ground fault (A-G) occurring at 410 km of relay RA are shown in Fig. 19.

In this figure, the impedance computed by both RA and RB relays is provided. The results pertain to the state where the transformer is not situated in the transmission line and the relays are therefore working properly. The impedance calculated by the relays for the two-phase fault (A-B) is also shown in Fig. 20. For this type of faults, the relay has also been capable of correctly identify the fault, and thus the proposed method can neutralize the effect of the transformer properly. Finally, based on the results, it is safe to say that proposed method can neutralize the detrimental effect of the transformer for both types of fault, and no complex algorithm is needed for this end, yet a smart grid is required in which PMUs are employed to analyze the performance and to control the network as the power system is expanded and PSTs are introduced.

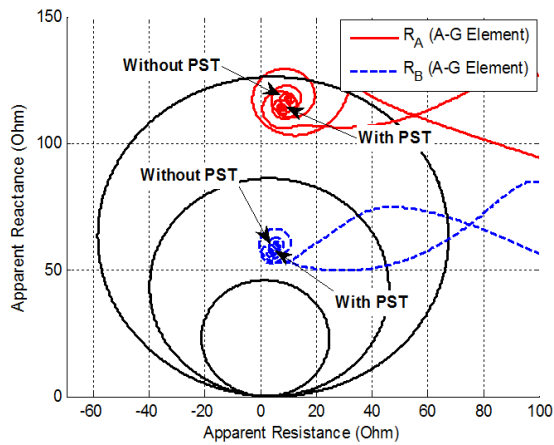


Fig. 19: Impedance calculated by Relays RA and RB for A-G fault at 410 Kilometers of RA.

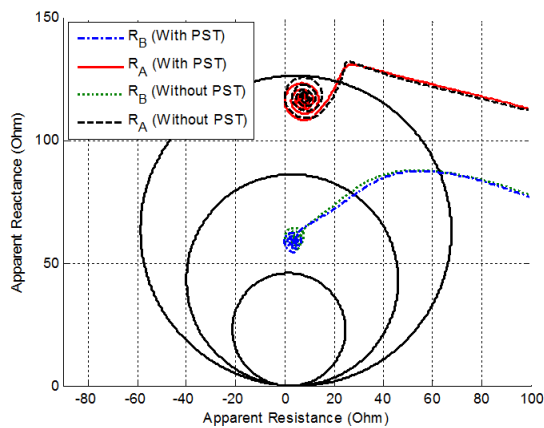


Fig. 20: Impedance calculated by Relays RA and RB for A-B fault at 410 Kilometers of RA.

Conclusion

In this study, the effect of phase shifting transformer on the performance of digital distance relay on a transmission line was investigated. The analytical and modeling results show that the presence of the phase shifting transformer in the fault loop causes the faulty operation of the relay. This disorder is mostly manifested in the form increase impedance. In other words, in all studied cases, the phase shifting transformer reduces the range of distance relays. This means that in spite of the fault occurring in the functional range of the relay, the presence of the phase shifting transformer renders the relay unable to identify the fault. During the fault, the presence of the phase shifting transformer disrupts and the voltage measured by the relay, thus interrupting the function of the relay. The effect of phase shifting transformers on phase-to-ground faults is more heavily pronounced than phase-to-phase faults. Moreover, the effect of the phase shifting transformer in operating mode where the transmission power of the line is reduced is greater than where the transmission power is increased, to such extent that if the phase shifting transformer changes the direction of transmission power, the impedance calculated by the relay will have a negative resistance. It was also observed in high-resistance faults that the presence of a phase shifting transformer causes a two-fold separation of the protective boundaries. To the extent that the parts pertaining to the right-hand side of the PST are more affected, meaning that the phase shifting transformer is in their fault loop. The aforementioned change in the protective boundary is far more severe in the cases where the phase shifting transformers is in the operational mode of reducing transmission power. Results from analysis and modelling shows that the effect of phase shifting transformers in relay-computed impedance has two faces, the first of which is related to the internal impedance of the transformer, while the other regards the voltage of the transformer. The latter face is much more influential than the former one. This fact renders the mere inner Impedance of phase-shifting transformer insufficient for using it to eliminate its effect. To this end, a method has been developed in which the voltages of both ends of the phase shifting transformer are measured by the PMUs and then sent to the facility for protecting power system after synchronization. There, this voltage is reduced from the voltage calculated by the relay, which renders the effect of the phase shifting transformer in the impedance calculated by the relay completely eliminated.

Author Contributions

Dr. Mohammad Tolou Askari supervised and proposed the main problem. Hosein Sahraei simulated

the problem. Results has been interpreted and then the manuscript has been written the by Dr. Mohammad tolou Akasri and Hosein Sahraei.

Acknowledgment

The authors gratefully acknowledge the IEEE I. X. Austan, A. H. Burgmeyer, C. J. Essel, and S. H. Gold for their work on the original version of this document.

Conflict of Interest

The authors declare no potential conflict of interest regarding the publication of this work. In addition, the ethical issues including plagiarism, informed consent, misconduct, data fabrication and, or falsification, double publication and, or submission, and redundancy have been completely witnessed by the authors.

Abbreviations

| | |
|--------------|------------------------------------|
| <i>PST</i> | Phase Shifting Transformer |
| <i>FACTS</i> | Flexible AC Transmission Systems |
| <i>EMTP</i> | Electromagnetic Transients Program |
| <i>SPC</i> | System Protection Center |
| <i>VT</i> | Voltage Transformer |
| <i>CT</i> | Current Transformer |
| <i>A-G</i> | Phase A to Ground |
| <i>A-B</i> | Phase A to Phase B |

Reference

- [1] J.M. Gers, E.J. Holmes, *Protection of Electricity Distribution Networks*, vol. 47: IET, 2004.
- [2] A. Ghosh, G. Ledwich, *Power Quality Enhancement Using Custom Power Devices*: Springer Science & Business Media, 2012.
- [3] S. Jamali, *Protection of Digital Signaling and Power Systems*: Industrial and Science university, 2014.
- [4] H.A. Toliyat, G.B. Kliman, *Handbook of electric motors vol. 120*: CRC press, 2018.
- [5] R. Kumar, R. Singh, H. Ashfaq, "Stability enhancement of multi-machine power systems using Ant colony optimization-based static Synchronous Compensator," *Comput. Electr. Eng.*, 83: 106589, 2020.
- [6] A. Hooshyar, M.A. Azzouz, E.F. El-Saadany, "Distance protection of lines connected to induction generator-based wind farms during balanced faults," *IEEE Trans. Sustainable Energy*, 5: 1193-1203, 2014.
- [7] A. Ghorbani, H. Mehrjerdi, H. Heydari, S. Ghanimati, "A pilot protection algorithm for TCSC compensated transmission line with accurate fault location capability," *Int. J. Electr. Power. Energ. Syst.*, 122: 106191, 2020.
- [8] S.J.T. Shahrabad, V. Ghods, M.T. Askari, "Power transformer fault diagnosis using dga and artificial intelligence," *Recent Advances in Computer Science and Communications (Formerly: Recent Patents on Computer Science)*, 13(4): 579-587, 2020.
- [9] R.R. Mohassel, A. Fung, F. Mohammadi, K. Raahemifar, "A survey on advanced metering infrastructure," *Int J Electr Power Energ Syst*, 63: 473-484, 2014.
- [10] T. Bednarczyk, M. Szablicki, A. Halinka, P. Rzepka, P. Sowa, "Phase shifting transformer electromagnetic model dedicated for power system protection testing in a transient condition," *Energies*, 14(3): 627, 2021.
- [11] M.H. Okba, M.H. Saied, M. Mostafa, T. Abdel-Moneim, "High voltage direct current transmission-A review, part I," in *Proc. 2012 IEEE Energytech*: 1-7, 2012.
- [12] M.T. Askari, M.A.A. Kadir, M. Izadi, "On the trend of improvement of thermal model for calculating the TOT and HST," *Prz. Elektrotech*, 88: 297-301, 2012.
- [13] T.S. Sidhu, R.K. Varma, P.K. Gangadharan, F.A. Albasri, G.R. Ortiz, "Performance of distance relays on shunt-FACTS compensated transmission lines," *IEEE Trans. Power Delivery*, 20(3): 1837-1845, 2005.
- [14] C.-S. Yu, "A discrete Fourier transform-based adaptive mimic phasor estimator for distance relaying applications," *IEEE Trans. Power Delivery*, 21(4): 1836-1846, 2006.
- [15] X. Zhou, H. Wang, R. Aggarwal, P. Beaumont, "Performance evaluation of a distance relay as applied to a transmission system with UPFC," *IEEE Trans. Power Delivery*, 21(3): 1137-1147, 2006.
- [16] A. Ghorbani, M. Arablu, "Ground distance relay compensation in the presence of delta-hexagonal phase shifting transformer," *IET Gener. Transm. Distrib.*, 9(15): 2091-2098, 2015.
- [17] A. Ghorbani, "An adaptive distance protection scheme in the presence of phase shifting transformer," *Electr. Power Syst. Res.*, 129: 170-177, 2015.
- [18] A. Ghorbani, M. Ghorbani, S.Y. Ebrahimi, "Synchrophasors-based transmission line protection in the presence of STATCOM," *J.Control Autom. Electr. Sys.*, 28: 147-157, 2017.
- [19] B. Dewangan, N. Kumar, "distance algorithm for transmission line with mid-point connected statcom," 2019.
- [20] P.S. Georgilakis, N.D. Hatziargyriou, "Unified power flow controllers in smart power systems: models, methods, and future research," *IET Smart Grid*, 2: 2-10, 2019.
- [21] S. Mohammadzadeh, S.G. Seifossadat, M. Joorabian, "Providing a new method for protecting the loss of excitation of generator in the presence of phase-shifting transformer," *Int. Trans. Electr. Energy Syst.*, 29: e12023, 2019.
- [22] M. Kundu, S. Debnath, "Fault location in UPFC compensated double circuit transmission line using negative sequence current phasors," *Electr. Power Syst. Res.*, 184: 106347, 2020.
- [23] A. Ghorbani, H. Mehrjerdi, M. Sanaye-Pasand, "An accurate non-pilot scheme for accelerated trip of distance relay zone-2 faults," *IEEE Trans.Power Delivery*, 2020.
- [24] M.R. Barzegar-Bafrooei, A.A. Foroud, "Performance evaluation of distance relay in the presence of hybrid SFCL," *IET Sci. Meas. Technol.*, 12(5): 581-593, 2018.
- [25] L. Ji, X. Tao, Y. Fu, Y. Fu, Y. Mi, Z. Li, "A new single ended fault location method for transmission line based on positive sequence superimposed network during auto-reclosing," *IEEE Trans. Power Delivery*, 34(3): 1019-1029, 2019.
- [26] A. Keri, A. Mehraban, X. Lombard, A. Eiriachy, A. Edris, "Unified power flow controller (UPFC): modeling and analysis," *IEEE Trans. Power Delivery*, 14(2): 648-654, 1999.
- [27] U. Khan, T. S. Sidhu, "New algorithm for the protection of delta-hexagonal phase shifting transformer," *IET Gener. Trans. Distrib.*, 8(1): 178-186, 2014.
- [28] M. Khederzadeh, A. Ghorbani, "Impact of VSC-based multiline FACTS controllers on distance protection of transmission lines," *IEEE Trans. Power Delivery*, 27(1): 32-39, 2011.
- [29] J. Verma, R. Sharma, "Distance algorithm for Transmission Line with Mid-Point Connected STATCOM," ed: IRJECT, 2019.
- [30] M. Thwala, A. Nnachi, K. Moloi, A. Akumu, "The effect of a phase shift transformer for power flow control," in *Proc. 2019 Southern African Universities Power Engineering Conference/Robotics and*

Mechatronics/Pattern Recognition Association of South Africa (SAUPEC/RobMech/PRASA): 425-430, 2019.

- [31] A. Kazemi, S. Jamali, H. Shateri, "Effects of SSSC on distance relay tripping characteristic," in *Proc. 2006 IEEE International Power and Energy Conference*: 624-629, 2006.

Biographies



Hossein Sahraei is official employee of Zanjan Regional Electricity with 25 years of service as an organizational substation operation expert and job title Expert in managing and operating facilities and electricity networks. He is resident of Zanjan province in Abhar city. His bachelor's degree is in IT engineering from Payame Noor University and a master's degree in electrical engineering from the University of Islamic Azad University- Semnan branch in July 2016. He obtained his MSc in Power Electrical Engineering under the supervision of Dr. Mohammad Tolou Askari. The title of his research was Investigation of the effects of phase shift transformers (PST) in the protection of distance relays of transmission lines".



Mohammad Tolou Askari was born in Mashhad Iran. He obtained his Bachelor's Degree in Power Electrical Engineering at the University of Applied Science and Technology of Mashhad in 2005. He proceeded to obtain his Master's in Power Electrical Engineering in 2008. His research thesis was on "dynamic thermal model approach to estimate loss of life of mineral oil immersed transformers". He obtained his Ph.D. in Power Electrical Engineering at the University Putra Malaysia in 2011 under the supervision of Prof. Ir. Dr. Mohd Zainal Abidin Ab Kadir, Assoc. Prof. Dr. Hashim Hizam and Dr. Jasronita Jasni. The title of his research was "dynamic investment modeling in the restructured power market with the presence of wind resources". Currently, he is senior lecturer in Islamic Azad University (Semnan Branch). He is also the director of Growth Centre of Islamic Azad University of Semnan. He has supervised 40 M.Sc. students with another 8 doctoral and 6 master's level candidates on the way. His research interests include generation expansion planning, scheduling, uncertainties, and loss of life of the transformers.

Copyrights

©2021 The author(s). This is an open access article distributed under the terms of the Creative Commons Attribution (CC BY 4.0), which permits unrestricted use, distribution, and reproduction in any medium, as long as the original authors and source are cited. No permission is required from the authors or the publishers.



How to cite this paper:

H. Sahraei, M. Tolou Askari, "Influence of phase-shifting transformers (PSTs) on the distance protection of transmission lines and improving the performance of distance relay," *J. Electr. Comput. Eng. Innovations*, 9(2): 173-184, 2021.

DOI: [10.22061/JECEI.2021.7549.403](https://doi.org/10.22061/JECEI.2021.7549.403)

URL: https://jecei.sru.ac.ir/article_1520.html





Research paper

Realization of Ultra-Compact All-Optical Universal NOR Gate on Photonic Crystal Platform

F. Parandin*

Department of Electrical Engineering, Islamic Azad University, Kermanshah Branch, Kermanshah, Iran.

Article Info

Article History:

Received 26 August 2020
Reviewed 13 October 2020
Revised 21 December 2020
Accepted 25 January 2021

Keywords:

Photonic crystals
Optical NOR gate
Universal gate
PBG

*Corresponding Author's Email Address:

f.parandin@iauksh.ac.ir

Abstract

Background and Objectives: Universal NOR gate is one of the most important gates in digital design. The all-optical NOR gate can be designed using photonic crystals. These types of gates have a small size and can be integrated.

Methods: In this paper, an optical NOR gate is designed based on 2D photonic crystals. A square lattice has been used to design this structure. This logic gate has two main inputs, a bias input and an output. Because the output of the NOR gate must be "1" for zero inputs, a bias input is required. A combination of linear and point defects has also been used to create waveguides.

Results: One of the characteristics of this structure is its small size for use in optical integrated circuits. The use of a small number and simple point defects makes the design of this gate easier. The obtained delay time for this gate is 0.06ps. Due to these features, this gate can be used in high-speed optical integrated circuits.

Conclusion: In this paper, an all-optical NOR logic gate is designed and simulated using photonic crystals. The use of a small number of point defects has reduced the delay time of this gate. The proposed NOR gate can be used in high-speed optical integrated circuits.

©2021 JECEI. All rights reserved.

Introduction

Transistors are the basis of today's electronic devices used to transmit information. A variety of logic gates are designed using transistors. Logic circuits are also designed using logic gates. Logic integrated circuits that are the basis of computer design are also composed of the same logic circuits. To design high-speed computers, it is necessary to use high-speed transistors. The speed of transistors depends on their dimensions. The smaller the transistors, the faster they will be. Given that the dimensions of transistors have become very small today, it seems that downsizing technology can hardly meet the reduced dimensions of nano-transistors. Therefore, electronic researchers are looking for a new base for computer design. Among the structures used so far, it

seems that photonic crystals are suitable for designing new generation computers due to their properties as a base structure [1], [2].

The reason why this structure has been considered by researchers is that, firstly, these structures are flexible and most circuits used in digital electronics, can be implemented based on photonic crystals. Secondly, due to the fact that light is used in these circuits, the energy-carrying particle is a photon, which has a much higher speed than electrons. Therefore, if the information is transmitted optically, their transmission speed will be higher. Photonic crystals are composed of two materials with different refractive indexes. The refractive index of these two materials is relatively high. These two materials are placed next to each other alternately to

create an alternating structure of two materials with different refractive indexes. The characteristic of these structures is that they prevent the propagation of a continuous range of wavelengths. That is, a continuous range of wavelengths cannot pass through the structure. This range of wavelengths is called the photonic band gap (PBG). If the refractive index distances of the two materials in the photonic crystal increase, the width of the PBG will increase [3]-[5].

Photonic crystals are divided into three categories. These three categories include one-dimensional, two-dimensional, and three-dimensional photonic crystals. In one-dimensional photonic crystals, the structure alternates in one direction. In two-dimensional photonic crystals, the structure is alternating in two directions, and in three-dimensional photon crystals, the alternation will be in three directions. Therefore, three-dimensional photonic crystals restrict light in three directions and are more suitable for use in optical circuits. However, due to the fact that their construction is very complex and the current technology is not widely available for their construction, more two-dimensional photonic crystals are used. Two-dimensional photonic crystals can be created by placing rods with a certain refractive index, in one environment with a different refractive index [6]-[8].

For a two-dimensional photonic crystal to be used as an optical circuit, the wavelength used must be within the PBG range. Therefore, the light wave that radiates from the source to the photonic crystal reflects after hitting the structure. For a light wave to pass through the structure of a photonic crystal, we must create paths for light to propagate through it. These pathways can be created by removing or changing the rods. In other words, by disrupting the alternating structure in a path, light can be directed in that direction. These changes are called defects and the paths in which the defect is created are called waveguides. If one of the bars changes, it is called a point defect, and if some of them change in the same direction, it is called a linear defect. So far, photonic crystals have been used as the base structure for various circuits. One of these circuits is a variety of sensors. Also, different types of fibers are designed using photonic crystals. Photonic crystals can also be used to design a variety of logic circuits [9]-[21].

In the field of logic circuits, Photonic crystals can also be used as a base structure. So far, logic gates such as NOT, OR, AND, XOR and XNOR have been designed and simulated based on photonic crystals [22][23]-[33].

The most important logic gates are NAND and NOR universal gates. Using each of these gates, all logic functions can be implemented. The design of these gates using photonic crystals has been done so far. In some of these structures, the circuit size is large or the delay time is long, which is not suitable for use in high-speed optical

integrated circuits. Also, some of them have a lot of defects with high variety, which causes problems during construction [34]-[41]. One of the advantages of these structures in designing various optical devices is their small size and also their ability to design a wide range of devices. The limitation of these structures is their fabrication. The fabrication technology of these structures is not yet complete and so far limited work has been done. Photonic crystals can be used in two structures. In the first structure, the holes in the dielectric substrate and in the second one, dielectric rods in the air are used. The holes in the dielectric substrate is used for the control of electric modes and the rods in the air is used for magnetic modes. In this paper the second structure is implemented. Both types are commonly used in the design of logic gates. In this paper, a low-dimensional, low delay time optical NOR gate is designed and simulated using two-dimensional photonic crystals. In this structure, a square lattice and very few point defects have been used in the design of the proposed NOR gate. Also, the same point defects are considered to have a simple design. According to these features, it can be said that this gate is suitable for use in optically integrated circuits.

NOR Logic Gate

NOR logic gate is one of the universal gates. The universal gate is a gate that can be used to implement all logic functions. The NOR gate is complementary to the OR gate. The output of this gate is only in the "1" mode when all inputs are equal to "0". If one of the inputs of this gate is in the "1" position, the output will be equal to "0". The importance of this gate is because by using this gate alone, all logical gates can be implemented, without using other gates. Figure 1(a) shows the circuit diagram of the NOR gate with two inputs, and Fig. 1(b) shows its accuracy table.

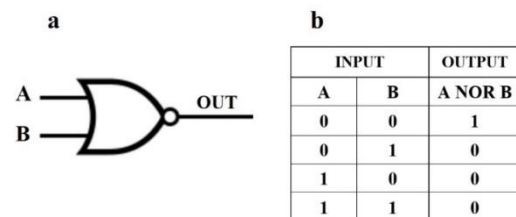


Fig. 1: a) NOR gate circuit diagram and b) its accuracy table.

All-Optical NOR Gate

A photonic crystal structure with a square lattice has been used to design the NOR optical gate. Designing square lattice is easier than other structures. In this structure, several paths are considered for light propagation, which is shown in Fig. 2.

In optical circuits, logic "0" means very low light power, and logic "1" means light power close to the input source in on state. At the optical NOR gate, the

output is in the "1" state, when all inputs are equal to "0". Therefore, when all input sources are off, the output should have optical power close to the "on" source. Therefore, when both inputs are off, there must be an auxiliary source that causes the output to be "1". This input is called the bias input. Figure 2 schematically shows the paths created in the structure to propagate light.

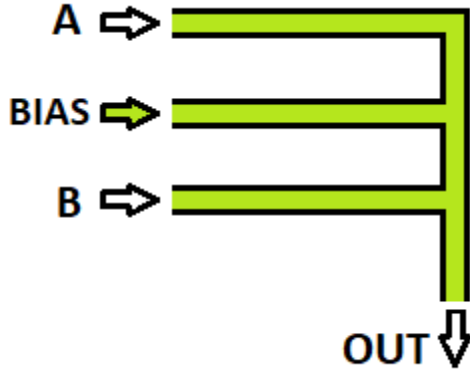


Fig. 2: Light propagation paths for the NOR gate.

The primary photonic crystal structure intended for the realization of the NOR gate consists of silicon rods. The number of these rods is 19×13 , which are arranged in a square lattice in the air background. Because this structure is designed for a wavelength of $1.55\mu\text{m}$, the refractive index of the rods is 3.48 at this wavelength. The air refractive index is also equal to 1. The lattice constant, which is the distance between the centers of adjacent rods, is assumed to be $a=0.56\mu\text{m}$. The radius of the silicon rods is also equal to $r=0.2a$.

To simulate the structure, first, the band structure calculations are obtained for the initial structure. In the band structure, the structure behavior is determined for different wavelengths. Figure 3 shows the obtained band structure for the initial structure.

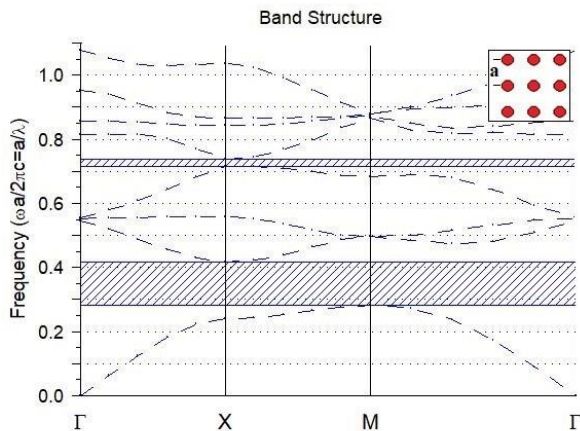


Fig. 3: The band structure for the initial structure.

Figure 3 shows a PBG in the normalized range of 0.28

to 0.42. The wavelength equivalent to this range can be written as $1.33\mu\text{m}$ to $2\mu\text{m}$. Therefore, at this distance from the wavelength, light cannot enter the structure. In order for this structure to be able to direct light in certain directions, the wavelength of light sources must be within the PBG distance. The wavelength used in this simulation is $1.55\mu\text{m}$. In the next step, the desired paths for light diffusion are created. For this purpose, the location of input sources is determined first. In this structure, two main inputs are provided for the NOR gate, and one input is provided for the bias input. These paths are created in parallel by removing all the rods. The input paths are then connected using a vertical defect path. One rod at the end of path B is not removed and its radius is changed to $r_d = 0.5r$. Three rods a, b and c in the vertical path are also selected as defect rods. The radius of these rods is also considered as $r_a = r_b = r_c = 0.5r$.

Figure 4 shows the creation of defect paths for the realization of the NOR gate. For better performance of the proposed NOR gate and to increase the distance of the logical values "0" and "1" at the output, the bias source has a phase delay of 130° compared to the two inputs. To create a phase difference between bias signal and input signals, all sources must be coherent and have the same phase. To do this, the input waves must come from the same source. Now, to create a phase difference, the paths taken by these waves must be different. In other words, by adjusting the paths traveled by these light waves, the desired phase difference can be created.

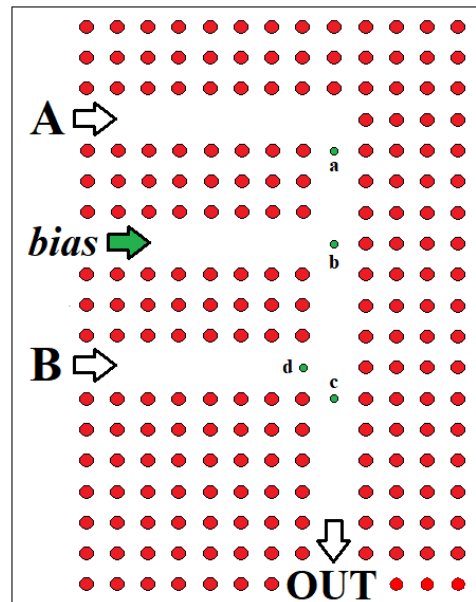


Fig. 4: Proposed structure for optical NOR gate.

Results and Discussion

According to the accuracy table of the two-input NOR gate, four different modes must be analyzed. In the

following, these four modes are analyzed and the distribution of optical power in different paths is obtained for each state. Also, the amount of normalized power at the output is obtained for each of the four input modes. The normalized value is used to calculate the output power. This means that the power of a source in the "on" state is considered as the basis, and the power at the output is calculated relative to that source. Therefore, the minimum optical power will be zero and, the maximum output power will be equal to 1.

State 1(A=B=0): This is the case when both inputs are equal to zero. That is, both input sources A and B are off. In this case, the optical power is emitted from the bias source to the output and causing the output to be in the "1" logic state. Figure 5(a) shows the distribution of optical power in waveguide paths.

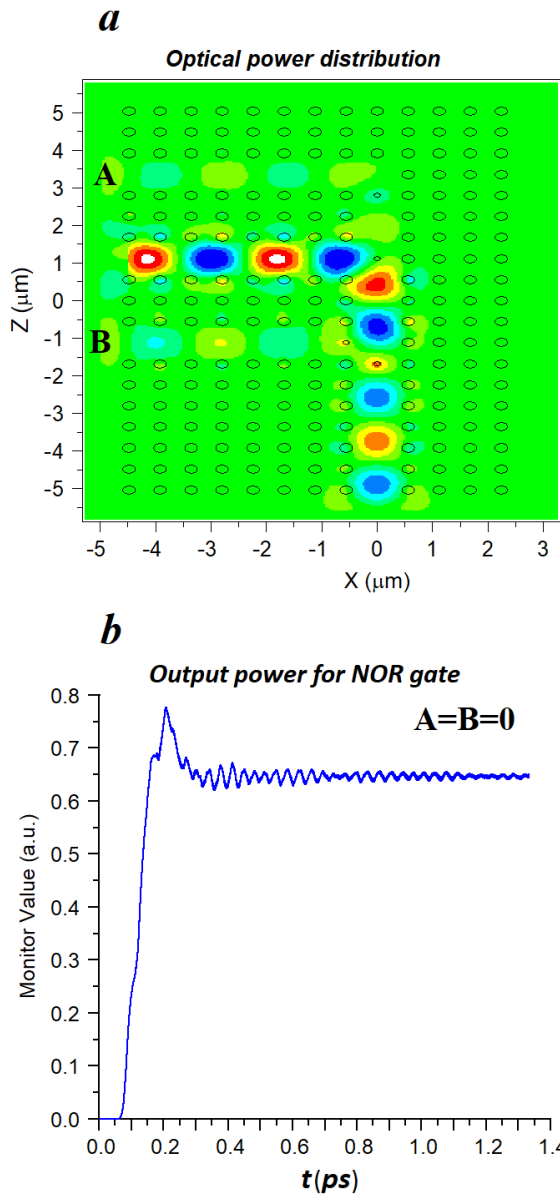


Fig. 5: a) Optical power distribution and b) Normalized optical power for A=B=0.

Figure 5(b) shows the amount of normalized power at the output. This figure shows that the amount of normalized power at the output is 0.65. In other words, 65% of the source optical power is transferred to the output, which can be considered as logic "1". The delay time, in this case, is about 0.06ps, as shown in Fig. 5(b). When one or more sources are on, some optical power is reflected in the bias and input paths. The simulation results show that for this case the normalized power reflected the input paths A and B is 0.06 and 0.11, respectively, and also to the bias path is 0.01.

State 2(A=0, B=1): In this case, where only one of the inputs is on, the output is expected to be in the "0" state.

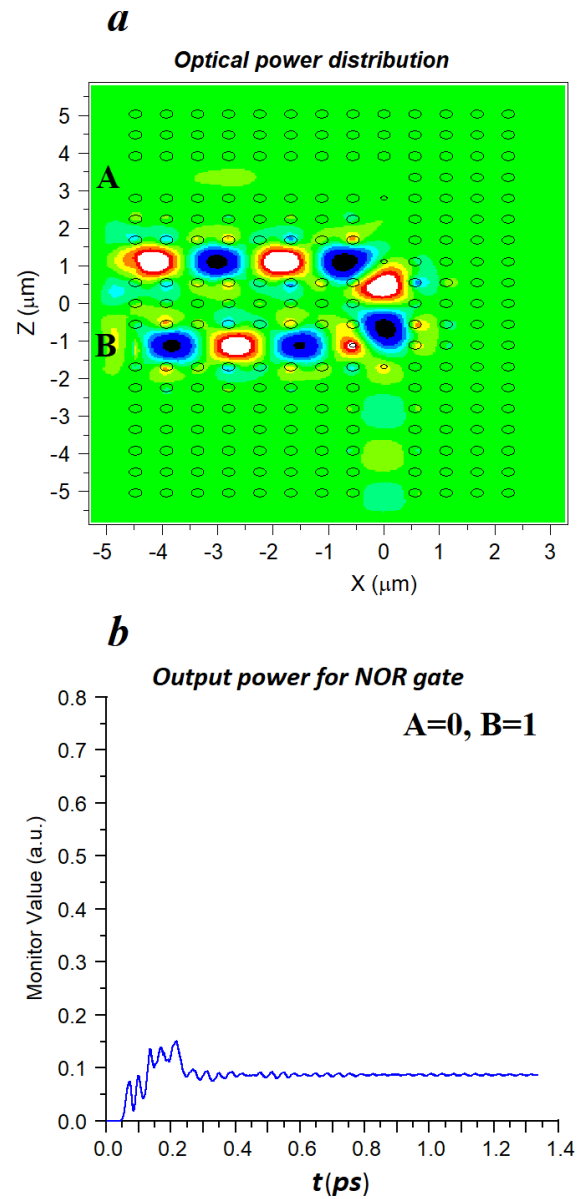


Fig. 6: a) Optical power distribution and b) Normalized optical power for A=0, B=1.

Figure 6(a) shows that in this case the output power distribution in the output path is very low. In this case, the propagating waves from source B and the bias source at the point of collision of the waveguides, interfere in such a way that the amplitude of the output waves is reduced due to the phase difference. Some of the optical power is also reflected to the input paths.

Figure 6(b) shows that in this case ($A = 0$, $B = 1$) the normalized power at the output is 0.08. This value can be considered as a logical "0".

The normalized power reflected in the A input, in this case, is zero. While the optical power reflected the B input is 0.27. Also, this power at the bias input is about 0.1.

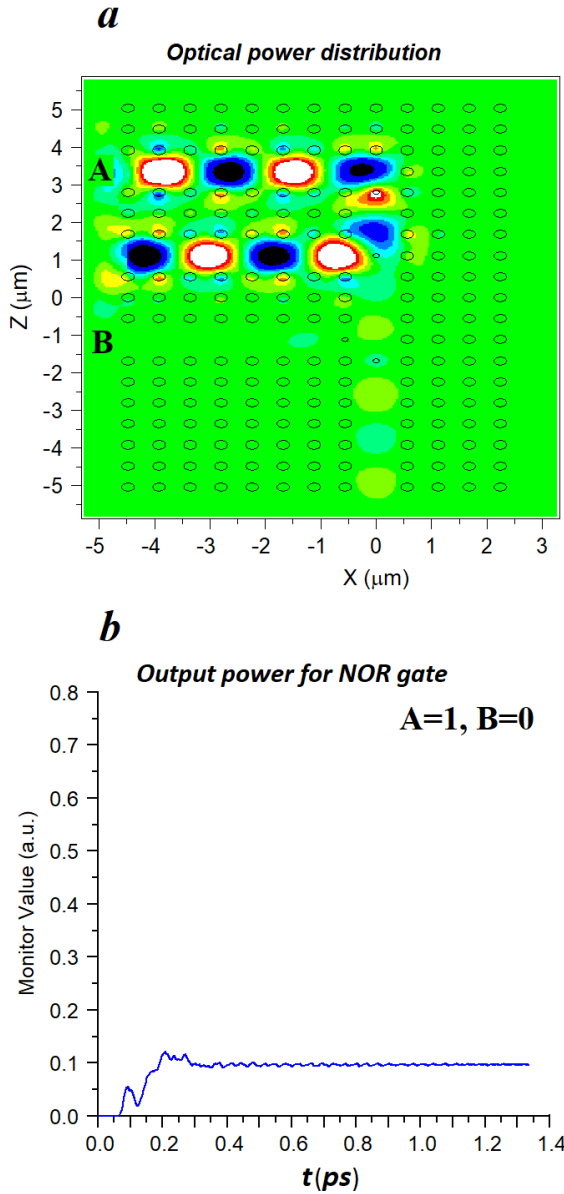


Fig. 7: a) Optical power distribution and b) Normalized optical power for $A=1$, $B=0$.

State 3($A=1$, $B=0$): In this case, as in case 2, only one input source is on. The simulation results show that the optical power distribution in the output path is very low. Light waves from two sources, bias and source A, are attenuated at the point of collision and the power emitted to the output is low. Figure 7(a) shows the optical power distribution in this case.

Time calculations for this situation show that the normalized power propagated to the gate output is 0.09. This amount of power at the output is equivalent to the "0" logic state. The output power diagram, in this case, is shown in Fig. 7(b). In this case, the normalized power reflected the input paths A and B is 0.3 and 0.01, respectively, and also to the bias path is 0.08.

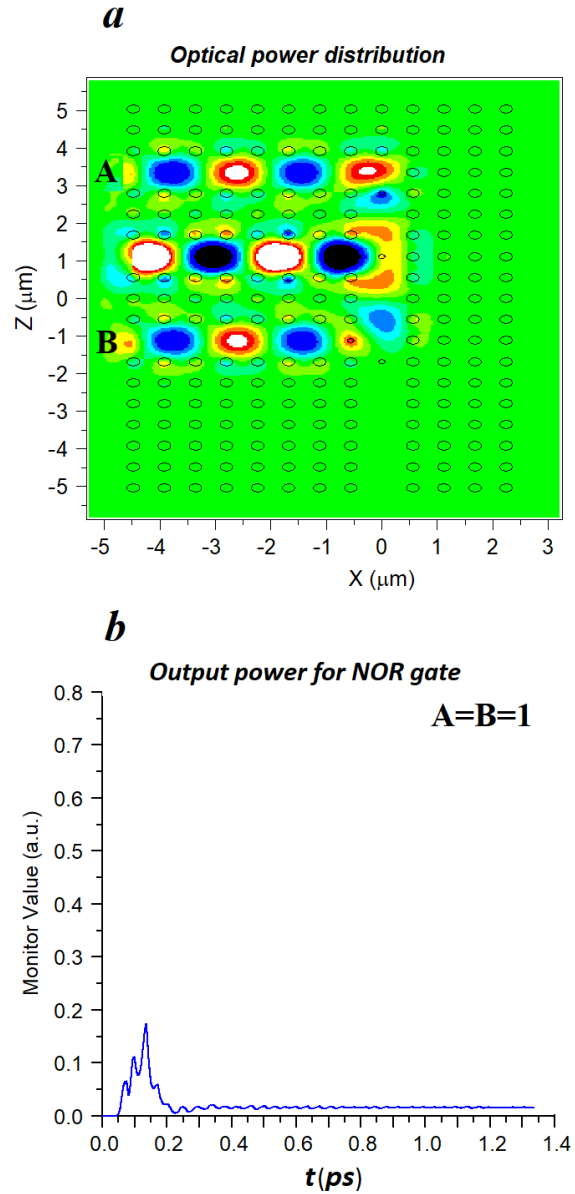


Fig. 8: a) Optical power distribution and b) Normalized optical power for $A=B=1$.

State 4(A=B=1): When both input sources are on, according to the accuracy table, the output is expected to be zero.

The simulation results are shown in Fig. 8. Figure 8(a) shows the optical power distribution in waveguides. This diagram shows that the emitted waves from the two input sources are attenuated in the event of a bias source wave. Some optical power is also reflected in the input paths.

The emission power to the output is very small in this case.

The normalized optical power at the output is equal to 0.02 in this case, which is equivalent to a logical "0". The output power diagram is shown in Fig. 8(b).

The simulation results show that in this case the amount of normalized power reflected to A and B inputs, is 0.12. Also, this power is calculated to be 0.28 in the bias path.

All the different input modes and their equivalent output power as well as their equivalent logic values are given in Table 1.

According to Table 1, it can be said that the output of the designed gate will be equal to "1" only when both inputs are off. In other words, the output will be "1" when both inputs are in the "0" position. This behavior is the same as the NOR gate function.

Table 1: Optical power at the output

| Input | | Output power(Logic) |
|-------|---|---------------------|
| A | B | |
| 0 | 0 | 0.65 (1) |
| 0 | 1 | 0.08 (0) |
| 1 | 0 | 0.09 (0) |
| 1 | 1 | 0.02 (0) |

The results show that this gate has a small amount of power in the "0" mode. The worst value for logical "0" is 0.09. The normalized optical power in logic "1" mode is also equal to 0.65.

It can be seen that this gate has a low "0" and its value of "1" is relatively high. Therefore, the difference between the two logic levels is acceptable, and this causes the correct detection of logic values at the output, and thus reduces the detection error at the output.

To illustrate the strengths of the proposed optical gate, a number of recently designed structures are listed in Table 2. Important parameters in optical logic gates including size, values of logic levels, and delay time for each of these papers have been investigated and compared with the proposed work.

Table 2: Compare the proposed NOR gate with previous works

| Reference | Footprint (μm^2) | "0" Max power | "1" Min power | Delay Time (ps) |
|-----------|-------------------------------|---------------|---------------|-----------------|
| [32] | 202 | 0.35 | 0.75 | 0.07 |
| [35] | 134 | 0.06 | 0.58 | 0.10 |
| [37] | 144 | 0.20 | 0.51 | 0.07 |
| [38] | 104 | 0.13 | 0.62 | 0.10 |
| [40] | 129 | 0.43 | 0.60 | - |
| This work | 68 | 0.09 | 0.65 | 0.06 |

According to Table 2, it can be seen that the proposed structure has a very small size compared to previous structures, which makes it suitable for use in optically integrated circuits. The footprint of the designed structure is $68\mu\text{m}^2$. Also, the distance between two logical values has been improved so that in this gate, the bit detection error in the output will be reduced. In some previous structures, ring resonators have been used, which complicates the structure and causes problems in fabrication.

Ring resonators also increase the gate delay time. In some other structures without ring resonators, the number of point defects is large and unequal, which also causes problems in their design. The proposed gate does not use ring resonators and also the number of point defects is very small and they are all the same. Therefore, this gate is designed using a simple structure. Another advantage of this structure is its very low delay time, which is due to the use of a small structure. The delay time has also been reduced due to the use of simple defects. The obtained delay time in this structure is equal to 0.06ps.

Low delay time at this gate will increase the data bit rate (BR). Therefore, this optical gate is suitable for use in small and integrated circuits with high speed.

Conclusion

In this paper, an all-optical NOR logic gate is designed and simulated using photonic crystals. The purpose of designing this structure is to use it in high speed optical integrated circuits. For this purpose, its size has been chosen as small as possible. The footprint of the designed NOR gate is $68\mu\text{m}^2$. In the design of this gate, simple linear and point defects have been used. The use of a small number of point defects has reduced the delay time of this gate. Another feature of this gate is that the optical power distance is relatively large for high and low logic values. Due to these features, this gate can be used in high-speed and low-error optical integrated circuits.

Author Contributions

F. Parandin designed, simulated, carried out the data analysis, collected the data and interpreted the results and wrote the manuscript.

Acknowledgment

This paper was written with the support of Kermanshah Branch, Islamic Azad University and a research project entitled "Increase of contrast ratio in photonic crystal based all optical logic gates".

Conflict of Interest

The author declares that there is no conflict of interests regarding the publication of this manuscript. In addition, the ethical issues, including plagiarism, informed consent, misconduct, data fabrication and/or falsification, double publication and/or submission, and redundancy have been completely observed by the authors.

References

- [1] Z. Kordrostami, S. hamed, F. Khalifeh, "Design of high frequency single and double gate laterally-contacted InGaAs/InAlAs HEMTs," *J. Electr. Comput. Eng. Innovations*, 2020, 7(2): 155-162, 2019.
- [2] D.J. Joannopoulos, G. Steven Johnson, N.J. Winn, R.D. Meade, "Photonic Crystals: Modeling the Flow of Light," second Ed., Princeton University Press, 2008.
- [3] Z. Hui, B.J. JUN, G. Peng, W.X. Hui, C.S. Jiang, "Design of tunable terahertz photonic crystal narrow-band filters," *Optoelectron. Lett.*, 5: 169-172, 2009.
- [4] E. Yablonovitch, "Photonic Crystals: Semiconductors of Light," *Science American*, 46-55, 2001.
- [5] D. Liu, Y. Gao, A. Tong, S. Hu, "Absolute photonic band gap in 2D honeycomb annular photonic crystals," *Phys. Lett. A*, 379: 214-217, 2015.
- [6] K.M. Leung, Y.F. Liu, "Photon band structures: the plane-wave method", *Phys. Rev. B Condens Matter*, 41(14): 10188-10190, 1990.
- [7] S. Olyae, M. Seifouri, A. Mohebzadeh-Bahabady, M. Sardari, "Realization of all-optical NOT and XOR logic gates based on interference effect with high contrast ratio and ultra-compact size," *Opt. Quant. Electron.*, 50: 385, 2018.
- [8] A. Rostami, H. Soofi, "Correspondence between effective mode area and dispersion variations in defected core photonic crystal fibers," *J. Lightwave Technol.*, 29(2): 234-241, 2011.
- [9] S. Olyae, F. Taghipour, "Design of new square-lattice photonic crystal fibers for optical communication applications," *Int. J. Physical Sci.*, 6(18): 4405-4411, 2011.
- [10] T. Sadeghi, S. Golmohammadi, A. Farmani, H. Baghban, "Improving the performance of nanostructure multifunctional graphene plasmonic logic gates utilizing coupled-mode theory," *Appl. Phys. B*, 125: 189, 2019.
- [11] A. Vahdati, F. Parandin, "Antenna patch design using a photonic crystal substrate at a frequency of 1.6 THz," *Wireless Pers. Commun.*, 109: 2213-2219, 2019.
- [12] M. Ghadrddan, M.A. Mansouri-Birjandi, "Low-threshold ultrafast all-optical switch implemented with metallic nanoshells in the photonic crystal ring resonator," *Superlattices Microstruct.*, 111: 789-795, 2017.
- [13] S. Olyae, A. Naraghi, V. Ahmadi, "High sensitivity evanescent-field gas sensor based on modified photonic crystal fiber for gas condensate and air pollution monitoring," *Optik*, 125(1): 596-600, 2014.
- [14] F. Parandin, M.M. Karkhanehchi, M. Naseri, A. Zahedi, "Design of a high bitrate optical decoder based on photonic crystals," *J. Comput. Electron.*, 17: 830-836, 2018.
- [15] M.M. Karkhanehchi, F. Parandin, A. Zahedi, "Design of an all optical half-adder based on 2D photonic crystals," *Photon. Netw. Commun.*, 33:159-165, 2017.
- [16] A. Farmani, A. Mir, M. Irannejad, "2D-FDTD simulation of ultra-compact multifunctional logic gates with nonlinear photonic crystal," *J. Opt. Soc. Am. B*, 36(4): 811-818, 2019.
- [17] F. Parandin, M.R. Malmir, M. Naseri, "All-optical half-subtractor with low-time delay based on two-dimensional photonic crystals," *Superlattices Microstruct.*, 113: 737-744, 2018.
- [18] M. Abdollahi, F. Parandin, "A novel structure for realization of an all-optical, one-bit half-adder based on 2D photonic crystals," *J. Comput. Electron.*, 18: 1416-1422, 2019.
- [19] M.H. Sani, A.A. Tabrizi, H. Saghaei, et al., "An ultrafast all-optical half adder using nonlinear ring resonators in photonic crystal microstructure," *Opt. Quant. Electron.*, 52: 107, 2020.
- [20] S. Serajmohammadi, H. Alipour-Banaei, F. Mehdizadeh, "All optical decoder switch based on photonic crystal ring resonators," *Opt. Quant. Electron.*, 47: 1109-1115, 2015.
- [21] F. Parandin, "High contrast ratio all-optical 4×2 encoder based on two-dimensional photonic crystals," *Opt. Laser Technol.*, 113: 447-452, 2019.
- [22] H. Saghaei, A. Zahedi, R. Karimzadeh, F. Parandin, "Line defects on As₂Se₃-Chalcogenide photonic crystals for the design of all-optical power splitters and digital logic gates," *Superlattices Microstruct.*, 110: 133-138, 2017.
- [23] A. Mohebzadeh-Bahabady, S. Olyae, "All-optical NOT and XOR logic gates using photonic crystal nano-resonator and based on an interference effect," *IET Optoelectron.*, 12(4): 191-195, 2018.
- [24] F. Parandin, M.R. Malmir, "Low delay time all optical NAND, XNOR and OR Logic gates based on 2D photonic crystal structure," *J. Electr. Comput. Eng. Innovations*, 8(1): 1-8, 2020.
- [25] M. Seifouri, S. Olyae, M. Sardari, A. Mohebzadeh-Bahabady, "Ultra-fast and compact all-optical half adder using 2D photonic crystals," *IET Optoelectron.*, 13(3): 139-143, 2019.
- [26] F. Parandin, M.R. Malmir, "Reconfigurable all optical half adder and optical XOR and AND logic gates based on 2D photonic crystals," *Opt. Quant. Electron.*, 52: 56, 2020.
- [27] Z. Mohebbi, N. Nozhat, F. Emami, "High contrast all-optical logic gates based on 2D nonlinear photonic crystal," *Opt. Commun.*, 355: 130-136, 2015.
- [28] H. Alipour-Banaei, S. Serajmohammadi, F. Mehdizadeh, "All optical NAND gate based on nonlinear photonic crystal ring resonators," *Optik*, 130: 1214-1221, 2017.
- [29] A. Salmanpour, S. Mohammadnejad, P. Taghinejad "All-optical photonic crystal NOT and OR logic gates using nonlinear Kerr effect and ring resonators," *Opt. Quant. Electron.*, 47: 3689-3703, 2015.
- [30] M. Pirzadi, A. Mir, D. Bodaghi, "Realization of ultra-accurate and compact all-optical photonic crystal OR logic gate," *IEEE Photonics Technol. Lett.*, 28(21): 2387-2390, 2016.
- [31] F. Parandin, M. Moayed, "Designing and simulation of 3-input majority gate based on two dimensional photonic crystals," *Optik*, 216: 164930, 2020.
- [32] J. Bao, J. Xiao, L. Fan, X. Li, Y. Hai, T. Zhang, C. Yang, "All-optical NOR and NAND gates based on photonic crystal ring resonator," *Optics Commun.*, 329: 109-112, 2014
- [33] M.H. Rezaei, R. Boroumandi, A. Zarifkar, A. Farmani, "Nano-scale multifunctional logic gate based on graphene/hexagonal boron

- nitride plasmonic waveguides," *IET Optoelectron.*, 14(1): 37-43, 2020.
- [34] K. Goudarzi, A. Mir, "All-Optical logic gates based on phase difference between beams in two-dimensional photonic crystal waveguides," *Majlesi J. Electr. Eng.*, 9: 37-41, 2015.
- [35] H. Alipour-Banaei, S. Serajmohammadi, F. Mehdizadeh, "All optical NOR and NAND gate based on nonlinear photonic crystal ring resonators," *Optik*, 125: 5701–5704, 2014.
- [36] F. Parandin, M.M. Karkhanechi, "Terahertz all-optical NOR and AND logic gates based on 2D photonic crystals," *Superlattices Microstruct.*, 101: 253–260, 2017.
- [37] P. Rani, S. Fatima, Y. Kalra, R.K. Sinha, "Realization of all optical logic gates using universal NAND gates on photonic crystal platform," *Superlattices Microstruct.*, 109: 619-625, 2017.
- [38] E. Shaik, N. Rangaswamy, "Realization of all-optical NAND and NOR logic functions with photonic crystal based NOT, OR and AND gates using De Morgan's theorem," *J. Opt.* 47: 8–21, 2018.
- [39] F. Parandin, M.R. Malmir, M. Naseri, A. Zahedi, "Reconfigurable all-optical NOT, XOR, and NOR logic gates based on two dimensional photonic crystals," *Superlattices Microstruct.*, 113: 737-744, 2018.
- [40] X.S. Christina, A.P. Kabilan, "Design of optical logic gates using self-collimated beams in 2D photonic crystal," *Photonic Sens.*, 2(2): 173–179, 2012.
- [41] K.E. Muthu, V.J.U. Firthouse, S.S. Deepa, A.S. Raja, S. Robinson, "Design and analysis of 3-Input NAND/NOR/XNOR gate based on 2D photonic crystals," *J. Opt. Commun.*, 2019.

Biographies



Fariborz Parandin received the B.Sc and M.Sc degrees in electrical engineering from the Razi University, Kermanshah, Iran in 2000 and 2002. He obtained his PhD degree in Optoelectronic from Razi University, Kermanshah, Iran in 2017. He is currently the assistant professor of electrical engineering at Islamic Azad University. His research interests include optoelectronics, semiconductor lasers, photonic crystals and photonic integrated circuits.

Copyrights

©2021 The author(s). This is an open access article distributed under the terms of the Creative Commons Attribution (CC BY 4.0), which permits unrestricted use, distribution, and reproduction in any medium, as long as the original authors and source are cited. No permission is required from the authors or the publishers.



How to cite this paper:

F. Parandin, "Realization of ultra-compact all-optical universal NOR gate on photonic crystal platform," *J. Electr. Comput. Eng. Innovations*, 9(2): 185-192, 2021.

DOI: [10.22061/JECEI.2021.7637.414](https://doi.org/10.22061/JECEI.2021.7637.414)

URL: https://jecei.sru.ac.ir/article_1531.html





Research paper

Real-time Lane Detection Based on Image Edge Feature and Hough Transform

A.A. Fallah*, A. Soleimani, H. Khosravi

Department of Electronics, Faculty of Electrical Engineering, Shahrood University of Technology, Shahrood, Iran.

Article Info

Article History:

Received 03 September 2020
Reviewed 18 November 2020
Revised 11 January 2021
Accepted 06 March 2021

Keywords:

Lane Detection
Real-time Processing
Region of Interest
Hough Transform
Edge Detection

*Corresponding Author's Email Address:

aliasghar.fallah@shahroodut.ac.ir

Abstract

Background and Objectives: Lane detection systems are an important part of safe and secure driving by alerting the driver in the event of deviations from the main lane. Lane detection can also save the lives of car occupants if they deviate from the road due to driver distraction.

Methods: In this paper, a real-time and illumination invariant lane detection method on high-speed video images is presented in three steps. In the first step, the necessary preprocessing including noise removal, image conversion from RGB colour to grey and the binarizing input image is done. Then, a polygon area as the region of interest is chosen in front of the vehicle to increase the processing speed. Finally, edges of the image in the region of interest are obtained with edge detection algorithm and then lanes on both sides of the vehicle are identified by using the Hough transform.

Results: The implementation of the proposed method was performed on the IROADS database. The proposed method works well under different daylight conditions, such as sunny, snowy or rainy days and inside the tunnels. Implementation results show that the proposed algorithm has an average processing time of 28 milliseconds per frame and detection accuracy of 96.78%.

Conclusion: In this paper a straightforward method to identify road lines using the edge feature is described on high-speed video images.

©2021 JECEI. All rights reserved.

Introduction

Due to the growing number of cars, there are many accidents in the world each year and lots of financial and human losses [1]. The main cause of many accidents is human errors such as fatigue, drowsiness, lack of concentration or unawareness of the road conditions [1]. In recent years, car companies have made efforts to add driver assistance systems to the car to help the driver control and steer the car [2]. Driver assistance systems are now increasingly being used as an option to provide greater security for luxury cars [3]. Road diversion warning systems, crash warning systems, lane detection systems for lane departure, intersection and traffic light

detection systems, and objects detection systems in front of the vehicle are some of the driver assistance system [4]-[6]. Among the driver assistance systems that have been proposed so far, the lane detection system is very important in preventing vehicle deviations and road accidents. Cars that have driver assistance systems are called smart cars [2]. The role of road line detection is significant in the field of intelligent vehicles and has many applications in unmanned vehicles [2]. Smart cars collect information from road lines and guide the car in between these lines [3].

Lane detection means locating the boundaries of the lines in an image of the road without prior knowledge of

the location of the road lines [2]. The lane detection system is designed for the quick response and timely warning to the driver in the event of a deviation from the main route, which allows better control over the vehicle. Lane detection system has been proposed as an important technology for safe driving. This system prevents the vehicle from deviating by correctly determining the position of the vehicle and moving between the road lines.

In lane detection systems, there are several ways to extract road lines. These include the installation of magnetic indicators on roads and the use of sensors, high-precision GPS and image processing [7]. The most accurate way to find road lines is to embed magnetic markers all over the road that can be detected by sensors on the car [7]. Another way to determine the current location of a vehicle is to determine the global difference in position relative to road lines [8], which is also relatively expensive. The most accessible and affordable way to identify road lines is image processing that uses a video camera to extract road lines from the image [8]. Since video images contain valuable information about the environment [9], they play an important role in lane detection. In lane detection systems, in-car cameras are used which are placed behind the windshield.

For example, the study by Bertozzi (1998) has applied the GOLD system which is one of the most popular lane detection systems based on road imaging by a camera installed in a car [10]. The detection of the route is based on the technique of matching the model that obtains the road lines. Furthermore, the location of the obstacles in front of the car is done based on the processing of stereo images. In this method, the perspective effect of the image is removed so that the pattern matching technique can be used [11]. Then, the parts of the straight lines of the image are extracted by searching for horizontal patterns of dark-light-dark lighting using a horizontal edge detector. Then parts that are close together or have the same direction are combined to eliminate the possibility of error by noise or blockage. Finally, the lines that match with a road model are selected [12].

A. Literature Review

This study has done a review of 9 papers conducted from 2015-2020. For the aim of this study, all reviewed studies have applied have Hough transform with more details in the following:

The study by Bhujbal and Narote (2015), uses Hough transform and Euclidean distance. First, the image is transferred from the RGB space to the YCbCr space. The Y component of the image is used to identify the lines since the human visual system is more sensitive to light. To improve the speed and accuracy of the system, the

lower part of the image is selected as the area of interest. Equalization of histograms is used in the area of interest to increase the contrast between the road surface and the road lines, and, a binary image is obtained by Otsu thresholding [13]. The area of interest is then divided into two sub-areas and for each sub-area, the Canny edge detection and the Hough transform algorithms are used to identify the left and right lines of the road separately [14].

In the study by Son, et.al. (2015), a method of detecting road lines is provided that is resistant to changes in lighting. In this method, first, the edges of the image are extracted using the Canny edge detection, the image lines are obtained using Hough transform, and the collision location of the identified lines is calculated. The centre of the district with the most votes is chosen as the vanishing point and the bottom area of the vanishing point in the image is selected as the region of interest. For the proposed algorithm to be resistant to changes in brightness, the yellow and white lines of the road are determined separately. Then, the binary image is created by determining the binary value 1 for the areas related to the road lines and the value 0 for the rest of the image areas. Then, the areas of the lines are marked and the centre of each area is calculated using the connected component clustering method in the binary image. The angle of each area and the point of contact with the y-axis are also calculated. Areas that have the same angle and intersection are combined to form an area, and the left and right lines of the road are determined in the image [15].

In the study by Duong, et.al. (2016), the input image is first taken out of perspective mode so that the road lines are parallel to each other [16]. The image obtained from the colour mode is then converted to grey, and the edges of the grey image are extracted using the edge recognition algorithm [17]. Small image noises are removed using the morphology expansion operator. Then, the road lines are identified using the Hough transform and compared with the previous image frame lines. If lines fit, they are preserved, otherwise, the next Hough transform lines are checked.

To simplify the process of recognizing lines, in the study by Lotfy, et. al. (2016) the road image in front of the car is obtained from the bird's eye view, which makes the road lines parallel. Two one-dimensional filters of Gaussian and Laplace are used to identify the edges of the image [18], and the binary image is obtained by using the Otsu threshold and calculated using the Hough transform of the image lines. Next, the main road lines are obtained using a series of horizontal lines and their points of contact with the image lines are identified with the help of the least mean square algorithm [19].

The study by Ozgunalp and Kaymak (2017) has presented a robust lane detection algorithm in Hough domain. The proposed algorithm uses road images to statistically estimate expected position and deviation on the road width. Furthermore, a mask is created in Hough domain to apply necessary restrictions to road width and vehicle position [20].

The study by Li, et. al. (2018) has proposed a new method for pre-processing and selecting the area of interest. In this method, the input frame is read first and then, the preprocessing process is performed on the input image, then the region of interest is selected, and the road lines are identified. In the pre-processing process, the image is first transferred to the HSV space and the white features of the image are extracted. Then, a Gaussian filter is used to reduce the noise effect and smooth the image. The image is then converted to binary by threshold processing. The bottom half of the image is then selected as the area of interest. The edges of the image are extracted using the edge detection algorithm, and the main lines of the road are identified using the Hough transform. Finally, the extended Kalman filter is used to detect and track road lines in real-time [21].

The study by Andrade, et. al. (2018) has presented a novel strategy for lane detection with good accuracy levels. The input image is reduced from three to one layer and the sharpness is improved. In this study, the region of interest is defined based on the minimum safe distance from the vehicle ahead. Hough Transform is used to achieve a smooth lane fitting [22].

In the study by Sun, et. al. (2019), a multi-stage Hough space calculation is proposed for a lane-detection task. An efficient Hough Transform was introduced to extract and classify line segments from images [23]. Kalman filtering was employed to smooth the probabilistic Hough space across frames to eliminate the disturbance from occlusion [24], movement of the vehicle, and classification error. The filtered probabilistic Hough space was used to remove line segments with low probability values (threshold was set as 0.7) and to keep those with high probability values [25].

The study by Marzougui, et. al. (2020) has defined a Region of Interest (ROI) [26] to ensure reliable real-time system. Hough Transform is defined to extract boundary information and to detect road lane markings edges. Otsu's threshold is used to enhance pre-processing results [27], to deal with lighting problems and to obtain gradients information. The proposed method ensures accurate lane tracking and collects valid information on vehicle orientation [28].

B. Aim and Objectives

There are several challenges in providing a suitable algorithm for detecting road lines including sunlight at

different times of the day, the shade of buildings, trees and cars, different weather conditions, the darkness of night, headlights at night, the light inside tunnels, faint lines, continuous and discrete lines and covering Lines by other cars. This study aims to develop an algorithm that detects road lines in real-time and with high speed. The developed algorithm is resistant to changes in lighting conditions during the day.

Methodology

This paper detects road lines in real-time using video images taken from the road by a camera installed inside the car. The camera is installed inside the car behind the windshield and almost in the middle to provide an image of the road. The proposed method for identifying road lines consists of three steps: the pre-processing, selection of the region of interest, and determination of road lines. The pre-processing stage includes noise removal, conversion of the image from RGB colour space to grey space and binarization of the input image. Then, a polygonal area is selected in front of the car as the area of interest as road lines are in a certain area in front of the car. In the third step, edges of the image in the area of interest are detected using Canny edge detection algorithm, and the main lines of the road are identified using the Hough transform. The flow chart of the algorithm is presented in Fig. 1.

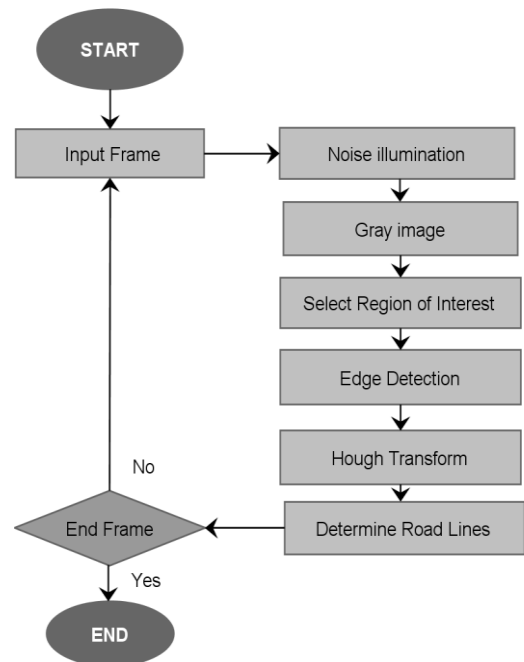


Fig. 1: Flowchart of the proposed method.

Preprocessing

At this stage, the images noise captured by the camera installed inside the car is removed using a

Gaussian filter [29] and the image becomes smoother. Figure 2 and Fig. 3 show input and output image after applying the Gaussian filter, respectively.



Fig. 2: An example of the input image.



Fig. 3: Input image after noise removal.

To reduce the algorithm calculations, the input image is converted from RGB colour space to grey space. Fig. 4 shows the input image in grey mode. Then, the input image is changed from grey space (Fig. 4) to binary image (Fig. 5) using the Otsu algorithm [30] to get the adaptive threshold.



Fig. 4: Input grey image.

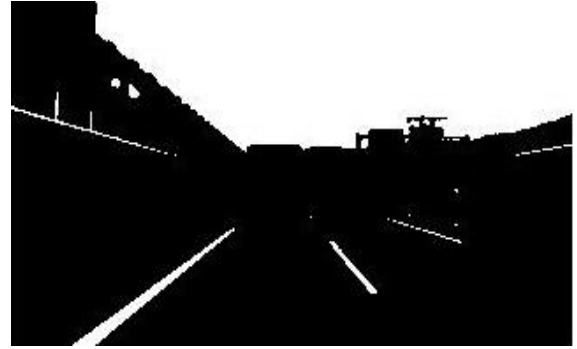


Fig. 5: Input binary image.

Selecting the Region of Interest

In the images obtained from the road surface, the road lines are in front of the car and on both sides. In this paper, a dynamic polygonal area of the image in front of the car is selected as the region of interest using a trapezoidal mask. In the design of the trapezoidal mask, the information of the vanishing point of the image is used. A trapezoid is created in the lower part of the vanishing point that covers the area in front of the car. Figure 6 shows a mask designed for the input image sample in which the part related to the area of interest is one and the rest of the image is zero. By applying this mask to the input binary image, the favourite area that includes the road lines in front of the car is selected.

Figure 7 shows the output binary image after applying the designed mask to the input binary image.

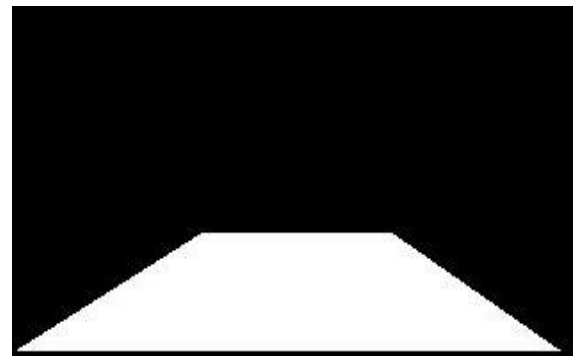


Fig. 6: Mask to determine the interest area.



Fig. 7: Binary image after applying a mask.

Determination of Road Lines

One of the most useful and effective features in identifying objects in images is the use of image edges. The edge of the image is the part where the brightness suddenly changes. Assuming that the amount of light intensity on the road is uniform and is different from the brightness of the lines, the boundary between the lines and the road (edge) can be found. There are many algorithms in this field, including Sobel, Canny, Roberts, and Prewitt [15]. This paper uses the Canny edge detection algorithm [31]. Identifying the edge in the Canny edge detection algorithm involves six steps. The first step is to filter the original image and remove the noise, for which a gaussian filter with a simple mask is used. The second step is to find strong edges using the gradient amplitude at any point. For this purpose, two masks are applied to the image, the gradient amplitude is calculated in the direction of x and y and the edge strength is calculated using (1).

$$|G| = |G_x| + |G_y| \quad (1)$$

where $|G|$ is the edge strength, $|G_x|$ is the gradient amplitude in the direction of x and $|G_y|$ is the gradient amplitude in the direction of y.

The Canny algorithm consists of two masks, one vertical and the other horizontal, as can be seen in Fig. 8.

| | | | | | |
|----|---|----|----|----|----|
| -1 | 0 | +1 | +1 | +2 | +1 |
| -2 | 0 | +2 | 0 | 0 | 0 |
| -1 | 0 | +1 | -1 | -2 | -1 |
| Gx | | | Gy | | |

Fig. 8: Canny algorithm masks.

The third step obtains the direction of the image edges obtained using Canny masks by (2).

$$\theta = \arctan\left(\frac{G_y}{G_x}\right) \quad (2)$$

Where θ is the direction of edge, G_x is the gradient in the direction of x and G_y is the gradient in the direction of y.

In the fourth step, the directions obtained in the previous step are matched to one of the four directions of 0, 45, 90 and 135 degrees. The fifth step is to suppress the non-maximum edges in which the direction is checked and the edges that cannot be detected are removed. In the sixth step, the hysteresis method is used in the Canny algorithm, for which two upper and lower threshold values are defined. Any pixel with a gradient greater than the lower threshold is accepted and with a

gradient lower than the lower threshold is rejected. By applying the Canny edge detection to the binary image, we get the edges of the image are obtained. Figure 9 shows the result of applying the edge finder algorithm to the previous step image.

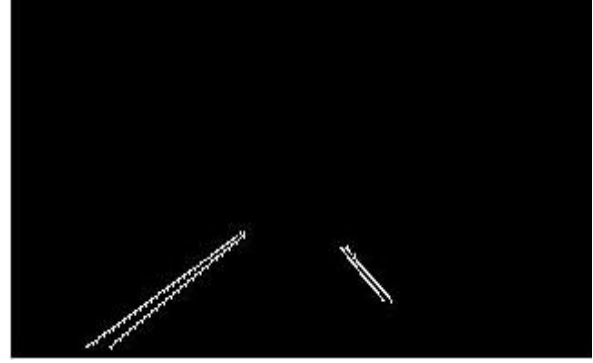


Fig. 9: Apply the Canny algorithm to the image.

In the following, the main lines of the road are identified by using the Hough transform. Hough transform is a feature extraction technique used in digital image processing, machine vision and image analysis [28]. The purpose of this conversion is to find different shapes in the image. Hough transform was initially used to identify image lines and it was used to identify various shapes such as circles and oval. In this algorithm, Hough transform is used to estimate the location of road lines and mark them. Then the closest lines to the car on both sides are considered as road lines on the left and right as shown in Fig. 10.



Fig. 10: Algorithm output image.

Results

The IROADS database [32] is used to evaluate the performance of the proposed algorithm. The database consists of 7 collections with a total of 4700 image strings. It covers almost all possible road conditions, including daylight, night darkness, excessive sunlight, tunnel light, day and night rainfall, and snowy roads. The dimension of each frame in this database is 360 * 640. Given that this paper examines the different lighting

conditions per day, four sets of data from the IROADS database, including daytime driving in sunny, rainy, snowy, and in-tunnel conditions, are reviewed.

Figure 11 shows the results of road line detection using the proposed algorithm in different driving conditions per day.

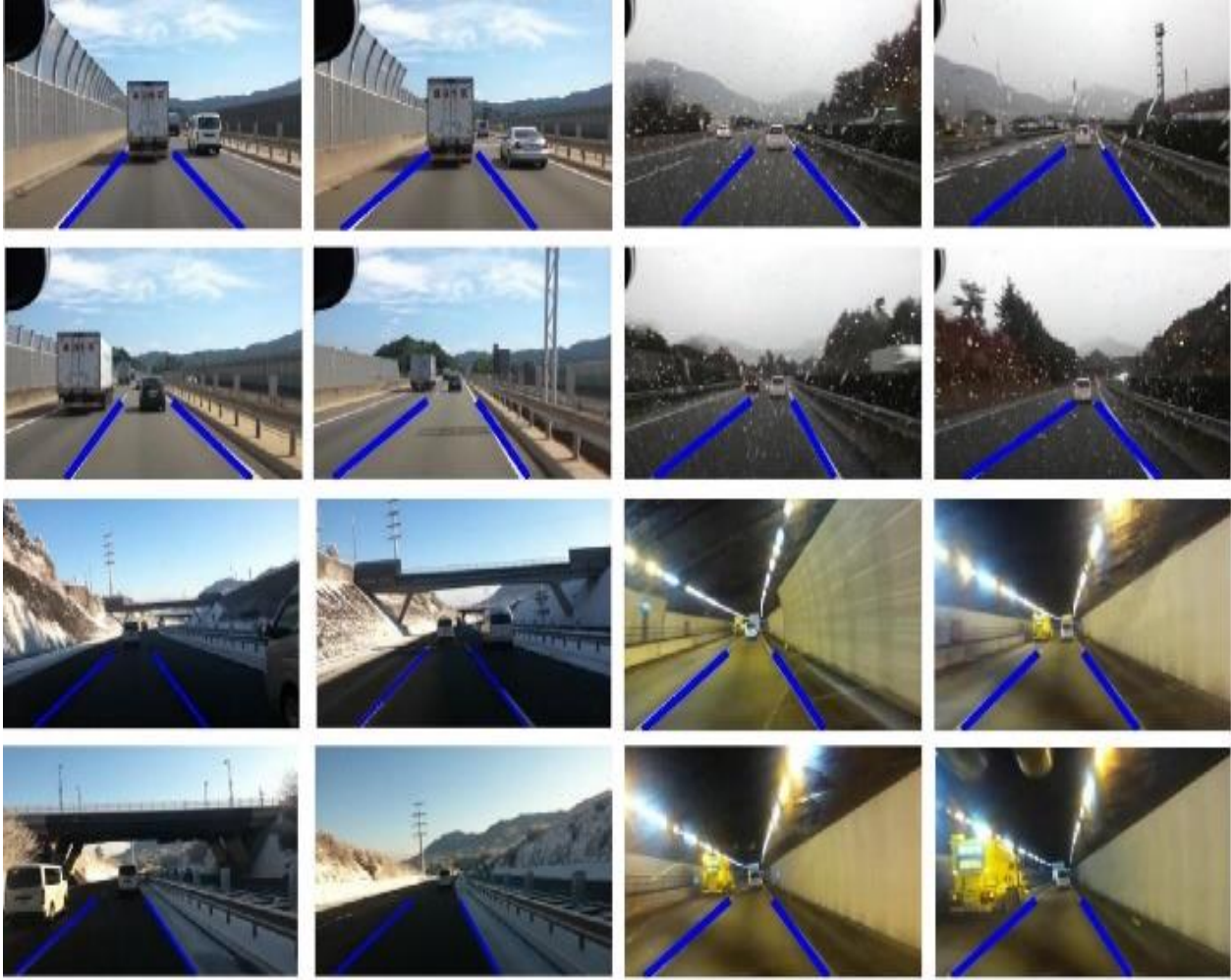


Fig. 11: Several results of the proposed algorithm.

The results of the proposed algorithm on each frame of the input image have the following two modes.

1) Correct detection, in which the lines on both sides of the car are identified correctly.

2) Incorrect detection, in which the lines on both sides or one side of the car are not correctly identified. The identification rate of the proposed algorithm is measured by the labels prepared earlier using (3).

$$DR = \frac{C}{T} \times 100 \quad (3)$$

Where DR is the detection rate (%), C is the number of correctly recognized frames and T is the total number of frames.

The average detection rate for 2828 frames of IROADS database in different daylight conditions is 96.78%, which is summarized in Table 1.

The proposed method is implemented by MATLAB software on laptop with 1/8 GHz CPU and 8 GB RAM and the average time required to process each frame is 28 milliseconds. Therefore, the proposed algorithm detects road lines in good time with high accuracy.

Discussion

To verify the performance of the lane detection algorithm, the proposed algorithm was compared with several algorithms mentioned in the literature.

Table 2 shows the comparison of results by Son's method [15], Cao's method [33], Hu's method [34] and the method applied in this study on the IROADS database [32].

According to the results of this experiment, the proposed method achieves better results in all categories except for in the Tunnel scenario. This is

mainly because the line indicators in this scenario are dimmed due to the lights inside the tunnel and are not recognized for the proposed method.

However, results can be improved if information from previous frames is used.

Table 1: Identification rate of the proposed algorithm under different conditions

| IROAD database | Total number of frames | Number of incorrect detection frames | Identification rate (Percentage) | Number of frames per second |
|-----------------|------------------------|--------------------------------------|----------------------------------|-----------------------------|
| IROAD Daylight | 903 | 32 | 96.45 | 35.2 |
| IROAD Rainy Day | 1049 | 7 | 99.33 | 35.6 |
| IROAD Snowy Day | 569 | 31 | 94.55 | 36.2 |
| IROAD Tunnel | 307 | 21 | 93.16 | 35.8 |
| Total | 2828 | 91 | 96.78 | 35.7 |

Table 2: Detection result comparison

| Methods | Evaluation Index | IROAD Daylight (903) | IROAD Rainy Day (1049) | IROAD Snowy Day (569) | IROAD Tunnel (307) | Total (2828) |
|--------------------------|-------------------------|----------------------|------------------------|-----------------------|--------------------|--------------|
| Son's Method [15] | Identification Rate (%) | 95.79 | 88.27 | 86.64 | 93.51 | 90.81 |
| Cao's Method [33] | Identification Rate (%) | 96.12 | 93.42 | 92.44 | 94.14 | 94.17 |
| Hu's Method [34] | Identification Rate (%) | 96.23 | 94.75 | 93.67 | 94.46 | 94.99 |
| The method in this Study | Identification Rate (%) | 96.45 | 99.33 | 94.55 | 93.16 | 96.78 |

The results show the effectiveness of the proposed algorithm in detecting lanes with varying conditions.

The proposed algorithm doesn't use tracking yet as detecting lanes is carried out in each image independently without using any temporal information.

Although the proposed algorithm for detecting road lines works correctly in 97% of the time, it can have errors in 3% of the cases, such as the fading of road lines, the coverage of road lines by the side car and car's direction change by the driver.

Figure 12 shows several frames in which the proposed algorithm has erroneous detection or non-detection of road lines.

The current algorithm works on the image edge property with acceptable results. Future studies by authors plan to use the color information to classify different lane boundaries (white solid lines, double yellow lines, etc.) and to employ tracking on top of the detection step which would help get rid of a lot of these false detections.



Fig. 12: False detections samples.

Conclusion

Lane detection means locating lane boundaries in a road image without prior knowledge of its location.

Lane detection system is designed to alert the driver in the event of deviations from the main lane, which enables better control of the vehicle on the road. In this paper, a straightforward method to identify road lines using the edge feature is described on high-speed video images.

In the proposed algorithm, first the necessary pre-processing, including noise removal, image conversion to the grey mode and then to binary mode, was performed.

Then, a polygonal area in front of the car was determined as the preferred area. Finally, road lines were identified using the Canny edge detection algorithm and Hough transform.

The IROADS database has been used to evaluate the performance of the proposed algorithm with the dimensions of each frame being 640*360.

In this paper, four datasets from IROADS database including daytime driving in sunny, rainy, snowy conditions and indoor tunnels are examined. The proposed algorithm has an average execution time of 28 milliseconds per frame and detection accuracy of 96.78%.

Author Contributions

A.A. Fallah and A. Soleimani proposed the main idea of the innovation of the paper and designed road map of the research. A. Soleimani and H. Khosravi verified the analytical methods. All authors discussed the results and contributed to the final manuscript.

Acknowledgment

The authors thank the anonymous reviewers and the editor of JECEI for their useful comments and suggestions.

Conflict of Interest

The authors declare no potential conflict of interest regarding the publication of this work. In addition, the ethical issues including plagiarism, informed consent, misconduct, data fabrication and, or falsification, double publication and, or submission, and redundancy have been completely witnessed by the authors.

Abbreviations

| | |
|-----|---------------------------|
| GPS | Global Positioning System |
| ROI | Region Of Interest |
| DR | Detection Rate |

References

- [1] J. R. Mani, N.D. Gangadhar, V.K. Reddy, "A real-time video processing based driver assist system," *SASTech*, 9: 9-16, 2010.
- [2] F. You, R. Zhang, L. Zhong, H. Wang, J. Xu, "Lane detection algorithm for night-time digital image based on distribution feature of boundary pixels," *J. Opt. Soc. Korea*, 17: 188-199, 2013.
- [3] A. Saha, D.D. Roy, T. Alam, K. Deb, "Automated road lane detection for intelligent vehicles," *Global J. Comput. Sci. Tech.*, 12(6): 1-6, 2012.
- [4] M. Rashid, M.A. Khan, M. Alhaisoni, S.H. Wang, S.R. Naqvi, A. Rehman, T. Saba, "A sustainable deep learning framework for object recognition using multi-layers deep features fusion and selection," *Sustainability*, 12(12): 5037, 2020.
- [5] N. Hussain, M.A. Khan, M. Sharif, S.A. Khan, A.A. Albeshier, T. Saba, A. Armaghan, "A deep neural network and classical features based scheme for objects recognition: an application for machine inspection," *Multimed. Tool. Appl.*, 2020.

- [6] M. Rashid, M.A. Khan, M. Sharif, M. Raza, M.M. Sarfraz, F. Afza, "Object detection and classification: a joint selection and fusion strategy of deep convolutional neural network and SIFT point features," *Multimed. Tool. Appl.*, 78: 15751–15777, 2019.
- [7] A.D. Forrest, M. Konca, "Autonomous Cars & Society," Worcester Polytechnic Institute, 2007.
- [8] K.H. Lee, J.H. Bak, C.H. Lee, "Study on active steering control of vehicle for safe driving in highway with GPS information," in *Proc. IEEE Intelligent Vehicles Symposium*: 554-557, 2012.
- [9] M.A. Khan, K. Javed, S.A. Khan, T. Saba, U. Habib, J.A. Khan, A.A. Abbasi, "Human action recognition using fusion of multiview and deep features: an application to video surveillance," *Multimed. Tool. Appl.*, 2020.
- [10] M. Bertozzi, A. Broggi, "GOLD: A parallel real-time stereo vision system for generic obstacle and lane detection," *IEEE Trans. Image Process.*, 7: 62-81, 1998.
- [11] H. Arshad, M.A. Khan, M.I. Sharif, M. Yasmin, J.M.R. Tavares, Y.D. Zhang, S.C. Satapathy, "A multilevel paradigm for deep convolutional neural network features selection with an application to human gait recognition," *Expert Syst.*, 2020.
- [12] M. Bertozzi, A. Broggi, "Vision-based vehicle guidance," *Computer*, 30: 49-55, 1997.
- [13] N. Naheed, M. Shaheen, S.A. Khan, M. Alawairdhi, M.A. Khan, "Importance of features selection, attributes selection, challenges and future directions for medical imaging data: a review," *CMES-Comp. Model. Eng. Sci. CMES*, 125: 314-344, 2020.
- [14] P.N. Bhujbal, S.P. Narote, "Lane departure warning system based on Hough transform and Euclidean distance," in *Proc. 2015 Third International Conference on Image Information Processing (ICIIP)*: 370-373, 2015.
- [15] J. Son, H. Yoo, S. Kim, K. Sohn, "Real-time illumination invariant lane detection for lane departure warning system," *Expert Syst. Appl.*, 42: 1816-1824, 2015.
- [16] T.T. Duong, C.C. Pham, T.H. P. Tran, T.P. Nguyen, J.W. Jeon, "Near real-time ego-lane detection in highway and urban streets," in *Proc. 2016 IEEE International Conference on Consumer Electronics-Asia (ICCE-Asia)*: 1-4, 2016.
- [17] R. Jiang, M. Terauchi, R. Klette, S. Wang, T. Vaudrey, "Low-level image processing for lane detection and tracking," in *Proc. International Conference on Arts and Technology*: 190-197, 2009.
- [18] A. Mehmood, M.A. Khan, M. Sharif, S.A. Khan, M. Shaheen, T. Saba, N. Riaz, I. Ashraf, "Prosperous human gait recognition: An end-to-end system based on pre-trained CNN features selection," *Multimed. Tool. Appl.*, 2020.
- [19] O.G. Lotfy, A.A. Kassem, E.M. Nassief, H.A. Ali, M.R. Ayoub, M.A. El-Moursy, M.M. Farag, "Lane departure warning tracking system based on score mechanism," in *Proc. IEEE 59th International Midwest Symposium on Circuits and Systems (MWSCAS)*: pp. 1-4, 2016.
- [20] U. Ozgunalp, S. Kaymak, "Lane detection by estimating and using restricted search space in Hough domain," *Procedia Comput. Sci.* 120: 148-155., 2017.
- [21] M. Li, Y. Li, M. Jiang, "Lane detection based on connection of various feature extraction methods," *Adv. Multimedia*, 2018: 1-14, 2018.
- [22] D.C. Andrade, F. Bueno, F.R. Franco, R.A. Silva, J.H.Z. Neme, E. Margraf, W.T. Omoto, F.A. Farinelli, A.M. Tusset, S. Okida, M.M.D. Santos, "A novel strategy for road lane detection and tracking based on a vehicle's forward monocular camera," *IEEE Trans. Intell. Transp. Syst.*, 20: 1497-1507, 2018.
- [23] M. Fakhredanesh, S. Roostaie, "Action change detection in video based on HOG," *J. Electr. Comput. Eng. Innovations (JECEI)*, 8(1): 135-144, 2020.
- [24] M.A. Khan, Y.D. Zhang, S.A. Khan, M. Attique, A. Rehman, S. Seo, "A resource conscious human action recognition framework using 26-layered deep convolutional neural network," *Multimed. Tool. Appl.*, 2020.
- [25] Y. Sun, J. Li, Z. Sun, "Multi-stage hough space calculation for lane markings detection via IMU and vision fusion," *Sensors*, 19(10): 1-14, 2019.
- [26] M. Taheri, M. Rastgarpour, A. Koochari, "A novel method for medical image segmentation based on convolutional neural networks with SGD optimization," *J. Electr. Comput. Eng. Innovations (JECEI)*, 9(1): 37-46, 2021.
- [27] H. Arshad, M.A. Khan, M. Sharif, M. Yasmin, M.Y. Javed, "Multi-level features fusion and selection for human gait recognition: an optimized framework of Bayesian model and binomial distribution," *Int. J. Mach. Learn. Cybern.*, 10: 3601–3618, 2019.
- [28] M. Marzougui, A. Alasiry, Y. Kortli, J. Baili, "A lane tracking method based on progressive probabilistic hough transform," *IEEE Access*, 8: 84893-84905, 2020.
- [29] H. Xu, H. Li, "Study on a robust approach of lane departure warning algorithm," presented at the 2nd International Conference on Signal Processing Systems, Dalian, China, 2010.
- [30] N. Otsu, "A threshold selection method from gray-level histograms," *IEEE Trans. Syst. Man Cybern.: Syst.*, 9: 62-66., 1979.
- [31] W. Rong, Z. Li, W. Zhang, L. Sun, "An improved CANNY edge detection algorithm," in *Proc. 2014 IEEE International Conference on Mechatronics and Automation*: 577-582, 2014.
- [32] M. Rezaei, M. Terauchi, "Vehicle detection based on multi-feature clues and Dempster-Shafer fusion theory," in *Proc. 2013 Pacific-Rim Symposium on Image and Video Technology*: 60-72, 2013.
- [33] J. Cao, C. Song, S. Song, F. Xiao, S. Peng, "Lane detection algorithm for intelligent vehicles in complex road conditions and dynamic environments," *Sensors*, 19(14): 1-21, 2019.
- [34] J. Hu, S. Xiong, Y. Sun, J. Zha, C. Fu, "Research on Lane Detection Based on Global Search of Dynamic Region of Interest (DROI)," *Appl. Sci.*, 10(7): 1-22, 2020.

Biographies



Ali Asghar Fallah received his M.Sc. in electrical-electronic engineering in 2008 from Shahroud University of Technology. He is currently a Ph.D. student in electrical-electronic engineering at Shahroud University of Technology. His research interests include signal processing, image processing and pattern recognition.



Ali Soleimani received his M.Sc. and Ph.D. in electrical-electronic engineering in 1994 and 2000 from Iran University of Science and Technology. He completed his master's project in signal processing with fuzzy logic and his doctoral project in controlling multi-output multi-input systems using fuzzy neural networks. He has been a member of the faculty of Shahroud University of Technology since 2001. His research interests include digital signal processing, fuzzy neural networks and evolutionary algorithms.



Hossein Khosravi received his B.Sc. in electronics from Sharif University of Technology in 2003. In 2005, he graduated from Tarbiat Modares University with a M.Sc. in system electronics, and in 2008, he received a Ph.D. in electronics from the same university. He has been a member of the faculty of Shahrood University of Technology since 2009 and the

CEO of Shahab Company (active in the field of image processing) since 2015. His research interests include image processing, machine vision, pattern recognition and Persian OCR.

Copyrights

©2021 The author(s). This is an open access article distributed under the terms of the Creative Commons Attribution (CC BY 4.0), which permits unrestricted use, distribution, and reproduction in any medium, as long as the original authors and source are cited. No permission is required from the authors or the publishers.



How to cite this paper:

A.A. Fallah, A. Soleimani, H. Khosravi, "Real-time lane detection based on image edge feature and hough transform," J. Electr. Comput. Eng. Innovations, 9(2): 193-202, 2021.

DOI: [10.22061/JECEI.2021.7659.418](https://doi.org/10.22061/JECEI.2021.7659.418)

URL: https://jecei.sru.ac.ir/article_1543.html





Research paper

A Variational Level Set Approach to Multiphase Multi-Object Tracking in Camera Network Base on Deep Features

E. Pazouki^{1,*}, M. Rahmati²

¹Artificial Intelligence Department, Faculty of Computer Engineering, Shahid Rajaei Teacher Training University, Tehran, Iran.

²Artificial Intelligent and Robotics Department, Faculty of Computer and Information Technology Engineering, Amirkabir University of Technology, Tehran, Iran.

Article Info

Article History:

Received 02 September 2020

Reviewed 15 December 2020

Revised 25 January 2021

Accepted 01 March 2021

Keywords:

Multi-object tracking

Camera network tracking

MultiPhase level set representation

Variational tracking

Deep features

*Corresponding Author's Email Address:

ehsan.pazouki@sru.ac.ir

Abstract

Background and Objectives: Object tracking in video streams is one of the issues in machine vision that has many applications. Depending on the type of the object, the number of objects and other inputs used in tracking, object tracking is divided into several different categories. Multi-object tracking in a camera network is one of the most complex types of object tracking. In this type of tracking, the goal of the algorithm is to extract the persistent trace of several objects moving simultaneously in a wide area that is monitored by a network of cameras. This type of tracking is often done in two steps. In the first step, the traces of each object in each camera is called tracklets are extracted. Then, the persistent trace of the objects are obtained by associating the extracted tracklets of all cameras in the monitored wide area. Here, we introduce a novel variational approach based on the deep features to associate the tracklets.

Methods: For this purpose a variational model with multiphase level set representation is introduced. The persistent trace of all objects are obtained by optimizing the proposed variational model. The proposed variational model is optimized by employing the Euler-Lagrange equation. CNN and deep learning are used to extract the deep features of appearance and motion of objects. Here, a ResNet50 network that is pre-trained on ImageNet and a transformer neural network which is trained with motion parameters of tracklets such as acceleration and orientation change rate are used for extracting deep features.

Results: The multiphase model using deep features presented in this paper provide 9% better results than the multiphase model without deep features based on TCF and FS metrics and 8% better results based on MT metric.

Conclusion: The results on the three well-known datasets which are real and a synthesized dataset show that the proposed model takes competitive performance, while using less extra context information of the camera network and objects, compared to the other proposed methods. The evaluations show the quality of the proposed model in solving complex problems using the minimum required initial knowledge.

©2021 JECEI. All rights reserved.

Introduction

Object tracking in wide areas which is monitored by a

network of cameras is one of the most challenging issues in the machine vision. The tracking module extract

trajectories of objects presented and which are viewed by a camera network covering the area. The high level analysis is performed on the extracted trajectories and appropriate alarms are set. Multi-object tracking in a camera network is performed in two steps [1]. In the first step, moving objects are captured by all of the cameras within the view of camera network and are tracked by a tracking algorithms. Extensive research has been reported to deal with single camera tracking [2], [3]. There are various challenges exist for extracting accurate trace of objects in each camera, among them pose and illumination variations, occlusion, clutter and sensor noise are more common. Advancement of algorithms to resolve object tracking in a single camera have reached to a satisfactory extent [4], [5]. In this paper, the admissible trace of the objects in a single camera using the existing algorithms are extracted and are called tracklets. In the second step of multi-object tracking of a camera network, the extracted tracklets are associated to the corresponding objects and the persistent trace of objects are extracted. Usually, the association is performed based on the appearance of objects and motion models of the objects which are extracted from the tracklets. The solution space of the association task grows exponentially with the number of the tracklets [6]. Our proposed method provides a remedy for this problem. This problem is an ill-posed inverse problem [7]. The tracklets are the observation and are assumed to be known and the persistent trace is the ideal output and unknown. The variational model is an effective solution for solving the ill-posed inverse problem [8]. This model solves the ill-posed inverse problem in the image processing and computer vision [9], [10], [11] and [12]. In this paper, our main objective is to propose a variational multiphase model for solving the association problem.

Previous attempts on associating tracklets with corresponding objects place different restricted assumptions on the problem, thus deviating their application from real world problem [1]. In [13], [14] and [15], first order Markovian model is used for association. Using Markovian model for tracking objects in a single camera is a reasonable assumption but in a non-overlapped camera network is not a good choice where this assumption increases the probability of a wrong association. In some previous researches [14] and [16], the topology of cameras and the moving model of the objects are assumed to be known, while it is difficult to extract. Also, modeling the moving pattern and updating the changes are challenging.

Multi-object tracking in a camera networks is important issue. Associating of corresponding objects between different cameras distinguishes single camera and multi-camera tracking. Thus, the main challenge of

the proposed model for tracking multi-object in camera networks is the association [1]. In some studies [17], [13], [16], [14], [18], and [6], the main goal is to associate the traces of objects and extract their persistent trace. In these researches, various tools and algorithms are used, including a planar tracking correspondence model (TCM), a Bayesian modeling, Parzen windows, the path coverage of a directed graph, a multi-objective optimization framework, a path smoothness, a statistical model function, a graphical representation and a network flow algorithm for modeling and association. In [19], an approach to improve the detection and tracking performance in multi-camera scenarios with overlapping field-of-views is provided, which allows for better handling of occlusion problem. It mainly includes monocular people detection, projection, fusion, probabilistic occupancy map generation and multi-object tracking steps. The objective of the study is to detect and track individuals within a designated open area where multiple cameras are set up, implement a robust multi-camera people detection and tracking method and improve the experimental performance.

With the introduction of deep learning [20] methods and the development of its applications in various issues, the use of models based on deep learning in objects tracking was also introduced in different methods. In some methods, the features of deep neural networks are used as visual or temporal features of objects [21] and [22]. For example in [21] the 2048-dim fully connected layer of ResNet50 [23] before the classification layer is used to represent the appearance of the objects. In some methods, models based on convolutional neural network (CNN) and deep learning are used to extract tracklets or persistent trace of the objects [22], [24], [25] and [26]. In [22], a CNN-based model called TrackletNet is introduced that uses the a graph to extract the trace of objects. In [24] a Long Short-Term Memory (LSTM) is used for tracking object. In [25] is provided a model based on Recurrent Neural Network(RNN) that models the changes made in the object by updating the features of the tracking object and performs better tracking of the object. In [26] a CNN-based model called Siam R-CNN is proposed which combine a Siamese re-detection architecture with a tracklet-based dynamic programming algorithm. In [27] a tracklet processing algorithm cleave and re-connect tracklets on crowd or long term occlusion which uses Siamese Bi-Gated Recurrent Unit (GRU). In this study, the tracklet is generated using deep features which are extracted by CNN and RNN to create the high-confidence tracklet candidates in sparse scenario. This proposed neural network model is trained using a dataset which contains more than 95160 pedestrian images. In [28] a multi-object tracking framework called DROP (Deep Re-identification Occlusion Processing) is

proposed. A lightweight convolutional neural network that can solve the re-tracking problem is constructed by increasing and learning the affinity of appearance features of the same object in different frames. In this study the occlusion of the object is judged using the data association result of the appearance features of the object, and to reduce the matching error by improving the data association formula.

In some studies, the main objective is to introduce compositional features that are more effective in recognizing objects. In [29] a procedure is introduced which, using the classic features PHOG and CS-LBP and combining them with deep features and also using a new feature selection tools such as JEKNN, proposes an efficient combined features for classifying objects. This combined feature is able to significantly improve results relative to similar models. In [30] deep features are combined with multiview features and a set of features is obtained for recognizing human behavior, which has good results compared to similar models. In order to model the objects with the aim of properly classifying them in [31], the combination of deep features, Very Deep Convolutional Networks for Large-Scale Image Recognition and Inception V3, are used. The obtained combined features are able to provide good sustainable recognition rate in object classification. Also in [32], by combining the deep features obtained from the two deep networks, VGG and AlexNet, with SIFT which is the classical feature for object detection, a combined feature has been created with the help of Reyni entropy-controlled method, which provides good results in classifying objects.

The combined features, some of which were reviewed in the above studies, are not practical in object tracking applications due to the considerable computational complexity involved in extracting them, as in object tracking the features of all objects in the image must be calculated for each frame. If they are used, the response time of the tracking algorithm will be significantly increased, which is not tolerable and acceptable in many real problems.

Another method of tracking objects is to use variational model, examples of which are presented in [33] and [34].

In [33] a variational model called single phase variational is introduced which is tracked the multi-objects in multi-camera network of wide area surveillance system. In [34] a novel variational model called multi phase variational model is proposed which is used the RGB color histogram as appearance model of the objects and the acceleration and orientation change rate as the motion model of the objects.

In this paper, we proposed a novel deep variational method for associating the tracklets. In this method,

persistent trace of each object is represented as a multiphase level set function. By solving this association problem with less restrictive assumption, the optimum solution is reachable and the method is more general and usable in realistic scenarios. CNN and deep learning are used to extract the features of appearance and motion of objects.

In this paper, we propose a multiphase variational model for associating tracklets based on deep features. The proposed model is a variational optimization model that is converted to an Ordinary Differential Equation (ODE) which is solved numerically for extracting the persistent trace of objects.

The structure of the paper is as follows. In Section Variational Model the proposed variational model and solving method are presented. The experimental results of the proposed model on the real and synthesized datasets is given in Section Experimental Results and finally, the conclusions is presented in Section Conclusion.

Variational Model

In this section, the proposed variational model and solving method are presented.

A. Problem Formulation

The main goal is to extract the persistent trace of the objects in a camera network which monitors the wide area. The wide area is monitored with k cameras C_1, \dots, C_k . Each image captured by a camera is mapped to the world plane using calibration parameters of the cameras C_{M_1}, \dots, C_{M_k} . Unknown n number of objects P_1, \dots, P_n moves in a wide area which is monitored by a network of cameras.

Any object denoted by P_t that is moving in the area which is covered by each camera in $[t_s, t_e]$ period is tracked by its corresponding single-camera tracking algorithm [2] and [4]. Therefore, for each camera C_i of the camera network, a set of the tracks is called tracklets T_{O_i} is exploited. So, the set of all tracklets of all cameras $T_C = \{T_{O_1}, \dots, T_{O_K}\}$ is obtained. For generating persistent track of the objects R_P , the obtained tracklets T_C are associated and the tracklets of each object in T_C are corresponded and persistent trace of this object is extracted and is denoted as r_{p_x} . By associating the tracklets of objects, the persistent trace of all objects $R_P = \{r_{p_1}, \dots, r_{p_n}\}$ is obtained. Therefore, the problem is represented as,

$$R_P = \text{Tracker}(T_C, \{C_{M_1}, \dots, C_{M_k}\}) \quad (1)$$

which it means the proposed $\text{Tracker}(\cdot)$ algorithm computes the persistent trace of objects as R_P using the extracted tracklets T_C and camera calibration parameters $\{C_{M_1}, \dots, C_{M_k}\}$. In our proposed method, this problem is modeled with a variational optimization

model as follow,

$$J[R_P] = \int_{r_{p_\tau} \in R_P} \left(\lambda_1 \times \int_{T_l \in T_C} CLS_{r_{p_\tau}}(T_l) dl \right. \\ \left. + \lambda_2 \times \int_{T_l \in r_{p_\tau}} SM_{r_{p_\tau}}(T_l) d\tau \right) d\tau \quad (2)$$

where $CLS_{r_{p_\tau}}(\cdot)$ is *closeness* part of the variational model, $SM_{r_{p_\tau}}(\cdot)$ is *smoothness* part of the model and $\lambda_1 > 0$ and $\lambda_2 > 0$ are positive constants. The closeness control similarity between tracklets and the smoothness control variations between tracklets.

In this paper, the closeness and smoothness parts which are proposed in [34] are used. The appearance model which is used in this paper is the 2048-dim fullyconnected layer before the classification layer of a ResNet50 [23] network that pre-trained on ImageNet to represent appearance of the objects. A transformer neural network [35] which is trained with motion parameters of tracklets such as acceleration and orientation change rate is used as a motion model of objects.

The transformer model which is used in this research is the same as the proposed model in [35] and is used with the same parameters and settings. In this research, two transformer models have been used, one to estimate the change rate of the angle of the object and the other to estimate the change rate of the acceleration of the object. To train both models, all tracklets which are the inputs of the tracking problem are used as the training set.

Also the parameters and algorithms which are used for training are the same as [35]. The angle change rate and acceleration change rate of the tracklets with a frequency of 1 Hz for each tracklets is calculated in the form of an array as a time series, and the time series which are created are used to train two transformer models.

When calculating the closeness and smoothness of the variational model, the angle change rate and acceleration change rate are estimated based on the association of tracklets for blind areas between two adjacent tracklets and then used in calculations.

In brief, the proposed model is a variational energy function declared as (2) which the extracted *tracklets* T_C are its inputs and the persistent traces of the objects R_P are their outputs.

In order to use this proposed model, an appropriate representation of the variational energy function must be employed. We propose a multiphase level set representation to solve the optimization model.

B. Multi Phase Level Set Representation

Proposing the level set representation of the model starts with representing persistent trace of the objects

as,

$$\begin{cases} T_l \in r_{p_x} & \text{if } \varphi_x(l) \geq 0 \\ T_l \notin r_{p_x} & \text{if } \varphi_x(l) < 0 \end{cases} \quad (3)$$

where persistent trace of each object r_{p_x} is presented as a level set function φ_x and persistent trace of all tracked objects are presented as $\phi = \{\varphi_1, \dots, \varphi_b\}$ which is a multiphase level set function. As stated in previous section the number of the objects which move in the wide area n is unknown and the number of tracked objects b is not necessarily equal to n . Now, the (2) can be rewritten as,

$$J[\phi] = \int_{\tau=1}^{|\phi|} \left(\lambda_1 \times \int_{l=1}^{|T_C|} CLS_{\varphi_\tau}(l) dl \right. \\ \left. + \lambda_2 \times \int_{l=1}^{|T_C|} SM_{\varphi_\tau}(l) \times H(\varphi_\tau(l)) d\tau \right) d\tau \quad (4)$$

where $H(\varphi_\tau(\cdot))$ is the Heaviside function and is defined as,

$$H(Z) = \begin{cases} 1 & Z \geq 0 \\ 0 & Z < 0 \end{cases} \quad (5)$$

The closeness and smoothness equations are redefined based on the level set representation, and are provided in [34].

C. Optimizing the Energy Function

In order to solve the persistent trace problem, the presented level set representation model must be optimized.

For optimizing this model, the Euler-Lagrange equation is used [36]. It must be noted that the regularized versions of the function $H(z)$, denoted here by $H_\epsilon(z)$, is used. The regularized version of (4) is defined as,

$$J_\epsilon[\phi] = \int_{\tau=1}^{|\phi|} \left(\lambda_1 \times \int_{l=1}^{|T_C|} CLS_{\varphi_\tau, \epsilon}(l) dl \right. \\ \left. + \lambda_2 \times \int_{l=1}^{|T_C|} SM_{\varphi_\tau, \epsilon}(l) \times H_\epsilon(\varphi_\tau(l)) d\tau \right) d\tau \quad (6)$$

where regularized version of the closeness and smoothness part of the model are redefined in [34].

In this paper, the regularized version of $H(z)$ which is proposed in [37] is used. this function is defined as,

$$H_\epsilon(z) = \frac{1}{2} \left(1 + \frac{2}{\pi} \arctan \left(\frac{z}{\epsilon} \right) \right) \quad (7)$$

The persistent trace of the objects is obtained by solving following optimization problem,

$$\phi^* = \underset{\phi}{\operatorname{argmin}} J_\epsilon[\phi]. \quad (8)$$

This optimization problem is solved by fixing, $F_{A, \epsilon}$, $F_{M, \epsilon}$, $\operatorname{Mean} F_{A, \epsilon}$ and $\operatorname{Mean} F_{M, \epsilon}$ then $J_\epsilon[\phi]$ is minimized with respect to ϕ using Euler-Lagrange equation [7]. The descent direction is parameterized by an artificial time

$t > 0$. Then, the equation $\varphi_\tau(t, l)$ is optimized. The numerical procedure required to solve (8) is presented in [34].

Experimental Results

The performance of our proposed model is evaluated by performing several experiments using three challenging real datasets and one synthesized complex dataset.

The quality of the results of our experiments are determined based on well-known metrics used in camera network applications. The datasets and the metrics that are used are introduced in the following subsections.

A. Datasets

In this paper four challenging datasets are used. Three of them are real video sequences and another is synthesized data which is developed in our Lab.

First, the CAVIAR dataset [38] and [39] is collected in a shopping mall corridor with two cameras.

Second, the NGSIM dataset [40] is captured from Peachtree street located in Atlanta, Georgia by using eight synchronized cameras.

Third, the PETS2009 dataset [41] was collected through 8 cameras which are set up to monitor a road corner of a university campus. But, in this paper only four cameras are used.

In order to generate thorough annotated dataset according to every complicated surveillance scenario based on the given information a tool has been developed [42] for syntesing virtual data.

Here, a synthesized dataset with 6 cameras and 10 objects is used as forth experimental dataset.

The characteristics of these dataset are presented in Table 1.

The datasets' details and the way they are used in this paper are consistent with the experiments performed in [34]. In order to show the status of the datasets, their figures are provided follow.

In Fig. 1 the sample image of one camera of the CAVIAR is presented and some samples of objects in different pose of this dataset are shown in Fig. 2.

In Fig. 3 five sample image of five different cameras of the NGSIM dataset are shown.

In Fig. 4 the sample images of two cars for 3 different pose are presented.

In Fig. 5 the sample images of the four different cameras of PETS2009 dataset are shown and the images of two different objects from different poses are shown in Fig. 6.

In Fig. 7 the world plane image of a wide area covered by 6 cameras from the simulator is presented.

In Fig. 8 some sample images of the objects from simulator are shown.



Fig. 1: A sample image from one of the cameras related to the CAVIAR dataset.

B. Evaluation Metrics

For evaluating the proposed model quantitatively, 10 well known metrics which are commonly used in scope of the proposed model are selected and the quality of the proposed model is measured using these metrics. The nomenclature and some information about these metrics are given in Table 2. Also, details of these metrics are provided in [34].



Fig. 2: Different pose of persons in the CAVIAR: a) First person (First Pose); b) First person (Second Pose); c) First person (Third Pose); d) Second person (First Pose); e) Second person (Second Pose); f) Second person (Third Pose).

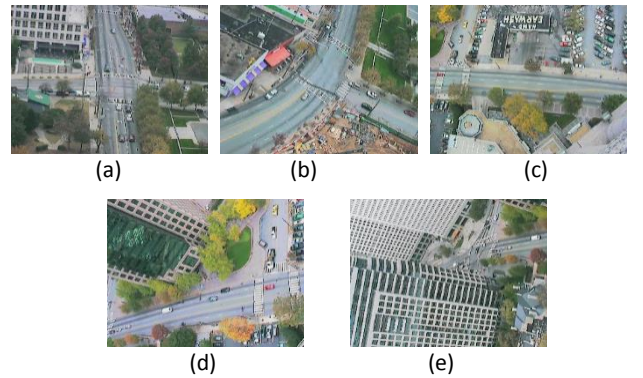


Fig. 3: The sample image of five cameras of the NGSIM; a) First camera; b) Second camera; c) Third camera; d) Fourth camera; e) Fifth camera.

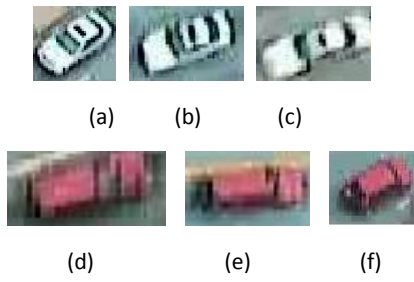


Fig. 4: Different pose of cars in the NGSIM: a) First car (First Pose); b) First car (Second Pose); c) First car (Third Pose); d) Second car (First Pose); e) Second car (Second Pose); f) Second car (Third Pose).

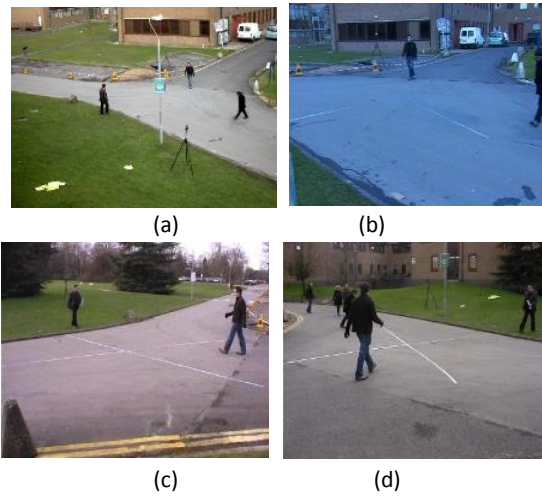


Fig. 5: The sample image of four cameras of the PETS2009; a) First camera; b) Second camera; c) Third camera; d) Fourth camera.



Fig. 6: Different pose of persons in the PETS2009: a) First person (First Pose); b) First person (Second Pose); c) First person (Third Pose); d) Second person (First Pose); e) Second person (Second Pose); f) Second person (Third Pose).

(Third Pose); d) Second person (First Pose); e) Second person (Second Pose); f) Second person (Third Pose).

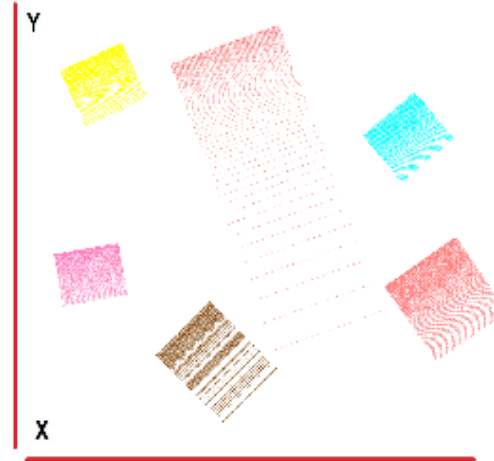


Fig. 7: The top view of the wide area of the synthesized dataset with coverage of cameras.



Fig. 8: Different pose of persons in the synthesized dataset: a) First person (First Pose); b) First person (Second Pose); c) First person (Third Pose); d) Second person (First Pose); e) Second person (Second Pose); f) Second person (Third Pose).

C. Results and Discussion

For evaluating the performance of the proposed model, the results are compared with four similar models in Table 3 and Table 4. As provided in Table 3 the proposed model tracks objects in wide area with the

average TCF metric of 78.8% and FS metric of 79.26% which means it extracts more than 79% of the objects' persistent trace. These results show that the multiphase model using deep features presented in this paper can provide 9% better results than the multiphase model without deep features [34].

Also, the proposed model tracks objects with average MT metric of 85.60% which means it tracks more than 80% of the persistent trace of more than 85% of the objects.

As a result, the deep features in terms of MT metric improve by an average of 8% compared to the other features [34]. In order to better compare the results of the proposed model with other models, two charts are presented in Fig. 9 and Fig. 10.

Figure 9 presents a chart for showing the effect of using the variational model and deep features simultaneously compared to the variational based models without deep features.

The numbers in this chart are obtained by averaging the results obtained from the entire datasets.

As can be seen in this figure, the proposed model in most metrics has provided better results than both variational models without deep features.

Also, in Fig. 10 the proposed model is compared with the results of the two other methods that are not variational based, which show the better performance of the proposed model. In other words, the proposed model presents competitive results compare to the similar models.

In Fig. 11, the computed persistent trace of one of the objects of NGSIM dataset and ground truth persistent trace of this object in the world plane are shown. As illustrated in this figure, the object are tracked in three cameras of the camera network. In Fig. 12, the persistent trace result of an object of PETS2009 dataset in two cameras is presented. Also, the extracted persistent trace of an object of synthesized dataset which has been tracked in four cameras of the camera network is given in Fig. 13.

Table 1: The characteristics of the datasets

| Name | Wide Area Width(meter) | Wide Area Height(meter) | #Cameras | #Tracklets | #objects |
|-----------|------------------------|-------------------------|----------|------------|----------|
| CAVIAR | 30 | 65 | 1 | 413 | 88 |
| NGSIM | 150 | 650 | 5 | 691 | 195 |
| PETS | 50 | 55 | 4 | 53 | 10 |
| Synthesis | 50 | 50 | 6 | 102 | 10 |

Table 2: The characteristics of the Metrics

| Name | Abbreviation | Unit | Minimum | Maximum | Goal |
|---------------------------------------|--------------|------------|---------|---------|------|
| Track Completion Factor [18] | TCF | Percent% | 0% | 100% | Max |
| Track Fragmentation [18] | TF | Numerical# | 1 | - | Min |
| Physical Object ID Fragmentation [43] | POIF | Numerical# | 0 | 1 | Max |
| Precision [43] | PT | Percent% | 0% | 100% | Max |
| Sensitivity [43] | ST | Percent% | 0% | 100% | Max |
| F-Score [43] | FS | Percent% | 0% | 100% | Max |
| ID Switching [44] | IDS | Numerical# | 0 | - | Min |
| Fragment [44] | FG | Numerical# | 0 | - | Min |
| Mostly Tracked [44] | MT | Percent% | 0% | 100% | Max |
| Mostly Lost [44] | ML | Percent% | 0% | 100% | Min |

Table 3: The results of the proposed model

| Metrics | Our Proposed Model | | | | B. Song [39] | R. Pless [18] |
|---------|--------------------|--------|----------|-------------|--------------|---------------|
| | CAVIAR | NGSIM | PETS2009 | Synthesized | CAVIAR | NGSIM |
| TCF | 73.14% | 79.6% | 77.26% | 85.18% | - | 67% |
| TF | 1.52 | 1.18 | 1.16 | 1.28 | - | 1.39 |
| POIF | 0.38 | 0.34 | 0.48 | 0.35 | - | - |
| PT | 84.21% | 91.27% | 76.12% | 87.74% | - | - |
| ST | 73.28% | 70.11% | 77.29% | 78.15% | - | - |
| FS | 78.37% | 79.3% | 76.7% | 82.67% | - | - |
| IDS | 7 | 3 | 4 | 5 | 8 | - |
| FG | 5 | 8 | 4 | 8 | 6 | - |
| MT | 85.12% | 89.39% | 84.86% | 83.02% | 84.0% | - |
| ML | 0% | 0% | 0% | 0% | 4.0% | - |

Table 4: The Results of Single Variational Model [33] and Multi Variational Model [34]

| Metrics | CAVIAR | | NGSIM | | PETS2009 | | Synthesized | |
|---------|--------|--------|--------|--------|----------|--------|-------------|--------|
| | Single | Multi | Single | Multi | Single | Multi | Single | Multi |
| TCF | 71% | 71.97% | 74% | 76.3% | 74% | 75.52% | 83% | 64.13% |
| TF | 1.61 | 2 | 1.21 | 1.27 | 2 | 1.22 | 2 | 2.5 |
| POIF | 0.37 | 0.31 | 0.31 | 0.32 | 0.46 | 0.41 | 0.33 | 0.28 |
| PT | 83.76% | 79.68% | 80.43% | 89.39% | 75.35% | 70.04% | 87.50% | 76.52% |
| ST | 72.58% | 68.56% | 69.83% | 62.12% | 76.14% | 74.62% | 77.62% | 68.85% |
| FS | 75.74% | 71.33% | 71.09% | 69.69% | 72.43% | 68.79% | 79.61% | 69.40% |
| IDS | 9 | 11 | 28 | 3 | 5 | 5 | 8 | 6 |
| FG | 6 | 7 | 35 | 9 | 8 | 5 | 10 | 12 |
| MT | 80.10% | 78.32% | 73.40% | 87.09% | 83.33% | 70% | 81.00% | 75% |
| ML | 2.00% | 0% | 12% | 0% | 0% | 0% | 0% | 0% |



Fig. 9: Graph comparing the results of the proposed model with two other variational models, including the single-phase model [33] and the multi-phase model [34] without using deep features.

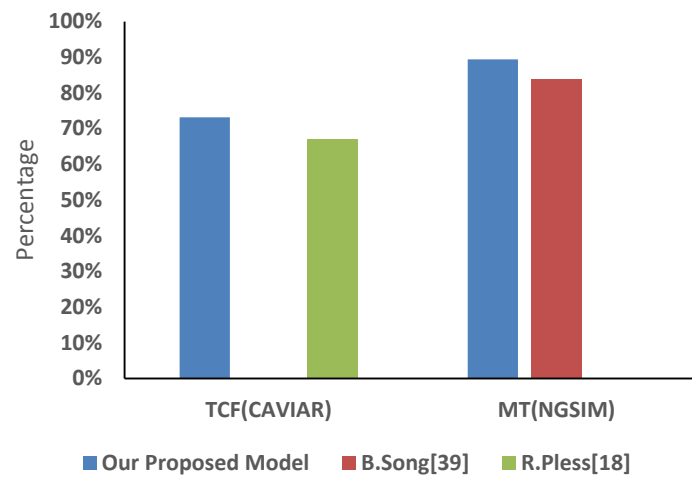


Fig. 10: Graph comparing the results of the proposed model with the other two models.

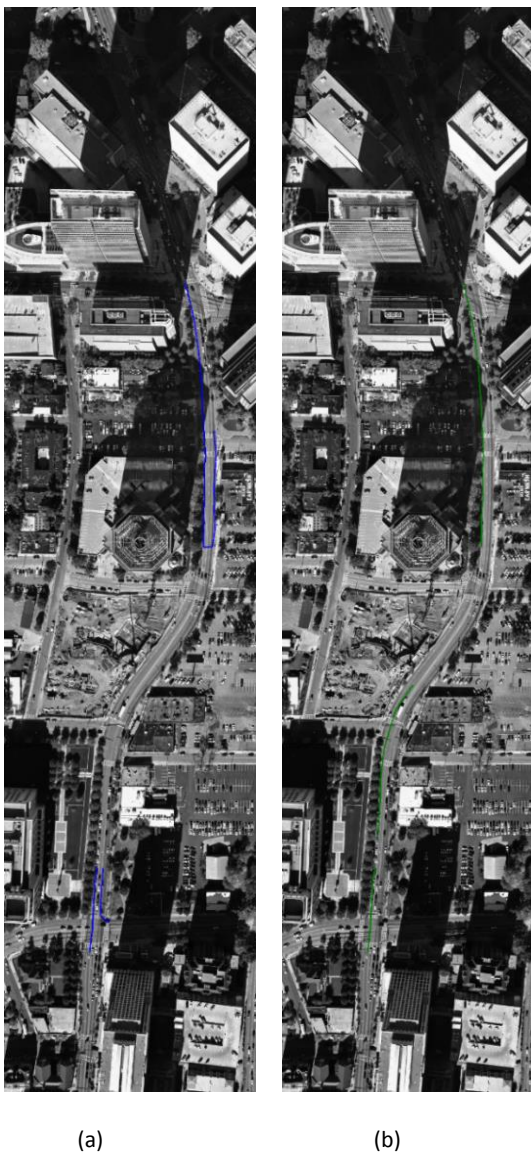


Fig. 11: The persistent tracking results of the NGSIM for one object: a) Extracted result; and b) Ground truth result.

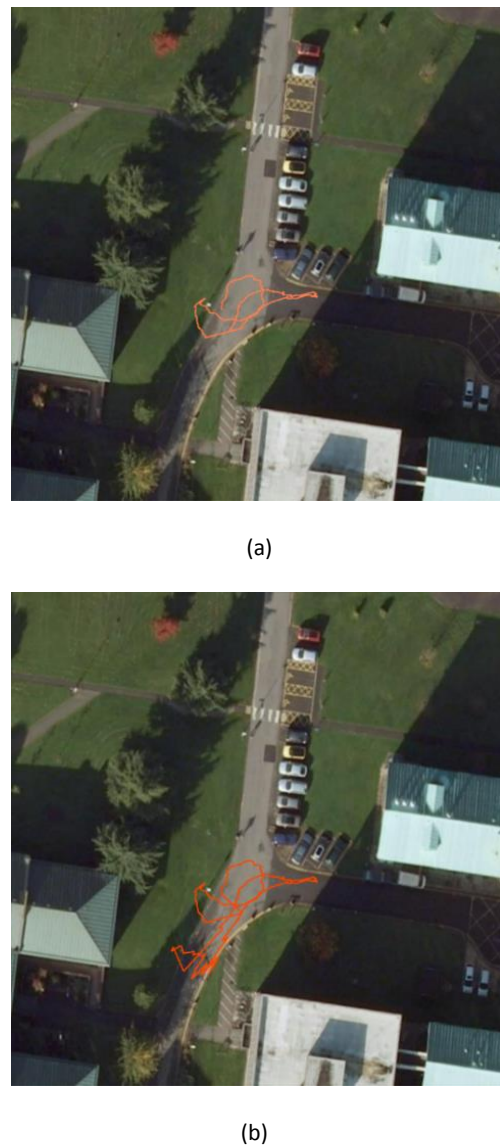


Fig. 12: The persistent tracking results of the PETS2009 for one object: a) Extracted result; and b) Ground truth result.

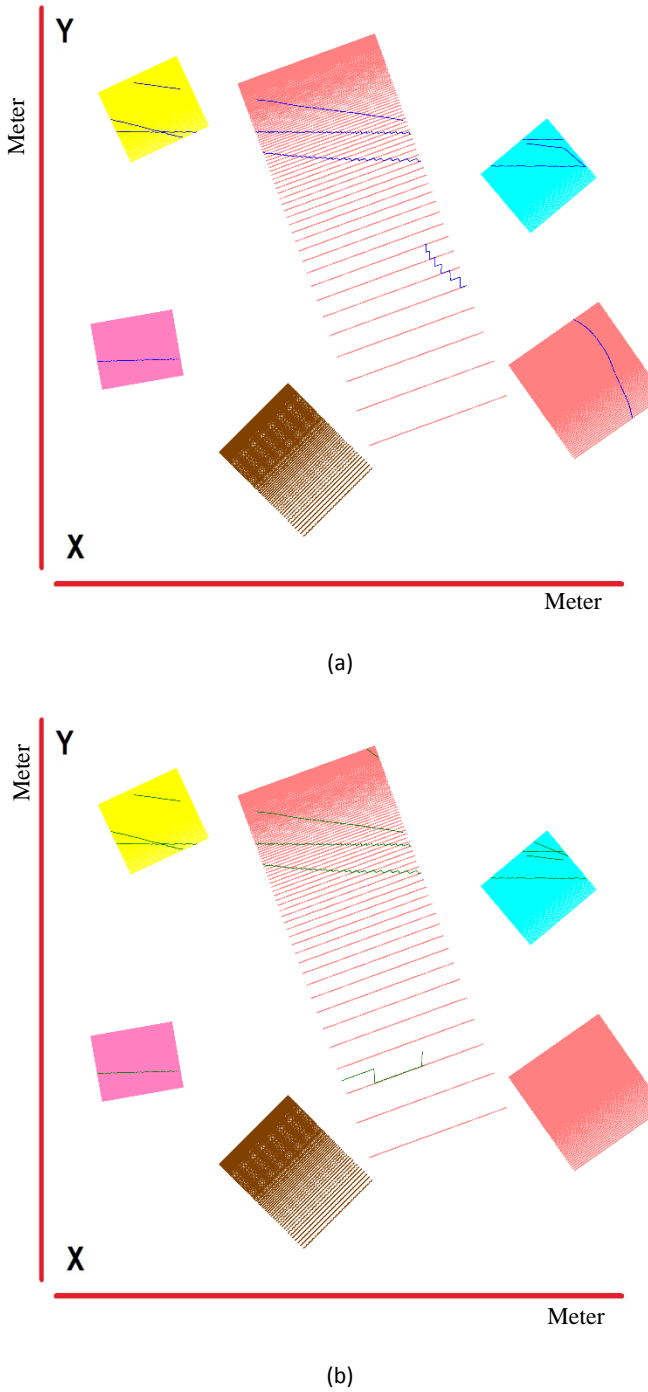


Fig. 13: The persistent tracking results of the synthesized data for one object: a) Extracted result; and b) Ground truth result.

Conclusion

In this paper, we proposed a variational multiphase model for associating the tracklets of the objects in the camera network and determining their persistent trace. We proposed a new representation of the multi-object tracking problem in a camera network which can solve this problem with less restricted assumption. So, this model is a more general model for multi-object tracking in camera network which doesn't need the serious

prerequisite information of the wide area, the camera topology and the objects' models. We use the deep feature for appearance and motion representation of objects.

We have evaluated our proposed model by four complicated datasets using 10 well known and common metrics. These evaluations show the quality of the proposed model in solving complex problems using the minimum required initial knowledge.

Author Contributions

Ehsan Pazouki designed and simulated, carried out the data analysis and collected the data and Mohammad Rahmati interpreted the results and wrote the manuscript.

Acknowledgment

The authors gratefully thank the anonymous reviewers and the editor of JECEI for their useful comments and suggestions.

Conflict of Interest

The author declares that there is no conflict of interests regarding the publication of this manuscript. In addition, the ethical issues, including plagiarism, informed consent, misconduct, data fabrication and/or falsification, double publication and/or submission, and redundancy have been completely observed by the authors.

Abbreviations

| | |
|----------------|--|
| C_i | The i th Camera |
| C_{M_i} | Calibration Parameters of the i th Camera |
| P_τ | The τ th Object |
| t_s | Start tracking time windows |
| t_e | End tracking time windows |
| T_C | Tracklets of all Cameras |
| T_{O_i} | Tracklets of the i th camera |
| R_P | Persistent trace of all objects |
| r_{P_x} | Persistent trace of the x th object |
| n | Count of moving objects |
| b | Count of persistent tracked of objects |
| ϕ | Multiphase Level Set representation of R_P |
| φ_τ | Level Set representation of r_{P_τ} |
| $ \cdot $ | The cardinal of the set |

References

- [1] A.K. Roy-Chowdhury, B. Song, *Camera Networks: The Acquisition and Analysis of Videos over Wide Areas*. Morgan & Claypool Publishers, 2012: 134.
- [2] A. Yilmaz, O. Javed, M. Shah, "Object tracking: A survey," *ACM Comput. Surv. (CSUR)*, 38(4):1-45, 2006.
- [3] S. Challa, *Fundamentals of object tracking*. Cambridge, UK; New York: Cambridge University Press, 2011.
- [4] J. Bins, L.L. Dohl, C. R. Jung, "Target tracking using multiple patches and weighted vector median filters," *J. Math. Imaging Vision*, 45(3): 293-307, 2013.
- [5] Y. Sun, L. Bentabet, "A particle filtering and DSMT based approach for conflict resolving in case of target tracking with multiple cues," *J. Math. Imaging Vision*, 36(2): 159-167, 2010.
- [6] G. Castanon, L. Finn, "Multi-target tracklet stitching through network flows," in *Proc. IEEE Aerospace Conf.*, 1-7, 2011.
- [7] J.-F. Aujol, "Calculus of variations in image processing," september 2008.
- [8] A.G. Jagola, W. Yanfei, C. Yang, *Computational Methods for Applied Inverse Problems*. Berlin: De Gruyter, 2012.
- [9] T.F. Chan, J.J.S.p. cm., *Image processing and analysis: variational, PDE, wavelet, and stochastic methods*. Siam: 400, 2005.
- [10] G. Unal, A. Yezzi, "A variational approach to problems in calibration of multiple cameras," in *Proc. of the IEEE Computer Society Conf. on Computer Vision and Pattern Recognition (CVPR)*: I-172- I-178, 2004.
- [11] N. Paragios, Y. Chen, O. Faugeras, *Handbook of Mathematical Models in Computer Vision*. Printed in the United States of America.: Springer, 2006.
- [12] C. Liu, F. Dong, S. Zhu, D. Kong, K. Liu, "New variational formulations for level set evolution without reinitialization with applications to image segmentation," *J. Math. Imaging Vision*, 41(3): 194-209, 2011.
- [13] O. Javed, Z. Rasheed, K. Shafique, M. Shah, "Tracking across multiple cameras with disjoint views," in *Proc. Ninth IEEE International Conference on Computer Vision*: 952-957, 2003.
- [14] B. Song, A.K. Roy-Chowdhury, "Robust tracking in a camera network: A multi-objective optimization framework," *IEEE IEEE J. Sel. Top. Signal Process.*, 2(4): 582-596, 2008.
- [15] W. Hu, T. Tan, L. Wang, S. Maybank, "A survey on visual surveillance of object motion and behaviors," *IEEE Trans. Syst. Man Cybern. Part C Appl. Rev.*, 34(3): 334-352, 2004.
- [16] D. Makris, T. Ellis, J. Black, "Bridging the gaps between cameras," in *Proc. of the 2004 IEEE Computer Society Conference on Computer Vision and Pattern Recognition*: II-205- II-210, 2004.
- [17] S. C, K. Tieu, "Automated multi-camera planar tracking correspondence modeling," in *Proc. 2003 IEEE Computer Society Conference on Computer Vision and Pattern Recognition*: I-259- I-266, 2003.
- [18] R. Pless et al., "Persistence and tracking: Putting vehicles and trajectories in context," in *Proc. 2009 IEEE Applied Imagery Pattern Recognition Workshop (AIPRW)*: 1-8, 2009.
- [19] C. Zhu, "Multi-Camera People Detection and Tracking," Independent thesis Advanced level (degree of Master (Two Years)) Student thesis, 2019.
- [20] Y. LeCun, Y. Bengio, G. Hinton, "Deep learning," *Nature*, 521(7553): 436-444, 2015.
- [21] H.-M. Hsu, T.-W. Huang, G. Wang, J. Cai, Z. Lei, J. Hwang, "Multi-camera tracking of vehicles based on deep features Re-ID and trajectory-based camera link models," in *CVPR Workshops*, 2019.
- [22] G. Wang, Y. Wang, H. Zhang, R. Gu, J.-N. Hwang, "Exploit the connectivity: Multi-Object Tracking with TrackletNet," *ArXiv*: 1811.07258, 2018.
- [23] K. He, X. Zhang, S. Ren, J. Sun, "Deep residual learning for image recognition," *ArXiv*:1512.03385, 2015.
- [24] M.P. Ghaemmaghami, "Tracking of humans in video stream Using LSTM recurrent neural network," Master in Machine Learning, School of Computer Science And Communication, KTH Royal Institute of Technology School of Computer Science And Communication, 2019.
- [25] D. Gordon, A. Farhadi, D. Fox, "Re3 : Real-time recurrent regression networks for object tracking," *ArXiv*: 1705.06368, 2017.
- [26] P. Voigtlaender, J. Luiten, P. Torr, B. Leibe, "Siam R-CNN: visual tracking by re-detection," in *Proc. 2020 IEEE/CVF Conference on Computer Vision and Pattern Recognition (CVPR)*: 6577-6587, 2020.
- [27] C. Ma et al., "Trajectory factory: Tracklet cleaving and re-connection by deep siamese bi-gru for multiple object tracking," *ArXiv*:1804.04555 [cs], 2018.
- [28] X. Zhang, X. Wang, C. Gu, "Online multi-object tracking with pedestrian re-identification and occlusion processing," *Visual Comput.*, 2020.
- [29] N. Hussain et al., "A deep neural network and classical features based scheme for objects recognition: an application for machine inspection," *Multimed. Tool. Appl.*, 2020: 1-23, 2020.
- [30] M.A. Khan et al., "Human action recognition using fusion of multiview and deep features: an application to video surveillance," *Multimed. Tool. Appl.*, 2020: 1-27, 2020.
- [31] M. Rashid et al., "A sustainable deep learning framework for object recognition using multi-layers deep features fusion and selection," *Sustainability*, 12(12): 5037, 2020.
- [32] M. Rashid, M.A. Khan, M. Sharif, M. Raza, M.M. Sarfraz, F. Afza, "Object detection and classification: a joint selection and fusion strategy of deep convolutional neural network and SIFT point features," *Multimed. Tool. Appl.*, 78(12): 15751-15777, 2019.
- [33] E. Pazouki, M. Rahmati, "Variational method for wide area surveillance," *J. Ambient Intell. Smart Environ.*, 8: 189-203, 2016.
- [34] E. Pazouki, M. Rahmati, "Multiphase vs. single-phase variational level set approach for video data association," *Intell. Data Anal.*, 20: 679-699, 2016.
- [35] R. Mohammadi Farsani, E. Pazouki, "A transformer self-attention model for time series forecasting," *J. Electr. Comput. Eng. Innovations (JECEI)*, 9(1): 1-10, 2021.
- [36] B. Dacorogna, *Introduction to the Calculus of Variation*. World Scientific Publishing Company, 2004: 240.
- [37] T.F. Chan, L.A. Vese, "Active contours without edges," *IEEE Trans. Image Process.*, 10(2): 266 – 277, 2001.
- [38] "CAVIAR 2003 and 2004", accessed 23 February 2021.
- [39] B. Song, R.J. Sethi, "Robust wide area tracking in single and multiple views," *Rev. Lit. arts Am.*, 2011: 1-18, 2011.
- [40] "ngsim peachtree street." accessed 23 February 2021.
- [41] "Eleventh ieee international workshop PETS." accessed 23 February 2021.
- [42] "Image Processing & Pattern Recognition Laboratory." accessed 23 February 2021.
- [43] S. Inria, "Internal Technical note Metrics Definition version 2.0 – Approved," Inria, IN_ETI_1_004, 2006.
- [44] Y. Li, C. Huang, R. Nevatia, "Learning to associate: HybridBoosted multi-target tracker for crowded scene," in *Proc. IEEE Conference on Computer Vision and Pattern Recognition*: 2953-2960, 2009.

Biographies



Ehsan Pazouki is a Professor in the school of Computer Engineering at Shahid Rajaei Teacher Training University where he has been a faculty member since 2016. Ehsan completed his Ph.D. and M.S. at Amirkabir University. His research interests lie in the area of wide area surveillance, ranging from theory to design to implementation. He has collaborated actively with researchers in several other disciplines of computer science, particularly Cognitive Science.

Ehsan has experience in various industries related to his specialization for more than 10 years. For additional information see <https://www.sru.ac.ir/en/school-of-computer/ehsan-pazouki/>



Mohammad Rahmati received the M.Sc. degree in electrical engineering from the University of New Orleans, in 1987 and the Ph.D. degree in electrical and computer engineering from the University of Kentucky, Lexington, Kentucky, in 1994. He is currently an associate professor in the Computer Engineering Department, Amirkabir University of Technology (Tehran Polytechnic). His research interests include the fields of pattern recognition, image processing, bioinformatics, video processing, and data mining. He is the chair of the department and he is also a member of IEEE Signal Processing Society.

Copyrights

©2021 The author(s). This is an open access article distributed under the terms of the Creative Commons Attribution (CC BY 4.0), which permits unrestricted use, distribution, and reproduction in any medium, as long as the original authors and source are cited. No permission is required from the authors or the publishers.



How to cite this paper:

E. Pazouki, M. Rahmati, "A variational level set approach to multiphase multi-object tracking in camera network base on deep features," J. Electr. Comput. Eng. Innovations, 9(2): 203-214, 2021.

DOI: [10.22061/JECEI.2021.7649.417](https://doi.org/10.22061/JECEI.2021.7649.417)

URL: https://jecei.sru.ac.ir/article_1542.html





Research paper

State Space Modeling and Sliding Mode Current Control of the Grid Connected Multi-Level Flying Capacitor Inverters

N. Ghaffari¹, A. Zakipour^{1,*}, M. Salimi²

¹Department of Electrical Engineering, Arak University of Technology (AUT), Arak, Iran.

²Department of Electrical Engineering, Ardabil Branch, Islamic Azad University, Ardabil, Iran.

Article Info

Article History:

Received 22 July 2020

Reviewed 15 September 2020

Revised 02 November 2020

Accepted 02 January 2021

Keywords:

Multi-level inverters

Grid connected inverter

Sliding mode control

Nonlinear control

Lyapunov stability

Active power filter

Abstract

Background and Objectives: In this paper, a novel approach for regulation of the output current in the grid-connected three-level flying capacitor inverter is presented by using the sliding mode (SM) method. In the proposed method, it is possible to control the active and reactive components of the inverter output current independently, and therefore it can be employed for grid connection of the renewable energy resources or for harmonic and reactive power compensation of the local loads. The designed controller uses an external loop to control the voltage of the inverter DC link and has a constant switching frequency. The stability of the proposed method has also been proved by using the Lyapunov stability theory. The simulation results show that in different operating conditions, the proposed controller has a stable and robust response.

Methods: Grid-connected three-level flying capacitor inverter is modeled by using averaged state space technique. Considering nonlinearity of the obtained model, an equivalent SM controller is developed for output current control of the multilevel grid connected inverter. To improve robustness and stability of the system against uncertainty of model parameters, a nonlinear component is added to the equivalent controller.

Results: The proposed controller enjoys very fast dynamic response, so it can be employed in wide ranges of application e.g. reactive compensation and harmonic mitigation modes. In active power filtering operation, it is able to eliminate harmonic components of the grid from 20.61% to 1.34% which is compatible with IEEE and IEC standards.

Conclusion: The stability of the proposed method has also been proved by using the Lyapunov stability theory. The simulation results show that in different operating conditions, the proposed controller has a stable and robust response.

*Corresponding Author's Email Address:

zakipour@arakut.ac.ir

©2021 JECEI. All rights reserved.

Introduction

Application of the grid-connected inverters has increased significantly in recent years [1]. For example, in photovoltaic power plants, these inverters are used to inject active power generated by solar panels into the grid. In flexible AC transmission systems [2], grid-

connected inverters are used for load and line compensation through reactive power exchange. Also in active power filters [3], these power electronics converters are employed for harmonic compensation of the nonlinear loads. Other applications include wind power conversion systems [4], solid-state transformers

[5], connecting electric vehicles to the grid for peak shaving [6], and more.

From power circuit topology viewpoint, the standard H-bridge voltage source inverter is one of the most widely used power electronics converters which are employed in grid connected three-phase and single-phase systems. However, other topologies have been proposed in recent years to improve the performance of grid-connected systems. For example, the use of impedance and quasi-impedance source inverters for efficiency improvement of power converters in renewable energy systems is reported [7]. Also, to reduce switching losses and improve inverter output power quality, application of the multilevel inverters has been suggested in [8]. It is well-known that one of the main applications of the multilevel inverters is reduction of the switching harmonics and improvement of the output power quality. In fact, if IGBT based multilevel inverter with fast PWM switching is used, harmonic components of the inverter output current can be reduced significantly.

One of the main challenges in design and implementation of the grid-connected inverters is synchronizing of the inverter output voltage with the grid power. In such a case, exchanged power be controlled by adjusting the amplitude as well as the angle of the inverter output voltage vector [9]. However, in such a method, a small error in the output voltage phase can lead to a significant error in amount of the power which is exchanged between the inverter and the grid. For this reason, intrinsic delay in electronic systems such as analog-to-digital converters, mathematical calculations, and current and voltage sensors essentially complicates design of the closed-loop system. On the other hand, since the grid is essentially a voltage source, therefore, by controlling the output current of the inverter, the exchanged power between the grid and the inverter can be indirectly adjusted [10]. During output current control of the voltage source inverters, delay in response of electronic systems doesn't affect the amplitude of the current directly and therefore, it is more useful than direct control of the output voltage.

Briefly, output current and power control is one of the main blocks of inverters which are connected to the grid. If the reference values of the controller change sharply due to variation of the local load or DC input source, it is obvious that the dynamic response of the closed-loop controller must be fast enough to meet the system requirements of the grid-connected inverter. Also, considering the nonlinear nature of power electronics converters, basically the linear and conventional control methods will be able to stabilize and control the closed loop system only in a small range of the changes. For this reason, application of modern

and nonlinear methods for the current control of the grid connected voltage source inverters is proposed. For instance, adaptive [11], robust [12], backstepping [3], passivity-based [13], Lyapunov-based [14] controllers are used widely in closed loop control of the power electronics converters.

Among the mentioned methods, sliding mode (SM) controller is employed widely in power electronics converters [15]. Its main advantages are simplicity of the practical implementation, fast dynamic response and robustness to system uncertainties [16]. Also, in recent years, attempts have been made to eliminate the major drawbacks of the SM method, such as switching frequency changes, steady-state error, and chattering, by using the equivalent SM approach and in recent years, application of the SM controllers in grid-connected inverters has increased significantly. Also for mitigation of the chattering problem, combined PI and SM technique can be employed [17] where variable structure control approach is designed for shunt compensation of the local loads. To improve robustness and stability of the closed loop system, a SM controller in combination with conventional PI method is used in the final control law of the proposed method. During transient conditions, the PI controller is dominant and the gains of the linear controller should be tuned to meet the desired transient response characteristic. On the other hand, the sliding mode block determines steady-state behavior of the system. Briefly, in order to achieve desired response of the closed loop system and eliminate chattering problem, gains for the linear PI and SM controllers should be selected properly. The SM is employed for grid connection of the cascaded doubly fed induction generators [18]. Two sliding surfaces are defined for closed loop control of the active and reactive power components. Compared with conventional vector control, it is shown that the SM method is more robust against model uncertainties and enjoys better dynamic response. However, in the proposed method, stability of the closed loop system under different operating conditions has not been investigated.

In order to reduce the output current error of the inverter and thus improve the total harmonic distortion (THD) coefficient of the power system, in [19] a multi-resonance SM controller is used in the grid connected inverters. In this case, the performance of the system in compensating for the high order harmonics is increased. To reduce THD, in sliding surface the proposed controller, several resonant components from the grid current error are employed which complicates design of the controller and its practical implementation.

To improve the power quality in power distribution networks and reduce power losses in electrical equipment, the Integral SM method has been used to

control the output current of the grid connected inverter in [20]. A fourth-order band pass digital filter is used to extract the harmonic components and define the reference values of the closed-loop control system. Since the main component of the output current in the proposed method is regulated by using a linear PI controller, it can be concluded that the chattering will be significantly reduced. However, such an approach does not guarantee the overall stability of the controller over a wide range of output current changes. Also, for controlling of the fundamental current component, two PI blocks are used for calculation of the reference value and inverter amplitude modulation (control effort). As a result, the proposed closed-loop system has a cascade structure that cannot have a fast dynamic response and will lead to a steady-state error when compensating for high-order harmonic components. Also, a double band hysteresis SM controller is proposed for parallel operation of the active power filters with LCL coupling in reference [21]. Despite the fast dynamic response, the switching instances in the proposed method are determined by comparison of the slip surface in a hysteresis band. Hence, inverter switching frequency cannot be completely constant due to variation of the grid voltage. This issue results in injection of the undesired low-order harmonic components and deteriorates the THD of the grid current. However, if the hysteresis-based SM is replaced with equivalent controller, the problem of switching frequency variation in this nonlinear control method can be easily mitigated [22]. In [23], combination of the SM and backstepping control methods for harmonic compensation of the local loads is proposed in distributed generators. Such an idea can improved the performance and robustness of the closed loop system against model uncertainties, such as grid voltage and frequency, impedance of the coupling inductor, and uncertain load dynamics. However, due to design process of the adaptive backstepping approach, the controlling law will be completely complex and so, its real time calculation can be a time consuming task. As more powerful processors are required for implementation of the combined backstepping-SM controller, it may significantly increase the final cost of the system. Also in [1], adaptive SM approach is employed for closed-loop control of the single phase grid connected photovoltaic system. Current harmonic compensation of the local load as well as maximum power point tracking of the input renewable energy source are main aims of the developed controller. Voltage and parasitic inductance of the grid are estimated with an adaptive estimator. Output current of the inverter is controlled by using a SM and Lyapunov based methods. However, DC link voltage control is performed through a conventional PI controller. Hence,

stability and robustness of the DC link voltage cannot be guaranteed in a wide range of operation.

In Similar problem are also observed in the combination of adaptive control methods with SM [24].

In order to stabilize the non-minimum phase nature of the output current in grid connected voltage source inverters with LCL coupling, a two-loop control in [25] is proposed. The inner loop is used to control the output current of the converter and is designed by using SM method. Also, the reference value of the internal loop is generated in an external loop using a proportional-resonance (PR) controller. In this case, the controller design problem is reduced from a third-order system to a second-order one. However, it is clear that the whole system is not designed based on the SM method and the advantages of the mentioned nonlinear controlling method cannot be obtained in a wide range of system changes.

In recent years, application of the SM controller in other topologies of the grid-connected DC to AC converters, such as impedance source inverters [26] and semi-impedance source inverters [27] is studied. In this case, due to the complexity of the model and the high number of state variables, the extraction of reference values for each of the state variables is associated with complexities. Impedance source converters also have a multi-input-multi-output structure, which adds additional challenges to the controller design. There are similar problems with the application of the SM controlling method in grid-connected multilevel converters, and for this reason, number of articles related to output current control in grid connected multilevel inverters which employ SM approach is limited. The mentioned papers are reviewed below. It is worth noting that due to existence of fundamental differences in the dynamic model of the different multilevel inverters, design process of the SM controller for each of them (clamp diodes, series H-bridges and flying capacitors) is completely different task.

In the reference [28], the SM method is used to control the output current and inject a certain level of active and reactive powers into the grid in multi-level diode clamp inverter. In this paper, a constant voltage source is used in the DC link of the inverter, and for this reason, DC link voltage regulation is not studied. For this reason, if renewable energy sources are used at the DC link, the proposed method in [28] cannot be used to track the maximum power point. It is also necessary to adjust the DC link voltage in FACTS devices and shunt active filters. To do this, in the reference [29] the SM controller is modified with the idea of controlling DC link voltage in diode- clamp multilevel inverters. This is accomplished by introducing an active component in the output current reference value based on the DC link

voltage error by using a linear PI controller. However, in [29] the reference value of the reactive output current is zero, and only the injection of real power from the DC source is studied. It is obvious that the lack of reactive power management in distributed generators will result in high values of the reactive component in distribution network and significantly reduces the grid power factor.

In [30], a hysteresis-band SM controller is used to control the output current in a special 7-level packed U-cell inverter. Less tuning requirement and simplicity of the design are the most important advantages of the design. However, stability of the closed loop system in [30]. However, stability of the proposed method has not been investigated. Inverter switching frequency changes are also the most important disadvantages of the hysteresis-band SM controllers. To solve this problem in [31], equivalent control is used to design a nonlinear controller in a NPC three level topology. Therefore, it can be directly concluded that such a system is switched according to the PWM pattern and has a fixed frequency. Also in [31], by using the direct Lyapunov theory, stability of the closed-loop system in a wide range of changes in system parameters has been proved. Also, selection of the controlling gains are studied using the linearized model. The controller is able to compensate the reactive and harmonic components of the local load. However, in order to keep voltage of the inverter DC link, an independent current source is employed. So, the controller of [31] is not able to regulate DC link voltage. Moreover, additional modification of the controller for balancing of the DC link capacitors is mandatory.

According to the literature review and research performed by the authors of this article, there is no other report related to output current control in grid connected multi-level inverters.

In this paper, a novel approach for regulation of the output current in the grid-connected three-level flying

capacitor inverter is presented by using the SM method.

In the proposed method, it is possible to control the active and reactive components of the inverter output current independently, and therefore it can be employed for grid connection of the renewable energy resources or for harmonic and reactive power compensation of the local loads.

The designed controller uses an external loop to control the voltage of the inverter DC link and has a constant switching frequency. The stability of the proposed method has also been proved by using the Lyapunov stability theory. The simulation results show that in different operating conditions, the proposed controller has a stable and robust response.

This article is organized as follows. At first the proposed system topology and averaged state space model of the multi-level inverter is discussed. Then, by using the extracted model, the SM controller is designed to control the output current of the grid connected multilevel flying capacitor inverter. Finally, developed controller is investigated by PC based simulations in the MATLAB/SIMULINK software.

System Modeling

Circuit topology of the grid connected flying capacitor multilevel inverter is shown in Fig. 1. Also, phase-shifted pulse width modulation (PWM) switching of the phase-A is illustrated in Fig. 2. Similar waveforms can be introduced for phase B and C due to symmetrical operation of the different phases. In this figure, u_a is amplitude modulation index and control effort of the phase A. Duty cycles of the S_{1a} and S_{2a} can be calculated considering the similarity of the following triangles.

$$\Delta ABC \sim DBE : D_1 = \frac{T_{on1}}{T} = \frac{u_a + 1}{2} \quad (1)$$

$$\Delta ABC \sim AED : D_2 = \frac{T_{on2}}{T} = \frac{u_a + 1}{2} \quad (2)$$

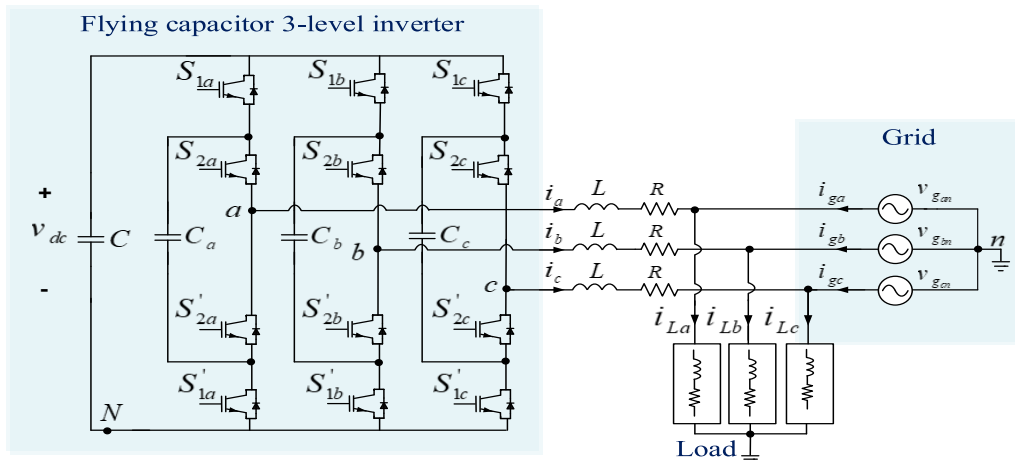


Fig. 1: Topology of the grid connected multi-level inverter.

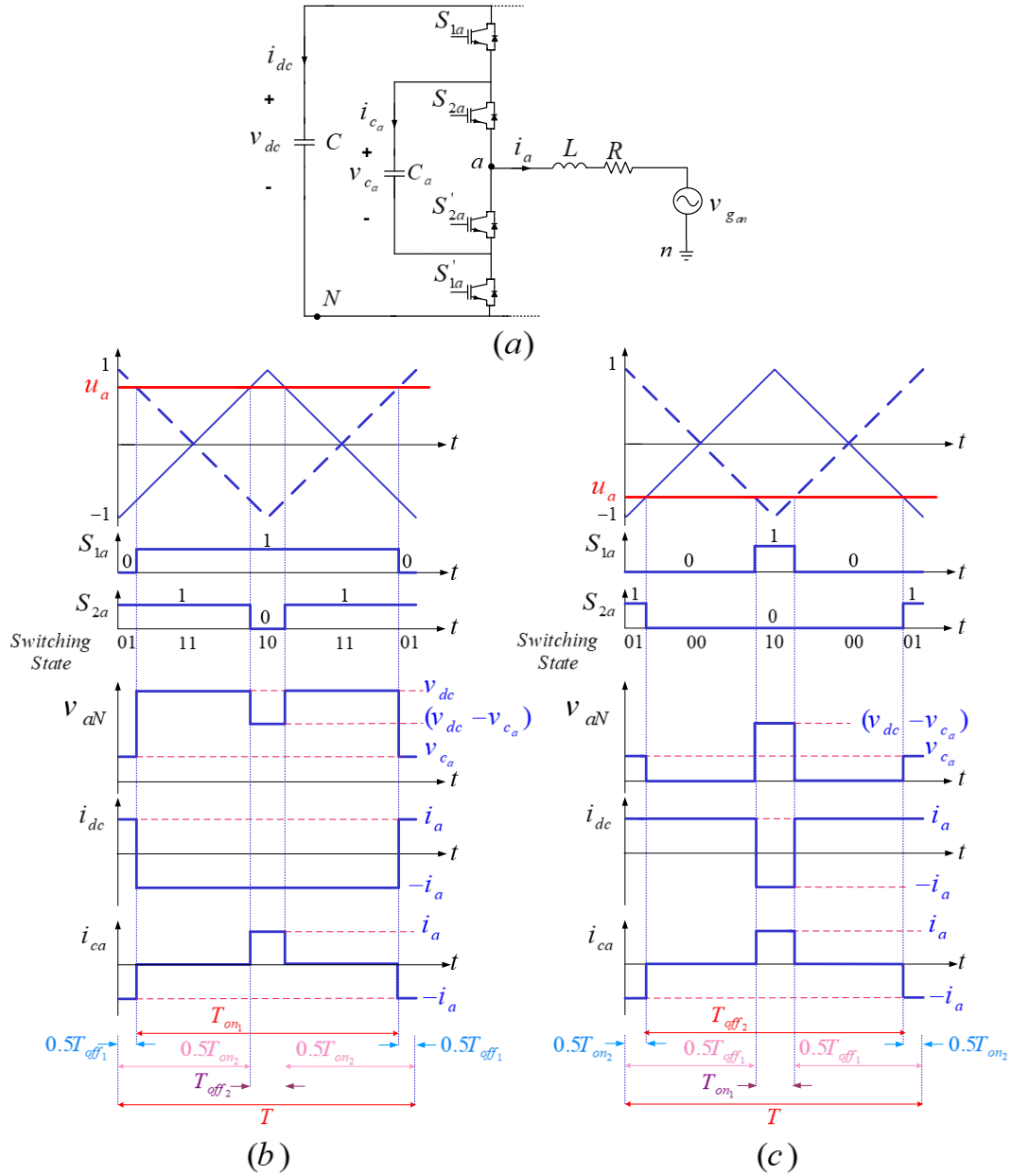


Fig. 2: Phase shifted PWM switching of the first leg (a) for positive (b) and negative (c) control efforts (u_a).

Clearly as u_a is amplitude modulation index of the inverter, so operation of the system can be divided into two different modes. When $u_a > 0$:

$$\begin{aligned} \bar{v}_{aN} &= \frac{1}{T} (v_{ca} T_{off_1} + v_{dc} T_{on_1} - v_{ca} T_{off_2}) \\ &= \frac{v_{dc}}{2} (u_a + 1) \end{aligned} \quad (3)$$

and for $u_a < 0$:

$$\begin{aligned} \bar{v}_{aN} &= v_{ca} (T_{on_2}) + (v_{dc} - v_{ca}) \frac{T_{on_1}}{T} \\ &= \frac{v_{dc}}{2} (u_a + 1) \end{aligned} \quad (4)$$

So, line voltages of the three-phase system can be written as:

$$\begin{cases} \bar{v}_{aN} = \frac{v_{dc}}{2} (u_a + 1) \\ \bar{v}_{bN} = \frac{v_{dc}}{2} (u_b + 1) \\ \bar{v}_{cN} = \frac{v_{dc}}{2} (u_c + 1) \end{cases}; \begin{cases} \bar{v}_{ab} = \frac{v_{dc}}{2} (u_a - u_b) \\ \bar{v}_{bc} = \frac{v_{dc}}{2} (u_b - u_c) \\ \bar{v}_{ca} = \frac{v_{dc}}{2} (u_c - u_a) \end{cases} \quad (5)$$

Equivalent model of the three phase system is illustrated in Fig. 3 where n' is virtual ground of the inverter DC link. So, average values of the three phase voltages can be related to its corresponding modulation index as:

$$\begin{cases} \bar{v}_{an'} = \frac{v_{dc}}{2} u_a \\ \bar{v}_{bn'} = \frac{v_{dc}}{2} u_b \\ \bar{v}_{cn'} = \frac{v_{dc}}{2} u_c \end{cases} \quad (6)$$

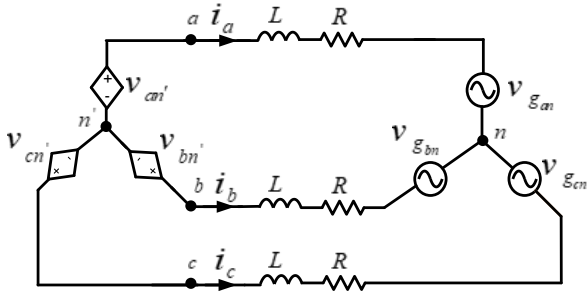


Fig. 3: Equivalent model of the grid connected inverter.

So, equivalent model of the grid connected inverter can be summarized according to Fig. 4.

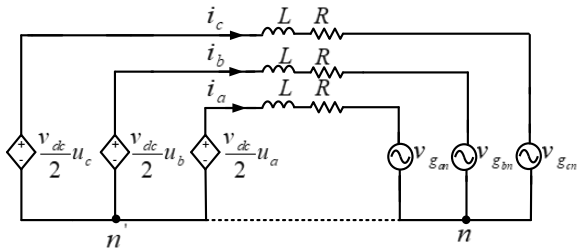


Fig. 4: Summarized equivalent model of the system.

In a balanced three phase systems, n and n' have a same potential. So:

$$\frac{di_a}{dt} = \frac{1}{L} (v_{an'} - v_{gan} - Ri_a) \quad (7)$$

$$\frac{di_b}{dt} = \frac{1}{L} (v_{bn'} - v_{gbn} - Ri_b) \quad (8)$$

$$\frac{di_c}{dt} = \frac{1}{L} (v_{cn'} - v_{gcn} - Ri_c) \quad (9)$$

With regard to current of the DC link capacitor and considering i_a , while $u_a > 0$, i_a the following equation can be written:

$$\begin{aligned} i_{dc} &= \frac{1}{T} i_a (T_{off1} - T_{on1}) = i_a (1 - 2D_1) \\ &= i_a \left(1 - 2 \left(\frac{u_a + 1}{2} \right) \right) \\ &= -i_a u_a \end{aligned} \quad (10)$$

So considering the three phase system, current of the DC link capacitor will be modeled as:

$$i_{dc} = -(i_a u_a + i_b u_b + i_c u_c) = C \frac{dv_{dc}}{dt} \quad (11)$$

and while $u_a < 0$:

$$i_{dc} = i_a \left(\frac{T_{off1} - T_{on1}}{T} \right) = -i_a u_a \quad (12)$$

Also, current of the C_a can be summarized in different operating modes as:

$$u_a > 0 : i_{ca} = \frac{1}{T} i_a (-T_{off1} + T_{off1}) = 0 \quad (13)$$

$$u_a < 0 : i_{ca} = \frac{1}{T} i_a (-T_{on2} + T_{on1}) = 0 \quad (14)$$

So, if $T_{on1} = T_{on2}$ and $T_{off1} = T_{off2}$, average value of the i_{ca} will be zero and voltage of the C_a will not change in steady-state and dynamic operational conditions of the converter. As a result, voltages of the flying capacitors are not an independent state variables and hence the multilevel grid connected inverter in Fig.1 has 4 state variable which are currents of the coupling inductors as well as voltage of the DC link capacitor. Briefly, the following equations can be considered for dynamics of the flying capacitors in phase shifted PWM switching strategy:

$$\frac{dv_{ca}}{dt} = 0; \frac{dv_{cb}}{dt} = 0; \frac{dv_{cc}}{dt} = 0 \quad (15)$$

So considering equations (6)-(9) and (11), averaged state space model of the system can be written as follows:

$$\begin{bmatrix} \frac{di_a}{dt} \\ \frac{di_b}{dt} \\ \frac{di_c}{dt} \\ \frac{dv_{dc}}{dt} \end{bmatrix} = \begin{bmatrix} -\frac{R}{L} & 0 & 0 & \frac{u_a}{2L} \\ 0 & -\frac{R}{L} & 0 & \frac{u_b}{2L} \\ 0 & 0 & -\frac{R}{L} & \frac{u_c}{2L} \\ -\frac{u_a}{C} & -\frac{u_b}{C} & -\frac{u_c}{C} & 0 \end{bmatrix} \begin{bmatrix} i_a \\ i_b \\ i_c \\ v_{dc} \end{bmatrix} + \begin{bmatrix} -\frac{1}{L} v_{gan} \\ -\frac{1}{L} v_{gbn} \\ -\frac{1}{L} v_{gcn} \\ 0 \end{bmatrix} \quad (16)$$

Sliding Mode Controller Design

Averaged state space model of the converter is given in (16). In this section, an SM controller is developed for output current control of the multilevel grid connected inverter. As dynamics of the DC link capacitor voltage is completely slow compared to output currents of the converter, so during the SM controller design, changes of the DC link capacitor voltage can be neglected for simplicity of the developed closed loop system. So, model of the converter $dq0$ frame can be rewritten as follows:

$$\begin{aligned} \frac{d}{dt} \begin{bmatrix} i_q \\ i_d \\ i_0 \end{bmatrix} &= \begin{bmatrix} -\frac{R}{L} & -\omega & 0 \\ \omega & -\frac{R}{L} & 0 \\ 0 & 0 & -\frac{R}{L} \end{bmatrix} \begin{bmatrix} i_q \\ i_d \\ i_0 \end{bmatrix} \\ &+ \begin{bmatrix} -\frac{1}{L} & 0 & 0 \\ 0 & -\frac{1}{L} & 0 \\ 0 & 0 & -\frac{1}{L} \end{bmatrix} \begin{bmatrix} v_{gq} \\ v_{gd} \\ v_{g0} \end{bmatrix} \\ &+ \begin{bmatrix} \frac{V_{dc}}{2L} & 0 & 0 \\ 0 & \frac{V_{dc}}{2L} & 0 \\ 0 & 0 & \frac{V_{dc}}{2L} \end{bmatrix} \begin{bmatrix} u_q \\ u_d \\ u_0 \end{bmatrix} \end{aligned} \quad (17)$$

It should be noted that $f^{abc} = [T_{qd0}(\theta)]^{-1} f^{qd0}$ is employed for transformation between abc and dq0 frames -where:

$$T^{-1}(\theta) = \begin{bmatrix} \cos(\theta) & \sin(\theta) & 1 \\ \cos(\theta - \frac{2\pi}{3}) & \sin(\theta - \frac{2\pi}{3}) & 1 \\ \cos(\theta + \frac{2\pi}{3}) & \sin(\theta + \frac{2\pi}{3}) & 1 \end{bmatrix} \quad (18)$$

In (17), $X(t) = [i_q \ i_d \ i_0]^T$ is state vector of the dynamic model. In this case, u_q , u_d and u_0 are controlling inputs of the system. Also, state variables of the model are control outputs.

According to (17), distributed model of the grid connected multilevel inverter can be rewritten as follows:

$$\dot{x}_1 = \left(-\frac{R}{L}x_1 - \omega x_2 - \frac{1}{L}v_{gq} \right) + \left(\frac{V_{dc}}{2L}u_q \right) \quad (19)$$

$$\dot{x}_2 = \left(\omega x_1 - \frac{R}{L}x_2 - \frac{1}{L}v_{gd} \right) + \left(\frac{V_{dc}}{2L}u_d \right) \quad (20)$$

$$\dot{x}_3 = \left(-\frac{R}{L}x_3 - \frac{1}{L}v_{g0} \right) + \left(\frac{V_{dc}}{2L}u_0 \right) \quad (21)$$

In the general form, system dynamics can be described as:

$$\begin{aligned} \dot{x}_1 &= f_1(x_1, x_2, x_3, t) + b_1(x_1, x_2, x_3, t)u_q \\ &= (\bar{f}_1 + \tilde{f}_1) + (\bar{b}_1 + \tilde{b}_1)u_q \end{aligned} \quad (22)$$

$$\begin{aligned} \dot{x}_2 &= f_2(x_1, x_2, x_3, t) + b_2(x_1, x_2, x_3, t)u_d \\ &= (\bar{f}_2 + \tilde{f}_2) + (\bar{b}_2 + \tilde{b}_2)u_d \end{aligned} \quad (23)$$

$$\begin{aligned} \dot{x}_3 &= f_3(x_1, x_2, x_3, t) + b_3(x_1, x_2, x_3, t)u_0 \\ &= (\bar{f}_3 + \tilde{f}_3) + (\bar{b}_3 + \tilde{b}_3)u_0 \end{aligned} \quad (24)$$

where \bar{f} and \bar{b} are nominal values of the model parameters. Also, \tilde{f} and \tilde{b} are uncertainty of f and b respectively. In order to control output current of the inverter in d and q axes, two sliding surface can be defined as follows:

$$\begin{aligned} S &= \alpha[X_{ref} - X] + \beta X_{int} = \begin{bmatrix} S_1 \\ S_2 \end{bmatrix} \\ &= \begin{bmatrix} \alpha_1 & 0 \\ 0 & \alpha_2 \end{bmatrix} \begin{bmatrix} (x_1^* - x_1) \\ (x_2^* - x_2) \end{bmatrix} \\ &\quad + \begin{bmatrix} \beta_1 & 0 \\ 0 & \beta_2 \end{bmatrix} \begin{bmatrix} \int (x_1^* - x_1) dt \\ \int (x_2^* - x_2) dt \end{bmatrix} \end{aligned} \quad (25)$$

where x_1^* and x_2^* are references of the state variables x_1 and x_2 . As it is seen in (25), integrals of the current errors are added to sliding surfaces to cancel the steady state error of the response. In this equation, α and β are

positive design parameters.

In order to present SM controller design in a general form, state space model of the converter can be rewritten in a compact form as follows:

$$\begin{aligned} \dot{X} &= \begin{bmatrix} \dot{x}_1 \\ \dot{x}_2 \end{bmatrix} = \underbrace{(\bar{F} + \tilde{F})}_{\bar{F}} + \underbrace{(\bar{B} + \tilde{B})}_{\bar{B}} U \\ &= \begin{bmatrix} f_1 \\ f_2 \end{bmatrix} + \begin{bmatrix} b_1 & 0 \\ 0 & b_2 \end{bmatrix} \begin{bmatrix} u_q \\ u_d \end{bmatrix} \end{aligned} \quad (26)$$

The proposed SM controller includes equivalent (\bar{u}_q, \bar{u}_d) and nonlinear (\tilde{u}_q, \tilde{u}_d) components as:

$$U = \bar{U} + \tilde{U} = \begin{bmatrix} u_q \\ u_d \end{bmatrix} = \begin{bmatrix} \bar{u}_q + \tilde{u}_q \\ \bar{u}_d + \tilde{u}_d \end{bmatrix} \quad (27)$$

Nonlinear component of the SM controller is responsible for improvement of the robustness and stability of the system against changes of the uncertain parameters. These components can be assumed as follows:

$$\tilde{u}_q = k_1 \text{sgn}(S_q) \quad (28)$$

$$\tilde{u}_d = k_2 \text{sgn}(S_d) \quad (29)$$

Equivalent SM controllers can be obtained by setting derivative of the sliding surface into zero in (25) as:

$$\dot{S} = \alpha(\dot{X}_{ref} - \dot{X}) + \beta \dot{X}_{int} = 0 \quad (30)$$

By substituting (26) in (30), equivalent SM controller can be obtained in the general form as:

$$\bar{U} = (\bar{B})^{-1}(\dot{X}_{ref} - \bar{F} + \alpha^{-1}\beta\dot{X}_{int}) \quad (31)$$

$$\begin{aligned} \bar{u}_q &= \frac{2 \left(\alpha_1 V_{gq} + \alpha_1 L \frac{dx_1^*}{dt} - \beta_1 L x_1 + \beta_1 L x_1^* + \alpha_1 R x_1 + \alpha_1 L \omega x_2 \right)}{\alpha_1 V_{dc}} \end{aligned} \quad (32)$$

$$\begin{aligned} \bar{u}_d &= \frac{2 \left(\alpha_2 V_{gd} + \alpha_2 L \frac{dx_2^*}{dt} - \beta_2 L x_2 + \beta_2 L x_2^* + \alpha_2 R x_2 - \alpha_2 L \omega x_1 \right)}{\alpha_2 V_{dc}} \end{aligned} \quad (33)$$

Finally, according to averaged state space model of the converter, equivalent sliding mode controller in (31) can be summarized for three level grid-connected flying capacitor as (32) and (33).

As it has been described previously, to improve robustness of the proposed controller against changes of the uncertain parameters, developed equivalent SM controller in (31) is combined with a nonlinear component.

$$\bar{U} = (\bar{B})^{-1}(\dot{X}_{ref} - \bar{F} + \alpha^{-1}\beta\dot{X}_{int} + K \text{sgn}(S)) \quad (34)$$

where the parameter K is

$$K = \begin{bmatrix} k_1 & 0 \\ 0 & k_2 \end{bmatrix} \quad (35)$$

The extracted SM controller in (34) has two parts. First one is equivalent SM and second component $[Ksgn(S)]$ is used for improving stability and robustness of the closed-loop system. It should be noted that the equivalent controllers of the system are given in (32) and (33).

Based on (30) and (34):

$$\begin{aligned} \dot{S} = & \alpha \dot{X}_{ref} - \alpha(F + B(\bar{B})^{-1}(\dot{X}_{ref} - \bar{F} \\ & + \alpha^{-1}\beta \dot{X}_{int} + Ksgn(S))) \\ & + \beta \dot{X}_{int} \end{aligned} \quad (36)$$

In order to investigate stability of the developed controller, the input matrix, B can be introduced as

$$B = \bar{B} + \tilde{B} = (I + \Delta)\bar{B} \quad |\Delta_{ij}| \leq D_{ij} \quad i, j = 1, 2 \quad (37)$$

where $I_{2 \times 2}$ is an identity matrix. So, it is clear that $B(\bar{B})^{-1} = (I + \Delta)$. Also, elements of the $\Delta_{2 \times 2}$ are defined as Δ_{ij} .

According to (26), it can be concluded that $\Delta_{12} = \Delta_{21} = 0$. So, \dot{S} in (36) can be simplified as

$$\begin{aligned} \dot{S} = & -\alpha\Delta\alpha^{-1}\beta\dot{X}_{int} + \alpha(\bar{F} - F) \\ & - \alpha(\Delta + I)Ksgn(S) \\ & - \alpha\Delta\dot{X}_{ref} + \alpha\Delta\bar{F} \end{aligned} \quad (38)$$

To evaluate stability and robustness of the proposed controller, the following criteria should be considered

$$S_i \dot{S}_i \leq -\mu_i |S_i| \quad (\mu_i > 0) \quad (39)$$

where μ_i is the design constant. Considering (38), (39) can be simplified as follows for S_1

$$\begin{aligned} S_1(\alpha_1(\bar{f}_1 - f_1) - \alpha_1 k_1(1 + \Delta_{11})sgn(S_1) \\ - \beta_1 \Delta_{11}(x_1^* - x_1) \\ + \alpha_1 \Delta_{11}(\bar{f}_1 - \dot{x}_1^*)) \\ \leq |S_1|(\alpha_1 |\bar{f}_1 - f_1| \\ - \alpha_1 k_1(1 - D_{11}) \\ - \beta_1 D_{11}|x_1^* - x_1| \\ + \alpha_1 D_{11}|\bar{f}_1 - \dot{x}_1^*|) \\ \leq -\mu_1 |S_1| \end{aligned} \quad (40)$$

Since $|f_i - \hat{f}_i| \leq f_{i,max}$, (40) can be reduced to

$$\alpha_1 f_{1,max} - \beta_1 D_{11}|x_1^* - x_1| + \alpha_1 D_{11}|\bar{f}_1 - \dot{x}_1^*| + \mu_1 \leq \alpha_1 k_1(1 - D_{11}) \quad (41)$$

Similarly, (39) can be written as follows for S_2

$$\alpha_2 f_{2,max} - \beta_2 D_{22}|x_2^* - x_2| + \alpha_2 D_{22}|\bar{f}_2 - \dot{x}_2^*| + \mu_2 \leq \alpha_2 k_2(1 - D_{22}) \quad (42)$$

Considering (41) and (42), in order to guarantee the stability of the developed SM controller, the control

gains should be selected according to the following conditions

$$\begin{aligned} k_1 \geq & (1 - D_{11})^{-1}(f_{1,max} \\ & - \alpha_1^{-1}\beta_1 D_{11}|x_1^* - x_1| \\ & + D_{11}|\bar{f}_1 - \dot{x}_1^*| + \alpha_1^{-1}\mu_1) \end{aligned} \quad (43)$$

$$\begin{aligned} k_2 \geq & (1 - D_{22})^{-1}(f_{2,max} \\ & - \alpha_2^{-1}\beta_2 D_{22}|x_2^* - x_2| \\ & + D_{22}|\bar{f}_2 - \dot{x}_2^*| + \alpha_2^{-1}\mu_2) \end{aligned} \quad (44)$$

The final SM control law can be obtained by adding of the nonlinear component into equivalent terms in (32) and (33). Its block diagram is illustrated for u_q in Fig. 5. Also, in order to adjust voltages of the flying capacitor, final modulation indexes of the multilevel inverter should be modified. In fact, small changes should be applied according to flying capacitor voltage error and sign of the output current. This idea is shown for lag A in Fig. 6 where u_{a1} and u_{a2} are amplitude modulation indexes for switches S_{a1} and S_{a2} respectively.

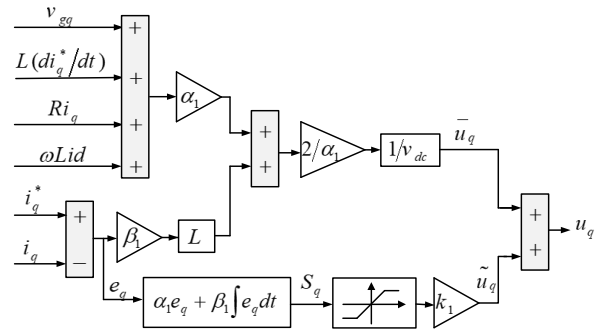


Fig. 5: Implementation of the proposed SM controller for u_q .

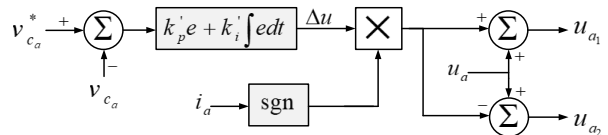


Fig. 6: Modification of the amplitude modulation index for regulation of the flying capacitors voltage (phase A).

Finally, block diagram of the proposed controller is shown in Fig. 7. The current controller is calculated based on reference currents and grid voltage in dq frame. Active reference current (i_d^*) is defined based on DC link voltage error through a linear PI controller. In shunt compensators, there is no independent voltage source on DC link and hence, DC link capacitor voltage is regulated by absorbing an active power from the grid which is equal to inverter power loss in shunt compensators. Also, inactive reference current (i_q^*) is calculated based on local load requirement. For example in shunt active power filters, i_q^* is equal to inactive component of the load current.

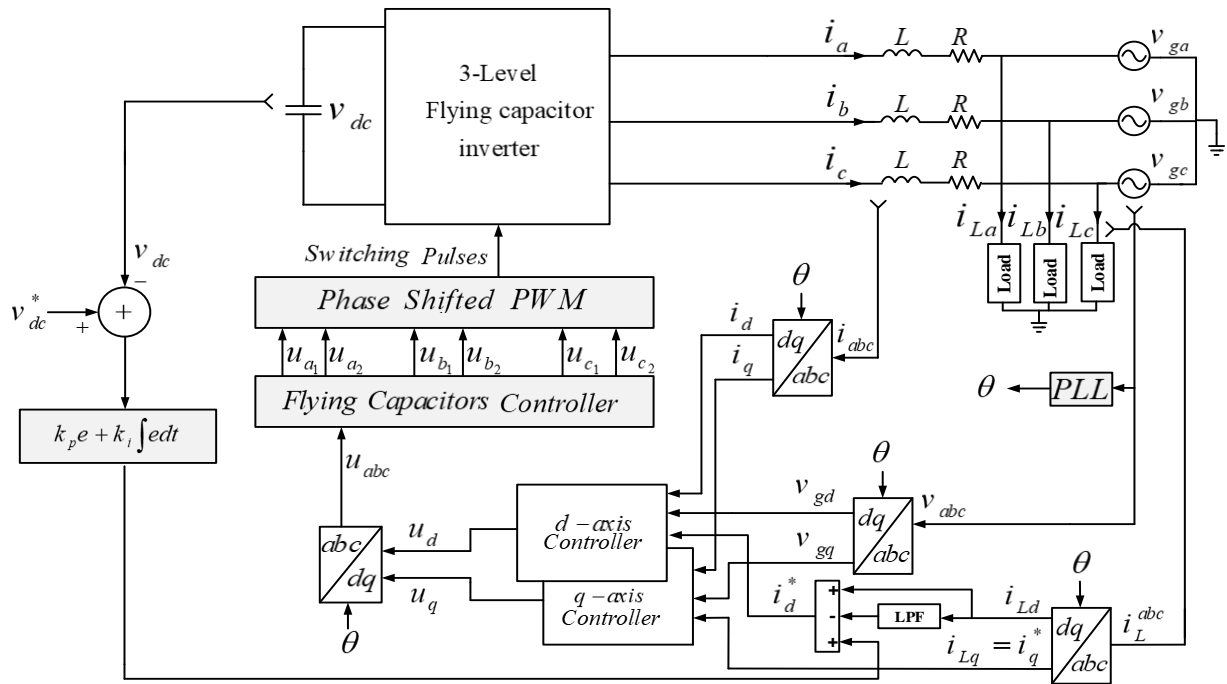


Fig. 7: Block diagram of the proposed SM controller for grid connected multilevel flying capacitor inverter

Simulation Results

In order to verify response of the proposed current controller in Fig. 7, grid connected three level flying capacitor inverter is simulated in MATLAB/Simulink software.

Nominal values of the system parameters as well as controller gains are listed in Table 1 and Table 2.

To investigate the steady-state and dynamic responses of the proposed closed loop system in reactive power compensating mode, the 20kVA resistive-inductive (RL) branch with 0.6 power factor is employed as a main local load. Also, active power filtering capability of the system is studied in the next tests.

Table 1: Nominal values of the system parameters

| Parameter | Symbol | Value |
|-------------------------------------|----------------------------|-------------|
| Grid voltage(rms) | v_g | 220V |
| Grid frequency | f | 50Hz |
| Switching frequency | f_s | 20kHz |
| DC-Link and flying capacitors | C, C_a, C_b and C_C | $1200\mu f$ |
| DC-side capacitor reference voltage | v_{dc}^* | 800V |
| AC-side coupling inductor | L | 1mH |
| AC-side coupling resistor | R | 0.1Ω |

Table 2: Controller gains

| Parameter | Value |
|----------------------|-------|
| k_p | 0.8 |
| k_i | 15 |
| α_1, α_2 | 20 |
| β_1, β_2 | 100 |
| k_1, k_2 | 1 |
| k'_p | 0.05 |
| k'_i | 0.1 |

A. Test 1

In this test, considering nominal value of the RL local load, response of the designed controller is investigated during system startup. Reference values of the DC link and flying capacitors are 800 V and 400 V respectively. Reactive reference current (i_q) of the closed loop system is defined according to local load reactive component. Also considering power loss of the inverter, the active current reference (i_d) is generated in the outer loop to stabilize the capacitor voltages on their desired values. According to Fig. 8a, Fig. 8b and Fig. 8c, it is seen that the proposed controller is able to stabilize the reactive power compensator satisfactorily. Also, during the steady-state conditions, steady-state error of the system state variables is zero. Due to reactive power compensation through the grid connected inverter, grid voltage and current are in phase after the transient interval of the response.

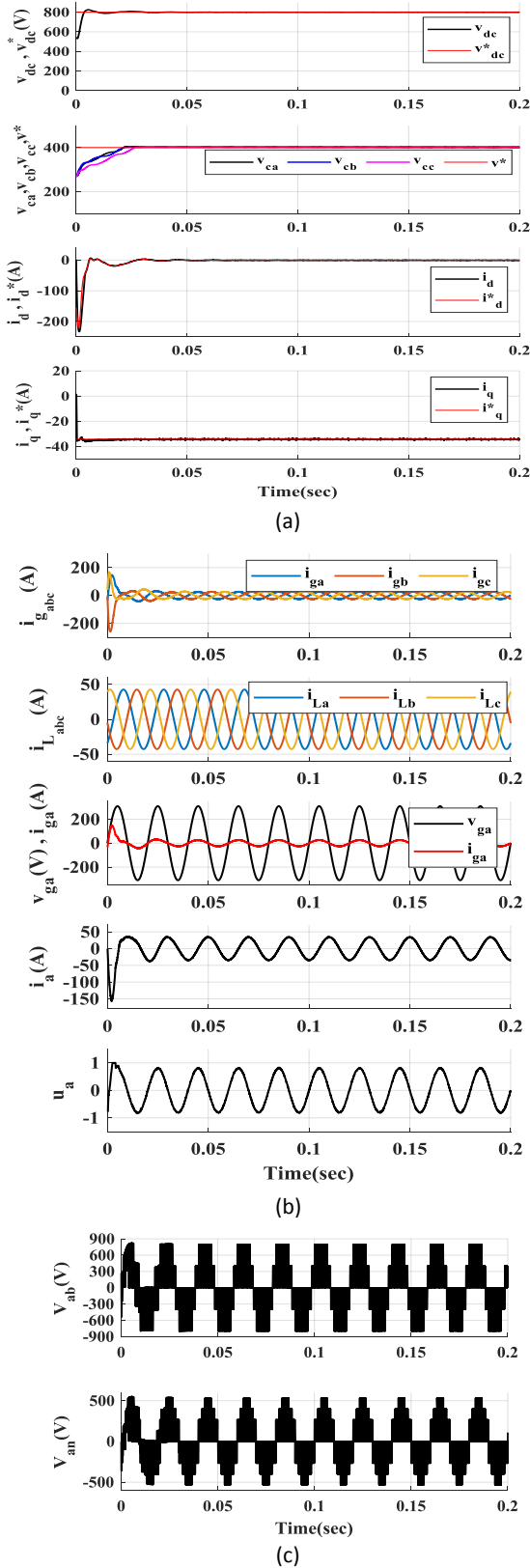


Fig. 8: Response of the system during startup and steady-state conditions; (a) State variables and reference values, (b) Grid currents and voltages, (c) Phase and line voltages of the inverter.

B. Test 2

In Fig. 9, dynamic response of the inner current controller is evaluated. At first, it is assumed that outer

controller regulates the DC link voltage without reactive compensation. Then, in $t=0.15$ s internal current loop is activated to compensate the nominal RL local load. It is seen that the proposed SM controller has fast dynamic response and is able to stabilize the output current of the grid-connected multilevel inverter with zero steady state error.

C. Test 3

In Fig. 10, dynamic response of the DC link and flying capacitor voltages are studied. At first, the closed loop system starts to compensate the nominal local load. Then, DC link voltage reference is stepped up from 750 V to 950 V. Also, references of the flying capacitor voltages are increased from 375 V to 475 V. In spite of changes of the reference voltage in a wide range, it is seen that the outer loop is stabilizing the DC link voltage with fast dynamics. Moreover, the overshoot of the response is completely acceptable which guarantees safe operation of the electrolyte type capacitors on the inverter's DC link. Furthermore, outer voltage loop has no steady state error due to employment of the integral term in the final controlling law of the controller.

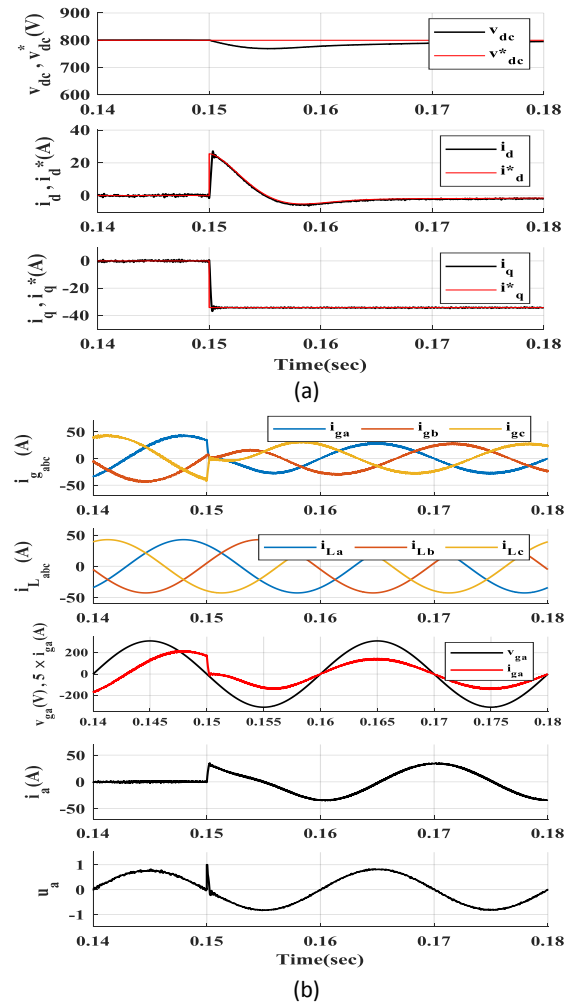


Fig. 9: Transient response of the internal SM current controller; (a) State variables and reference values, (b) Grid currents and voltages.

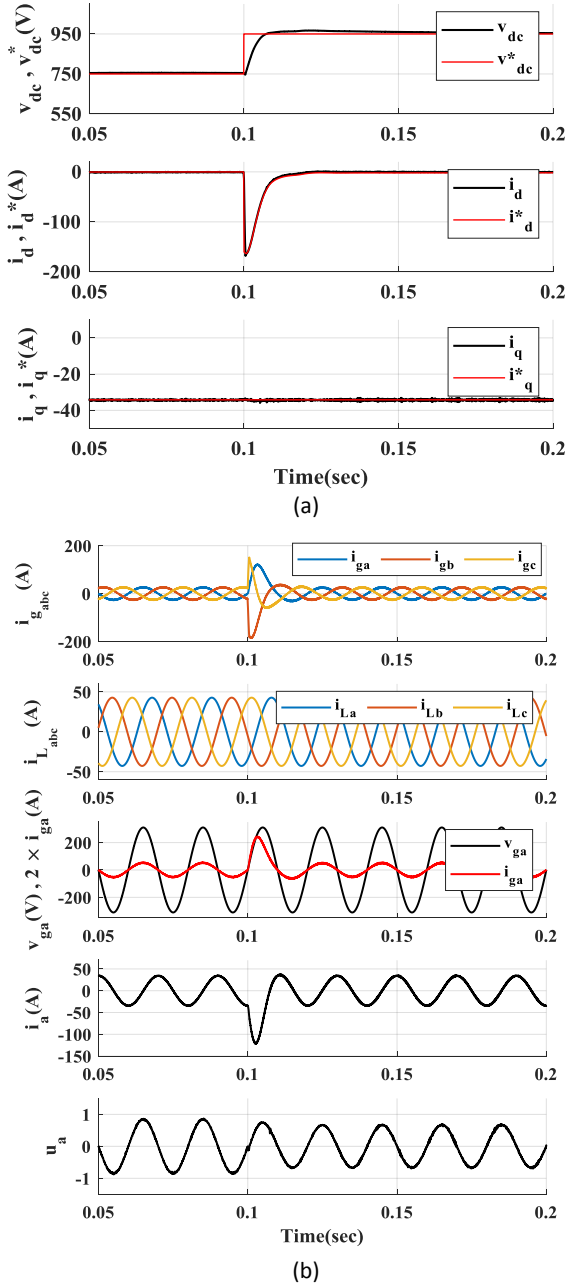


Fig. 10: Transient response of outer voltage controller during step changes of the DC link voltage references; (a) State variables and reference values, (b) Grid currents and voltages.

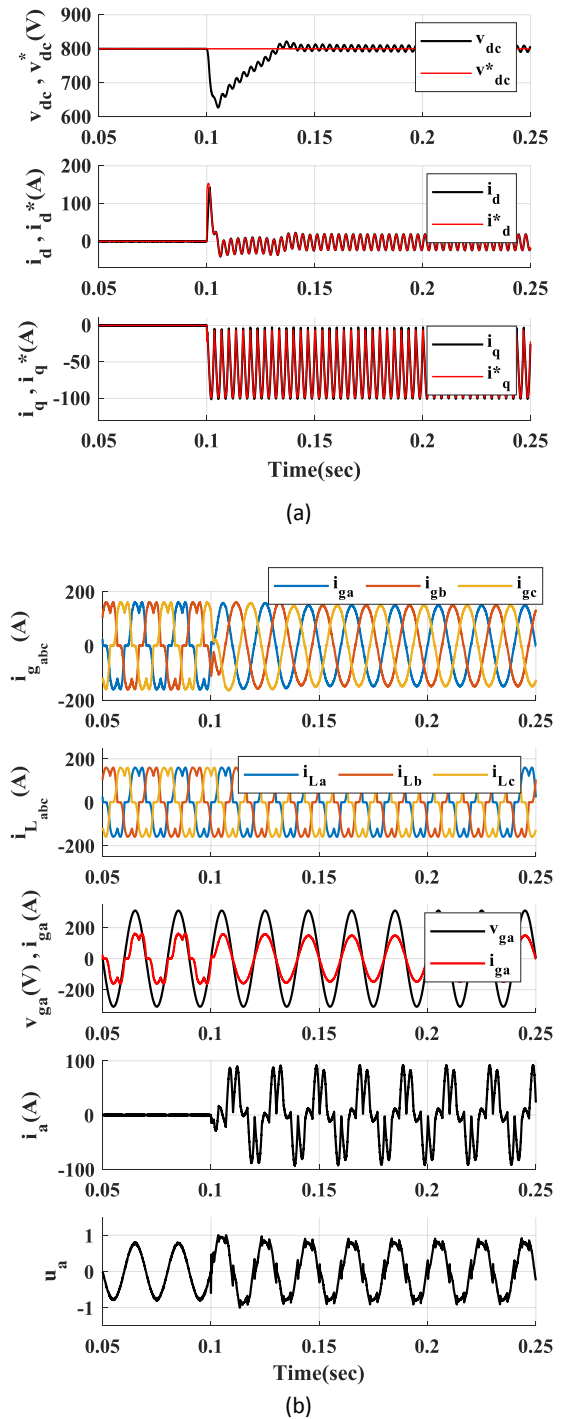
D. Test 4

In Fig. 11, dynamic response of the proposed controller during active power filtering mode is illustrated. At first, system is started to regulate the DC link capacitors. In this condition, reference of the i_q is zero and inverter output power is equal to its power loss to keep the DC link capacitors regulated. Then, in $t=0.1s$, the internal SM control system is activated to compensates the local load.

So, the grid current is non-sinusoidal before compensation as it includes harmonic components of

the nonlinear load. It is seen that after startup of the internal current loop, grid current will be pure sinusoidal with acceptable THD value. It should be noted that THD of the grid current is 20.61% before compensation that is reduced to 1.34% after activation of the internal loop of the proposed control approach.

So, proposed control strategy can be employed in active power filtering mode as well. It is seen that, in spite of fast changes of the inverter reference current, the proposed control strategy can track the reference value accurately.



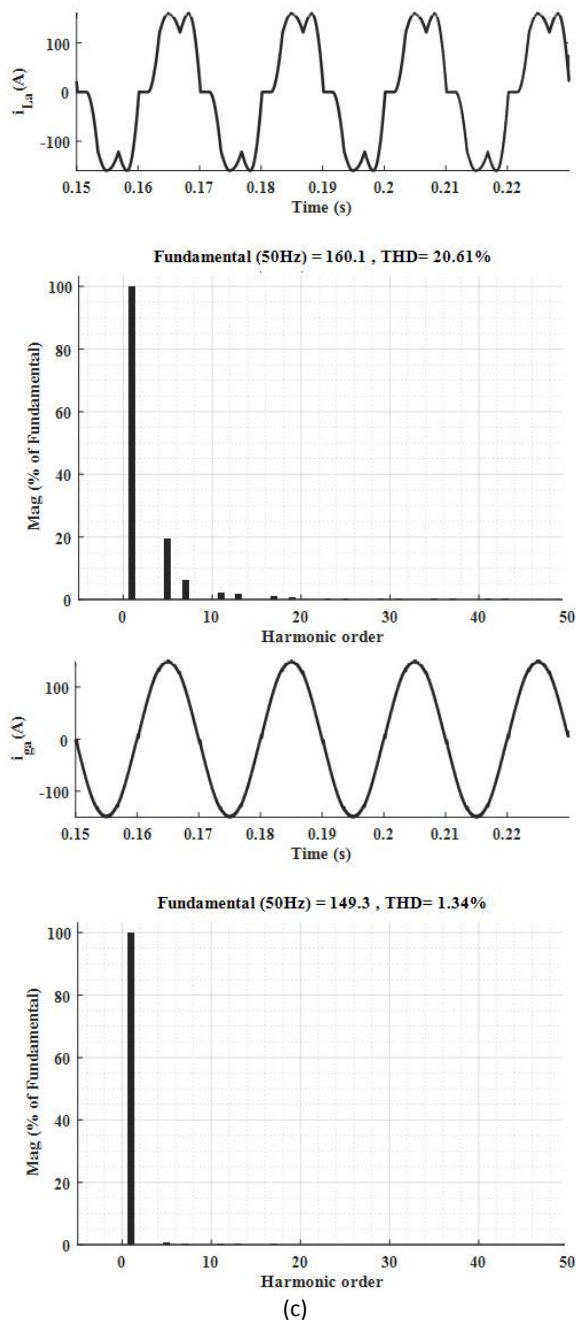


Fig. 11: Dynamic response of the proposed controller during active power filtering mode; (a) State variables and reference values, (b) Grid currents and voltages, (c) THD of the load and grid currents for phase A.

Conclusion

In this paper, a general purpose sliding mode controller is proposed for output current control of the grid connected multi-level flying capacitor inverter. The proposed controller enjoys very fast dynamic response, so it can be employed in wide ranges of application e.g. reactive compensation and harmonic mitigation modes. In active power filtering operation, it is able to eliminate harmonic components of the grid from 20.61% to 1.34% which is compatible with IEEE and IEC standards. The

designed controller uses an external loop to control the voltage of the inverter DC link and has a constant switching frequency. The stability of the proposed method has also been proved by using the Lyapunov stability theory. The simulation results show that in different operating conditions, the proposed controller has a stable and robust response.

Author Contributions

This paper is related to M.Sc. thesis of Miss Negin Ghaffari. All of the authors have the same contribution in different parts of the paper including system modeling, controller design and simulation.

Acknowledgment

The author gratefully acknowledges the Power Quality Lab of Arak University of Technology.

Conflict of Interest

The author declares that there is no conflict of interests regarding the publication of this manuscript. In addition, the ethical issues, including plagiarism, informed consent, misconduct, data fabrication and/or falsification, double publication and/or submission, and redundancy have been completely observed by the authors.

Abbreviations

| | |
|-------|----------------------------------|
| SM | Sliding Mode |
| PWM | Pulse Width Modulation |
| PI | Proportional Integral |
| THD | Total Harmonic Distortion |
| FACTS | Flexible AC Transmission Systems |
| NPC | Neutral Point Clamped |

References

- [1] Z. Hekss, A. Abouloifa, I. Lachkar, F. Giri, S. Echali, J.M. Guerrero, "Nonlinear adaptive control design with average performance analysis for photovoltaic system based on half bridge shunt active power filter," *Int. J. Electr. Power Energy Syst.*, 125, 2021.
- [2] Q. Su, W. Quan, W. Quan, G. Cai, J. Li, "Improved robust adaptive backstepping control approach on STATCOM for non-linear power systems," *IET Gener. Transm. Distrib.*, 11(3): 3428-3437, 2017.
- [3] M. Salimi, J. Soltani, A. Zakipour, "Experimental design of the adaptive backstepping control technique for single-phase shunt active power filters," *IET Power Electron.*, 10(8): 911-918, 2017.
- [4] A. Zakipour, S.S. Kojori, M. Salimi, "Low-Cost wind power conversion system based on permanent magnet synchronous generator and grid connected single-phase impedance source inverter," in *Proc. 2019 International Power System Conference (PSC)*: 616-622, 2019.
- [5] M.A. Hannan, P.J. Ker, M.S.H. Lipu, Z.H. Choi, M.S.A. Rahman, K.M. Muttaqi, et al., "State of the art of solid-state transformers: Advanced topologies, implementation issues, recent progress and improvements," *IEEE Access*, 8: 19113-19132, 2020.
- [6] X. Li, Y. Tan, X. Liu, Q. Liao, B. Sun, G. Cao, et al., "A cost-benefit analysis of V2G electric vehicles supporting peak shaving in Shanghai," *Electr. Power Syst. Res.*, 179: 106058, 2020.

- [7] Y.P. Siwakoti, P. Fang Zheng, F. Blaabjerg, L. Poh Chiang, G.E. Town, "Impedance-Source Networks for Electric Power conversion Part I: A topological review," *IEEE Trans. Power Electron.*, 30(2): 699-716, 2015.
- [8] P. Hamedani, A. Shoulai, "Utilization of CHB multilevel inverter for harmonic reduction in fuzzy logic controlled multiphase LIM drives," *J. Electr. Comput. Eng. Innovations (JECEI)*, 8(1): 19-30, 2019.
- [9] M.T. Bina, D.C. Hamill, "Average circuit model for angle-controlled STATCOM," *IEEE J. Electr. Power Appl.*, 152(3): 653-659, 2005.
- [10] X. Zhao, L. Chang, "Active and reactive power decoupling control of grid-connected inverters in stationary reference frame," *Chin. J. Electr. Eng.*, 3(3): 18-24, 2017.
- [11] M. Cespedes, J. Sun, "Adaptive control of grid-connected inverters based on online grid impedance measurements," *IEEE Trans. Sustainable Energy*, 5(2): 516-523, 2014.
- [12] Y. Wang, B. Ren, Q.-C. Zhong, "Robust power flow control of grid-connected inverters," *IEEE Trans. Ind. Electron.*, 63(11): 6887-6897, 2016.
- [13] A. Akhavan, H.R. Mohammadi, J.C. Vasquez, J. M. Guerrero, "Passivity-based design of plug-and-play current-controlled grid-connected inverters," *IEEE Trans. Power Electron.*, 35(2): 2135-2150, 2019.
- [14] H. Makhamreh, M. Sleiman, O. Kükrer, K. Al-Haddad, "Lyapunov-based model predictive control of a PUC7 grid-connected multilevel inverter," *IEEE Trans. Ind. Electron.*, 66(9): 7012-7021, 2018.
- [15] M. Salimi, J. Soltani, A. Zakipour, N.R. Abjadi, "Hyper-plane sliding mode control of the DC-DC buck/boost converter in continuous and discontinuous conduction modes of operation," *IET Power Electron.*, 8(8): 1473-1482, 2015.
- [16] J.-J.E. Slotine, W. Li, *Applied nonlinear control* vol. 199: Prentice hall Englewood Cliffs, NJ, 1991.
- [17] S. Mohammadi, H. Mosaddegh, M. Yousefian, "Mitigation of switching harmonics in shunt active power filter based on variable structure control approach," *J. Electr. Comput. Eng. Innovations (JECEI)*, 1(2): 83-88, 2013.
- [18] H. Zahedi, G. Arab Markadeh, S. Taghipour, "Real-time implementation of sliding mode control for cascaded doubly fed induction generator in both islanded and grid connected modes," *J. Electr. Comput. Eng. Innovations (JECEI)*, 8(2): 285-296, 2020.
- [19] H. Xiang, Y. Xu, L. Tao, H. Lang, C. Wenjie, "A Sliding-Mode controller with multiresonant sliding surface for single-phase grid-connected VSI with an LCL Filter," *IEEE Trans. Power Electron.*, 28(5): 2259-2268, 2013.
- [20] S.-W. Kang, K.-H. Kim, "Sliding mode harmonic compensation strategy for power quality improvement of a grid-connected inverter under distorted grid condition," *IET Power Electron.*, 8(8): 1461-1472, 2015.
- [21] H. Komurcugil, S. Ozdemir, I. Sefa, N. Altin, O. Kükrer, "Sliding-mode control for single-phase grid-connected LCL-Filtered VSI with double-band hysteresis scheme," *IEEE Trans. Ind. Electron.*, 63(2): 864-873, 2016.
- [22] S.M. Parida, P.K. Rout, S.K. Kar, "An auxiliary control aided modified sliding mode control for a PMSG based wind energy conversion system," *World J. Eng.*, 16(6): 725-736, 2019.
- [23] N.M. Dehkordi, N. Sadati, M. Hamzeh, "A robust backstepping high-order sliding mode control strategy for grid-connected DG units with harmonic/interharmonic current compensation capability," *IEEE Trans. Sustainable Energy*, 8(2): 561-572, 2016.
- [24] J. Ritonja, D. Dolinar, B. Polajzer, "Adaptive and robust controls for static excitation systems," *Compel: Int. J. Comput. Math. Electr. Electron. Eng.*, vol. 34(3): 864-881, 2015.
- [25] R.P. Vieira, L.T. Martins, J.R. Massing, M. Stefanello, "Sliding mode controller in a multiloop framework for a grid-connected VSI with LCL filter," *IEEE Trans. Ind. Electron.*, 65: 4714-4723, 2017.
- [26] A. Zakipour, S. Shokri Kojori, M. Tavakoli Bina, "Closed-loop control of the grid-connected Z-source inverter using hyper-plane MIMO sliding mode," *IET Power Electron.*, 10(15): 2229 – 2241, 2017.
- [27] U.K. Shinde, S.G. Kadwane, S.Gawande, M.J.B. Reddy, D. Mohanta, "Sliding mode control of single-phase grid-connected quasi-Z-source inverter," *IEEE Access*, 5: 10232-10240, 2017.
- [28] F. Sebaaly, H. Vahedi, H.Y. Kanaan, N. Moubayed, K. Al-Haddad, "Design and implementation of space vector modulation-based sliding mode control for grid-connected 3L-NPC inverter," *IEEE Trans. Ind. Electron.*, 63: 7854-7863, 2016.
- [29] F. Sebaaly, H. Vahedi, H.Y. Kanaan, N. Moubayed, K. Al-Haddad, "Sliding mode fixed frequency current controller design for grid-connected NPC inverter," *IEEE J. Emerging Sel. Top. Power Electron.*, 4: 1397-1405, 2016.
- [30] H. Makhamreh, M. Trabelsi, O. Kükrer, H. Abu-Rub, "An effective sliding mode control design for a grid-connected puc7 multilevel inverter," *IEEE Trans.Indu. Electron.*, 67: 3717-3725, 2019.
- [31] M. Mehrasa, E. Pouresmaeil, M.F. Akorede, B.N. Jørgensen, J.P. Catalão, "Multilevel converter control approach of active power filter for harmonics elimination in electric grids," *Energy*, 84: 722-731, 2015.

Biographies



Negin Ghaffari received the B.Sc. Degree in Electrical Engineering from the Arak University of Technology (ArakUT), Arak, Iran, in 2018 and presently she is studying on M.Sc. Degree in Power electronics, Arak University of Technology (ArakUT), Arak, Iran. Her research interests include nonlinear control of the active power filters and grid connected inverters.



Adel Zakipour was born in Ardabil, Iran, in 1981. He received his Ph.D. degrees in Electrical Engineering from K.N.Toosi University of technology, Tehran, Iran, in 2017. Currently, he is an assistant professor in power electronics at department of electrical engineering, Arak university of technology. His research interests include design and control of the DC/DC and DC/AC converter, grid connected inverters and variable speed drive.



Mahdi Salimi was born in Ardabil, Iran, in 1979. He received his B.S. and M.S. degrees in Electrical Engineering from K.N.T University of Technology, Tehran, Iran, in 2000 and 2002, respectively, and his Ph.D. degree in Power Electronics from Science and Research Branch, Islamic Azad University, Tehran, Iran, in 2012. Dr. Salimi has joined university of Nottingham, UK as a research fellow from 2019-2020. Since 2003, he has been with Islamic Azad University, where he is currently assistant professor at the department of electrical engineering. His research interests include closed-loop control of power electronics converters, high gain DC-DC converters, grid-connected inverters, and renewable energy.

Copyrights

©2021 The author(s). This is an open access article distributed under the terms of the Creative Commons Attribution (CC BY 4.0), which permits unrestricted use, distribution, and reproduction in any medium, as long as the original authors and source are cited. No permission is required from the authors or the publishers.



How to cite this paper:

N. Ghaffari, A. Zakipour, M. Salimi, "State space modeling and sliding mode current control of the grid connected multi-level flying capacitor inverters," J. Electr. Comput. Eng. Innovations, 9(2): 215-228, 2021.

DOI: [10.22061/JECEI.2021.7626.412](https://doi.org/10.22061/JECEI.2021.7626.412)

URL: https://jecei.sru.ac.ir/article_1521.html





Research paper

The Feasibility of Machine-Learning Methods to Extract the Surface Evaporation Quantity Using Satellite Imagery

E. Norouzi, S. Behzadi*

Surveying Engineering Department, Faculty of Civil Engineering, Shahid Rajaee Teacher Training University, Tehran, Iran.

Article Info

Article History:

Received 27 October 2020
Reviewed 25 December 2020
Revised 19 January 2021
Accepted 21 March 2021

Keywords:

Climatic phenomena
Remote sensing
Machine learning
Decision tree
GIS

*Corresponding Author's Email Address:
behzadi.saeed@gmail.com

Abstract

Background and Objectives: Climate phenomena such as quantity of surface evaporation are affected by many environmental factors and parameters, which makes modeling and data mining difficult. On the other hand, the estimation of surface evaporation for a target station can be difficult as a result of partial or complete lack of local meteorological data under many conditions. In this regard, satellite imagery can play a special role in modeling and data mining of climatic phenomena, because of their significant advantages, including availability and their potential analysis. Therefore, addressing the improvement and expansion of machine learning methods and modeling algorithms along with remote sensing data is inevitable.

Methods: In this research, we intend to study the ability of 11 machine-learning modeling algorithms to model data and surface evaporation phenomena using satellite imagery. We used two methods to prepare the database: PCA and its opposite method using standard deviation and correlation.

Results: The calculation of the Root Mean Squared Error (RMSE) indicated that, in general, the use of the PCA method has a better result in preparing and reducing the dimensions of large databases for all methods of machine learning. The SEGPR model was ranked first with the least error (93.49%) in the Principal Component Analysis (PCA) method, and the Artificial Neural Network (ANN) model performed well in both data preparation methods (93.42, 93.38), and the Classification-Tree-Coarse model had the highest error in both methods (92.66, 92.67).

Conclusion: Consequently, it can be said that by changing the methods of database preparation in order to train models, the modeling results can be changed effectively.

©2021 JECEI. All rights reserved.

Introduction

The loss of water from lakes, rivers, oceans, vegetation, and the earth, as well as man-made structures such as reservoirs and irrigation conduits, is a major concern of hydrologists and irrigation specialists. This loss, compounded by the lack of usable water in some areas, indicates a need for field and laboratory research that will contribute to the understanding of the processes

and parameters that comprise and contribute to evaporation [1]. Since the role of environmental variables in the amount and distribution of surface evaporation is undeniable, and the difference in the surface evaporation of neighboring points in small basins is justified by the involvement of local factors, consideration of these factors are important in modeling and analysis. In this regard, remote sensing technology

plays an unparalleled role in obtaining surface evaporation data, because satellite images have advantages and privileges that the availability and analysis of them are the most important points [2]. Considering the importance of changing the future climate of the planet and the wide-reaching effects on various aspects of meteorological and hydrological issues on the planet, extensive efforts have been made to extract climate data more accurately as well as less costly, and fewer human and physical errors in measuring climate data in the future. On the other hand, evaporation is a non-linear process which occurs in nature due to temperature differences [3]; the changes in climate variables in regional scales are also not explicitly identified. Therefore, addressing the improvement and extension of machine learning methods and modeling algorithms along with remote sensing data is inevitable.

In interpolation methods, a good number of scattered terrestrial stations is required to be used in the target area, so in areas where these conditions are not available, one cannot expect an appropriate approximation for the result of interpolation and modeling [4]. In contrast, recently satellite imagery is widely available at very low cost and even free of charge [5]. Therefore, using remote sensing data to model climate data is a convenient and economical way. In recent times, the artificial intelligence approaches such as coactive neuro-fuzzy inference system (CANFIS), adaptive neuro-fuzzy inference system (ANFIS) which is hybrid of artificial neural networks (ANN) and fuzzy inference system (FIS), fuzzy-logic (FL) [6], radial basis neural network (RBNN) which is a type of ANN, support vector machines (SVM), generalized regression neural network (GRNN) which is a type of ANN, genetic algorithm (GA) [7], wavelet transformation (WT) and multi-layer perceptron neural network (MLPNN) have been significantly utilized in diverse fields such as modeling daily evaporation [3, 8-11]. In order to model the target data, the researchers used terrestrial station data as inputs, which have many limitations. So many researchers tend to use satellite imagery [2, 12-14]. In studying model trees and the neural network for modeling the rainfall, [15] concluded that tree models could be a suitable substitute for the neural network for precipitation modeling. Meike Kühnlein, in a study [16], on improving the accuracy of rainfall rates from optical satellite sensors with machine learning, showed that using machine learning methods can accurately improve the rates of precipitation even up to hourly rates. Doña et al [17] used remote sensing to estimate the temporal variation of the flooded area and their associated hydrological patterns related to the seasonality of precipitation and evapotranspiration. He applied several

inverse modeling methods, such as two-band and multispectral indices, single-band threshold, classification methods, artificial neural network, support vector machine algorithm and genetic programming and the genetic programming approach yielded the best results, with a kappa value of 0.98 and a total error of omission-commission of 2%. Xu et al [13] up-scaled evapotranspiration from eddy covariance flux tower sites to the regional scale with machine learning algorithms. Five machine learning algorithms were employed for evapotranspiration upscaling including artificial neural network, Cubist, deep belief network, random forest, and support vector machine. They demonstrated that the artificial neural network, Cubist, random forest, and support vector machine algorithms have almost identical performance in estimating evapotranspiration and have slightly lower root mean square error than deep belief network at the site scale. On the other hand, in spite of the considerable importance of preparing the initial data to enter the model, in many cases it is not taken into account as much as required.

In this research, we intend to investigate the relationship between Landsat 8 satellite imagery and terrestrial station data for surface evaporation quantity using different machine learning methods, including Artificial Neural Network, Neuro-Fuzzy (ANFIS), Classification-Tree-Coarse, Classification-KNN-Coarse, and Regression-Tree-Medium, Regression-interactions linear, Fine Gaussian SVM, Medium Gaussian SVM, Gaussian Process Regression- SEGPR, Ensemble-Boosted Trees, and Ensemble-Bagged Trees. Then we compare the different methods to find the optimal method. This study was conducted with the following objectives: (i) selecting appropriate input variables combination for the models using two ways, one of them is Principal Component Analysis (PCA) and the other one is applying standard deviation and correlation as an indicator; (ii) calibrating and validate the heuristic models with selected input variables; and (iii) comparing the results from the listed models with those of the interpolation based models, IDW.

Technical Work Preparation

Study Area and Data Acquisition

The study area includes three provinces of Tehran, Alborz and Qazvin in Iran, which are located between $48^{\circ} 43' 38.83''$ E to $53^{\circ} 09' 11.70''$ E longitude and $34^{\circ} 50' 14.29''$ N to $36^{\circ} 47' 1.33''$ N latitude at an altitude of 1495.9m above MSL (Mean Sea Level) Fig. 1. In Fig. 1, the study area and the position of stations, which have the ability to measure surface evaporation, are shown on the region map. Daily surface evaporation data are collected from Meteorological Organization and Water Resources Management Organization of Iran.

The primary data source was a series of Landsat-8 satellite images. The spatial resolution of the band 8 for the satellite is 15 m; other bands (1,2,3,4,5,6,7,9,10,11) have a spatial resolution of 30 m. The selected Landsat-8 scenes are path 164 / row 35 and path 165/ row 35, which covers the extent of the area of interest. Scenes that were mostly cloud-free from 2013 to 2016 are obtained from the United States Geological Survey Earth Explorer website [18]. All images were Level 1T products, which have been precision and terrain corrected in the GeoTIFF format and are in the UTM Zone 39S projection and WGS datum [19]. The resulting dataset comprised 65 full scenes.

Preparing the Initial Datasets for Machine Learning

Machine Learning (ML) depends heavily on data. It is the most crucial aspect that makes algorithm training possible and explains why machine learning became so popular in recent years. Regardless of actual terabytes of information and data science expertise, if data records are not prepared and organized, a machine will be nearly useless or perhaps even harmful. All datasets are always needed correction. That's why data preparation is such an important step in the machine learning process. In a nutshell, data preparation is a set of procedures that helps make the dataset more suitable for machine learning. In broader terms, the data preparation also includes establishing the right data collection mechanism. These procedures consume most of the time spent on machine learning. Sometimes it takes months before the first algorithm is built [20, 21].

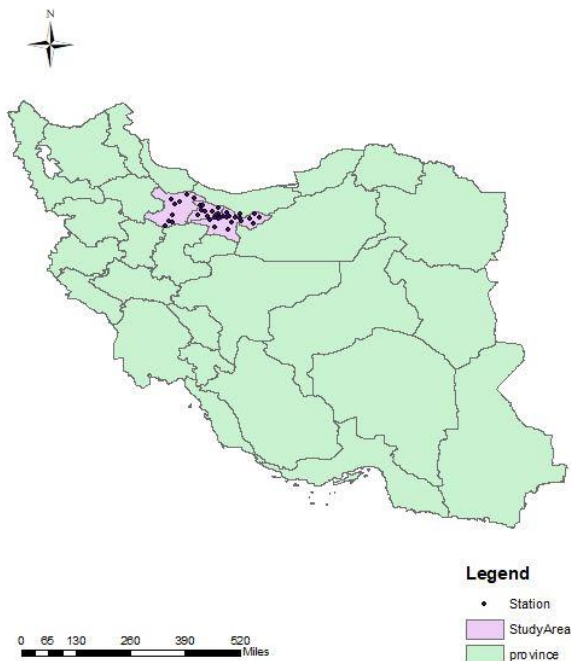


Fig. 1: Location map of the study area and Distribution of terrestrial stations.

Knowing what must be modeled or estimated will help to decide which data may be more valuable to collect. When formulating the problem, data exploration must be conducted, and it must be tried to think in the categories of classification, clustering, regression, and ranking. For instance, when an algorithm needs to answer binary yes-or-no questions, classification is the best method, or when it comes to finding the rules of classification and the number of classes, clustering is a suitable choice etc. Generally since the surface evaporation dataset is formed by numerical values, regression algorithm is more beneficial to this case [20, 21]; however, (i) it must be considered that surface evaporation depends on numerous factors which makes it too complicated to be formulated accurately; (ii) On the other hand, It is tempting to include as much data as possible. Since the target attribute (what value you want to model) is known, common sense will guide the further. It can be assumed which values are critical and which are going to add more dimensions and complexity to the dataset without any useful contribution. This approach is called attribute sampling. (iii) Since missing values can tangibly reduce prediction accuracy, this issue must be addressed as a priority. In terms of machine learning, assumed or approximated values are “more right” for an algorithm than just missing ones. Hence in this study, all the well-known methods of machine learning are almost applied with two statistical data preparation techniques, one of them is PCA and the other one is the way which uses standard deviation and correlation, in order to find the best algorithm for the purpose of the study.

A. Determining Optimal Bands Using PCA Technique

Major databases are increasingly expanding and publicizing, while making them more difficult to interpret. Principal Component Analysis (PCA) is a technique for reducing the size of such databases, increasing the capability of interpreting, and simultaneously minimizing data problem. The PCA technique does this by creating a new variable that maximizes the variance successively [22]. Table 1 illustrates the result of PCA technique. All bands of Landsat-8 images except for bands 8 and 11 were used to extract 4 optimal bands.

B. Determine Optimal Bands Using Standard Deviation and Correlation

Using standard deviation and correlation statistics, parameters that have greater correlation and amplitude than each other are determined, and then a number of optimal parameters is used instead of using all of the parameters. In this study it is done according to (1). This formula is set for three parameters but it is applied for

five parameters (including four bands of satellite imagery and surface evaporation values):

$$x = \frac{(std(B1) + std(B2) + std(B3))}{|corr(B1, B2)| + |corr(B1, B3)| + |corr(B2, B3)|} \quad (1)$$

where x is the benchmark for optimization, B_i is parameter (bands and surface evaporation value), std

and $corr$ are standard deviation and correlation respectively. The x index in (1) was calculated for all possible states in selecting 4 among 9 bands of satellite images. The state which had maximum value of the optimization index is considered as the best quadr-combination of 9 bands of landsat-8 images. The selected state was the combination of bands 1, 2, 9, and 10. Table 2 shows the result of calculations.

Table 1: The result of the PCA technique. Extraction of four optimal parameters using nine satellite image bands and with respect to surface evaporation values (where B1, B2, ... are bands of satellite images, SE is surface evaporation values and P1,P2,.. are PCA method outputs).

| B1 | B2 | B3 | B4 | B5 | B6 | B7 | B9 | B10 | SE(mm) | | P1 | P2 | P3 | P4 | SE(mm) |
|---------|---------|---------|---------|--------|--------|-------|-------|--------|--------|--|--------|--------|--------|--------|--------|
| ... | ... | ... | ... | ... | ... | ... | ... | ... | ... | | ... | ... | ... | ... | ... |
| ... | ... | ... | ... | ... | ... | ... | ... | ... | ... | | ... | ... | ... | ... | ... |
| 89.901 | 90.358 | 89.790 | 84.962 | 65.623 | 18.771 | 5.453 | 0.171 | 10.915 | 6.6 | | -0.739 | -0.756 | -0.067 | -0.061 | 6.6 |
| 81.208 | 83.540 | 87.441 | 86.594 | 68.547 | 19.050 | 5.144 | 0.144 | 9.718 | 3.1 | | 6.164 | -3.217 | 1.999 | 0.643 | 3.1 |
| 85.637 | 86.940 | 83.352 | 76.810 | 68.990 | 15.933 | 4.429 | 0.165 | 10.383 | 10.9 | | -0.287 | 1.138 | -0.058 | 0.234 | 10.9 |
| 75.756 | 75.191 | 70.831 | 74.459 | 64.291 | 15.270 | 3.951 | 0.114 | 8.206 | 3.5 | | -0.413 | 0.443 | -0.104 | -0.069 | 3.5 |
| 100.999 | 104.870 | 111.148 | 111.205 | 80.569 | 23.728 | 7.140 | 0.190 | 12.126 | 11 | | -0.295 | 1.289 | 0.069 | -0.171 | 11 |
| 108.146 | 110.718 | 107.014 | 97.934 | 66.238 | 17.571 | 5.264 | 0.199 | 12.254 | 15 | | -0.905 | 0.713 | -0.082 | 0.743 | 15 |
| 108.220 | 106.200 | 97.357 | 83.510 | 80.723 | 14.908 | 3.963 | 1.700 | 8.051 | 8.7 | | -1.460 | -0.177 | -0.056 | 0.508 | 8.7 |
| 79.493 | 82.053 | 85.722 | 82.855 | 65.064 | 17.944 | 4.952 | 0.208 | 8.961 | 2.6 | | -1.549 | -0.456 | 0.103 | -0.158 | 2.6 |
| 74.560 | 72.920 | 71.325 | 73.404 | 58.903 | 14.413 | 3.984 | 0.116 | 11.620 | 10.6 | | -1.482 | 0.178 | 0.012 | 0.617 | 10.6 |
| 61.609 | 58.271 | 53.319 | 52.317 | 40.409 | 10.218 | 2.820 | 0.082 | 9.775 | 5.4 | | -1.680 | 0.234 | 0.261 | 0.051 | 5.4 |
| ... | ... | ... | ... | ... | ... | ... | ... | ... | ... | | ... | ... | ... | ... | ... |
| ... | ... | ... | ... | ... | ... | ... | ... | ... | ... | | ... | ... | ... | ... | ... |

Table 2: The result of calculations using equation (1). Extraction of four optimal bands using nine satellite image bands and with respect to surface evaporation values (where B1, B2, ... are bands of satellite images, SE is surface evaporation values and the item specified in the middle table is a suitable combination of satellite imagery bands).

| B1 | B2 | B3 | B4 | B5 | B6 | B7 | B9 | B10 | SE(mm) | | | B1 | B2 | B9 | B10 | SE(mm) |
|--------|--------|--------|--------|--------|-------|------|-------|------|--------|--|-----------------|---------|--------|--------|------|--------|
| ... | ... | ... | ... | ... | ... | ... | ... | ... | ... | | State | X | ... | ... | ... | ... |
| ... | ... | ... | ... | ... | ... | ... | ... | ... | ... | | ... | ... | ... | ... | ... | ... |
| 300.92 | 310.34 | 275.27 | 242.53 | 156.84 | 26.02 | 7.14 | 5.85 | 4.11 | 1.7 | | B1,B2,B4,B10,SE | 197.45 | 300.92 | 310.34 | 5.85 | 4.11 |
| 198.18 | 198.89 | 169.72 | 146.19 | 93.33 | 13.43 | 3.89 | 3.99 | 4.26 | 3.2 | | B1,B2,B5,B6,SE | 52.66 | 198.18 | 198.89 | 3.99 | 4.26 |
| 265.91 | 272.65 | 228.21 | 200.82 | 130.33 | 16.66 | 4.32 | 3.70 | 4.19 | 1.3 | | B1,B2,B5,B7,SE | 48.90 | 265.91 | 272.65 | 3.72 | 4.19 |
| 267.38 | 240.27 | 235.58 | 206.36 | 133.30 | 17.62 | 4.62 | 5.08 | 3.88 | 1.3 | | B1,B2,B5,B9,SE | 46.20 | 267.38 | 272.16 | 3.70 | 3.88 |
| 236.44 | 273.45 | 205.74 | 179.50 | 115.60 | 14.53 | 4.26 | 5.37 | 3.94 | 2.4 | | B1,B2,B5,B10,SE | 167.80 | 236.44 | 240.27 | 5.08 | 3.94 |
| 268.55 | 285.21 | 232.88 | 203.74 | 130.84 | 15.71 | 4.29 | 6.72 | 3.85 | 1.8 | | B1,B2,B6,B7,SE | 47.97 | 268.55 | 273.45 | 5.37 | 3.85 |
| 279.17 | 267.14 | 247.85 | 216.60 | 139.04 | 16.83 | 4.76 | 8.01 | 3.38 | 3 | | B1,B2,B6,B9,SE | 55.83 | 279.17 | 285.21 | 6.72 | 3.38 |
| 262.84 | 291.40 | 227.43 | 200.02 | 128.73 | 8.10 | 3.09 | 12.61 | 2.76 | 3.3 | | B1,B2,B6,B10,SE | 177.32 | 262.84 | 267.14 | 8.01 | 2.76 |
| 322.41 | 327.09 | 281.54 | 244.48 | 156.40 | 7.56 | 2.78 | 6.82 | 3.52 | 3.8 | | B1,B2,B9,B10,SE | 282.454 | 322.41 | 327.09 | 6.82 | 3.52 |
| 228.78 | 232.34 | 196.86 | 172.96 | 111.20 | 6.55 | 2.35 | 5.26 | 3.44 | 0.8 | | B1,B3,B4,B5,SE | 48.133 | 228.78 | 232.34 | 5.26 | 3.44 |
| ... | ... | ... | ... | ... | ... | ... | ... | ... | ... | | ... | ... | ... | ... | ... | ... |

Machine Learning Algorithms

In general, 11 machine learning methods were used to model the surface evapotranspiration using satellite imagery. In this section, each of which is briefly

described:

A. Artificial Neural Network (ANN)

Neural network is one of the techniques of machine learning that its application in modeling and predicting

many phenomena including climate phenomena has been proved in numerous studies. Sulaiman and Wahab [10] describe the modeling and prediction of heavy rainfall. Although it is difficult to model and predict climatic phenomena, machine learning methods, especially artificial neural networks, are reliable and it can be used for climate phenomena such as precipitation and surface evaporation [4].

B. Neuro-Fuzzy (ANFIS)

An artificial neural network based on the Takagi-Sugeno fuzzy system [23]. Since this system combines neural networks and fuzzy logic concepts, both of them can be used in the same frame [24].

C. Classification-Tree-Coarse

This technique is a tool to support decisions that use trees to model. The Decision Tree is commonly used in various research and operations. Specifically, in the decision analysis, it is used to identify the strategy that is most likely to reach the goal. Another use of Decision Trees is the description of conditional probability calculations [25].

D. Classification-KNN-Coarse

The KNN algorithm is one of the simplest data mining and classification algorithms. This algorithm performs simple classification operations and returns reliable results as predictions. In a literal sense, this method chooses the tracks in which the selected neighborhood has the highest number of records attributed to them. Therefore, traces that are more closely related to each other in the K nearest neighbor are considered as the new record category [26].

E. Regression-Tree-Medium

This method is one of the machine learning regression techniques that uses a decision tree to predict and model, and acts as a combination. Classification and regression tree algorithm is one of the widely used algorithms in water resources management related fields since it is easy to understand and interpretable prediction model [27, 28].

F. Regression-Interactions Linear

Linear regression is a modeling method and the relationship between an associated variable and one to several other variables that can be used to solve many real-world problems. Regression interactions allow for the detection of effect heterogeneity but require that heterogeneity is a linear function of an observed and reliably measured predictor of heterogeneity [29].

G. Fine Gaussian SVM

One of the most common methods in the data classification domain is the SVM algorithm or support vector machine. In simple terms, support vectors are a collection of points in the n-dimensional data that

defines the boundaries of the categories, and the classification of the data is based on them, and by moving one of them, the output of the classification may be Change [30].

H. Medium Gaussian SVM

SVM is basically a binary separator. A multi-class pattern recognition can be achieved by combining two-class vector machines [30].

I. Gaussian Process Regression- SEGPR

Gaussian process consists of a set of random variables as one of the new methods of data mining, with its normal characteristics and using kernel functions, has a high ability to solve nonlinear problems. The Gaussian regression models are based on the assumption that the regulatory observation should carry information about each other. Gaussian processes are a way to specify the priority directly on the function space [31].

J. Ensemble-Boosted Trees

Instead of using only one decision tree, Ensemble methods use the combination of multiple decision trees to predict better performance. The main idea behind these models is that weaker learners combine to form a stronger learner [32]. Boosting is an ensemble technique to create a collection of predictors. In this technique, learners are learned sequentially with early learners fitting simple models to the data and then analyzing data for errors. In other words, consecutive trees (random sample) are fitted at every step, and the goal is to solve for net error from the prior tree.

K. Ensemble-Bagged Trees

Bagging is another Ensemble technique that is used when the goal is to reduce the variance of a decision tree [32]. Here idea is to create several subsets of data from training sample chosen randomly with replacement. Now, each collection of subset data is used to train their decision trees. As a result, we end up with an ensemble of different models. Average of all the predictions from different trees are used which is more robust than a single decision tree.

Results and Discussion

In this study, after preparing (or so-called GIS-Ready) the surface evaporation data for 40 stations, along with corrected reflectance values of their Landsat-8 satellite imagery, four optimal bands of the nine bands (1,2,3,4,5,6,7,9,10) are selected in Landsat-8 satellite imagery to continue the work. In this study two ways are applied: first one through the PCA method and the other one with using (1).

In each of these two methods the data is divided into two categories: Train and Test.

In the next step, in order to model the relationship between satellite images and surface evaporation values

and generate a decision function, train data is introduced into each of the modeling methods described briefly in the previous section, then the simulator or decision function is obtained for each of them.

Since 11 machine learning methods have been applied, 11 functions are obtained for the PCA method, and then 11 functions for the second method (Optimal Index).

Models' accuracies were evaluated according to (i) the Root Mean Square Error (RMSE) statistic and (ii) compared with the generated map of the interpolation method.

The RMSE can be expressed as

$$RMSE = \sqrt{\frac{1}{N} \sum_{i=1}^N (SE_{i,observed} - SE_{i,predicted})^2} \quad (1)$$

where N is the number of data points used in the study and SE represents surface evaporations.

A. Modeling Daily Surface Evaporations Using PCA Technique

In this part, mentioned machine learning methods were applied for estimating surface evaporations of 40 stations on the study area using 4 optimal bands obtained by the PCA method. In PCA method, all satellite image bands are used to select the optimal bands for modeling. Each band has a coefficient, and the stronger the bands are related to the data, the larger the coefficient. Table 3 gives the test results of the applied models in estimating surface evaporation data. RMSE values range from 7.9417 to 8.9458 mm for the 11 models. The minimum RMSE value were found for SEGPR algorithm (test set) while the Classification-Tree-Coarse model provided the worst accuracy. Therefore, according to RMSE values in this study, SEGPR is known as the best method among other applied algorithms for surface evaporation modeling. Figure 2 illustrates the error variation of the test results spatially for the SEGPR models. From the figure, it is clear that all the models generally provided similar accuracy.

Table 3: Test results of the applied models in estimating surface evaporation by using PCA technique

| Machine Learning Algorithms | RMSE (mm) | 100 - Normalized RMSE (%) |
|---------------------------------------|-----------|---------------------------|
| Artificial Neural Network | 8.017072 | 93.42863 |
| Neuro-Fuzzy (ANFIS) | 8.158462 | 93.31274 |
| Classification-Tree-Coarse | 8.945852 | 92.66733 |
| Classification-KNN-Coarse | 8.77615 | 92.80643 |
| Regression Interactions Linear | 8.3724 | 93.13738 |
| Regression-Tree-Medium | 7.9729 | 93.46484 |
| Fine Gaussian SVM | 8.1792 | 93.29574 |
| Medium Gaussian SVM | 7.9944 | 93.44721 |
| Squared Exponential GPR | 7.9417 | 93.49041 |
| Ensemble Boosted Trees | 7.9928 | 93.44852 |
| Ensemble Bagged Trees | 8.0257 | 93.42156 |

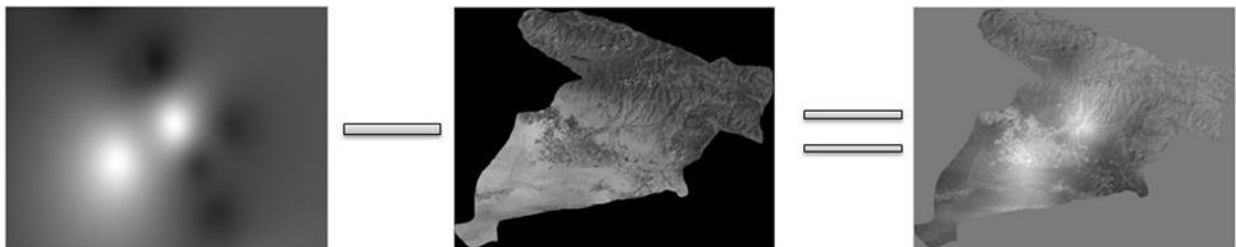


Fig. 2: The error variation of the test results spatially for the SEGPR model. From the left, the map obtained from the IDW interpolation method and the SEGPR machine learning algorithm and spatial distribution of errors.

B. Modeling Daily Surface Evaporations Using the X Index in (1)

At this stage, all the steps taken for output of the PCA technique are performed in the previous section for the optimal bands obtained from the index X (introduced in Section 2) method. The 11 machine learning methods are applied for estimating surface evaporations of 40 stations in the studied area using 4 optimal bands obtained by the index X. Table 4 shows test results of the applied models in estimating surface evaporation data.

The minimum and maximum RMSE values are 8.0649 and 8.9417 for Artificial Neural Network and Classification-Tree-Coarse methods, respectively. Therefore, according to RMSE values in this study, the neural network method is known as the best method among other methods for modeling surface evaporation.

Figure 3 illustrates the error variation of validation results spatially for the Artificial Neural Network model. It is also clear from the results of this section that all models generally offer the same precision.

Table 4: Test results of the applied models in estimating surface evaporation by using the x index

| Machine Learning Algorithms | RMSE (mm) | 100 - Normalized RMSE (%) |
|--------------------------------|-----------|---------------------------|
| Artificial Neural Network | 8.064963 | 93.38937 |
| Neuro-Fuzzy (ANFIS) | 8.120741 | 93.34365 |
| Classification-Tree-Coarse | 8.941777 | 92.67067 |
| Classification-KNN-Coarse | 8.482914 | 93.04679 |
| Regression Interactions Linear | 8.64715 | 92.91217 |
| Regression-Tree-Medium | 8.0694 | 93.38574 |
| Fine Gaussian SVM | 8.208877 | 93.27141 |
| Medium Gaussian SVM | 8.189189 | 93.28755 |
| Squared Exponential GPR | 8.1486 | 93.32082 |
| Ensemble Boosted Trees | 8.270296 | 93.22107 |
| Ensemble Bagged Trees | 8.17696 | 93.29757 |

Generally, calculating Root Mean Squared Error (RMSE) indicated that the use of PCA technique in preparing and reducing the dimensions of large databases has better results for all methods. On the other hand, in the method of Optim index factor (OIF), normalization is performed neither for remote sensing data nor the surface evaporations, but in the PCA, the normalization has been taken into account for only remote sensing data, and surface evaporation values are intact into modeling algorithms. Therefore, significant

changes are seen in the mean square error of the PCA method compared to the OIF. Therefore, it is easy to see the effect of normalization and the use of the PCA method in preparing and reducing the size of large databases in Table 3 and Table 4. Most models have very close RMSE values, which proves that machine learning decision making models are valid in modeling climatic phenomena such as surface evaporation using remote sensing data, and applying these decision models for modeling and data mining is inevitable in the future.

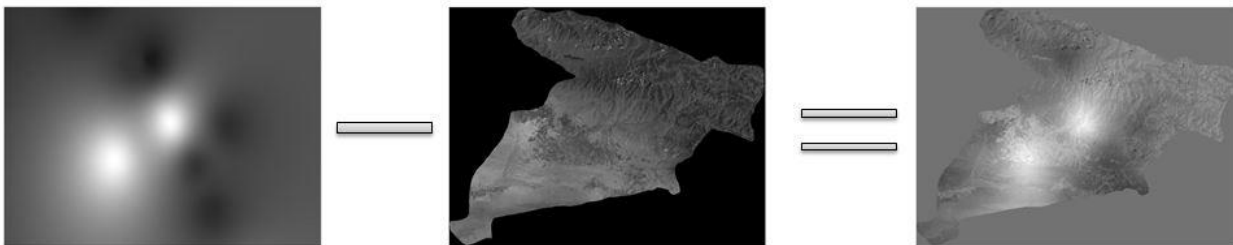


Fig. 3: The error variation of the test results spatially for the ANN model. From the left, the map obtained from the IDW interpolation method and the ANN machine learning algorithm and spatial distribution of errors.

In the method of OIF, the least error belongs to Artificial Neural Network method and the maximum error is related to Classification-Tree method. In the

opposite manner, using the PCA technique, SEGPR with the least error and the Classification-Tree model still with the highest RMSE have the highest and lowest

ratings, respectively. Artificial Neural Network (ANN) model has a good performance in both methods, and the Classification-Tree model has the highest error in both methods. Therefore, it is clear that by changing the methods of database preparation in order to train the models, the modeling results can be changed effectively.

Conclusion

With regard to the importance of changing the future climate of the planet and the wide effects on the various aspects of meteorological and hydrological issues, extensive efforts have been made in order to extract climatic data, more accurate and at the same time less costly and without human and physical errors in the future. On the other hand, the changes in climate variables in regional scales are not explicitly identified, they depend on a large number of local factors. Hence, addressing the improvement and expansion of machine learning methods and modeling algorithms using remote sensing data is inevitable. One of the outputs of this research is simulation models for data mining through

satellite imagery, which is shown in Fig. 4. This figure shows an example of these products.

In this research, in order to study the appropriate methods for modeling and data mining for the surface evaporation, we employed the important methods of the machine learning and the time series of remote sensing and meteorological data and their integration, as well as the impact of the use of the methods like PCA and OIF which were used to prepare data due to training the models.

According to the results obtained in the previous section, the Artificial Neural Network model had acceptable result in both methods and it was quite evident that the impact of the methods of database preparation could be impressively significant. Since the discussion of data preparation in order to training modeling algorithms has not yet been sufficiently considered, and given the significant effect of this on the results of the obtained models, it is suggested to pay more attention to this issue in future studies.

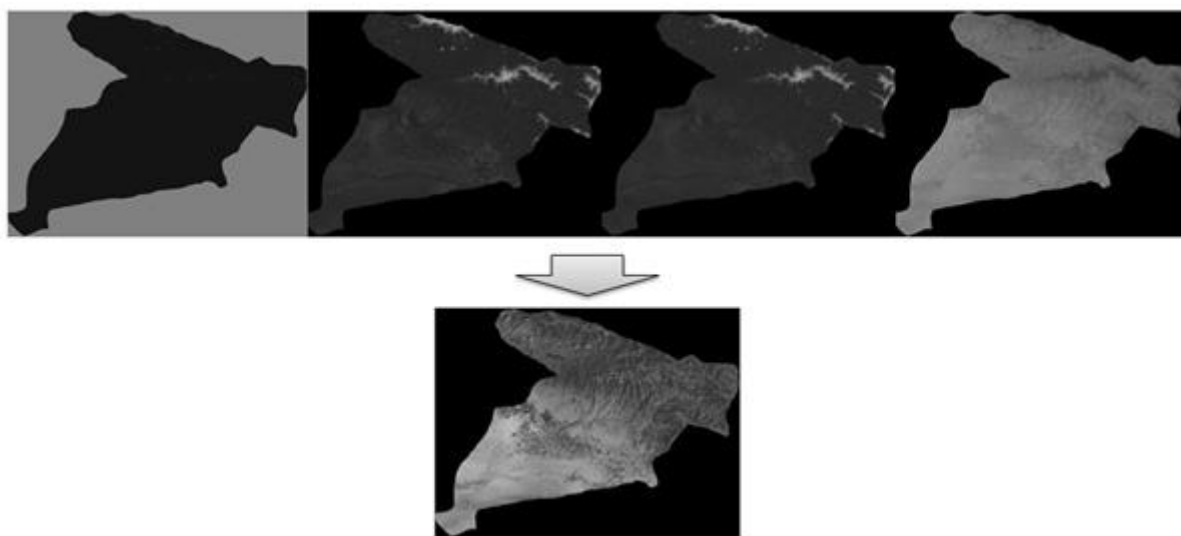


Fig. 4: An example of this study's products. Top, four optimized bands selected by using PCA technique, Down, Surface evaporation map prepared from these optimal bands through the ANN algorithm.

Author Contributions

E. Norouzi and S. Behzadi, designed the methodology. E. Norouzi collected the data. S. Behzadi carried out the data analysis. S. Behzadi and E. Norouzi interpreted the results and wrote the manuscript.

Acknowledgment

The authors gratefully thank the anonymous reviewers and the editor of JECEI for their useful comments and suggestions.

Conflict of Interest

The authors declare no potential conflict of interest regarding the publication of this work. In addition, the

ethical issues including plagiarism, informed consent, misconduct, data fabrication and, or falsification, double publication and, or submission, and redundancy have been completely witnessed by the authors.

Abbreviations

| | |
|--------------|---------------------------------------|
| <i>PCA</i> | Principal component analysis |
| <i>ANFIS</i> | Adaptive neuro fuzzy inference system |
| <i>ANN</i> | Artificial Neural Network |
| <i>KNN</i> | K-Nearest Neighbors |
| <i>SVM</i> | Support Vector Machines |

GPR Gaussian Process Regression

RMSE Root Mean Square Error

References

- [1] F.E. Jones, *Evaporation of water with emphasis on applications and measurements*: CRC Press, 2018.
- [2] G.A. Martin, A.C. Kidd, S. Tsim, P. Halford, A. Bibby, N. A. Maskell, et al., "Inter-observer variation in image interpretation and the prognostic importance of non-expansile lung in malignant pleural effusion," *Respirology*, 25(3): 298-304, 2020.
- [3] A. Malik, A. Kumar, O. Kisi, "Monthly pan-evaporation estimation in Indian central Himalayas using different heuristic approaches and climate based models," *Comput. Electron. Agric.*, 143: 302-313, 2017.
- [4] S. Behzadi, A. Jalilzadeh, "Introducing a novel digital train model using artificial neural network algorithm," *Civ. Eng. Dimen.*, 22(2): 47-51, 2020.
- [5] A. Jalilzadeh, S. Behzadi, "Machine learning method for predicting the depth of shallow lakes using multi-band remote sensing images," *Soft Comput. Civ. Eng.*, 3(2): 59-68, 2019.
- [6] S. Behzadi, Z. Mousavi, E. Norouzi, "Mapping historical water-supply qanat based on fuzzy method. an application to the Isfahan Qanat (Isfahan, Iran)," *Int. J. Numer. Methods in Civ. Eng.*, 3(4): 24-32, 2019.
- [7] S. Behzadi, M. Kolbadinejad, "Introducing a novel method to solve shortest path problems based on structure of network using genetic algorithm," *Int. Arch. Photogramm. Remote Sens. Spatial Inf. Sci.*, 2019.
- [8] A. Malik, A. Kumar, S. Kim, M. H. Kashani, V. Karimi, A. Sharafati, et al., "Modeling monthly pan evaporation process over the Indian central Himalayas: application of multiple learning artificial intelligence model," *Eng. Appl. Comput. Fluid Mech.*, 14(1): 323-338, 2020.
- [9] L. Wang, B. Hu, O. Kisi, M. Zounemat-Kermani, and W. Gong, "Prediction of diffuse photosynthetically active radiation using different soft computing techniques," *Q. J. R. Meteorolog. Soc.*, 143(706): 2235-2244, 2017.
- [10] J. Sulaiman, S.H. Wahab, "Heavy rainfall forecasting model using artificial neural network for flood prone area," in *IT Convergence and Security 2017*, ed: Springer: 68-76, 2018.
- [11] X. Lu, Y. Ju, L. Wu, J. Fan, F. Zhang, Z. Li, "Daily pan evaporation modeling from local and cross-station data using three tree-based machine learning models," *J. Hydrol.*, 566: 668-684, 2018.
- [12] S. Ghimire, R.C. Deo, N.J. Downs, N. Raj, "Self-adaptive differential evolutionary extreme learning machines for long-term solar radiation prediction with remotely-sensed MODIS satellite and Reanalysis atmospheric products in solar-rich cities," *Remote Sens. Environ.*, 212: 176-198, 2018.
- [13] T. Xu, Z. Guo, S. Liu, X. He, Y. Meng, Z. Xu, et al., "Evaluating different machine learning methods for upscaling evapotranspiration from flux towers to the regional scale," *J. Geophys. Res.: Atmos.*, 123: 8674-8690, 2018.
- [14] Q. Zhou, A. Flores, N.F. Glenn, R. Walters, B. Han, "A machine learning approach to estimation of downward solar radiation from satellite-derived data products: An application over a semi-arid ecosystem in the US," *PLoS One*, 12: e0180239, 2017.
- [15] D.P. Solomatine, K.N. Dulal, "Model trees as an alternative to neural networks in rainfall—runoff modelling," *Hydrol. Sci. J.*, 48: 399-411, 2003.
- [16] M. Kühnlein, T. Appelhans, B. Thies, T. Nauss, "Improving the accuracy of rainfall rates from optical satellite sensors with machine learning—A random forests-based approach applied to MSG SEVIRI," *Remote Sens. Environ.*, 141: 129-143, 2014.
- [17] C. Doña, N.-B. Chang, V. Caselles, J. M. Sánchez, L. Pérez-Planells, M.D. M. Bisquert, et al., "Monitoring hydrological patterns of temporary lakes using remote sensing and machine learning models: Case study of la Mancha Húmeda Biosphere Reserve in central Spain," *Remote Sens.*, 8(8): 618, 2016.
- [18] E. Norouzi, S. Behzadi, "Evaluating machine learning methods and satellite images to estimate combined climatic indices," *Int. J. Numer. Methods Civ. Eng.*, 4(1): 30-38, 2019.
- [19] F. Ling, G. M. Foody, H. Du, X. Ban, X. Li, Y. Zhang, et al., "Monitoring thermal pollution in rivers downstream of dams with Landsat ETM+ thermal infrared images," *Remote Sens.*, 9(11): 1175, 2017.
- [20] M. Kaidan, T. Maksymyuk, V. Andrushchak, M. Klymash, "Intelligent data flow aggregation in edge nodes of optical label switching networks," in *Proc. 2019 3rd International Conference on Advanced Information and Communications Technologies (AICT)*: 145-148, 2019.
- [21] R. Mitchell, J. Michalski, T. Carbonell, *An artificial intelligence approach*: Springer, 2013.
- [22] I.T. Jolliffe, J. Cadima, "Principal component analysis: a review and recent developments," *Philos. Trans. Roy. S. A: Math. Phys. Eng. Sci.*, 374: 20150202, 2016.
- [23] D. Karaboga, E. Kaya, "Adaptive network based fuzzy inference system (ANFIS) training approaches: a comprehensive survey," *Artif. Intell. Rev.* 52(4): 2263-2293, 2019.
- [24] J. Wu, Y. Su, Y. Cheng, X. Shao, C. Deng, C. Liu, "Multi-sensor information fusion for remaining useful life prediction of machining tools by adaptive network based fuzzy inference system," *Appl. Soft Comput.*, 68: 13-23, 2018.
- [25] S.J. Narayanan, I. Paramasivam, R.B. Bhatt, "On the estimation of optimal number of clusters for the induction of fuzzy decision trees," *Int. J. Data Sci.*, 2(3): 221-245, 2017.
- [26] K. Khamar, "Short text classification using kNN based on distance function," *Int. J. Adv. Res. Compu. Commun. Eng.*, 2(4): 1916-1919, 2013.
- [27] O. Kisi, O. Genc, S. Dinc, M. Zounemat-Kermani, "Daily pan evaporation modeling using chi-squared automatic interaction detector, neural networks, classification and regression tree," *Comput. Electron. Agric.*, 122: 112-117, 2016.
- [28] O. Genç, B. Gonen, M. Ardicoglu, "A comparative evaluation of shear stress modeling based on machine learning methods in small streams," *J. Hydroinf.*, 17(5): 805-816, 2015.
- [29] M.L. Van Horn, T. Jaki, K. Masyn, G. Howe, D.J. Feaster, A.E. Lamont, et al., "Evaluating differential effects using regression interactions and regression mixture models," *Educ. Physiol. Meas.*, 75(4): 677-714, 2015.
- [30] H. Jafarian, S. Behzadi, "Evaluation of PM2. 5 emissions in Tehran by means of remote sensing and regression models," *Pollution*, 6(3): 521-529, 2020.
- [31] M. Pal, S. Deswal, "Modelling pile capacity using Gaussian process regression," *Comput. Geotech.*, 37(7-8): 942-947, 2010.
- [32] R.U. Maheswari, S. Rajalingam, T. Senthilkumar, "Condition monitoring of coal mine using ensemble boosted tree regression model," in *Intelligent Communication Technologies and Virtual Mobile Networks*: 19-29, 2019.

Biographies



Esmail Norouzi has a B.Sc. in Geomatics engineering, and currently studying at master degree in Geographic Information Systems at Shahid Rajaei teacher training University. His professional and research interests include Geospatial Data mining, Geoinformatics (GIS).



Computer Science.

Saeed Behzadi is an Assistant Professor in Surveying Engineering Department of Shahid Rajaei Teacher Training University, Iran. He received his M.Sc. degree in Geospatial Information Science in 2008 and a Ph.D. degree in 2013, and has worked within the industry and academia in Iran since 2013. He teaches in the Department of Surveying Engineering and Civil Engineering in the area of GIS, Remote sensing, and

Copyrights

©2021 The author(s). This is an open access article distributed under the terms of the Creative Commons Attribution (CC BY 4.0), which permits unrestricted use, distribution, and reproduction in any medium, as long as the original authors and source are cited. No permission is required from the authors or the publishers.



How to cite this paper:

E. Norouzi, S. Behzadi, "The feasibility of machine-learning methods to extract the surface evaporation quantity using satellite imagery," J. Electr. Comput. Eng. Innovations, 9(2): 229-238, 2021.

DOI: [10.22061/JECEI.2021.7563.406](https://doi.org/10.22061/JECEI.2021.7563.406)

URL: https://jecei.sru.ac.ir/article_1541.html





Research paper

A High Voltage Isolated Pulse Generator using Magnetic Pulse Compression and Resonant Charging Techniques for Dielectric Barrier Discharge Applications

A.H. Nejadmalayeri^{*}, A. Bali Lashak, H. Bahrami, I. Soltani

Faculty of Electrical Engineering, Malek-Ashtar University of Technology (MUT), Tehran, Iran.

Article Info

Article History:

Received 19 September 2020
Reviewed 27 November 2020
Revised 19 January 2021
Accepted 26 March 2021

Keywords:

Magnetic pulse compression (MPC)
Resonant charging
Forward technique
Dielectric barrier Discharge (DBD)
High voltage pulse generator (HVPG)
Pulse generator (PG)

^{*}Corresponding Author's Email Address:

A.Nejadmalayeri@mut.ac.ir

Abstract

Background and Objectives: Dielectric Barrier discharge (DBD) is a suitable method to generating Non-thermal plasma at atmospheric pressure, which utilizes Pulsed power supplies as exciters. Increasing pulse voltage range and frequency and compactness are important issues that should be taking into consideration.

Methods: The high voltage pulse generators which are introduced in the literature have some disadvantages and complexities such as need of additional winding to reset the transformer core and operating under hard switching which increases electromagnetic noise and loss. The leakage inductance of the high voltage transformer increases the rise time of the pulse which is undesirable for DBD applications. The energy stored in the leakage inductance causes the voltage spike across the switch, which necessitates the use of snubber circuits. The main contribution of this paper is a new high voltage pulse generator with the following characteristics, 1) a capacitor is paralleled with the main switch to reset the transformer core and to provide the soft switching condition for the switch. 2) The resonant charging technique is used which doubles the secondary winding voltage which reduces the turns ratio of high voltage transformer for a certain output pulse peak. 3) The sharpening circuit using magnetic switch produces a sharp high voltage pulse.

Results: The proposed high voltage pulse generator is designed and simulated using Pspice software. To verify the theoretical results, a prototype with the input voltage 48 V, the output voltage pulse 1.5 kV, and the rise time of the output pulse 50 ns is constructed and tested.

Conclusion: This paper proposes a new pulse generator (PG). The proposed PG uses three techniques named forward, resonant charging, and magnetic switch to produce a high-voltage nanosecond pulse. The resonant charging double the secondary voltage of the pulse transformer, which causes reduction in turn ratio of the pulse transformer and decreases the weight, volume, and price of the PT. The magnetic switch section finally produces a nanosecond high-voltage pulse. The magnitude of the output pulse can be varied using the input source voltage, the MS reset current and the duty cycle. The core of the pulse transformer resets by using a capacitor paralleled with the switch and the PG does not need any additional reset winding like the conventional DC-DC forward converter.

©2021 JECEI. All rights reserved.

Introduction

Dielectric barrier Discharge (DBD) is an applicable technology for generating Non-thermal plasma at atmospheric pressure.

Non-thermal plasma has various industrial applications such as ozone formation, exhaust gas treatment, surface modification of materials, engine

ignition systems and so on [1]–[10]. At first, high voltage ac power supplies were used to excite DBD reactors. But DBD generated by an AC source of periodic sine waves has a relatively low energy input [11], [12]. With the development of semiconductor devices, high voltage pulsed power supplies replaced by ac power supplies for DBD excitation [13]–[16]. Many studies have shown that output pulse parameters of pulsed power supplies like voltage amplitude, rise time and pulse width affect significantly the quality of plasma generated by DBD [17]–[19]. The pulse amplitude is in order of KV, depending on the load requirements. As the pulse rise time decreases, electric field intensity increases in a short time in air gap and produces the higher energy electron to excite and ionize gas molecules [20].

In [21]–[23], three non-isolated solid state pulse generators (PGs) are presented with the combination of pulse forming network (PFN) and boost converter using many MOSFETs switches, capacitors, and inductors. The boost converters provide the initial voltage conditions for the PFNs capacitors. A non-isolated pulse generator is proposed in [24] to produce the high-voltage square waveform. The peaking switch is a series combination of the low voltage switches. Moreover, the proposed converter needs a high voltage power supply at the input side. A non-isolated solid state pulse generators is presented in [25] using buck-boost technique to provide unipolar and bipolar high-voltage output pulses. The significant mentioned merit of the proposed PG is that the peaking switch tolerates the half of the output pulse voltage magnitude. A combination of a solid-state Marx generator along with the MPC network is proposed in [26] with six IGBTs, three diodes, and two magnetic switches. A boost inverter non-isolated based pulse generator is presented in [25] to produce the bipolar high-voltage pulses. Generally, the non-isolated solid state pulse generators need too many solid-state switches to control the maximum voltage stress across the switches, which increases complexity and cost and decreases reliability.

Moreover, the magnitude of the output pulse voltage is limited because the voltage stress across the switches is comparable with the peak of the output pulse voltage. The pulse transformer applied with solid state pulse generators has several merits such as establishing the galvanic isolation between the input and output lines, reduction of the maximum voltage stress across the switches, using the low voltage source at the input line, and makes the switch gate driver simpler. In [27], a modular isolated pulse generators is proposed using full bridge multilevel technique. In addition, another modular solid state pulse generators is presented in [28] with the buck chopper technique. In the modular strategies, each module is independent in terms of power supply and pulse generation; therefore, too many components are required. These modular pulse generators are reasonable in the view of the price and complexity for high power application. A compact unipolar nanosecond pulse generator is presented in [29] for DBD applications with two inductors, three capacitors, a pulse transformer and magnetic switch. An isolated PG is presented in [30] with the parallel resonant technique using a transformer, four switches, two capacitors, and a magnetic switch.

This paper proposes a PG with forward technique. The conventional DC-DC forward converter needs an additional winding with complexity to reset the transformer. The proposed PG employs a capacitor paralleled with the switch to reset the transformer. The high-voltage pulsed capacitor is resonantly charged using the leakage inductance of the pulse transformer maximum to twice the secondary winding voltage, which decreases the turn ratio of the pulse transformer, volume and weight, also the efficiency increases. The energy stored in the leakage inductance of the transformer is lost in the resistor-capacitor-diode (RCD) clamp circuit in [15], [16] but the proposed PG employs it beneficially. Moreover, the switch of the PG operates under the low voltage condition.

Modes Analysis of the Proposed PG

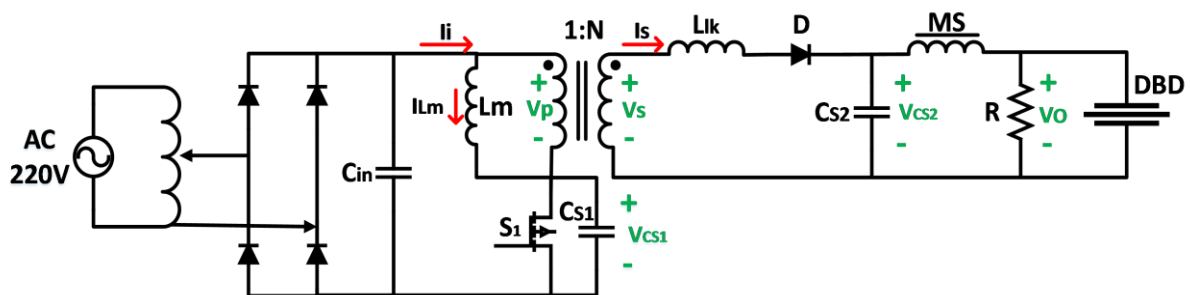


Fig. 1: The Proposed high voltage pulse generator

Figure 1 shows the structure of the proposed forward pulse generator. As shown, the proposed PG includes a pulse transformer (PT) modeled by the magnetizing inductance L_m and ideal transformer by the turns ratio 1:N and the leakage inductance L_{lk} , the switch S_1 , the capacitor C_{S1} for resetting the PT, the high-voltage diode D , the high-voltage capacitor C_{S2} , the magnetic switch (MS), and the resistor R used to stabilize the output pulse waveform. When the switch S_1 is turned on, the low voltage V_i is stepped up by the pulse transformer and the capacitor C_{S2} is resonantly charged maximum to twice the peak voltage of V_s . After the capacitor C_{S2} is fully charged, the magnetic switch is opened and the output pulse voltage with the fast rise time is established. Two main modes is identified for the proposed PG, which is analyzed in details, and the key waveforms are considered.

A. Capacitor Charging (C_{S2}) Mode

This mode begins when the switch S_1 is turned on. At the low voltage side, the voltage V_i is placed on the primary winding of PT and as shown in Fig. 2 the magnetic inductance L_m is charged as the following equation:

$$i_m(t) = i_m(t_0) + \frac{V_i}{L_m}(t - t_0) \quad (1)$$

At the high voltage side, the voltage V_i is converted to the high voltage V_s through the PT. The model of this mode to analysis the high voltage section is shown in Fig. 3. During this mode, as shown in Fig. 2, the high voltage capacitor C_{S2} is charged resonantly as follows:

$$v_{CS2}(t) = V_s(1 - \cos(\omega(t - t_0))) \quad (2)$$

where ω is the resonant frequency of the resonant charging and is obtained as follows:

$$\omega = \frac{1}{\sqrt{L_{lk}C_{S2}}} \quad (3)$$

Moreover, the current i_s flowing the resonant circuit is achieved as follows:

$$i_s(t) = V_s \sqrt{\frac{C_{S2}}{L_{lk}}} \sin(\omega(t - t_0)) \quad (4)$$

From (4) and Fig. 2 the maximum peak current following the diode D is given as follows:

$$I_{sm} = V_s \sqrt{\frac{C_{S2}}{L_{lk}}} \quad (5)$$

The charge time of the capacitor C_{S2} as shown in Fig. 2 is obtained as follows:

$$T_{ch} = \pi \sqrt{L_{lk}C_{S2}} \quad (6)$$

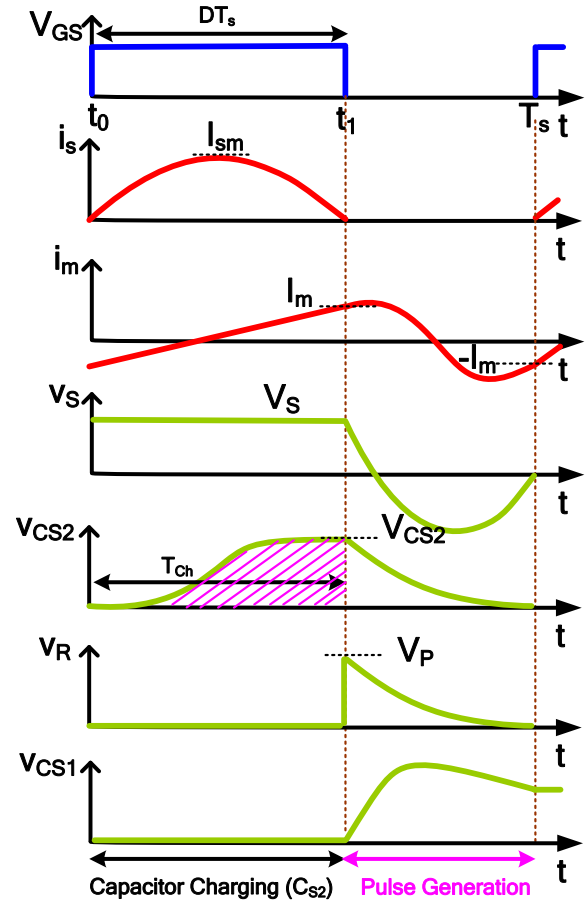


Fig. 2: The proposed PG key waveforms. (a) Capacitor charging (C_{S2}). (b) Pulse generation.

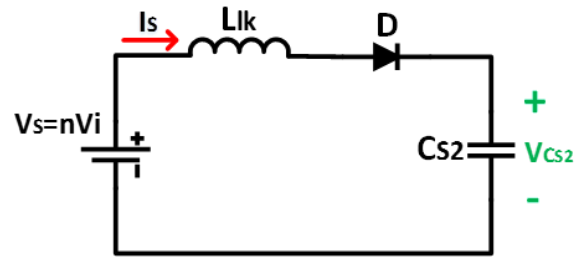


Fig. 3: The model for analyzing of the proposed forward PG in capacitor charging (C_{S2}) mode.

As shown from Fig. 2, the maximum voltage of the capacitor C_{S2} is equal to $2V_s$, therefore the turns ratio of the PT can be reduced. This event can save the copper and reduce the volume and weight of the PT. The equivalent circuit of this mode is illustrated in Fig. 4a.

B. Pulse Generation Mode

When the charge of the capacitor C_{S2} begins at t_0 , by neglecting the leakage current of the MS, the whole voltage of V_{CS2} is placed across the MS. The flux density of the MS core changes as follows:

$$B_{MS}(t) = B_{MS}(t_0) + \frac{1}{N_{MS}A_{MS}} \int_{t_0}^{t_0+T_{ch}} v_{CS2}(t) dt \quad (7)$$

where N_{MS} and A_{MS} are the turns ratio and the cross section of the MS respectively as shown in Fig. 6a. In this circuit a reset circuit can be used to adjust the term $B_{MS}(t_0)$. The integral term of (7) is equal to the below area of the voltage V_{CS2} from t_0 to t_1 , as shown in Fig. 2.

At the end of the previous mode, the flux density of the MS reaches to the saturation flux density and the MS is saturated. The value of this inductance is small and the circuit model of this mode at the high voltage side is shown in Fig. 4b.

The differential equation of the current i_{MS} is obtained as follows using KVL inside the circuit shown in Fig. 4b:

$$\frac{d^2 i_{MS}}{dt^2} + \frac{R}{L_S} \frac{di_{MS}}{dt} + \frac{1}{L_S C} i_{MS} = 0 \quad (8)$$

The damping factor (DF) of (8) is defined as follows:

$$\xi = \frac{R}{2} \sqrt{\frac{C_{S2}}{L_S}} \quad (9)$$

Based on the value of the DF, there are three answer categories for the equation (8). The following equations are related to the over damped condition ($\xi > 1$):

$$i_{MS} = A_1 e^{-s_1 t} + A_2 e^{-s_2 t} \quad (10)$$

$$s_1 = -\omega(\xi + \sqrt{\xi^2 - 1}) \quad (11)$$

$$s_2 = -\omega(\xi - \sqrt{\xi^2 - 1}) \quad (12)$$

$$A_1 = \frac{1}{s_1 - s_2} \frac{V_o}{L_S} \text{ and } A_1 = -A_2 \quad (13)$$

The equations related to the critically damped condition ($\xi = 1$) are given as follows:

$$i_{MS} = (A_3 t + A_4) e^{-\omega \zeta t} \quad (14)$$

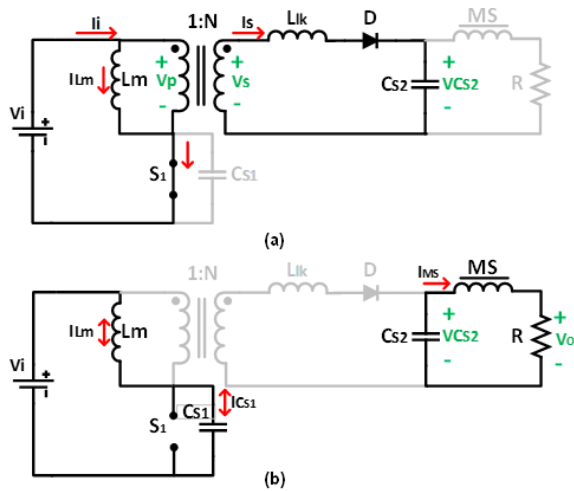


Fig. 4: The equivalent circuit for each operating mode of the proposed forward PG. (a) Capacitor charging (C_{S2}) mode, (b) Pulse generation mode.

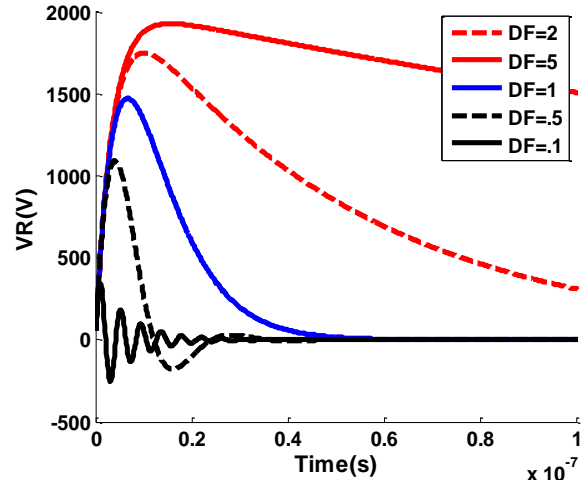


Fig. 5: The waveform of the voltage V_R versus time with $V_o=2kV$, $L_S=1\mu H$, and $R=300$ ohms, based on the various damping factor (DF).

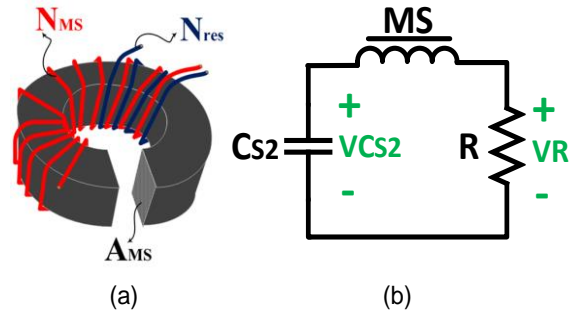


Fig. 6: (a) The image of the magnetic switch, (b) The equivalent circuit of the magnetic switch section.

$$A_3 = \frac{V_o}{L_S} \text{ and } A_4 = 0 \quad (15)$$

The following equations are related to the underdamped condition ($\xi < 1$):

$$i_{MS} = A_5 e^{-\omega \zeta t} \cos(\omega_d t) + A_6 e^{-\omega \zeta t} \sin(\omega_d t) \quad (16)$$

$$A_3 = \frac{V_o}{\omega_d L_S} \text{ and } A_5 = 0 \text{ and } \omega_d = \omega \sqrt{1 - \xi^2} \quad (17)$$

Figure 5 shows the voltage V_R corresponding to the various DF using (10), (14), and (16). As shown, when the DF increases for a certain V_R , L_S , and R , the peak value of the output pulse V_R increases at the cost of increasing the fall time of the V_R .

Moreover, by decreasing the DF, the oscillations appears on the V_R waveform. The magnetic switch in the critical damping has a fast fall time without any

oscillation. Based on the load requirements, the DF can be adjusted.

At the low voltage side, the magnetizing inductance L_m establishes a resonant circuit with the input voltage V_i and C_{S1} .

The following equations are determined for both i_i and V_{CS1} .

$$v_{CS1}(t) = V_i(1 - \cos(\omega_i(t - t_1))) + \frac{I_m}{C_{S1}\omega_i} \sin(\omega_i(t - t_1)) \quad (18)$$

$$i_i = C_{S1}\omega_i \left(\frac{I_m}{C_{S1}\omega_i} \cos(\omega_i(t - t_1)) + V_i \sin(\omega_i(t - t_1)) \right) \quad (19)$$

where I_m is the current of i_i at t_0 and the ω_i is given as follows:

$$\omega_i = \frac{1}{\sqrt{L_m C_{S1}}} \quad (20)$$

During this mode, the current of I_m is reversed, from (1) the following equation is determined as follows:

$$I_m = \frac{V_i T_{ch}}{2L_m} \quad (21)$$

During this mode, the PT core becomes reset using C_{S1} . The conventional forward DC-DC converters employ an additional winding to reset the transformer, which makes the circuit complex.

Design Procedure of the Proposed PG

By considering the roles of the magnetic pulse compression, resonant charging circuit and the PT, the turns ratio of the PT is designed as follows:

$$N = \frac{K_1 V_p}{2V_i} \quad (22)$$

where from Figure 2, V_p is the peak of the output voltage pulse, and K_1 is defined as follows:

$$K_1 = \frac{V_{CS2}}{V_p} \quad (23)$$

The K_1 coefficient is related to the magnetic pulse compression and is dependent on the DF. For example, for the over damping condition the value of K_1 is one.

By considering the fixed values for the load resistance R and the saturation inductance L_s , for a certain DF, the capacitor C_{S2} is determined as follows:

$$C_{S2} = \left(\frac{2\zeta}{R} \right)^2 L_s \quad (24)$$

According to Fig. 2, and using equations (2) and (7), the following equation is given for the magnetic switch:

$$N_{MS} A_{MS} = \frac{T_{ch} V_s}{2\Delta B} = \frac{T_{ch} N V_i}{2\Delta B} \quad (25)$$

By choosing a core with a certain cross section, the turns of the MS is obtained. The flux density of the MS core can be adjusted using a reset circuit.

The current stress of the switch S_1 and diode D are achieved from (4) as follows:

$$I_{Dmax} = V_s \sqrt{\frac{C_{S2}}{L_{lk}}} \quad (26)$$

$$I_{S1max} = N V_s \sqrt{\frac{C_{S2}}{L_{lk}}} \quad (27)$$

The voltage stress of the diode D and the switch $S1$ is given as follows:

$$V_{Dmax} = 2V_s \quad (28)$$

$$V_{S1max} = \max(V_{CS1}) \quad (29)$$

From (21), for a given I_m , the magnetizing inductance is calculated.

For a given I_m , and a maximum voltage for C_{S1} from (18) the capacitance C_{S1} is calculated. The switch S_1 is selected based on maximum voltage and current across the switch. The equations (27) and (29) present the maximum current and voltage of the switch S_1 , respectively.

Simulation Results

The proposed SSPG with the following specifications: $V_i = 48$ V, $f_s = 1$ kHz, $V_p = 2$ kV, $L_s = 1$ μ H, $N = 21$, $L_m = 50$ μ H, $C_{S1} = 100$ nF, $C_{S2} = 10$ nF, $\zeta = 15$, $Q = .03$, $N_{MS} = 30$, $A_{MS} = 1$ cm², and Ferrite material for the core of the PT is designed based on the previous section and is simulated using the Pspice software. Figure 7a shows the waveform of the voltages V_{CS2} and V_R . As shown, the capacitor C_{S2} is charged resonantly to twice of the voltage V_s . When the charge of the capacitor C_{S2} is ended, the MS opens and the output pulse is generated. Figure 7b illustrates the waveform of the input current i_i and the voltage of the switch S_1 . Due to the resonant charging performance, the input current is half a sinusoidal waveform. Moreover, the voltage across the switch S_1 is low due to the PT and the resonance between the magnetizing inductance and the capacitor C_{S1} .

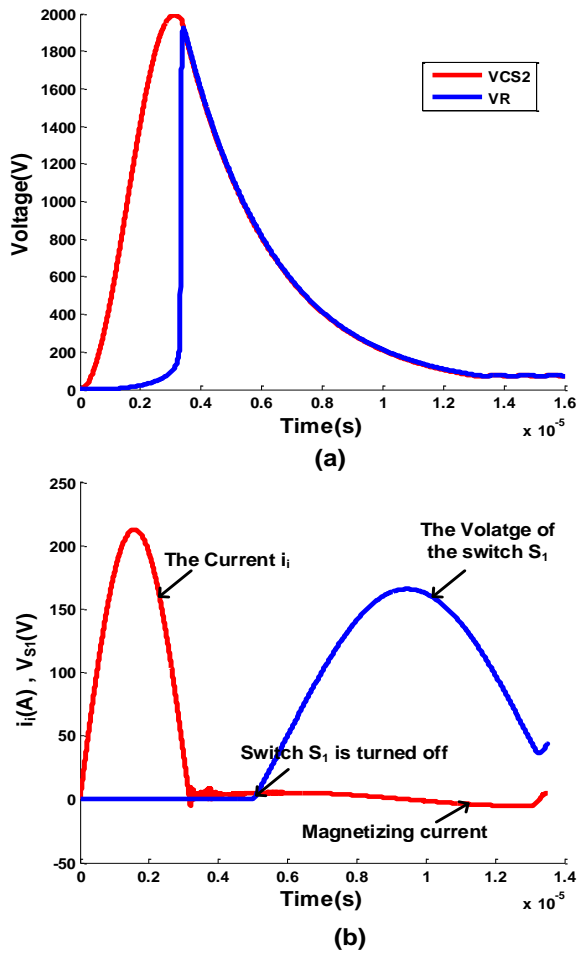


Fig. 7: The key waveforms of the proposed PG. (a) The voltage of the capacitor C_{S2} and the voltage V_R . (b) The input current and the voltage across the switch S_1 .

Experimental results

According to the design section, a i_i prototype constructed to verify the theoretical results. Figure 8 illustrates the experimental proposed PG.

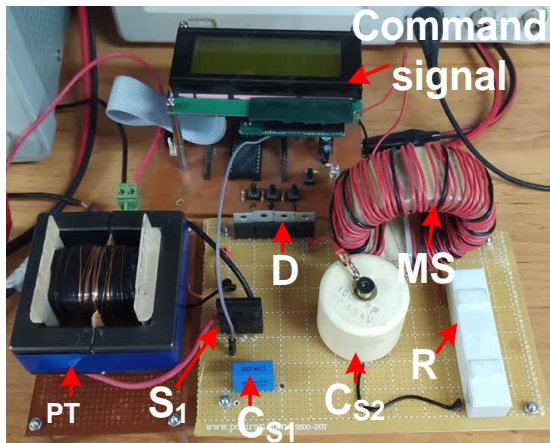


Fig. 8: The prototype configuration and construction of the proposed PG.

Table 1 shows the circuit specifications of the prototype. The input voltage of the proposed PG is 48V and the peak of the output pulse is chosen 1.5 kV. At first, the PT converts the input voltage 48V to 750V and then the resonance charging stage doubles the voltage 750V to 1.5kV. Designing the turn ratio 50 for the MS guarantees that the output pulse is produced at the end of the resonance charging operation.

Table 1: The circuit specification of the prototype

| Symbol | Parameters | Value |
|-----------|--|-------------|
| V_i | Input voltage | 48 V |
| V_P | The output pulse peak | 1.5 kV |
| V_{CS2} | The voltage peak of the capacitor C_{S2} | 1.5 kV |
| V_S | The secondary voltage of PT | 750 V |
| N | The turns ratio of the PT | 16 |
| $N_1:N_2$ | Primary turns: Secondary turns | 10:160 |
| L_m | The magnetizing inductance | 77 μ H |
| L_{lk} | The leakage inductance | 270 μ H |
| S_1 | The switch part number | IXTK120N20P |
| C_{S1} | The C_{S1} capacitance | 100 nF |
| C_{S2} | The C_{S2} capacitance | 9.4 nF |
| PT | The Ferrite core | E 58/11/38 |
| MS | The turns ratio | 50 |
| D | The four diodes are serried | MUR 860 |
| R | The load resistance | 300 ohms |

Table 2: The proposed PG and the counterparts

| Refs | Switch/Inductor Num | Cap/MS Num | PT Num | RCD Losses | Switch Voltage stress |
|-------------|---------------------|------------|--------|------------|-----------------------|
| [9] | 13/4 | 4/None | None | Yes | High |
| [10] | 15/4 | 4/None | None | Yes | High |
| [11] | 14/4 | 4/None | None | Yes | High |
| [12] | Many/None | 1/None | One | No | Moderate |
| [13] | 5/2 | 1/None | None | No | High |
| [14] | 6/None | 4/2 | None | No | Moderate |
| [15] | 2/2 | 2/None | None | No | High |
| [16] | Many/Many | Many/None | Many | No | Low |
| [17] | Many/Many | Many/None | Many | No | Low |
| [18] | 1/1 | 3/1 | One | Yes | Low |
| [19] | 4/None | 2/1 | One | No | Low |
| proposed PG | 1/None | 2/1 | One | None | Low |

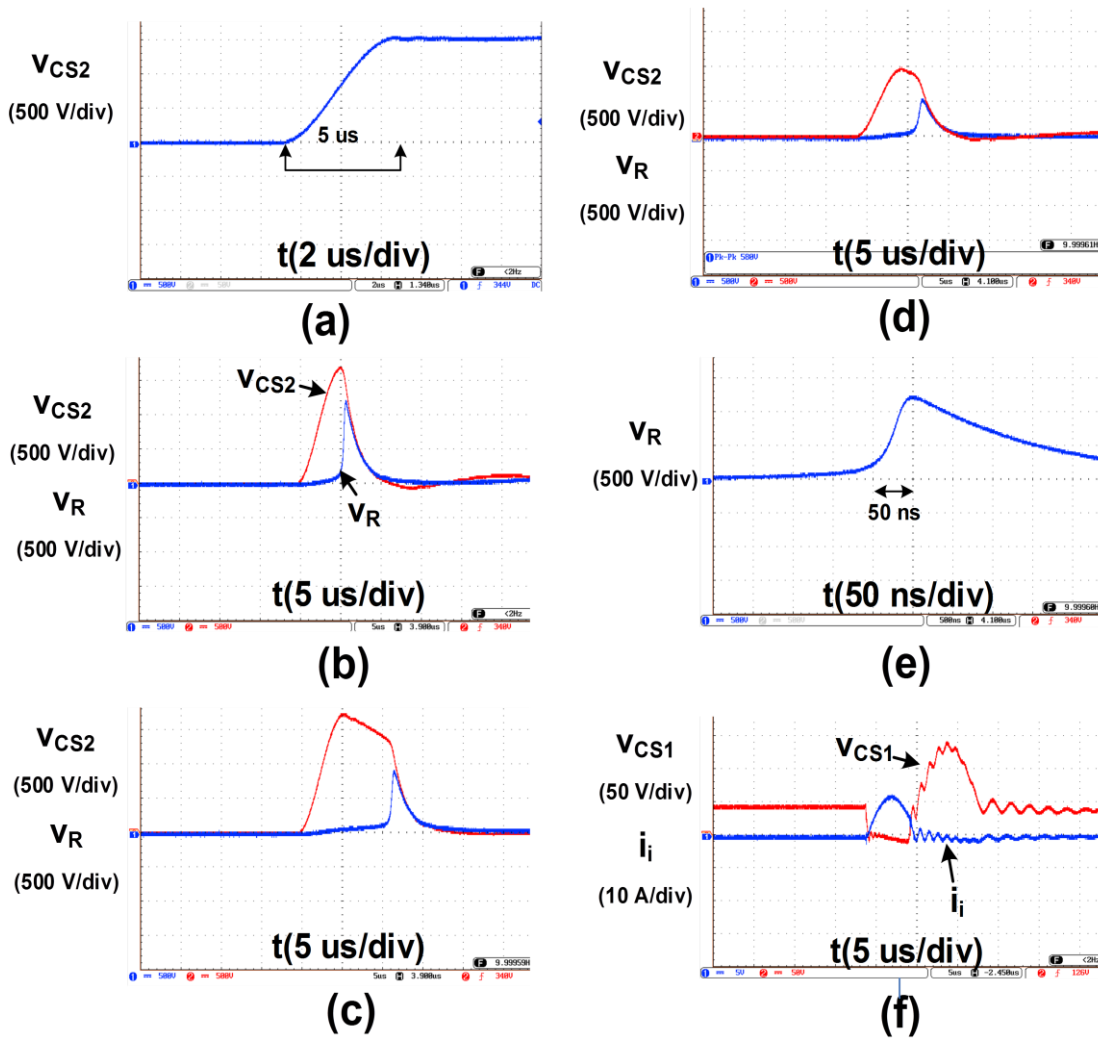


Fig. 9: The experimental results of the PG. (a) The voltage of the capacitor C_{S2} without the MS stage. (b) The output pulse voltage V_R and the output of the resonant charging stage V_{CS2} at the nominal input voltage (48 V). (c) The voltages V_R and V_{CS2} under reducing the reset circuit current at nominal input voltage (48 V). (d) The voltages V_R and V_{CS2} under reducing the input voltage (32V). (e) The rise time of the output pulse voltage. (f) The voltage of the switch S_1 and the current of the input source current.

Figure 9 shows the experimental results of the proposed PG. Figure 9a illustrates the voltage waveform of V_{CS2} without the MS stage. As expected, the voltage of the capacitor C_{S2} is charged to the twice the secondary voltage V_s during the time 5 μ s. As explained at previous sections, the time interval 5 μ s is obtained from the resonance between the capacitor C_{S2} and the leakage inductance L_{lk} .

The voltages V_{CS2} and V_R are shown at the Fig. 9b. As shown, at the end of charge of the capacitor C_{S2} , the MS is opened and the output voltage pulse is established due to the convenient turn ratio of the MS.

The peak of the output pulse V_p can be adjusted using the duty cycle, the input voltage V_i , and the current of the reset circuit of the MS.

As shown in Fig. 9c, under the constant voltage of V_i ,

the capacitor C_{S2} is fully charged but the pulse generation is delayed using the change of the MS core reset current. The voltage drop of C_{S2} is related to the leakage current of the MS when it is off. As shown in Fig. 9d, by decreasing the voltage of the input source from the nominal voltage, the capacitor C_{S2} is charged less than nominal; therefore, the peak of the output voltage is reduced.

By changing the turn-on time of the switch S_1 , also the charge of the capacitor C_{S2} and consequently the peak voltage of the output pulse are varied.

The rise time of the output pulse voltage is approximately 50 ns as shown in Fig. 9e. The rise time of the output pulse voltage is related to the DF and the MS core material.

Figure 9f illustrates the voltage across the switch S_1

and the input source current. As predicted, the input current is the half sinusoidal waveform due to the resonant charging performance.

As seen, the switch S_1 can be turned off softly which reduces the switching losses. Moreover, the voltage across the switch S_1 starts from zero due to the resonance between the magnetizing inductance L_m and the capacitor C_{S1} .

As shown, the proposed PG needs a low voltage switch to produce a high-voltage pulse. From the current i_p , it is seen the magnetizing current is reversed when switch is turned off, therefore the PT does not need any additional reset winding.

Figure 10 illustrates the experimental output pulse when the resistance R changes. As expected from the section two, when R increases, the rise time is constant, but the pulse duration increases due to increasing damping factor.

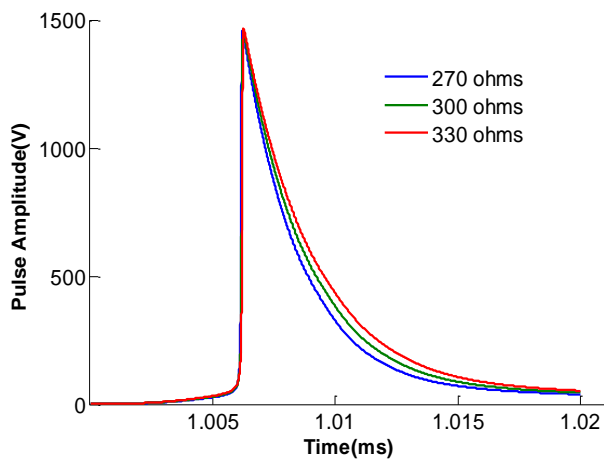


Fig. 10: The experimental output pulse amplitude versus the resistance R .

Conclusion

This paper proposes a novel pulse generator for DBD applications. The proposed PG uses three techniques named forward, resonant charging, and magnetic switch to produce a high-voltage nanosecond pulse. The resonant charging double the secondary voltage of the pulse transformer, this event reduces the turn ratio of the pulse transformer which decreases the weight, volume, and price of the PT.

The magnetic switch section finally produces a nanosecond high-voltage pulse. The magnitude of the output pulse can be varied using the input source voltage, the MS reset circuit current and the switch duty cycle.

In the proposed PG, a low-voltage switch is needed to produce the high-voltage pulses. At the input source,

using a capacitor paralleled with the switch can reset the core of the pulse transformer and the PG does not need any additional reset winding like the conventional DC-DC forward converter. The proposed PG is fully analyzed and the theoretical results are verified by the experimental results.

Author Contributions

Amir Hossein Nejadmalayeri in collaboration with Hamid Bahrami and Aref Balli, designed, simulated and carried out the data analysis, and Iman Soltani collected the data and interpreted the results and wrote the manuscript.

Acknowledgment

The authors gratefully thank the anonymous reviewers and the editor of JECEI for their useful comments and suggestions.

Conflict of Interest

The authors declare no potential conflict of interest regarding the publication of this work. In addition, the ethical issues including plagiarism, informed consent, misconduct, data fabrication and, or falsification, double publication and, or submission, and redundancy have been completely witnessed by the authors.

Abbreviations

| | |
|------------|------------------------------|
| <i>PT</i> | Pulse Transformer |
| <i>MS</i> | Magnetic Switch |
| <i>MPC</i> | Magnetic Pulse Compression |
| <i>PG</i> | Pulse Generator |
| <i>PFN</i> | Pulse Forming Network |
| <i>DBD</i> | Dielectric Barrier Discharge |

References

- [1] A. Chirokov, A. Gutsol, A. Fridman, "Atmospheric pressure plasma of dielectric barrier discharges," *pure Appl. Chem.*, 77(2): 487-495, 2005.
- [2] X. Xu, "Dielectric barrier discharge—properties and applications," *Thin solid films*, 390(1-2): 237-242, 2001.
- [3] G. Borgia, C. Anderson, N. Brown, "Dielectric barrier discharge for surface treatment: application to selected polymers in film and fibre form," *Plasma Sources Sci. Technol.*, 12(3): 335, 2003.
- [4] Y. Chen, L.-M. He, L. Fei, J. Deng, J.-P. Lei, H. Yu, "Experimental study of dielectric barrier discharge plasma-assisted combustion in an aero-engine combustor," *Aerosp. Sci. Technol.*, 99: 105765, 2020.
- [5] D. Breden, C. A. Idicheria, S. Keum, P. M. Najt, L. L. Raja, "Modeling of a dielectric-barrier discharge-based cold plasma combustion ignition system," *IEEE Trans. Plasma Sci.*, 47(1): 410-418, 2018.
- [6] Q. Niu, J. Luo, Y. Xia, S. Sun, Q. Chen, "Surface modification of bio-char by dielectric barrier discharge plasma for HgO removal," *Fuel Process. Technol.*, 156: 310-316, 2017.

- [7] T. Shao, F. Liu, B. Hai, Y. Ma, R. Wang, C. Ren, "Surface modification of epoxy using an atmospheric pressure dielectric barrier discharge to accelerate surface charge dissipation," *IEEE Trans. Dielectr. Electr. Insul.*, 24(3): 1557-1565, 2017.
- [8] S. Knust, A. Kuhlmann, T. de los Arcos, G. Grundmeier, "Surface modification of ZnMgAl-coated steel by dielectric-barrier discharge plasma," *RSC Adv.*, 9(60): 35077-35088, 2019.
- [9] C. Liang et al., "Using dielectric barrier discharge and rotating packed bed reactor for NOx removal," *Sep. Purif. Technol.*, 235: 116141, 2020.
- [10] W. Lu, Y. Abbas, M. F. Mustafa, C. Pan, H. Wang, "A review on application of dielectric barrier discharge plasma technology on the abatement of volatile organic compounds," *Front. Environ. Sci. Eng.*, 13(2): 1-19, 2019.
- [11] J.-S. Chang, P. A. Lawless, T. Yamamoto, "Corona discharge processes," *IEEE Trans. Plasma Sci.*, 19(6): 1152-1166, 1991.
- [12] U. Kogelschatz, "Dielectric-barrier discharges: their history, discharge physics, and industrial applications," *Plasma Chem. Plasma Process.*, 23(1): 1-46, 2003.
- [13] U. Kogelschatz, B. Eliasson, W. Egli, "Dielectric-barrier discharges. Principle and applications," *Le Journal de Physique IV*, 7(C4): C4-47-C4-66, 1997.
- [14] S. Tao, L. Kaihua, Z. Cheng, Y. Ping, Z. Shichang, P. Ruzheng, "Experimental study on repetitive unipolar nanosecond-pulse dielectric barrier discharge in air at atmospheric pressure," *J. Phys. D: Appl. Phys.*, 41(21): 215203, 2008.
- [15] N. D. Wilde, H. Xu, N. Gomez-Vega, S. R. Barrett, "A model of surface dielectric barrier discharge power," *Appl. Phys. Lett.*, 118(15): 154102, 2021.
- [16] W. Qian, L. Feng, M. Chuanrun, Y. Bing, F. Zhi, "Investigation on discharge characteristics of a coaxial dielectric barrier discharge reactor driven by AC and ns power sources," *Plasma Sci. Technol.*, 20(3): 035404, 2018.
- [17] T.-L. Sung et al., "Effect of pulse power characteristics and gas flow rate on ozone production in a cylindrical dielectric barrier discharge ozonizer," *Vacuum*, 90: 65-69, 2013.
- [18] H. K. Song, H. Lee, J.-W. Choi, B.-k. Na, "Effect of electrical pulse forms on the CO₂ reforming of methane using atmospheric dielectric barrier discharge," *Plasma Chem. Plasma Process.*, 24(1): 57-72, 2004.
- [19] H. Ayan, G. Fridman, A. F. Gutsol, V. N. Vasilets, A. Fridman, G. Friedman, "Nanosecond-pulsed uniform dielectric-barrier discharge," *IEEE Trans. Plasma Sci.*, 36(2): 504-508, 2008.
- [20] D. Yuan et al., "Characteristics of dielectric barrier discharge ozone synthesis for different pulse modes," *Plasma Chem. Plasma Process.*, 37(4): 1165-1173, 2017.
- [21] S.H. Hosseini, F. Faradjizadeh, "Increasing the voltage of PFN impulse generator capacitors by converting it to boost converter," *IEEE Trans. Dielectr. Electr. Insul.*, 20(2): 462-467, 2013.
- [22] S.M.H. Hosseini, H.R. Ghafourinam, M.H. Oshtaghi, "Modeling and construction of Marx impulse generator based on boost converter pulse-forming network," *IEEE Trans. Plasma Sci.*, 46(10): 3257-3264, 2018.
- [23] S.H. Hosseini, H.R. Ghafourinam, "Improving the pulse generator BOOST PFN to increase the amplitude and decrease the pulse duration of the voltage," *IEEE Trans. Dielectr. Electr. Insul.*, 23(3): 1699-1704, 2016.
- [24] J. Rao, L. Guo, H. Liu, Z. Li, S. Jiang, "Design of high-voltage square pulse generator based on cascade switches and time-delay driver," *IEEE Trans. Plasma Sci.*, 47(9): 4329-4334, 2019.
- [25] A.A. Elserougi, A.M. Massoud, S. Ahmed, "A unipolar/bipolar high-voltage pulse generator based on positive and negative buck-boost DC-DC converters operating in discontinuous conduction mode," *IEEE Trans. Ind. Electron.*, 64(7): 5368-5379, 2017.
- [26] D. Wang, J. Qiu, K. Liu, "All-solid-state repetitive pulsed-power generator using IGBT and magnetic compression switches," *IEEE Trans. Plasma Sci.*, 38(10): 2633-2638, 2010.
- [27] I. Abdelsalam, M.A. Elgenedy, S. Ahmed, B.W. Williams, "Full-bridge modular multilevel submodule-based high-voltage bipolar pulse generator with low-voltage dc input for pulsed electric field applications," *IEEE Trans. Plasma Sci.*, 45(10): 2857-2864, 2017.
- [28] T. Shao et al., "A cascaded microsecond-pulse generator for discharge applications," *IEEE Trans. Plasma Sci.*, 42(6): 1721-1728, 2014.
- [29] T. Shao et al., "A compact repetitive unipolar nanosecond-pulse generator for dielectric barrier discharge application," *IEEE Trans. Plasma Sci.*, 38(7): 1651-1655, 2010.
- [30] Y. Mi, J. Wan, C. Bian, Y. Zhang, C. Yao, C. Li, "A high-repetition-rate bipolar nanosecond pulse generator for dielectric barrier discharge based on a magnetic pulse compression system," *IEEE Trans. Plasma Sci.*, 46(7): 2582-2590, 2018.

Biographies



Amir Hossein Nejadmalayeri received his B.Sc. degree in electrical engineering from Shahid Bahonar University, Kerman, Iran, in 2018 and his M.Sc. degree in electrical engineering from Malek Ashtar University of Technology, Tehran, Iran, in 2021. His research interests include design, modeling of power converters, and pulsed power systems.



Hamid Bahrami was born in Yazd, Iran, in 1980. He received the B.Sc. degree in electrical engineering from Malek Ashtar University of Technology, Isfahan, Iran, in 2002, and the M.Sc. degree in electrical engineering from the Amirkabir University of Technology, Tehran, Iran, in 2007. He is currently a PhD Candidate at School of Electrical and Computer Engineering, College of Engineering, University of Tehran. His research interests include design, modeling and

control of power converters, photovoltaic, and renewable energy systems.



Iman Soltani received his Bachelor in Robotic Engineering in 2011 from the University of Shahrood, Iran. He received his M.Sc. degree in electrical engineering from Imam Khomeini International University (IKIU) 2013. He received his Ph.D. degree in electrical engineering from Malek Ashtar University of Technology (MUT) 2019. He has been working on several research and consulting projects in the area of powered converters. His research interests include all areas of power electronics, renewable energy,

power electronics, machine control, intelligent control, nonlinear systems control.

Copyrights

©2021 The author(s). This is an open access article distributed under the terms of the Creative Commons Attribution (CC BY 4.0), which permits unrestricted use, distribution, and reproduction in any medium, as long as the original authors and source are cited. No permission is required from the authors or the publishers.



How to cite this paper:

A.H. Nejadmalayeri, A. Bali Lashak, H. Bahrami, I. Soltani, "A high voltage isolated pulse generator using magnetic pulse compression and resonant charging techniques for dielectric barrier discharge applications," J. Electr. Comput. Eng. Innovations, 9(2): 239-248, 2021.

DOI: [10.22061/JECEI.2021.7519.400](https://doi.org/10.22061/JECEI.2021.7519.400)

URL: https://jecei.sru.ac.ir/article_1544.html





Research Paper

Hybrid Method of Recommender System to Decrement Cold Start and Sparse Data Issues

K. Vahidy Rodpysh, S.J. Mirabedini*, T. Baniroostam

Department of Computer Engineering, Central Tehran Branch, Islamic Azad University, Tehran, Iran.

Article Info

Article History:

Received 16 June 2020
Reviewed 09 August 2020
Revised 29 October 2020
Accepted 31 December 2020

Keywords:

Recommender systems
Singular value decomposition
Context and Similarity criteria
Cold start
Sparse data

*Corresponding Author's Email Address:

j_mirabedini@iauctb.ac.ir

Abstract

Background and Objectives: The primary purpose of recommender systems is to estimate the users' desires and provide a predicted list of items based on relevant data. Recommender systems that suggest items to users face two cold start and sparse data challenges.

Methods: This paper aims to propose a novel method to overcome such challenges in recommender systems. Singular value decomposition is a popular method to reduce sparse data in recommender systems by reducing dimensions. However, the basic singular value decomposition can only extract those feature vectors of users and items that may be recommended with lower recommendation precisions. Notably, using the similarity criteria between entities can reduce cold start to resolve the singular value decomposition problem by extracting more refined factor vectors. Besides, considering the context's dimensions as the third dimension of the matrix requires using another flexible algorithm, such as tensor factorization, which offers a viable solution to minimize the sparse data challenge. This study proposes TCSSVD, a novel method to resolve the challenges mentioned above in recommender systems. First, a two-level matrix is obtained using the similarity criteria between the user and the item to reduce the cold start challenge. In the second step, the contextual information is used by tensor in two-level singular value decomposition to reduce the challenge of sparse data.

Results: For reviewing the proposed method, these two data sets, IMDB and STS, were used because of applying user and item features and contextual information. The RMSE criterion (95% accuracy) was used to investigate the predictions' accuracy. However, since the user's rating of the item is particularly important in recommender systems, compared with other methods, such as tensor factorization, HOSVD, BPR, and CTLSVD, the TCSSVD method uses the following criteria: Precision, Recall, F1-score, and NDCG.

Conclusion: The findings indicated the positive effect of using the innovative similarity criteria on the extraction of user and item attributes to reduce the complications deriving from the cold start challenge. Also, the use of contextual information through the tensor in the TCSSVD method reduced the complications related to sparse data. The results improve the recommendation accuracy of the recommender systems.

©2021 JECEI. All rights reserved.

Introduction

The digital era has filled the lives of users with endless

lists of products and services. The number of products and services (items) in many cases is beyond what users

can handle. Also, the time spent rating every single option restricts users' selection. Recommender systems help users overcome such problems by collecting data from various sources to offer compatible items with their preferences or aims [45].

Recommender systems are classified into three types: collaborative filtering (CF), content filtering, and hybrid. The content-based method processes recommendations based on the similarity with users' previous preference. In other words, in that method, the existing items are compared with the previous items rated by the user to make recommendations. CF's underlying presumption is that users who agreed on something in the past tend to agree on it in the future. Therefore, CF searches for users with similar tastes and uses this information to generate predictions. A hybrid system is an accretion of CF and a content-based system [34].

CF techniques are generally divided into memory-based and model-based categories. Model-based approaches are first taught to apply the current information to be exerted later for estimating user ratings for new items. The singular value decomposition (SVD) algorithm is a popular matrix factorization (MF) technique. The decomposition of singular values creates a new space giving a new meaning to the relationship between users and items. Singular value decomposition (SVD) only considers the relationship between users and items to predict the likelihood of a user to like an item. However, it does not acquire more abstract features of the user and the item leading to the predictive rating's impreciseness. Therefore, to achieve a more precise predicted rating by exploiting more abstract features, we further decompose the user matrix and item matrix by SVD [10].

Tensor Factorization (TF) is an expanded version of MF, allowing preferable order tensor decomposition, and is used to determine the hidden parts within the data, which are represented as a multidimensional data structure [13].

The main challenges in the RS method are related to the cold start and sparse data. Sparse data is characterized by the low number of ratings for available items and the difficulty of finding a relationship between users and items [19], [40]. The factors related to cold start problems, including new users and new items, are significant issues hindering CF performance. In the case of a new user or a recently inactive user (consisting of ratings given to the items) in the system, the main challenge is to determine the item to the user. An item has zero ratings in the system when updated for the first time, hence the implausibility of item recommendation to the user [7].

The similarity criteria between users, items, and contextual dimensions are the solutions to the cold start

or sparse data challenges. CF techniques explain a similarity criterion to find an active user's neighbors or the items similar to the target item. The traditional similarity criteria, such as Pearson's correlation coefficient, cosine similarity, and their different types, are often used to calculate the similarity of a pair of users or between items [30]. Other popular metrics used in collaborative filterings, for instance, Bhattacharya Coefficient with correlation, NHSM, and PSS, are novel metrics [12]. The contextual dimensions in an RS consist of any information used to identify an entity. Villegas *et al.* divide the context into five categories: individual, location, time, activity, and relational contexts [52].

For the cold-start issue, recommender systems are designed based on the similarity criteria and MF methods. Similarly, to address the sparse data challenge, the MF method based on contextual information has been developed.

Our contributions are listed as follows:

- An MF method provides a similar measurement between users and items to use the existing data to resolve the cold start challenge in RS.
- The measurement of the proposed similarity between users and items in the RS framework is a generic method applicable to any recommendation domain. Here, the key idea is to use the available semantic features in users and items to make accuracy-improving recommendations.
- TCSSVD, as a MF method, that addresses the sparse data in an RS by the similarity matrix, similarity measurement of contextual information (individual, relational, activity, location, and time) as additional information, and feature tensor to improve the performance of recommendations.
- A set of experiments were conducted on IMDB and STS data sets to evaluate or justify the proposed method's contexts and users' similarity measures and recommend better items.

The remaining parts of this investigative article are ordered as follows: Second section discusses an overview of related works. The third section explains the proposed approach. Then, the fourth section describes TCSSVD. The fifth section provides a summary of the results and discussion. Finally, the last section deals with the conclusion and relevant recommendations for future research.

Related Works

This section surveys the techniques and challenges, the similarity criteria, contextual information, and hybrid methods associated with RSs. An RS is a set of information filtering tools that helps users in their information accessibility processes by prophecy and recommendations of items that can attract their attention [16].

Various techniques have been used in recommender systems: MF [10], KNN [58], neural network [24], decision tree [28], fuzzy [49], clustering [18], association rules [51], genetic [29], Bayesian [32], and graph [35].

Hoang Son conducted a comparative reading of the cold-start challenge in an RS [48] and proposed two solutions:

1. Investigating the recommender process by the MF and Bayesian methods [32] or using latent topical models like an MF [11], [36].
2. Using the similarity criteria in the preferences of the user [55], demographic data [4], [54], social data [15], [16], etc.

Idrissi & Zellou. The SLR is utilized to analyze the existing partnerships and efforts using new tools and concepts to reduce the sparse data problem. RS involves two common ways to solve sparse data [26]:

1. Machine learning techniques (MF, TF) and few other computing techniques try alleviating the sparse data challenge [26].
2. The problem is to find the weights or the similarity criteria of different contextual information and use them to use in recommendation techniques [53]. Machine learning methods are efficient in reducing the sparse data challenge for RSs by asking users to rate random items when entering the systems [15].

MF can reveal latent features that exhibit the interactions between three different kinds of entities (users, items, and context) [36]. Ren et al. proposed the TGSC-PMF method based on MF for recommendation making following the user's favorite point of view deriving from spatial correlation to resolve the sparse data challenge using the data extracted from the site [42]. An approach has also been developed using a biased MF technique to predict rating and Bayesian Personalized Ranking (BPR). The stochastic gradient descent (SGD) based optimization method has been developed to learn context-related parameters and latent factors of users and items [32].

SVD is one of the most widely used MF techniques based on dimensionality reduction, mainly used to solve the sparse data challenge in an RS [34]. SVD combined with demographics improves the recommendation performance [54], semantic SVD++ [44] and imputation-SVD [58]. A new MF method called enhanced SVD (ESVD) has been proposed that includes the basic MF algorithms with rating repletion based on active learning [15].

Cui et al. used a two-level MF technique called CTLSVD, which divides the challenge into two U matrices with user characteristics and I-matrix property. It also filters out inappropriate items to solve the sparse data challenge. Then, they combined it with the context (time) dimension and created the CTLSVD matrix to

examine the time dynamics based on users' preferences for time-based item [10].

TF is an MF technique to reduce each tensor (multidimensional array) to smaller-dimension vectors. The tensor uses different contexts in the multi-faceted interactions of the user-item relationship in the recommendation process [6].

There are many algorithms with specific features for an RS [30]. The similarity criteria including Pearson Correlation Coefficient [41], Cosine [4], and Jaccard [37] are mostly used by recommendation systems. The similarity criteria to solve some cold start challenges, such as MIPFGWC-CS [48], NHSM [48], and RES [50]

Using MIPFGWC-CS, fuzzy geographic clustering aims to identify similar users based on the demographic characteristics of a cold start challenge [48].

NHSM is used to replace the Pearson coefficient or the cosine similarity criteria. This exploratory similarity criterion is composed of PSS features, incorporates the improved Jaccard into the user rating distinction in the design [48]. Inspired by a physical resonance phenomenon named RES, Tan et al. proposed a new similarity criterion to address the cold start challenge. By conducting mathematical modeling compatible with users' rating behaviors, RES estimates the distances between user beliefs and the Jaccard factor with co-relevant and non-relevant ratings [50]. Gongna et al. used the information related to users' demography and item grouping to improve prophecy accuracy. The recommender systems' method and item grouping based on the existing metadata and their latent factor vectors have been specified for one or several classes so that these classes have distinct group labels [14].

SHAN et al. expanded a nonlinearly mindful similarity model via locally attentive embedding. NASM has been developed based on a neural mindful item similarity (NAIS) model and performs significantly better [47].

Algorithms such as PSS [23], URP [33], O-CHSM [12] E-CHSM [12] are the most popular similarity criteria for reducing sparse data using contextual information [12].

The PSS algorithm considers three factors to determine the similarity in recommender systems, especially with the context information's entry. Proximity determines the agreement/disagreement between the two ratings and assigns penalties to disagreement. Then, the significance is determined based on item importance. Singularity exhibits the difference of two ratings from their average rating [23].

The URP algorithm specifically evaluates users who share similarities with items. Some users rate items as so high or so low. Users are prioritized based on the average variance of their given ratings to reflect users' behavior [33].

The E-CHSM algorithm uses skin metering instead of overlapping for field similarity. Proposing similarity measures suggests overcoming traditional and appropriate similarity measures for scattered data, especially knowledge-based data set. The skin criterion is a trait that gives a relatively large weight to the mismatch of traits with higher categories [12].

The O-CHSM algorithm considers the Bhattacharyya coefficient for global rankings, the NHSM ratios of standard ratings, global user behavior, and priorities. Also, it is readily incorporated into other measurements [12].

A recommended approach based on a prediction method uses the behavioral information extracted from the similarity criteria to classify users and reduce the cold start challenge [15]. The similarity criteria driven from social network data should be used to reduce cold start and sparse data in RSs [7], [8].

The demographic criteria are one of the similarity criteria, especially among users. Recommender systems [46] classify users based on their demographic information, such as age, gender, seasonality, occupation, nationality, and preference. The advantage of this technique is it helps resolve the cold start challenge [3].

Yang et al. proposed a meta feature-based unified framework (MERF) to make cold-start recommendations without the need for historical rating records, focusing only on item features. They proposed a Personalized Feature Preference (PFP) vector to characterize the item features' different importance to a user. They also proposed a parallel learning algorithm and an incremental updating algorithm for PFP to improve MERF efficiency [57].

The similarity-based contextual recommendation is incorporated into the sparse linear method and MF as two base algorithms [61]. Generally, MF algorithms reduce cold start by combining other methods with the similarity criteria. Wang et al. estimated a cold start challenge model based on MF for every decision tree node [54].

Karimi et al. proposed an MF method for challenging cold start in RSs, in which they first use the latent factors to find new users similar to the existing users. Then, they choose the highest-rated item among similar users. Thus, the new user can rate an item that users have already rated with similar behavior [20]. Braunhofer proposed a demographic, contextual MF (CAMF-CC) based on the demographic method (gender, age group, personality traits) to reduce the cold start challenge. The performance of this SPF pre-filtering algorithm shows better performance for contextual conditions [4].

Using SVD with other techniques and context similarity criteria methods reduces the sparse data challenge. Reddy et al. used the APPRO SVD algorithm

based on CF to reduce sparse data challenge. In fact, they used this method of Euclidean distance as a similarity criterion to find the KNN [43]. A normalization SVD technique to model user contention for a cold start challenge or their tendency based on the particularity of items was used in the KNN models. The proposed normalization technique was appraised using two data sets, Movie Lens and Group Lens [59].

The limited research that addresses the evolutionary MF algorithm has concerning the similarity criteria is used to reduce both the challenges mentioned thus far. Codina et al. first used the SPF algorithm scattering S conditions and cosine similarity between vectors to reduce the cold start challenge, which uses context conditions according to implicit semantic relationships. It then uses the X_s training set to reduce sparse data to build local scoring [9]. Rafalides et al. first used the initial feedback learning tagging method followed by the item clustering methods, such as k-means and Tensor-based SVD, to reduce sparse data and cold start challenges [38]. Besides, social trust and SVD methods are used to resolve sparse data and cold start challenges [56].

Natarajan et al. proposed a new method to reduce the sparse data and the cold start challenges in CF. To the cold start challenge, RSs with Linked Open Data (LOD) model has been designed, and for sparse data challenge, the MF model based on SVD with Linked Open Data has been expanded. LOD similarity is a composition of improvised PCC and similarity PICSS used to detect semantically similar items of a target item to develop an item-factor vector in the SVD process. The experiments on Netflix and Movie Lens data sets represent the priority of the proposed techniques related to other available methods that improve the recommendation precision [34].

As mentioned earlier, the major challenges of recommending systems are the cold start and sparse data. CF and a content-filtering system should be used with demographic criteria to solve the cold start challenge [4]. The following measures should be taken to reduce sparse data: Personalized feature preference [57] Social trust [56] Linked open data [34]. Features of various context dimensions in context discussion such as using context composition [35] SVD matrix [8], [9], [56] items rated by users with similar relational context to new users by the MF [10], [20], [60].

Proposed approach

The proposed method, as shown in Fig. 1, is based on MF with a focus on the similarity criteria (users-items-contextual) and tensor concepts. Conversely, TCSSVD-based developed RSs take the semantic features of items or users and dimension context used to handle the cold

start and sparse data issues in RSs. Hence, the accuracy of the given suggestions is improved in RSs. Figure 1 illustrates an overview of the RS presented technique.

Table 1 shows the signs used to implement the proposed method. In the first step of the user demographic matrix, the properties of the item are designed.

In the second step, the user-item similarity matrix is obtained by comparing the user-item feature matrix with the user-item matrix. The user-item similarity matrix with the contextual information is created through the properties, and momentum stochastic gradient descent [17].

Table 1: Signs of TCSSVD algorithms

| Symbol | Description | Symbol | Description |
|--------|---|-------------------|--|
| u | A user | R | User-item matrix |
| i | An item | τ | Latent features central tensor |
| c | A contextual condition | S | Latent features context matrix |
| x | Number of user demographic features | Y | User-item-context ratings tensor |
| y | Number of item characteristics features | b_u | The bias of user u |
| t | Number of user context features | b_i | The bias of item i |
| U | A set of users | b_c | The bias of context c |
| I | A set of items | μ | The average rating for all items |
| M | User matrix | ρ | Context weight measure |
| N | Item matrix | W | Similarity measure between users |
| D | User demographic feature matrix | V | Similarity measure between items |
| E | Item feature matrix | Z | Similarity measure between contexts |
| P | Latent matrix of user feature matrix | α | Learning rate |
| Q | Latent matrix of item feature matrix | β | Regularization parameter |
| F | User-item feature matrix | λ | Momentum |
| A | User-item similarity matrix | $\hat{r}_{u,i,c}$ | The predicted rating that user u would give to item i with context |

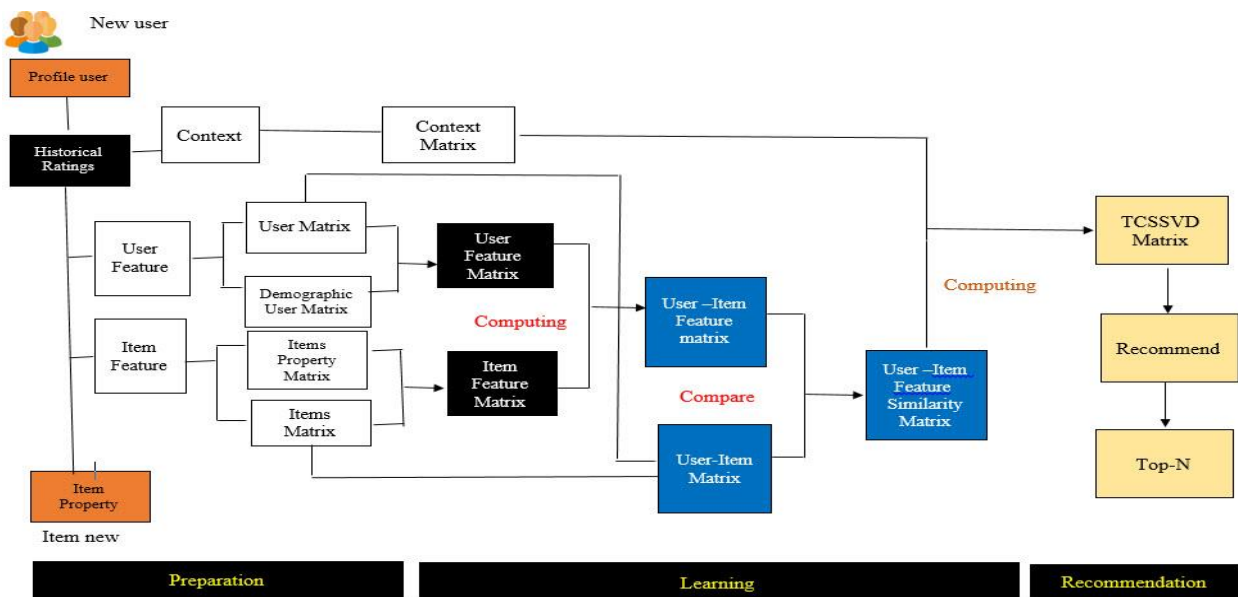


Fig. 1: The structure of proposed scheme.

TCSSVD method

As mentioned, the cold start challenge occurs when a new user enters a system or users who have been in the system for some time do not make any activity. However, new items that have recently entered the system also aggregate such challenges. SVD is a popular recommending algorithm. However, the original SVD can only extract the vector of users and items, preventing further feature refinement and damage recommendations accuracy. As mentioned above, this paper proposes an SVD-based similarity matrix that breaks down the user and item matrix into user demographics, item features, and contextual information to obtain a matrix from more refined features and improves result accuracy and user satisfaction. Users with sharing common features

generally decide based on each other's opinions.

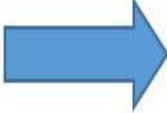
Therefore, this feature is used to solve the cold start challenge reduction for users who have recently logged in or have not shown any system performance. It is used to find similarities between users through the (1).

$$W(obj_a, obj_b) = \frac{\sum_{d=1}^x W_d(obj_{ad}, obj_{bd})}{x} \quad (1)$$

where d is the specific demographic feature of the user, and x is used to represent the total number of user demographic feature and obj_{ad} means the d -th attribute of the object obj_a . $obj_{bd} = obj_{ad}$ then the value of $W_d(obj_{ad}, obj_{bd})=1$; otherwise, it is 0.

With the assumption of 4 demographic variables, comparing four users based on the similarity criteria mentioned in (1) requires taking the following steps to construct the user's demographic feature matrix:

| | D1 | D2 | D3 | D4 |
|----|---------|------------|--------|----|
| U1 | Denmark | Copenhagen | Man | 30 |
| U2 | Denmark | Odense | Man | 28 |
| U3 | Uk | London | Female | 26 |
| U4 | France | Nice | Man | 35 |



| | D1 | D2 | D3 | D4 |
|----|---------------|---------------|----|---------------|
| D1 | 1 | $\frac{2}{4}$ | 0 | $\frac{1}{4}$ |
| D2 | $\frac{2}{4}$ | 1 | 0 | $\frac{1}{4}$ |
| D3 | 0 | 0 | 1 | 0 |
| D4 | $\frac{1}{4}$ | $\frac{1}{4}$ | 0 | 1 |

Fig. 2: A view of the user demographic feature matrix.

However, new items that enter the system resemble the items within the system. Hence, the peculiarity of item features to suggest new items in these systems is one solution to overcome the cold start challenge.

Equation (2) is used to find the similarities between items.

$$V(obj_a, obj_b) = \frac{\sum_{e=1}^y V_e(obj_{ae}, obj_{be})}{y} \quad (2)$$

where e is a specific feature of the item, and y is used to represent the total number of specific feature item and obj_{ae} means the attribute of the object obj_a . If $obj_{be} = obj_{ae}$ then the value of $V_e(obj_{ae}, obj_{be})=1$; otherwise, it is 0.

The following steps should be taken to construct the item feature matrix to compare these nine items based on the similarity criteria mentioned in (2), with the assumption of 9 item-specific feature variables. The second step, which is created by multiplying the

two matrices of user properties (P) and item properties (Q), creates the user-item matrix of items (F). In the construction of the matrix of user-item (F) properties, a decrease in k rank is used to reduce the dimensions. Moreover, a matrix of single values is created based on a decrease rank. In fact, k is considered the minimum reduction rank of x and y .

$$F_{u,i} = p_{uk} \sigma_{kk} q_{ik}^T \quad (3)$$

This study used the PSS similarity measure to compare the user-item feature matrix (F) with the SVD matrix (R), which is made by multiplying the user-item matrix based on the user ratings. The three main elements of the PSS similarity measure, including proximity, significance, and singularity can be considered based on (4).

Proximity whether or not the two score ranks in the two matrices agree Importance, the degree of importance of the desired rank is in the two matrices.

| | E1 | E2 | E3 | E4 | E5 | E6 | E7 | E8 | E9 |
|----|------|------|------|----|----|------|----|----|-----|
| I1 | 1378 | 61 | 862 | 18 | 7 | 2010 | 9 | 37 | 346 |
| I2 | 309 | 1622 | 704 | 21 | 14 | 2003 | 9 | 37 | 493 |
| I3 | 939 | 1562 | 1857 | 14 | 1 | 2010 | 9 | 37 | 98 |
| I4 | 535 | 513 | 172 | 1 | 7 | 2003 | 9 | 37 | 158 |
| I5 | 497 | 699 | 1622 | 3 | 1 | 2010 | 9 | 37 | 396 |
| I6 | 1562 | 1404 | 127 | 21 | 8 | 2009 | 9 | 37 | 542 |
| I7 | 660 | 513 | 1679 | 7 | 6 | 2002 | 9 | 37 | 253 |
| I8 | 1840 | 98 | 127 | 17 | 10 | 2001 | 9 | 37 | 506 |
| I9 | 366 | 1744 | 1504 | 7 | 1 | 2010 | 9 | 37 | 806 |



| | I1 | I2 | I3 | I4 | I5 | I6 | I7 | I8 | I9 |
|----|---------------|---------------|---------------|---------------|---------------|---------------|---------------|---------------|---------------|
| I1 | 1 | $\frac{2}{9}$ | $\frac{3}{9}$ | $\frac{3}{9}$ | $\frac{3}{9}$ | $\frac{2}{9}$ | $\frac{2}{9}$ | $\frac{2}{9}$ | $\frac{3}{9}$ |
| I2 | $\frac{2}{9}$ | 1 | $\frac{2}{9}$ | $\frac{2}{9}$ | $\frac{2}{9}$ | $\frac{2}{9}$ | $\frac{2}{9}$ | $\frac{2}{9}$ | $\frac{2}{9}$ |
| I3 | $\frac{3}{9}$ | $\frac{2}{9}$ | 1 | $\frac{2}{9}$ | $\frac{4}{9}$ | $\frac{3}{9}$ | $\frac{2}{9}$ | $\frac{2}{9}$ | $\frac{4}{9}$ |
| I4 | $\frac{3}{9}$ | $\frac{2}{9}$ | $\frac{2}{9}$ | 1 | $\frac{2}{9}$ | $\frac{2}{9}$ | $\frac{2}{9}$ | $\frac{2}{9}$ | $\frac{2}{9}$ |
| I5 | $\frac{3}{9}$ | $\frac{2}{9}$ | $\frac{4}{9}$ | $\frac{2}{9}$ | 1 | $\frac{2}{9}$ | $\frac{2}{9}$ | $\frac{2}{9}$ | $\frac{3}{9}$ |
| I6 | $\frac{2}{9}$ | $\frac{2}{9}$ | $\frac{3}{9}$ | $\frac{2}{9}$ | $\frac{2}{9}$ | 1 | $\frac{2}{9}$ | $\frac{2}{9}$ | $\frac{3}{9}$ |
| I7 | $\frac{2}{9}$ | $\frac{2}{9}$ | $\frac{2}{9}$ | $\frac{2}{9}$ | $\frac{2}{9}$ | $\frac{2}{9}$ | 1 | $\frac{2}{9}$ | $\frac{3}{9}$ |
| I8 | $\frac{2}{9}$ | $\frac{2}{9}$ | $\frac{2}{9}$ | $\frac{2}{9}$ | $\frac{2}{9}$ | $\frac{2}{9}$ | $\frac{2}{9}$ | 1 | $\frac{2}{9}$ |
| I9 | $\frac{2}{9}$ | $\frac{2}{9}$ | $\frac{4}{9}$ | $\frac{2}{9}$ | $\frac{3}{9}$ | $\frac{3}{9}$ | $\frac{3}{9}$ | $\frac{2}{9}$ | 1 |

Fig. 3: A view of the specific feature item matrix.

Uniquely, the difference in rank is the average of the ranking points in the two matrices. The PSS similarity measure is used to compare the two mentioned matrices and create a similarity SVD matrix. The similarity SVD matrix is obtainable from the more abstract factors (such as item features, lead actor, and user demographics). This way, the similarity matrix can reduce the problem of cold start in new users and items.

$$\begin{aligned}
 \text{Proximity}(f_{a,b} - r_{a,b}) &= 1 - \frac{1}{1 + \exp(-|f_{a,b} - r_{a,b}|)} \\
 \text{Significance}(f_{a,b} - r_{a,b}) &= \frac{1}{1 + \exp(-|f_{a,b} - f_{med}| * |r_{a,b} - r_{med}|)} \\
 \text{Singularity}(f_{u,a} - r_{v,b}) &= \frac{1}{1 + \exp(-|((f_{u,a} - f_a) + (r_{v,b} - r_b))/2|)}
 \end{aligned} \quad (4)$$

The similarity singular value decomposition matrix was able to somewhat reduce the cold start challenge; however, it still has a rating matrix obtained from those unrated points. In other words, the resulting matrix faces the sparse data challenge. The K cross-validation was based on the RMSE criterion to ensure all users' participation in rating items, to the extent that the obtained results were generalizable independent of the data. The RMSE measure in k repeats is less than the specific value of p , indicating that the item has not been rated by the user, hence the sparse data challenge.

Context dimensions in the SVD matrix features are used to reduce the challenge of sparse data, which were divided into five categories: relational, individual, activity, location, and time. The similarity measure (context weight performance) is used to calculate the contextual matrix.

For each of these categories, the standard dimensionality (ω) is considered for the search. If the user approves the criterion, the weight is one; otherwise, it is 0. Equation (5) is used to find the similarities between contexts.


$$Z(obj_a, obj_b) = \frac{\sum_{c=1}^t \omega Z_c(obj_{ac}, obj_{bc})}{t} \quad (5)$$

where c is a specific context of the user, and t is used to represent the total number of specific context feature and obj_{ac} means the c -the attribute of the object obj_a . If $obj_{bc} = obj_{ac}$ then the value of $Z_c(obj_{ac}, obj_{bc}) = 1$; otherwise, it is 0.

The following steps should be taken to construct the latent context matrix to compare these five context variables based on the similarity measure mentioned in (5), with the assumption of 5 users. Finally, a tensor MF was formed in an SVD matrix called TCSSVD. Besides, tensors are used in the matrix to minimize calculations and optimize the results, leading the three-dimensional matrices to have a higher performance and presentation of more suitable items to users. Regarding that, (6) calculates the actual value of r_{uic} . The approximate rate of user u to item i in field c is the actual value of r_{uic} . In (7), r_{uic} shows the predicted rate of i item selected by u user in c context. In this equation, μ is the mean score for all items, including b_u , b_i , and b_c , respectively, the average deviation of user u from the mean of the total rate the mean deviation of items i from the mean of the total rate, and the mean deviation of the mean of the c context. The study used the learning rate α and the regulatory parameter β to update the mean deviation of the items, users, and contexts. In (8), the error measure

is obtained from the difference between the actual value of r_{uic} and the prediction rate \hat{r}_{uic} . In (9), the study used

momentum stochastic gradient descent (MSGD) [39] through the coefficient of momentum (λ).



| | U1 | U2 | U3 | U4 | U5 |
|----|-----------|----------|---------|----------|--------------|
| C1 | Happy | positive | only | holiday | 3repetitions |
| C2 | Fear | Neutral | Family | Weekend | -1 |
| C3 | Surprised | -1 | Weekend | Partner | 2repetitions |
| C4 | -1 | Negative | -1 | Official | -1 |
| C5 | Angry | -1 | only | Official | -1 |

| | C1 | C2 | C3 | C4 | C5 |
|----|---------------|----|----|---------------|---------------|
| C1 | 1 | 0 | 0 | 0 | $\frac{1}{5}$ |
| C2 | 0 | 1 | 0 | 0 | 0 |
| C3 | 0 | 0 | 1 | 0 | 0 |
| C4 | 0 | 0 | 0 | 1 | $\frac{1}{5}$ |
| C5 | $\frac{1}{5}$ | 0 | 0 | $\frac{1}{5}$ | 1 |

Fig. 4: View of the context matrix

$$r_{uic} = \sum_{k=1}^K P_{uk} Q_{ik} S_{ck} \quad (6)$$

$$\begin{aligned} \hat{r}_{uic} &= \mu + b_u + b_i + b_c + \sum_{k=1}^K P_{uk} Q_{ik} S_{ck} \\ b_u &= b_u + \alpha \cdot (e_{ui} - \beta \cdot b_u) \\ b_i &= b_i + \alpha \cdot (e_{ui} - \beta \cdot b_i) \\ b_c &= b_c + \alpha \cdot (e_{ui} - \beta \cdot b_c) \end{aligned} \quad (7)$$

$$e_{uic} = r_{uic} - \hat{r}_{uic} \quad (8)$$

$$\begin{aligned} P_u &= \lambda \cdot P_u + \alpha \cdot (e_{ui} \cdot Q_i S_c - \beta \cdot P_u) \\ Q_i &= \lambda \cdot Q_i + \alpha \cdot (e_{ui} \cdot P_u S_c - \beta \cdot Q_i) \\ S_c &= \lambda \cdot S_c + \alpha \cdot (e_{ui} \cdot P_u Q_i - \beta \cdot S_c) \end{aligned} \quad (9)$$

In the training process of the method presented in the TCSSVD matrix, the available parameters can be calculated by minimizing possible connections and errors using Fresenius norms based on (10):

$$L = \frac{1}{2} (e_{uic})^2 + \frac{\beta}{2} (\|P_u\|^2 + \|Q_i\|^2 + \|S_c\|^2 + b_u^2 + b_i^2 + b_c^2) \quad (10)$$

The New Heuristic Context Similarity Measure (NHCSM) method is used to calculate proposal based on (11) to estimate the similarity measure between k, the initial item, proposal, and the n item. Table 2 shows the pseudo-code of the TCSSVD algorithm.

$$\begin{aligned} Sim(a, b)^{NHCSM} &= \\ Sim(a, b)^{UDP} * Sim(a, b)^{IFP} * Sim(a, b)^{PSS} * Sim(a, b)^{CWP} \end{aligned} \quad (11)$$

Table 2: The pseudo-code of TCSSVD algorithm

Algorithm: Tensor Context Similarity Matrix Algorithm (TCSSVD)

Input: target users \mathbf{u}_{target} , new user, new item, rating matrix r , k , top- n

Output: The n recommended item for target users \mathbf{u}_{target}

Compute the average rating(μ)

initialize $b_u, b_i, b_c, e_{uic}, \hat{r}_{uic}$

Initialize matrices P, Q, S

While $RMSE < \rho$

 for each user u do

 Use (1) Calculate \mathbf{W} (**new user ,user**)

 for each item i do

 Use (2) Calculate \mathbf{V} (**new item ,item**)

 for each context c do

 Use (5) Calculate \mathbf{Z} (**context new entity ,context other entity**)

 if $r(u, i, c) \neq 0$

 Use (7) predict rating

 Compute e_{uic}

 Use (9) update the matrices P, Q, S

 end if

 end for

 end for

 end for

 calculate RMSE

end while

Predict unknown rating based on (7)

Select the k recommended item to the target users \mathbf{u}_{target}

Calculate the similarity between r_{uic} **and the** k recommended item using (11)

Select the k recommended item final to the target users \mathbf{u}_{target}

Select the n recommended item in the K items recommend to the target users \mathbf{u}_{target}

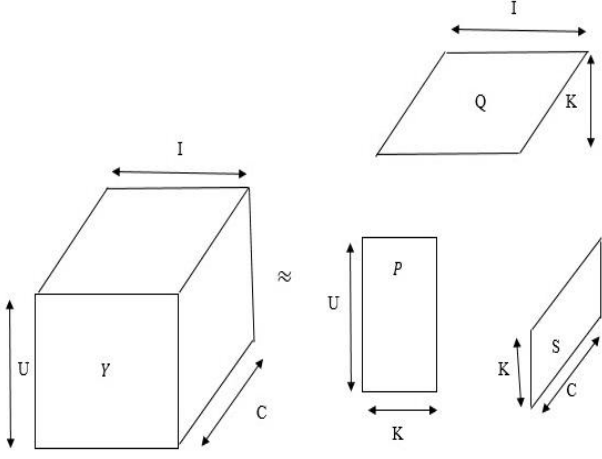


Fig. 5: A view of the TCSSVD matrix.

Results and Discussion

In this section, IMDB and STS data sets are used to evaluate the proposed method's performance. We compare the TF, HOSVD, BPR, and CTLSVD methods with Precision, Recall, F1-score, and NDCG.

A. Datasets

To create and appraise RS's efficiency, data set with all the related contextual information play an essential role [21].

The LDOS-CoMoDa [27] data set has various contextual attributes, like emotions and mood [26]. The IMDB data set includes information collected from the survey where the respondents have explicitly answered such dynamic contexts [4], [9], [11], [25], [60].

The created database is taken from the LDOS-CoMoDa database and the CIL group database is taken from a rich data set of videos suggested by IMDB, including the order number, user number, item number, and the level of the user's interest in the item. The suggested numbers range from 1 to 5. This data set including 1088 users and 2455 items and a total of more than 20759 have been examined. In fact, it is time for the user to use the item [1]. The context dimension consists of twelve variables, including time, day type, season, location, weather, social endEmo, dominantEmo, mood, physical, decision, and interaction.

The database created by STS [4], [5] is taken from a tourism-related android mobile app in Italy [22] and includes the user number, users' demographics, the item number, item characteristics, and the user's level of interest in the item (an offer ranging from 1 to 5). This data set covers 1625 users and 498 items and a total of more than 12675. The contextual information consists of 14 variables, including time, the available, season, daytime, mood, weather, emotional stability, temperature, budget, agreeableness, openness to experience, transport, companion, distance, and goal

travel [5]. The original data set was split into two subsets for appraising different approaches: an 80% share was allocated to the train data set, and the remaining 20% was allocated to the test data set. The data set used in the training set is intended for calculating.

Table 3: Details of IMDB and STS data set

| Data set | IMDB | STS |
|----------|-------|-------|
| Users | 1088 | 1625 |
| Movies | 2455 | 498 |
| Context | 12 | 14 |
| Ratings | 20759 | 12675 |

B. Evaluation Metrics

Evaluation measures are used in RS to evaluate the accuracy and efficiency of the methods used. The evaluation measure calculates mean squared error (MSE), mean absolute error (MAE), and K cross-validation errors between the actual rating of an item and the predicted rating in the RS [7].

K cross-validation determines the generalizability and independence of analysis results on a data set compared with the educational data [14], [31], [60].

For there to be no users who have not rated an item, hence the K cross-validation based on the root mean square error (RMSE) measure to the extent that the results presented can be generalized and independent of the data.

$$RMSE = \sqrt{\frac{\sum_{u,i} (R_{u,i} - \hat{R}_{u,i})^2}{|R|}} \quad (12)$$

R contains the actual rating values, \hat{R} consist of predicted ratings and $|R|$ is the cardinality of the rating matrix. Quality evaluation deals with measuring the recommendations to determine the level of system learning, including precision, recall, and f-score, and normalized discounted cumulative gain (NDCG) [25].

This study recovered the Top-N recommendations as a ranked list of current offers to users. Therefore, the mentioned system learning levels were used to appraise the proposed approach's quality and effective recommendation [7].

Recall measure ratio of the number of recommendations is exactly the number of interest items to the user. Recall is defined as in (13) [25], [34], [43].

$$Recall = \frac{\text{correct prediction}}{\text{total relevant items}} \quad (13)$$

The precision determines the correct recommendations' ratio to the provided recommendations [25], [34], [43]. Precision is defined as

in (14).

$$\text{Precision} = \frac{\text{correct predictions}}{\text{total predictions}} \quad (14)$$

The F-score measure can be described as a harmonic average of the precision and recall [25], [34], [43].

F-score is defined in (15).

$$\text{F-score} = \frac{2 * \text{Precision} * \text{Recall}}{\text{Precision} + \text{Recall}} \quad (15)$$

The normalized discounted cumulative gain was measured to evaluate the quality of recommendations to determine the amount of learning in an RS. A higher NDCG value for a list of recommended items indicates a higher rank of the list's related items. NDCG@N measures the relationship of Top-N results and is defined in (16) [9], [58].

$$\text{NDCG} = \frac{\text{DCG@N}}{\text{idcg@N}} \quad (16)$$

DCG@N : Value of the ideal ranking list.

$$\text{idcg} = \text{rel}_1 + \sum_{i=2}^{\text{pos}} \frac{\text{rel}_i}{\log_2^2} \quad (17)$$

pos : Situation up to which the relationship is accumulated.

rel_i : Recommendation relationship at situation i

The simulations were conducted using Python on a computer equipped with a 3.2 GHz Intel Core i7 processor and 12GB of Ram.

The following Python libraries were used for analyzing the anaconda software collection: NumPy, Panda, and Tensor Flow.

C. Comparisons Methods

The study's method was compared with HOSVD, BPR, TF, and CTLSVD methods for efficiency improvement.

- TF assumes that the rating tensor from users, items, and types of context can be factorized into a product of three low-rank matrices [55].
- The most well-known TF uses the tensor matrix kernel for the decomposition of individual values and its conversion to the HOSVD [5].
- Bayesian Personalized Ranking (BPR) with SGD based optimization procedure applies to sparse data challenge alleviation. The rating prediction is generated by sorting the target user's preference scores to candidate items, which are calculated as the user's inner product of latent factors, and the items with contextual information are considered in this method [31].
- CTLSVD algorithm decomposes the user, and the item features matrices again to obtain a more refined feature matrix. CTLSVD combines the contextual information with the TLSVD algorithm [10].

D. Results

The proposed TCSSVD was compared with the TF, HOSVD, BPR, and CTLSVD methods for performance validity check to evaluate the expressed methods based on the evaluation criteria precision, Recall, F1-score, and NDCG.

As reported in Table 4, the proposed approach performed better than the HOSVD, BPR, TF, and CTLSVD methods.

Since the contextual information can potentially reduce the sparse data, the contextual information is one of the influential factors in the evaluated methods.

TF methods poorly correlate with contextual information. Also, disregarding the similarity criteria between users and items can reduce suggestions' accuracy.

In HOSVD, the tensors are utilized in TF, but the multidimensional decomposition can use this method over the TF method.

The BPR method was used to learn the related parameters and latent factors of users, items, and contexts. The learning rate was used to estimate the recommendations' accuracy compared to the TF and HOSVD method in the data set IMDB and STS.

CTLSVD method decomposes the user feature matrix and the item feature matrix by SVD and adds the contextual information.

The same use of feature matrix and the item characteristic make the proposed method superior to the TF, HOSVD, and BPR methods by entering contextual information. The better performance of TCSSVD compared to CTLSVD relies on using the similarity criteria between users - items - contexts and the possibility of comparing the similarity matrix. Figure 6 and Fig. 7 represent the methods with precision, recall, and F-score criteria on IMDB and STS data sets, respectively.

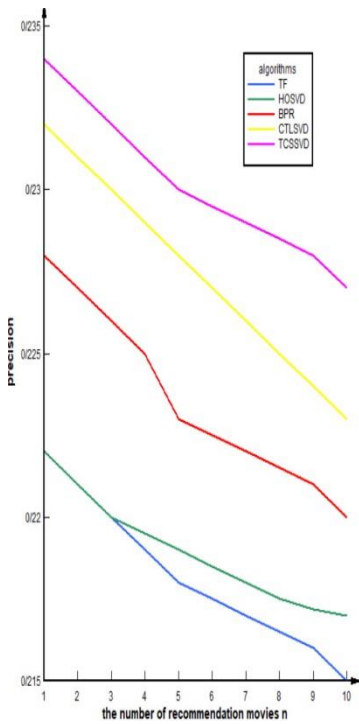
In all settings, the TCSSVD method outperforms other methods, demonstrating the advantage of the direct effect of contextual information on latent factors to learn context-aware latent representations. The latent factors are extracted in the users, and items and contextual information are considered. However, this observation shows that TF, HOSVD, BPR, and CTLSVD methods apply to reduce sparse data, but the TCSSVD approach can overcome the sparse data and cold start challenges.

The implicit ratings are evaluated to the Top-N predicted by different sequential approaches to calculating the NDCG of the recommendations.

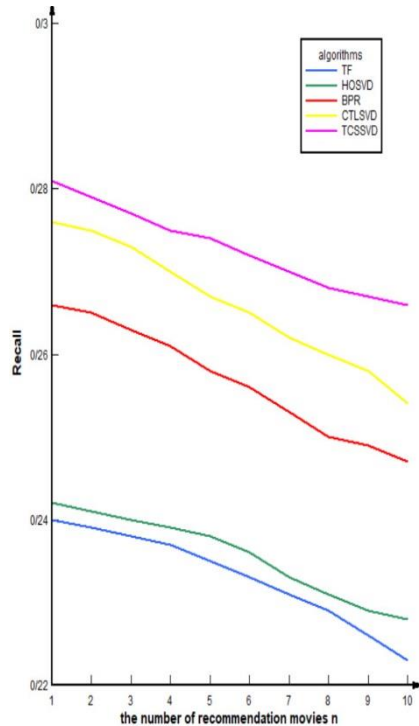
Figure 8 demonstrates the ranking effectiveness of the sequence recommendation approaches in terms of NDCG. Results indicate that the evaluated TF, HOSVD, BPR, and CTLSVD approaches predicted more relevant recommendations.

Table 4: Performance comparison

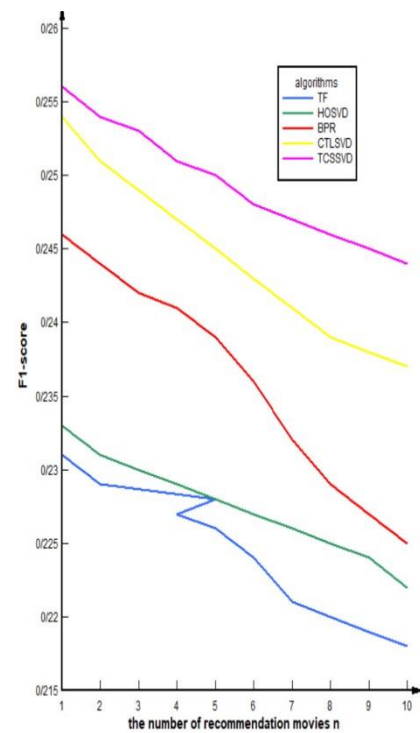
| Method | Top | IMDB | | | STS | | |
|--------|-----|-----------|--------|---------|-----------|--------|---------|
| | | Precision | Recall | F-score | Precision | Recall | F-score |
| CSSVD | 2 | 0.233 | 0.261 | 0.246 | 0.361 | 0.325 | 0.342 |
| | 5 | 0.230 | 0.264 | 0.245 | 0.353 | 0.331 | 0.341 |
| | 10 | 0.227 | 0.271 | 0.247 | 0.342 | 0.336 | 0.339 |
| CTLSVD | 2 | 0.231 | 0.257 | 0.243 | 0.331 | 0.307 | 0.318 |
| | 5 | 0.228 | 0.262 | 0.242 | 0.323 | 0.315 | 0.319 |
| | 10 | 0.223 | 0.269 | 0.244 | 0.318 | 0.321 | 0.320 |
| BPR | 2 | 0.227 | 0.246 | 0.236 | 0.313 | 0.266 | 0.287 |
| | 5 | 0.223 | 0.251 | 0.237 | 0.306 | 0.271 | 0.288 |
| | 10 | 0.220 | 0.256 | 0.236 | 0.295 | 0.278 | 0.286 |
| HOSVD | 2 | 0.222 | 0.233 | 0.227 | 0.297 | 0.256 | 0.274 |
| | 5 | 0.219 | 0.238 | 0.229 | 0.293 | 0.259 | 0.275 |
| | 10 | 0.217 | 0.241 | 0.228 | 0.289 | 0.264 | 0.276 |
| TF | 2 | 0.221 | 0.232 | 0.226 | 0.295 | 0.252 | 0.271 |
| | 5 | 0.218 | 0.234 | 0.225 | 0.291 | 0.258 | 0.274 |
| | 10 | 0.215 | 0.239 | 0.226 | 0.287 | 0.262 | 0.273 |



a) Precision



b) Recall



c) F-score

Fig. 6: The precision, recall and F-score of TF, HOSVD, BPR, CTLSVD and TCSSVD number of recommendations (IMDB).

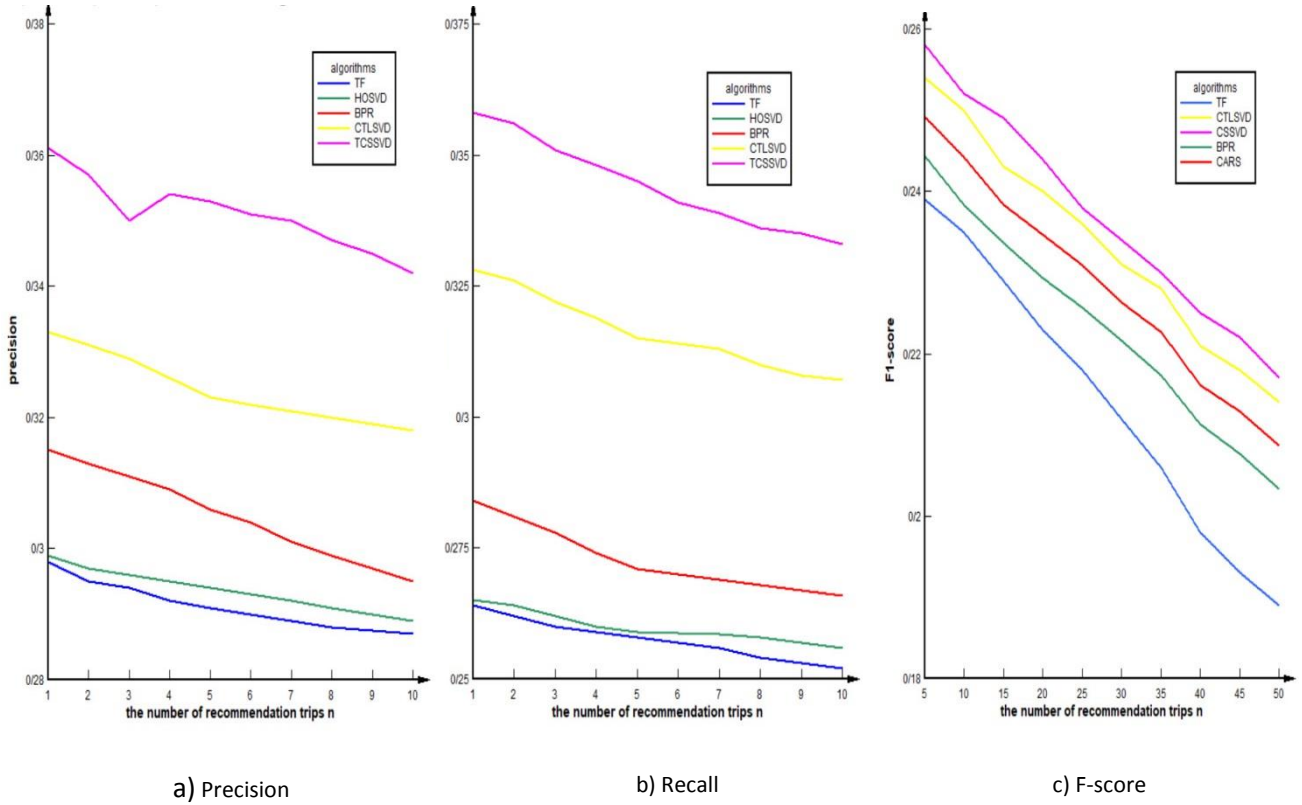


Fig. 7: The precision, Recall and F-score of TF, HOSVD, BPR, CTLSVD and TCSSVD number of recommendations (STS).

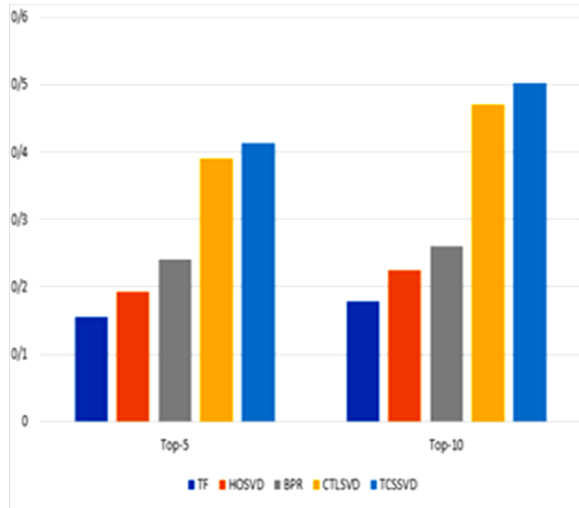


Fig. 8: NDCG measure for different approaches against the top number of recommendations.

Conclusion

This paper proposes a new technique that utilizes a similarity singular value decomposition matrix after reducing the cold start challenge using demographic and item features.

TCSSVD matrix was created using the tensor and contextual information and understanding the dimensions to reduce items not rated for users, also known as the sparse data.

Firstly, users' measured demographics and item property features were used to design the user-item feature matrix besides the PSS similarity measure to create a user-item similarity matrix to reduce the cold start challenge.

Finally, using the resulting matrix of a three-dimensional matrix to reduce calculations and higher convergence speed led to the utilization of the tensor property and the momentum stochastic gradient descent.

Based on results, the proposed technique resulted in an improvement, compared with the TF [6], [55], HOSVD [5], [36], BPR [31], [32] and CTLSVD methods [10].

In future work, we can use other machine learning techniques, such as neural network and LSTM techniques combined with the similarity, LOD, social data, and context criteria, to further improve the recommendations' performance.

Author Contributions

K. Vahidy Rodpysh, S.J. Mirabedini and T. Baniroostam conceived of the presented idea. K. Vahidy Rodpysh developed the theory and performed the computations. S.J. Mirabedini and T. Baniroostam verified the analytical methods. S.J. Mirabedini encouraged K. Vahidy Rodpysh to investigate and supervised the findings of this work. All authors discussed the results and contributed to the final manuscript.

Acknowledgment

The authors gratefully express sincere gratitude to the dear reviewers and editors for their guidance and valuable comments. Moreover, the authors would like to express their appreciation of developers of the “Journal of Electrical and Computer Engineering Innovations (JECEI)” package for their reviews, which have been extensively used in this manuscript, as well as their insight and expertise.

Conflict of Interest

The authors declare no potential conflict of interest regarding the publication of this work. In addition, the ethical issues including plagiarism, informed consent, misconduct, data fabrication and, or falsification, double publication and, or submission, and redundancy have been completely witnessed by the authors.

Abbreviation

| | |
|--------------|---|
| <i>RS</i> | Recommender Systems |
| <i>SVD</i> | Singular Value Decomposition |
| <i>CF</i> | Collaborative Filtering |
| <i>TF</i> | Tensor Factorization |
| <i>MF</i> | Matrix Factorization |
| <i>HOSVD</i> | Higher-Order Singular Value Decomposition |
| <i>LOD</i> | Linked Open Data |
| <i>BPR</i> | Bayesian Personalized Ranking |
| <i>SGD</i> | Stochastic Gradient Descent |
| <i>MSGD</i> | Momentum Stochastic Gradient Descent |
| <i>NDCG</i> | Normalized Discounted Cumulative Gain |
| <i>MSE</i> | Mean Squared Error |
| <i>MAE</i> | Mean Absolute Error |

RMSE

Root Mean Square Error

NHCSM

New Heuristic Context Similarity Measure

References

- [1] S.M. Abbas, K.A. Alam, S. Shamshirband, "A soft-rough set-based approach for handling contextual sparsity in context-aware video recommender systems," *Mathematics*, 7(8): 1-36, 2019.
- [2] M.Y.H. Al-Shamri, "User profiling approaches for demographic recommender systems," *Knowledge Based Syst.*, 100: 175-187, 2016.
- [3] A.B. Barragáns-Martínez, E. Costa-Montenegro, J.C. Burguillo, M. Rey-López, F.A. Mikic-Fonte, A. Peleteiro, "A hybrid content-based and item-based collaborative filtering approach to recommend TV programs enhanced with singular value decomposition," *Inf. Sci.*, 180(22): 4290-4311, 2010.
- [4] M. Braunhofer, "Hybridization techniques for cold-starting context-aware recommender systems," In *Proc. 8th ACM Conference on Recommender systems*: 405-408, 2014.
- [5] M. Braunhofer, M. Elahi, F. Ricci, "User personality and the new user problem in a context-aware point of interest recommender system," in *Proc. Information and communication technologies in tourism*: 537-549, 2015.
- [6] G. Cai, W. Gu, "Heterogeneous context-aware recommendation algorithm with semi-supervised tensor factorization," in *Proc. International Conference on Intelligent Data Engineering and Automated Learning*: 232-241, 2017.
- [7] L.A.G. Camacho, S.N. Alves-Souza, "Social network data to alleviate cold-start in recommender system: A systematic review," *Inform. Process. Manag.*, 54(4): 529-544, 2018.
- [8] Z.D. Champiri, S.R. Shahamiri, S.S.B. Salim, "A systematic review of scholar context-aware recommender systems," *Expert Syst. Appl.* 42(3): 1743-1758, 2015.
- [9] V. Codina, F. Ricci, L. Ceccaroni, "Local context modeling with semantic pre-filtering," in *Proc. 7th ACM Conference on Recommender Systems*: 363-366, 2013.
- [10] L. Cui, W. Huang, Q. Yan, F.R. Yu, Z. Wen, N. Lu, "A novel context-aware recommendation algorithm with two-level SVD in social networks," *Future Gener. Comput. Syst.*, 86: 1459-1470, 2018.
- [11] V.S. Dixit, P. Jain, "Recommendations with sparsity based weighted context framework," in *Proc. International Conference on Computational Science and Its Applications (a)*: 289-305, 2018.
- [12] V.S. Dixit, P. Jain, "An improved similarity measure to alleviate the sparsity problem in context-aware recommender systems," in *Proc. Towards Extensible and Adaptable Methods in Computing (b)*: 281-295, 2018.
- [13] A. Gautam, P. Chaudhary, K. Sindhwani, P. Bedi, "CBCARS: Content boosted context-aware recommendations using tensor factorization," in *Proc. 2016 International Conference on Advances in Computing, Communications and Informatics (ICACCI)*: 75-81, 2016.
- [14] A. Gogna, A. Majumdar, "A comprehensive recommender system model: Improving accuracy for both warm and cold start users," *IEEE Access*, 3: 2803-2813, 2015.
- [15] X. Guan, C.T. Li, Y. Guan, "Matrix factorization with rating completion: An enhanced SVD model for collaborative filtering recommender systems," *IEEE Access*, 5: 27668-27678, 2017.
- [16] J. Herce-Zelaya, C. Porcel, J. Bernabé-Moreno, A. Tejeda-Lorente, E. Herrera-Viedma, "New technique to alleviate the cold-start

- problem in recommender systems using information from social media and random decision forests," *Inf. Sci.*, 536: 156-170, 2020.
- [17] M. Hong, J.J. Jung, "Multi-sided recommendation based on social tensor factorization," *Inf. Sci.*, 447: 140-156, 2018.
 - [18] Y. Hu, Q. Peng, X. Hu, "A time-aware and data sparsity tolerant approach for web service recommendation," in *Proc. IEEE International Conference on Web Services*: 33-40, 2014.
 - [19] N. Idrissi, A. Zellou, "A systematic literature review of sparsity issues in recommender systems," *Social Network Anal. Min.*, 10(1): 1-23, 2020.
 - [20] R. Karimi, C. Freudenthaler, A. Nanopoulos, L. Schmidt-Thieme, "Exploiting the characteristics of matrix factorization for active learning in recommender systems," in *Proc. the sixth ACM conference on Recommender systems*: 317-320, 2012.
 - [21] KDD IMDB dataset, 2020.
 - [22] KDD STS dataset, 2020.
 - [23] K.G. Saranya, G.S. Sadasivam, "A modified heuristic similarity measure for personalization using collaborative filtering technique," *Appl. Math. Inf. Sci.*, 1: 307-315, 2017.
 - [24] D. Kim, C. Park, J. Oh, S. Lee, H. Yu, "Convolutional matrix factorization for document context-aware recommendation" in *Proc. 10th ACM conference on recommender systems*: 233-240, 2016.
 - [25] M. Kolahkaj, A. Harounabadi, A. Nikravanshalmani, R. Chinipardaz, "A hybrid context-aware approach for e-tourism package recommendation based on asymmetric similarity measurement and sequential pattern mining," *Electron. Commerce Res. Appl.*, 42: 100978, 2020.
 - [26] S. Kulkarni, S.F. Rodd, "Context-aware recommendation systems: a review of the state of the art techniques," *Comput. Sci. Rev.*, 37: 100255, 2020.
 - [27] LDOS-CoMoDa dataset, 2019.
 - [28] X. Li, Z. Wang, L. Wang, R. Hu, Q. Zhu, "A multi-dimensional context-aware recommendation approach based on improved random forest algorithm," *IEEE Access*, 6: 45071-45085, 2018.
 - [29] S. Linda, K.K. Bharadwaj, "A genetic algorithm approach to context-aware recommendations based on spatio-temporal aspects," in *Proc. Integrated Intelligent Computing, Communication and Security*: 59-70, 2019.
 - [30] J. Liu, C. Wu, W. Liu, "Bayesian probabilistic matrix factorization with social relations and item contents for recommendation," *Decis. Support Syst.*, 55(3): 838-850, 2013.
 - [31] H. Liu, Z. Hu, A. Mian, H. Tian, X. Zhu, "A new user similarity model to improve the accuracy of collaborative filtering," *Knowledge-Based Syst.*, 56: 156-166, 2014.
 - [32] X. Liu, J. Zhang, C. Yan, "Towards context-aware collaborative filtering by learning context-aware latent representations," *Knowledge-Based Syst.*, 199: 105988, 2020.
 - [33] T. Mahara, "A new similarity measure based on mean measure of divergence for collaborative filtering in sparse environment," *Procedia Comput. Sci.*, 89: 450-456, 2016.
 - [34] A.H. Natarajan, S. Vairavasundaram, S. Natarajan, A.H. Gandomi, "Resolving data sparsity and cold start problem in collaborative filtering recommender system using linked open data," *Expert Syst. Appl.*, 149: 113248, 2020.
 - [35] V.D. Nguyen, S. Sriboonchitta, V.N. Huynh, "Using community preference for overcoming sparsity and cold-start problems in collaborative filtering system offering soft ratings," *Electron. Commerce Res. Appl.*, 26: 101-108, 2017.
 - [36] M. Nilashi, O. bin Ibrahim, N. Ithnin, "Multi-criteria collaborative filtering with high accuracy using higher order singular value decomposition and Neuro-Fuzzy system," *Knowledge-Based Syst.*, 60: 82-101, 2014.
 - [37] V.A. Patil, D.J. Jayaswal, "Context relevancy assessment in tensor factorization-based recommender systems," in *Proc. 3rd International Conference on Communication System, Computing and IT Applications (CSCITA)*: 141-145, 2020.
 - [38] D. Rafailidis, P. Daras, "The TFC model: Tensor factorization and tag clustering for item recommendation in social tagging systems," *IEEE Trans. Syst. Man Cybern.: Syst.*, 43(3): 673-688, 2012.
 - [39] S.K. Raghuwanshi, P.R.K. Pateriya, "Accelerated singular value decomposition (asvd) using momentum based gradient descent optimization," *J. King Saud Univ. Comput. Inf. Sci.*, 2018.
 - [40] S. Raza, C. Ding, "Progress in context-aware recommender systems-an overview," *Comput. Sci. Rev.*, 31: 84-97, 2019.
 - [41] M.S. Reddy, T. Adilakshmi, "Music recommendation system based on matrix factorization technique-SVD," in *Proc. International Conference on Computer Communication and Informatics*: 1-6, 2014.
 - [42] X. Ren, M. Song, E. Haihong, J. Song, "Context-aware probabilistic matrix factorization modeling for point-of-interest recommendation," *Neurocomputing*, 241: 38-55, 2017.
 - [43] S. Renjith, A. Sreekumar, M. Jathavedan, "An extensive study on the evolution of context-aware personalized travel recommender systems," *Inf. Process. Manage.*, 57(1): 102078, 2020.
 - [44] M. Rowe, "SemanticSVD++: incorporating semantic taste evolution for predicting ratings" in *Proc. 2014 IEEE/WIC/ACM International Joint Conferences on Web Intelligence (WI) and Intelligent Agent Technologies (IAT)*: 213-220, 2014.
 - [45] F. Ricci, L. Rokach, B. Shapira, In *Recommender Systems Handbook*, Springer, Boston, 1-35, 2011.
 - [46] L. Safoury, A. Salah, "Exploiting user demographic attributes for solving cold-start problem in recommender system," *Lect. Notes Software Eng.*, 1(3): 303-307, 2013.
 - [47] Z.P. Shan, Y.Q. Lei, D.F. Zhang, J. Zhou, "NASM: Nonlinearly attentive similarity model for recommendation system via locally attentive embedding," *IEEE Access*, 7: 70689-70700, 2019.
 - [48] L.H. Son, "Dealing with the new user cold-start problem in recommender systems: A comparative review," *Inf. Sys.*, 58: 87-104, 2016.
 - [49] A.R. Sulthana, S. Ramasamy, "Ontology and context based recommendation system using neuro-fuzzy classification," *Comput. Elec. Eng.*, 74: 498-510, 2019.
 - [50] Z. Tan, L. He, "An efficient similarity measure for user-based collaborative filtering recommender systems inspired by the physical resonance principle," *IEEE Access*, 5: 27211-27228, 2017.
 - [51] I. Viktoratos, A. Tsadiras, N. Bassiliades, "Combining community-based knowledge with association rule mining to alleviate the cold start problem in context-aware recommender systems," *Expert Syst. Appl.*, 101: 78-90, 2018.
 - [52] N.M. Villegas, C. Sánchez, J. Díaz-Cely, G. Tamura, "Characterizing context-aware recommender systems: A systematic literature review," *Knowledge Based Sys.*, 140: 173-200, 2018.
 - [53] M.G. Vozalis, K.G. Margaritis, "Using SVD and demographic data for the enhancement of generalized collaborative filtering," *Inf. Sci.*, 177(15): 3017-3037, 2007.
 - [54] S. Wang, C. Li, K. Zhao, H. Chen, "Learning to context-aware recommend with hierarchical factorization machines," *Inf. Sci.*, 409: 121-138, 2017.
 - [55] W. Wu, J. Zhao, C. Zhang, F. Meng, Z. Zhang, Y. Zhang, Q. Sun, "Improving the performance of tensor-based context-aware

recommenders using bias tensor factorization with context feature auto-encoding," *Knowledge Based Sys.*, 128: 71-77, 2017.

- [56] X. Xu, D. Yuan, "A novel matrix factorization recommendation algorithm fusing social trust and behaviors in micro-blogs," in *Proc. 2017 IEEE 2nd International Conference on Cloud Computing and Big Data Analysis (ICCCBDA)*: 283-287, 2017.
- [57] N. Yang, Y. Ma, L. Chen, S.Y. Philip, "A meta-feature based unified framework for both cold-start and warm-start explainable recommendations," *World Wide Web*, 23(1): 241-265, 2020.
- [58] X. Yuan, L. Han, S. Qian, G. Xu, H. Yan, "Singular value decomposition-based recommendation using imputed data," *Knowledge Based Sys.*, 163: 485-494, 2019.
- [59] A. Zahid, N.M. Sharef, A. Mustapha, "Normalization-based neighborhood model for cold start problem in the recommendation system," *Int. Arab J. Inf. Technol.*, 17(3): 281-290, 2020.
- [60] Z. Zhang, Y. Zhang, Y. Ren, "Employing neighborhood reduction for alleviating sparsity and cold start problems in user-based collaborative filtering," *Inf. Retr. J.*, 23(4): 449-472, 2020.
- [61] Y. Zheng, B. Mobasher, R. Burke, "Similarity-based context-aware recommendation," in *Proc. International Conference on Web Information Systems Engineering*: 431-447, 2015.

Biographies



Keyvan Vahidy Rodpysh is a Ph.D. student in the Department of Computer Engineering, Central Tehran Branch, Islamic Azad University, Tehran, Iran. His research interests include CRM, Data mining, Churn, Context-Aware Recommender System, Computing, Singular Value Decomposition. (keyvanvahidy@yahoo.com).



Seyed Javad Mirabedini is an Assistant Professor in the Department of Computer Engineering, Central Tehran Branch, Islamic Azad University, Tehran, Iran. His research interests include Computer Networks as well as Intelligent Systems, Information Technology, Business & Expert Systems. (j_mirabedini@iauctb.ac.ir).



Touraj Baniroostam is an Assistant Professor in the Department of Computer Engineering, Central Tehran Branch, Islamic Azad University, Tehran, Iran. His research interests include Cognitive Science Engineering, Artificial Intelligence, Learning, Self-Management Systems. (baniroostam@iauctb.ac.ir).

Copyrights

©2021 The author(s). This is an open access article distributed under the terms of the Creative Commons Attribution (CC BY 4.0), which permits unrestricted use, distribution, and reproduction in any medium, as long as the original authors and source are cited. No permission is required from the authors or the publishers.



How to cite this paper:

K. Vahidy Rodpysh, S.J. Mirabedini, T. Baniroostam, "Hybrid method of recommender system to decrement cold start and sparse data issues," *J. Electr. Comput. Eng. Innovations*, 9(2): 249-263, 2021.

DOI: [10.22061/JECEI.2021.7610.410](https://doi.org/10.22061/JECEI.2021.7610.410)

URL: https://jecei.sru.ac.ir/article_1519.html

